Utilising O_2 chemical potential difference to drive CO_2 separation by ceramic-carbonate dual phase membranes

School of Engineering

Thesis Submitted By

Yuhao Ji

For the Degree of Doctor of Philosophy

Newcastle University

February 2020

Abstract

Carbon dioxide (CO_2) separation using selective membranes is a promising technology for continuous CO_2 capture. However, driving force for CO_2 permeation is often limited, resulting large energy input to sustain CO_2 permeation flux. In this work, ceramic-carbonate dual phase membranes were fabricated for high temperature CO_2 separation at 600-850°C. These membranes consist of molten tertiary carbonate mixture (Li/Na/K, melting point 397°C) infiltrated into porous network of ceramic solid oxide support. When mixed ionic and electronic conductive $La_{0.6}Sr_{0.4}Co_{0.2}Fe_{0.8}O_{3-\delta}$ (LSCF6428) is used for membrane support, O_2 can co-permeate with CO_2 electrochemically via the molten salt (CO_3^{2-}) based on the principle of molten-carbonate fuel cells (MCFCs). Chemical potential gradient of O_2 can be exploited to drive CO_2 permeation. It overcomes the driving force limitation and potentially reduces the energy requirement for CO_2 capture, even allowing CO_2 to permeate against its own chemical potential gradient (uphill permeation).

This project aimed to investigate a novel approach on promoting CO_2 permeation flux by enhancing the thermodynamic driving force of O_2. Firstly, LSCF6428 membrane has been selected to investigate CO_2-O_2 co-permeation from a mechanistic viewpoint. Temperature dependence of CO_2 flux in presence of O_2 in feeding gas has been studied in order to find out the apparent activation energy for CO_2 permeation. Several CO_2 flux-driving force models have been established; each model was associated with a rate-determining scenario incorporating the driving force contribution from O_2. Experimentally observed CO_2 flux-driving force relationship revealed that the CO_2-O_2 co-permeation was likely limited by global interfacial reaction ($CO_2 + 1/2O_2 + 2e^- \leftrightarrow CO_3^{2-}$).

It was further proposed that permeate side O_2 removal may enhance the overall driving force and promote uphill CO_2 permeation flux. A system combining uphill CO_2 permeation with downstream O_2 removal has been developed, utilising LSCF6428 membrane to separate out CO_2 and O_2 from feeding gas (1:1:20 ratio of CO_2, N_2 and O_2), and Cu-based oxygen carrier for O_2 removal. The Cu successfully removed O_2 on membrane permeate side from 400 ppm to 30ppm at 600°C and from 3000ppm to 200ppm at 800°C. Uphill CO_2 flux at 800°C reached 7.62×10^{-4} $mol \cdot m^{-2} \cdot s^{-1}$ with O_2 removal, a 30% enhancement to the flux without O_2 removal. This result was consistent with the prediction from suitable flux-driving force model.

Table of Contents

List of figures

List of tables

Nomenclature

Air separation unit (ASU)

Backscattered electrons (BSE)

Calibration factor (CF)

Carbon dioxide capture and storage (CCS)

Chemical looping combustion (CLC)

Combined Electric Power and Carbon dioxide Separation (CEPACS)

Computed Tomography (CT)

Direct current (DC)

Doped bismuth oxide (BYS or $Bi_{1.5}Y_{0.3}Sm_{0.2}O_{3-\delta}$)

Electrochemical membrane (ECM)

Energy-dispersive X-ray spectroscopy (EDS)

Full width half maxima (FWHM)

Gadolinium-doped ceria (CGO or $Ce_{0.9}\ Gd_{0.1}O_{2-\delta}$)

Gas chromatography (GC)

High temperature shift (HTS).

Infrared CO_2 analyser (IR)

Integrated gasification combined cycle (IGCC)

Intergovernmental Panel on Climate Change (IPCC)

International Energy Agency (IEA)

Lanthanum Strontium Cobalt Ferrite (LSCF or $La_{1-x}Sr_xCo_{1-y}Fe_yO_{3-\delta}$)

Low temperature shift (LTS)

Mass spectrometer (MS)

Mercury intrusion porosimetry (MIP)

Mixed ionic and electronic conductive (MIEC).

Molten carbonate fuel cells (MCFC)

Monoethanolamine (MEA)

Natural gas combined cycle (NGCC).

Oxygen carrier materials (OCM)

Parts per million (ppm)

Polyethylene oxide (PEO)

Polyvinyl alcohol (PVA)

Polyvinyl amine (PVAm)

Pressure swing adsorption (PSA)

Radio frequency (RF)

Relative sensitivity (RS)

Samarium doped ceria (SDC or $Ce_{0.8}Sm_{0.2}O_{2-\delta}$)

Scanning electron microscope (SEM)

Secondary Electron Multiplier (SEM, mass spectrometer)

Secondary electrons (SE)

Silver-carbonate dual phase membrane (Ag-MC)

Solid electrolyte coulometry (SEC)

Standard Temperature and Pressure (STP, 273K and 10^5 Pa)

Support liquid membranes (SLM)

Temperature swing adsorption (TSA)

Thermal conductivity detector (TCD)

Thermogravimetric analysis (TGA)

Water gas shift (WGS)

X-ray diffraction (XRD)

Yttria-stabilized zirconia (YSZ)

Symbols

A_{IR}	Absorbance of the IR energy
ε_a	Absorption coefficient (IR analyser)
E_a	Activation energy
σ_C	Carbonate ion conductivity
$u_{CO_3^{2-}}$	Carbonate ion mobility
φ	Carbonate volumetric fraction
ΔH	Change of enthalpy
ΔS_{mix}	Change of entropy due to gas mixing
ΔG_{mix}	Change of Gibbs free energy of the gas mixing process
z_e	Charge number of an electron
z_C	Charge number of carbonate ion
C	Concentration
θ_C	Contact angle
ρ	Density
β	Difference between the observed peak FWHM and the standard FWHM of Si (111)
θ	Diffraction angle (XRD)
A	Effective permeation area
q	Electrical charge
σ_e	Electronic conductivity
ΔH_S	Enthalpy of sorption
K_d	Equilibrium dissociation constant
ξ	Extent of reaction
J	Flux (gas permeation or ion/charge transport)
J_g	Flux of gas phase mass transfer
y	Gaseous mole fraction
p	Intruding pressure (MIP)
D_k	Knudsen diffusion coefficient
l	Length of the optical path (IR analyser)
X	Liquid phase mole fraction
D	Mass diffusivity
k_g	Mass transfer coefficient in gas phase
L_C	Mean crystallite size (XRD)
u	Mean molecular speed
μ'	Membrane feed side gaseous chemical potential

y'	Membrane feed side gaseous mole fraction
p'	Membrane feed side gaseous partial pressure
P	Membrane permeability
B	Membrane permeance
μ"	Membrane permeate side gaseous chemical potential
y"	Membrane permeate side gaseous mole fraction
p"	Membrane permeate side gaseous partial pressure
d_p	Membrane pore diameter
r_p	Membrane pore size (radius)
ε	Membrane porosity
α	Membrane selectivity
SF	Membrane separation factor
δ	Membrane thickness
τ	Membrane tortuosity
ΔE_{min}	Minimum energy input for CO_2 separation
M	Molecular weight
r	Reaction rate
k	Reaction rate constant
K_S	Shape factor (XRD)
I	Signal intensity (Mass spectrometer)
S	Solubility constant
$\Delta_r G^{\ominus}$	Standard Gibbs free energy of reaction
ϕ	Static potential
γ	Surface tension
T	Temperature
a	Thermodynamic activity
K	Thermodynamic equilibrium constant
L	Thickness of the gas phase boundary layer
V	Volume
F	Volumetric flow rate
λ	Wavelength
m	Weight

Acknowledgements

I would like to sincerely thank my supervisor, Prof. Ian Metcalfe, for giving me the opportunity to work on this project, for his kind guidance and encouragement throughout my PhD that helped me grow not just as a researcher. I also want to thank my co-supervisors Dr Evangelos Papaioannou and Dr Wenting Hu, for their warm and generous support when I was facing challenges.

My work could not be completed without the help of my colleagues, my group members, the school, as well as the collaborators outside the school. Many expert researchers have made enormous efforts for material characterisation in my thesis. I particularly want to acknowledge Dr Maggie White for sharing her knowledge about XRD, Dr Liu Qu and Dr Georgios Triantafyllou for advising me on SEM analysis, Ms Tracey Davey and Mr Ross Laws from the Electron Microscopy Research Services at Newcastle University for providing excellent SEM equipment and trainings, Dr Jing Ji from The University of Bath for organising the mercury intrusion porosimetry tests, and of course Maria for sending the sample through to Jing and collecting the results back. I appreciate the SynFabFun research collaboration that allowed me to access funding and external resources.

In addition, I want to thank my panel of my project progression. Their valuable suggestions have been indispensable throughout my PhD. Ms Justine McGruther and Dr Katarina Novakovic were always my best mentors who guided me through my difficult times. I also want to give credit to Dr Greg Mutch for doing a mock viva with me – that made me a lot more confident during the real viva.

Finally, I would like to attribute the completion of this thesis to my parents and relatives. They have been standing by me all along the journey.

1. Introduction

1.1. Research background: global warming and CO_2 capture

Anthropogenic greenhouse gases emission, particularly the emission of carbon dioxide (CO_2), is believed to be a major factor that causes global warming. Since the industrial revolution, fossil fuels including coal, oil and natural gas have been extensively used to meet the growing energy demand. Large amount of CO_2 produced from fossil fuel combustion has been released to the atmosphere. In 2017, the global energy-related CO_2 emission reached a historic high of 32.5 Gigatonnes (Gt) [1]. The use of energy predominantly for electricity/heat generation and industrial processes sectors, contributes to 68% of global anthropogenic greenhouse gases emission according to the International Energy Agency (IEA) estimates for CO_2 from fuel combustion [2]. The average concentration of CO_2 in the atmosphere has been increasing from pre-industrial level of about 280 parts per million (ppm) to 403ppm in 2016 [2]. Meanwhile, a sharp 1°C rise of global annual average surface temperature was observed [3]. To mitigate the climate change, the Intergovernmental Panel on Climate Change (IPCC) suggested limiting global warming to 1.5°C above pre-industrial level. Accordingly, the global CO_2 emission would need to fall by 45% from current level by 2030, reaching 'net zero' around 2050 [4].

Tackling CO_2 emission requires the adoption of various strategies. The IPCC has summarised the key mitigation options for the energy sector:

- Switching to low carbon fuels such as natural gas, hydrogen and nuclear power.
- Renewable heat and power (hydropower, solar, wind, geothermal and bioenergy).
- Improving energy efficiency.
- Early applications of carbon dioxide capture and storage (CCS) for gas, biomass and coal-fired electricity generating facilities [5].

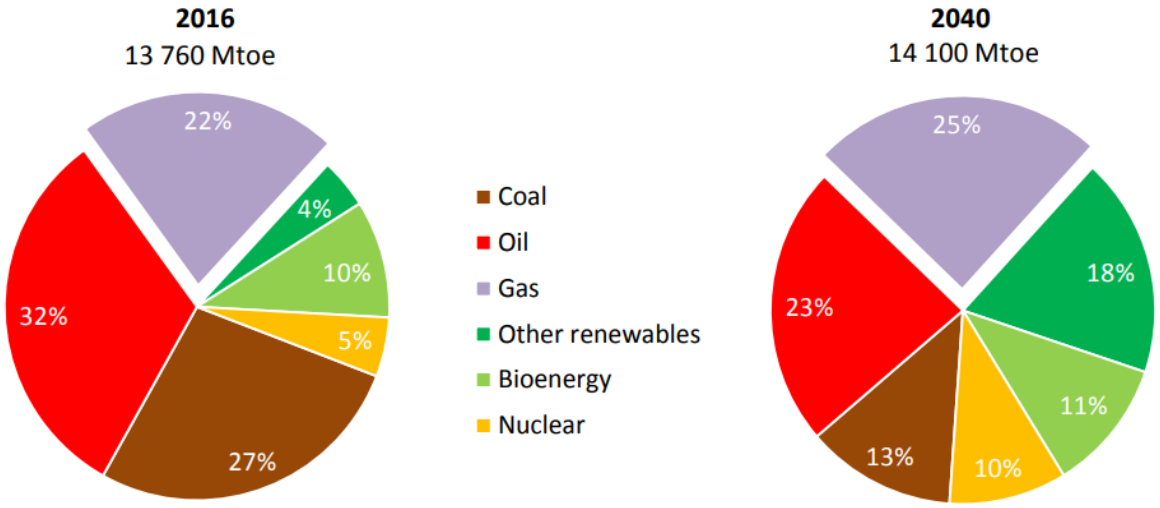

Figure 1.1: Global primary energy demand in the Sustainable Development Scenario – the most optimistic scenario on declining use of fossil fuels and progress towards a more sustainable energy future [6].

Although the renewable energy technologies are fast developing, the global demand on fossil fuels remains high at least in 21st century because of their low cost and high energy density. In 2016 more than three quarters of the global energy production was from the combustion of fossil fuels. Despite the use of coal is gradually being switched to natural gas, the IEA predicts that until 2040, the world would still rely on fossil fuels, which would contribute more than 60% of global primary energy demand (Figure 1.1) [6]. Considering CCS technologies are designed for existing fossil fuel based energy generation and industrial processes, it is important to develop relevant technologies so that the targets on reducing CO_2 emission can be achieved.

CO_2 capture is the first stage of CCS and often highly integrated with large point source of CO_2 emission such as a fossil fuel power plant. Based on the process design CO_2 capture can be classified into three different approaches: post-combustion CO_2 capture, pre-combustion CO_2 capture and oxy-fuel combustion. In post-combustion CO_2 capture, initially fossil fuels are combusted within the air and the exhaust gas stream containing CO_2 is directed to a CO_2 separation unit. Whilst for pre-combustion CO_2 capture gasification of fuels takes place instead of combustion. In gasifier, fossil fuels react with oxygen from an air separation unit (ASU) and produce syngas, followed by water gas shift (WGS) reaction, which converts water (H_2O) and carbon monoxide (CO) into hydrogen (H_2) and CO_2. CO_2 molecules are separated out at this point and H_2 can be further utilised as clean fuel. It is also feasible to combust fuels in oxygen rather than the air; this is known as oxy-fuel combustion. The products of this process are mainly high concentration CO_2 and steam therefore purified CO_2 can be easily obtained by condensation. However, the combustion with pure oxygen is associated to high temperatures and cooled flue gases are recycled back to the combustion furnace and used as heat sink [7]. In addition, chemical looping combustion (CLC) is a modified form of oxy-fuel combustion. In this case, oxygen carrier materials (OCM), often pure or mixed metal oxides, are used to transport oxygen from the air to the fuels such that the process avoids direct contact between the fuels and oxygen [8]. OCM undergoes oxidation and reduction cycles in separate air reactor and fuel reactor, generating exhaust with mainly CO_2 and steam. The schematic diagrams of the above processes are summarised in Figure 1.2 and 1.3.

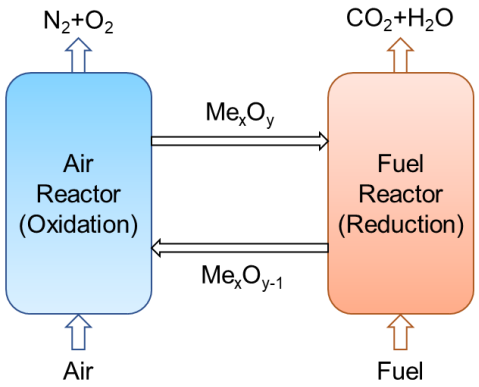

Figure 1.2: Schematic diagrams illustrating chemical-looping combustion. Me_xO_y/Me_xO_{y-1} denotes recirculating oxygen carrier material.

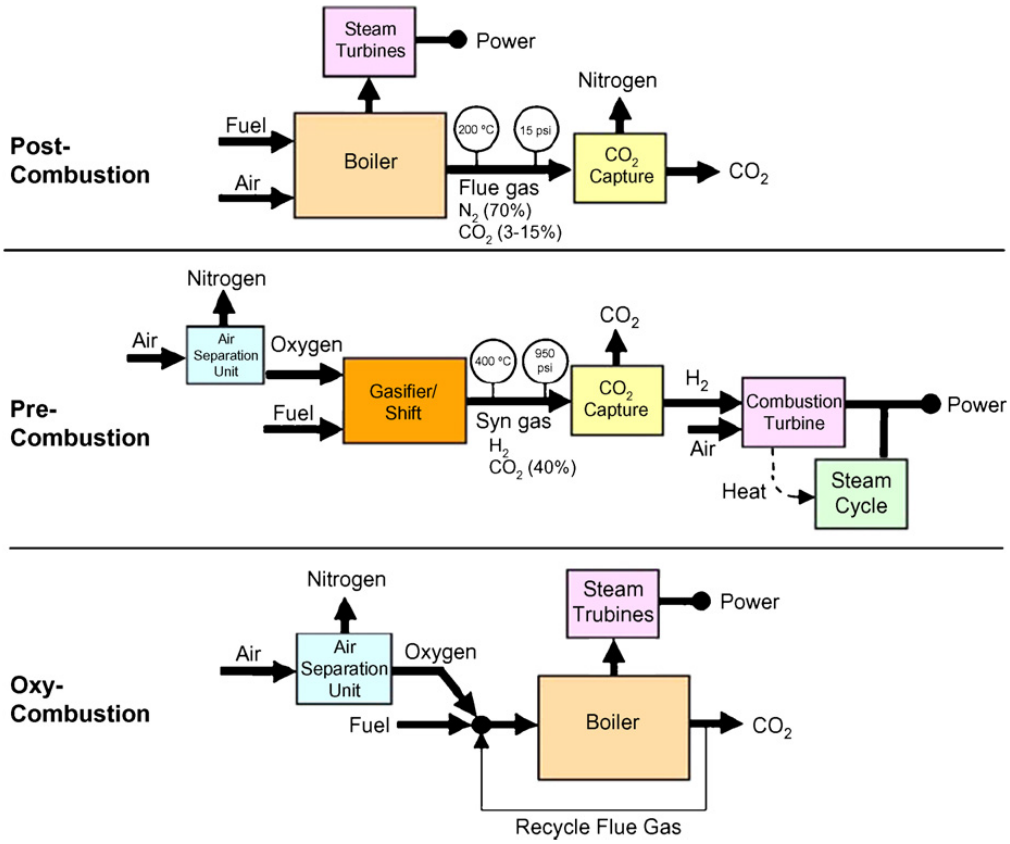

Figure 1.3: Block diagrams illustrating post-combustion, pre-combustion, and oxy-combustion [9]. Reproduced with permission of Elsevier.

Recently the idea of direct CO_2 capture from air became an active area of CCS development as an alternative approach to lower down the CO_2 concentration in the atmosphere. Direct air capture offers an option for addressing CO_2 emissions from mobile and distributed sources such as vehicles. Such a CO_2 separation plant can also be built within a region where the local CO_2 concentration is higher than in the atmosphere [8].

1.2. CO_2 separation technologies and their energy consumption

Among all the approaches, post-combustion, pre-combustion and direct air capture involve CO_2 separation steps that intrinsically subject to energy consumption. To separate CO_2 from a mixture of gases into its pure components, the minimum energy input (ΔE_{min}) is equal to the change of Gibbs free energy of the gas mixing process (ΔG_{mix}) [10]. By assuming the gases are ideal mixture and no chemical reaction or phase change takes place, the change of enthalpy (ΔH) is negligible. Which gives:

$$\Delta E_{min} = \Delta G_{mix} \equiv \Delta H - T\Delta S = -T\Delta S_{mix} \qquad (1.1)$$

The gas mixing process is spontaneous and must correspond to a negative ΔG_{mix} and positive change of entropy due to mixing (ΔS_{mix}). Accordingly, its reverse process requires a positive energy input. This minimum energy input is also related to the mole fraction of CO_2 in the mixture [10].

Table 1.1: Approaches of CO_2 separation applied to various types of power generation processes. Typical gas composition, gas pressure/temperature and CO_2 content associated with each process are reported.

Approaches	Process	Exhaust gas composition	Exhaust gas pressure/temperature	CO_2 concentration
Post-combustion	Coal fired power plant	N_2, CO_2, O_2	200~1000°C ~10^5 Pa [9, 11]	7-14 vol% [12]
	Natural gas combined cycle	N_2, CO_2, O_2, H_2O	615~630°C ~10^5 Pa [13]	4-8.5 vol% [13]
Pre-combustion	Integrated gasification combined cycle + Water gas shift	N_2, CO_2, CO, H_2, H_2O	300-500°C ~35×10^5 Pa [14]	30-60 vol% [15]
direct air capture	-	N_2, CO_2, O_2	25°C ~10^5 Pa	~0.04 vol%

In practical CO_2 separation processes, the energy consumption is expected to be much higher than the thermodynamic minimum energy consumption, due to various separation methods and broad ranges of gas conditions (Table 1.1). Currently solvent absorption is the most mature and commercialised method for post-combustion CO_2 separation [16]. Conventional amine solvent processes make use of 20-30 wt% aqueous monoethanolamine (MEA), which has a nature of high reactivity with gas phase CO_2 at close to room temperature (40°C). Nevertheless, a reboiler is required downstream in order to desorb CO_2 and regenerate the solvent at higher temperature (120°C). This step inevitably involves energy consumption as well as energy loss via heat exchange. Typical energy consumption of the solvent regeneration is 3.6-4.0 GJ per tonne CO_2 captured based on pilot scale plants with 90% CO_2 removal [16]. Since the energy supply normally comes from the combustion heat, around 10%-pts thermal efficiency loss of power plant is anticipated if CO_2 compression for transport is considered [17, 18]. Although the emerging of more advanced solvents has vastly promoted CO_2 capture capacity, it remains a challenge to significantly reduce the energy consumption of solvent regeneration [18].

Adsorption is another conventional method for CO_2 separation reaching beyond pilot plant stage. In general, this technology makes use of porous solid adsorbents including activated carbon, silica and zeolites [16]. When the gas stream passes through the adsorption bed, CO_2 molecules preferentially attach on the surface of adsorbents, by either van der Waals forces (physisorption) or new chemical bonds (chemisorption). Adsorption could potentially be a highly selective process for CO_2 separation, whilst it possesses similar regeneration issue as the solvent process. As adsorption is exothermic process, desorption can be energy intensive once the adsorbent is saturated. CO_2 desorption is normally achieved by periodically rising adsorbent bed temperature or shifting the gas pressure upon adsorbent

bed, known as temperature swing adsorption (TSA) and pressure swing adsorption (PSA) respectively. TSA processes are likely to have energy demands of more than 3 GJ per tonne CO_2 captured [16]. On the other hand, PSA seems to have an equivalent of 4.5-9 GJ/ton of energy demands based on pilot scale experiments [19], as large scale gas compression and vacuum pumping are required.

It appears that relatively developed CO_2 separation technologies share a common feature: most of them are cyclic processes in which temperature swings or pressure swings are necessary for removing CO_2 from capturing materials. As a result, high energy consumption is expected. In the industrial context, a continuous CO_2 separation process is ideal but the technologies often studied are the cyclic processes [7]. Developing continuous CO_2 separation processes with durable materials is an important research area so that more energy efficient CO_2 capture can be delivered.

Membrane based CO_2 separation are next generation technologies. They are made of a thin layer of organic or inorganic materials that are permeable to certain types of molecules through their interconnected channels. Various classes of membranes including polymeric membranes and ceramic membranes are capable of selective gas separation. The gas permeation is driven by the chemical potential gradient of relevant gas species across the membrane. As opposed to conventional technologies, membrane separation operates isothermally and avoids regeneration steps. Chemically and mechanically stable membrane materials are much more resistant to degradation comparing with solvents, which means long-term continuous operation is achievable. It is considered as less energy intensive than cyclic processes involving temperature swings or pressure swings, given that the driving force for gas permeation is sufficient and steady. So far, polymeric membranes for low temperature CO_2 separation are well developed. The main issue with polymeric membranes is they can only operate at a temperature up to 250°C, higher temperature could rapidly destroy the membrane [7, 20]. Referring back to Table 1.1, prior gas cooling process is necessary for polymeric membranes, making high temperature CO_2 separation more desirable as an energy and cost effective option.

Molten carbonate dual phase membranes are an emerging type of membranes allowing high temperature CO_2 separation. They consist of a porous metal or ceramic solid substrate infiltrated with molten binary or ternary mixture of lithium carbonate (Li_2CO_3), sodium carbonate (Na_2CO_3) and potassium carbonate (K_2CO_3). The operating temperature is above the melting point of the carbonate mixture, which is typically above 400°C depending on molten salts composition. They apply the idea of molten carbonate fuel cell (MCFC) by using ionic/electronic conductive solid phase and high carbonate ions (CO_3^{2-}) transport molten phase without requiring external electrodes. This feature enables facilitated CO_2 transport, which allows interfacial reactions involving CO_2 specifically. Hence, dual phase membranes may offer very high CO_2 selectivity. This unique property accounts for the great advantage over most polymeric and porous inorganic membranes, where solution diffusion or size selection mechanism is dominant on CO_2 transport [21]. This project focused on developing molten carbonate dual phase membranes for high temperature CO_2 separation.

1.3. Potential applications of dual phase membranes

Typical ionic conductive molten carbonate dual phase membranes are solely CO_2 selective. They can be applied to both pre-combustion and post-combustion CO_2 capture. CO_2 can be separated directly from the hot flue gas and water gas shift (WGS, reaction 1.2) product. In the scenario of pre-combustion, it is required to separate CO_2 from WGS product gas with high pressure, high concentration CO_2 and H_2, as well as minor components including CO, H_2O and N_2. With volume percentage of more than 30% and 3.5-4.0 MPa pressure on membrane feed side, sufficient CO_2 partial pressure gradient is available to drive CO_2 permeation to a high purity permeate stream at atmospheric pressure. A few energy/economic evaluation studies showed that applying CO_2 selective dual phase membranes onto an integrated gasification combined cycle (IGCC) + WGS system appeared to be more energy/cost efficient than conventional ethylene glycol based absorption (Selexol^{TM}) technology [14, 22]. due to lower energy consumption on gas compression and the absence of cooling/heating cycles [14]. The conversion of WGS reaction also benefits from the direct CO_2 separation. WGS reaction can be operated within two temperature regimes: 180 to 250°C and 350 to 420°C [23], namely low temperature shift (LTS) and high temperature shift (HTS). The temperature of LTS and HTS product gas are around 300 and 500°C respectively [14], Because of its exothermic nature, the conversion of CO decreases with increase of temperature [23]. The stand-alone reaction cannot maintain good conversion to produce H_2. With in-situ removal of the CO_2 from the reaction product, the thermodynamic equilibrium of the reaction will shift towards H_2 side and promote the conversion of WGS. The operating temperature of dual phase membrane potentially overlaps with the HTS product gas.

$$CO + H_2O \rightleftharpoons CO_2 + H_2 \qquad \Delta H^{\ominus} = -40.6 kJ/mol \qquad (1.2)$$

Applying molten carbonate dual phase membranes into post-combustion CO_2 capture is more challenging in terms of thermodynamic driving force. The flue gas is just above atmosphere pressure and the dominant component is nitrogen. The concentration range of CO_2 varies from 7% to 14% by volume in coal-fired power plant and as low as 4% for natural gas combined cycle (NGCC). If CO_2 is the only gas component involved on permeation, there must be a positive chemical potential difference across the membrane in order to provide the driving force for spontaneous permeation. According to thermodynamic laws, feed side CO_2 partial pressure (p'_{CO_2}) must be larger than permeate side (p''_{CO_2}) ('downhill' permeation). CO_2 partial pressure is much lower in flue gas for post-combustion CO_2 capture than pre-combustion. The limitation here is that the driving force is insufficient for producing concentrated CO_2 stream without compression of feeding gas or vacuuming the permeate stream. Large energy consumption is inevitable for setting up the driving force [24]. Various models have shown that for a general single-stage membrane system with 80% CO_2 removal to 80% purity in permeate stream, the energy required for applying feed mixture compression has stronger correlation to feed CO_2 concentration rather than the membrane selectivity. With 10% CO_2 in the feed, compression would

consume more than 6 GJ/tonne CO_2 recovered and the advantage over amine process is limited. Whilst with 20% feed CO_2 concentration would only consumes 2-3 GJ/tonne CO_2 recovered, which is a greatly reduced energy requirement comparing with amine processes [25, 26]. R. Anantharaman et al. also evaluated that applying CO_2 selective dual phase membrane into NGCC post-combustion carbon capture appeared to be less energy efficient than MEA absorption process, due to the compression of feed stream for setting up driving force over the membrane [14]. Therefore, application is limited to flue gases with more concentrated CO_2 content (20-30%) such as cement and steel production plants [27]. Enhancing driving force and reducing energy consumption for power plant post combustion CO_2 capture is a key area for further development on dual phase membranes.

One possible solution is developing CO_2 and O_2 co-permeable molten carbonate dual phase membranes [28]. These membranes generally consist of electronic conductive or mixed ionic and electronic conductive (MIEC) solid phase. Since both CO_2 and O_2 are involved in the interfacial reaction that facilitates CO_2-O_2 co-permeation, O_2 may offer extra chemical potential upon CO_2-O_2 co-permeation. CO_2 permeation from membrane feed to permeate side will be spontaneous if there is a positive driving force, represented by overall chemical potential difference across the membrane. According to the proposed interfacial reaction [28], this can be written as equation 1.3 in terms of chemical potential and equation 1.4 in terms of gaseous partial pressure.

$$\mu'_{CO_2}(T) + \frac{1}{2}\mu'_{O_2}(T) > \mu''_{CO_2}(T) + \frac{1}{2}\mu''_{O_2}(T) \qquad (1.3)$$

$$\left(\frac{p'_{O_2}}{p''_{O_2}}\right)^{1/2} > \left(\frac{p''_{CO_2}}{p'_{CO_2}}\right) \qquad (1.4)$$

$\mu'_{CO_2}(T)$ = feed side CO_2 chemical potential at temperature T.

$\mu''_{CO_2}(T)$ = permeate side CO_2 chemical potential.

p'_{CO_2} = feed side CO_2 partial pressure.

p''_{CO_2} = permeate side CO_2 partial pressure. (Likewise for O_2 on all symbols)

Hence, higher feed side CO_2 partial pressure would not be necessary for an O_2-CO_2 co-permeable dual phase membrane. With the aid of O_2 co-permeation, the membrane could overcome the driving force limitation when the feeding CO_2 partial pressure is low, such as post-combustion CO_2 separation. The presence of oxygen in flue gas can be exploited to enhance the driving force for CO_2 permeation, such that the energy consumption due to gas compression and vacuuming across the membrane can be potentially reduced. Furthermore, if the oxygen chemical potential difference is high enough, CO_2 will be able to permeate against its own chemical potential gradient, thus a more CO_2 rich permeate stream can be obtained from a feed stream relatively lower CO_2 partial pressure. This phenomenon of 'uphill' CO_2 permeation has been demonstrated experimentally [28]. From the application point of view, the uphill permeation may allow to concentrate CO_2 stream in single stage or stepwise.

Based on equation 1.3 and 1.4, reducing the value of permeate side O_2 partial pressure can potentially enlarge the chemical potential difference across the membrane. The system incorporating downstream O_2 removal could further promote the driving force for CO_2 transport. Meanwhile, O_2 can be separated out of CO_2 in permeate stream. Similarly, CO_2 or O_2 enrichment on membrane feed side is also expected to promote the driving force. In this project, a novel concept which combines O_2-CO_2 co-permeable dual phase membranes with permeate stream O_2 removal has been proposed. It has been primarily focused on using solid oxygen carrier materials (OCM) for O_2 removal for the purpose of driving force enhancement. The OCM acts as an oxygen sink when the permeate stream passes through, reacts with O_2 with itself being oxidised. The material would need to be in contact with reducing gas such as CO and H_2 periodically to recover the O_2 capacity. The schematic diagrams of the system are shown on the dual phase membrane unit in Figure 1.4.

It is possible to incorporate the concepts into practical CO_2 capture processes in two ways: (a) Combust the fuel under oxygen enriched atmosphere so that the flue gas contains higher CO_2 concentration. This is a hybrid combustion process merging the features of oxy-fuel combustion and post-combustion CO_2 capture [29]. An air separation unit is required before combustion process. Configuration is shown in Figure 1.4(a). (b) Incorporate an air separation unit before CO_2 separation so that the flue gas of air combustion is enriched with O_2. Configuration is shown in Figure 1.4(b). As it is not necessary to obtain high oxygen purity via ASU, the energy requirement of ASU process itself can be minimised to ensure that it does not compensate the mitigation of energy requirement for CO_2 separation [29].

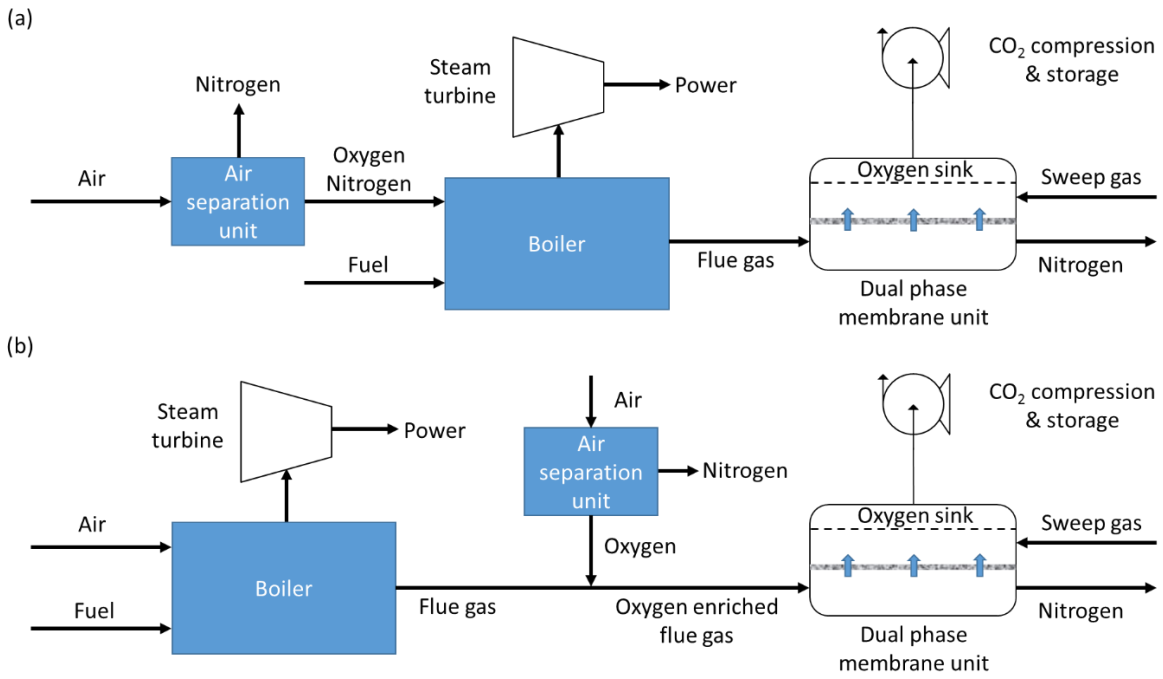

Figure 1.4: Schematic diagrams of post-combustion CO_2 separation, incorporating O_2-CO_2 co-permeable dual phase membrane and downstream O_2 removal. Configuration (a) uses gas mix with enriched O_2 content for combustion. Configuration (b) blends flue gas with O_2 upon membrane separation unit.

1.4. Aims and objectives

It has been recognised that enhancing driving force upon CO_2 permeation using dual phase membranes could be beneficial for reducing its energy requirement, especially when dual phase membranes are applied to post-combustion CO_2 capture. Considering a commercial scale power plant could generate flue gases at a rate of 500 m^3/s [30]. The membrane permeation flux is another key parameter to improve in order to achieve the desirable CO_2 removal rate in an energy and cost effective way. The concept of O_2-CO_2 co-permeable dual phase membranes combining with oxygen removal has been proposed for this project, aiming for enhancing the driving force for CO_2 permeation. Nevertheless, how the driving force affects CO_2 permeation flux is a question to be studied.

To find a relationship between the driving force and CO_2 permeation flux, deeper understanding on the CO_2 transport mechanisms through molten carbonate dual phase membranes is necessary. For this project, a well-established pressing and sintering technology is exploited for the fabrication of disk shape dual phase membranes. A laboratory scale high temperature membrane reactor and flow system are built for testing membrane performance under various gas atmosphere at high temperatures (600-850°C). The key objectives of this project are summarised as follows:

- Investigate how oxygen co-permeation affect CO_2 permeation flux on inert, ionic conductive and mixed ionic/electronic conductive (MIEC) dual phase membranes respectively. Alumina, Yttria-stabilized zirconia (YSZ) and $La_{0.6}Sr_{0.4}Co_{0.2}Fe_{0.8}O_{3-\delta}$ (LSCF6428) were chosen to represent each type of membrane support materials.

- Experimental study on the correlation between CO_2 flux and the driving force under 600 and 800°C temperature regimes for CO_2-O_2 co-permeable LSCF6428 membranes. Gain mechanistic insight of the CO_2 transport though LSCF6428-carbonates dual phase membranes.

- Test the system combining LSCF6428-carbonates dual phase membranes with permeate stream oxygen removal for CO_2 uphill permeation. Experimental study on the thermodynamic effect of permeate stream oxygen removal as well as the response of uphill CO_2 permeation flux.

2. Literature review

2.1. Membrane based technologies for CO_2 separation

2.1.1. Principles of gas separation membranes

Acting as a selective barrier, membrane processes are continuous and effective for gas separation. Various types of membranes have been developed and applied on gas separation in industry. The most fundamental gas permeation mechanisms through membranes are solution diffusion mechanism and pore diffusion mechanism. They correspond to the two most common types of membrane: organic polymeric membranes and inorganic porous membranes. Advanced composite membranes, particularly facilitated transport membranes and mixed matrix membranes, are also designed and studied extensively. They are usually governed by specific transport mechanisms, making them more selective to target gas molecules.

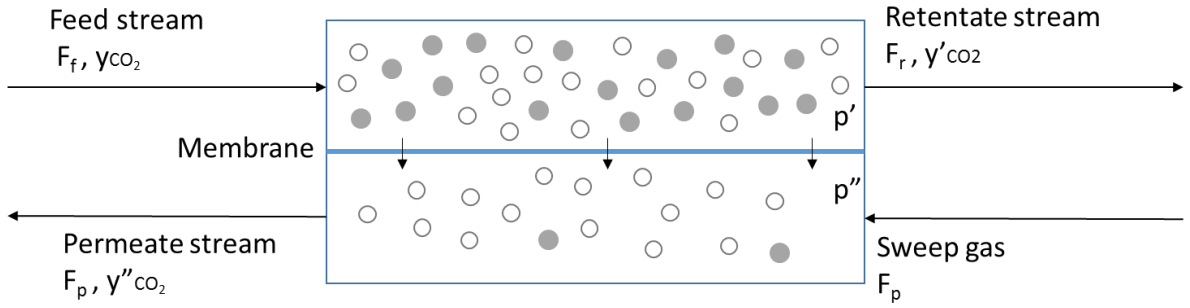

Figure 2.1: A simple illustration of membrane process for gas separation, setting CO_2/N_2 separation as an example. The filled blobs represent N_2 molecules and unfilled blobs represents CO_2 molecules.

The membrane module in operation as shown in Figure 2.1 generally consists of three flow streams: feed stream with molar flow rate of F_f and CO_2 mole fraction of y_{CO_2}, permeate stream with flow rate of F_P and CO_2 mole fraction of $y"_{CO_2}$, and retentate (non-permeating) stream with flow rate of F_r and CO_2 mole fraction of y'_{CO_2}. Mass balance on CO_2 can be written as equation 2.1:

$$F_f \times y_{CO_2} = F_p \times y"_{CO_2} + F_r \times y'_{CO_2} \qquad (2.1)$$

As mentioned in the previous chapter, permeation flux, permeability and selectivity are the most important parameters to describe the functionality of a membrane. Assuming perfect mixing along the membrane surfaces such that both sides of the membrane are exposed to the outlet gas partial pressures, the molar permeation flux of CO_2 and N_2 across the membrane J_{CO_2} and J_{N_2} with unit of $mol \cdot m^{-2} \cdot s^{-1}$ can be expressed as equation 2.2 and 2.3, based on the case in figure 2.1.

$$J_{CO_2} = \frac{F_p \times y"_{CO_2}}{A} = \frac{P_{CO_2}}{\delta}(p'y'_{CO_2} - p"y"_{CO_2}) \qquad (2.2)$$

$$J_{N_2} = \frac{F_p \times y"_{N_2}}{A} = \frac{P_{N_2}}{\delta}(p'y'_{N_2} - p"y"_{N_2}) \qquad (2.3)$$

In these equations, A and δ stand for effective membrane permeation area and membrane thickness respectively. P_{CO_2} and P_{N_2} denote the permeability of CO_2 and N_2. They reflect the property of the membrane material and are irrelevant to membrane geometry. The products within the brackets represent the partial pressure difference across the membrane as the driving force for gas permeation, with feed side pressure of p' and permeate side pressure of p''. The ratio of membrane permeability to CO_2 and N_2 with notation of α is defined as the selectivity of the membrane (equation 2.4). Separation factor is a similar concept and defined as equation 2.5.

$$\alpha = \frac{P_{CO_2}}{P_{N_2}} \qquad (2.4) \qquad\qquad SF = \frac{y''_{CO_2}/y''_{N_2}}{y'_{CO_2}/y'_{N_2}} \qquad (2.5)$$

2.1.2. Fundamental permeation mechanisms

Pore diffusion model is commonly used to describe the gas transport mechanism through porous membranes. The gas permeation behaviour may be dominated by various transport regimes depending on the ratio of the pore size (r_p) and the mean free path of the gas molecules (λ) [31]. Table 2.1 summarises the conditions for each pore diffusion regime with relevant illustrations in Figure 2.2.

Table 2.1: Conditions for each pore diffusion regime.

Pore diffusion regime	Conditions
Viscous flow	$r_p/\lambda > 3$ [32]
Slip flow	$0.05 < r_p/\lambda < 3$ [32]
Knudsen diffusion	$r_p/\lambda < 0.05$ [33]
Activated micropore diffusion	Pore size r_p becomes comparable to the molecular size [34].
Molecular sieving	Pore size r_p approaching the diameter of the permeating molecules [35].

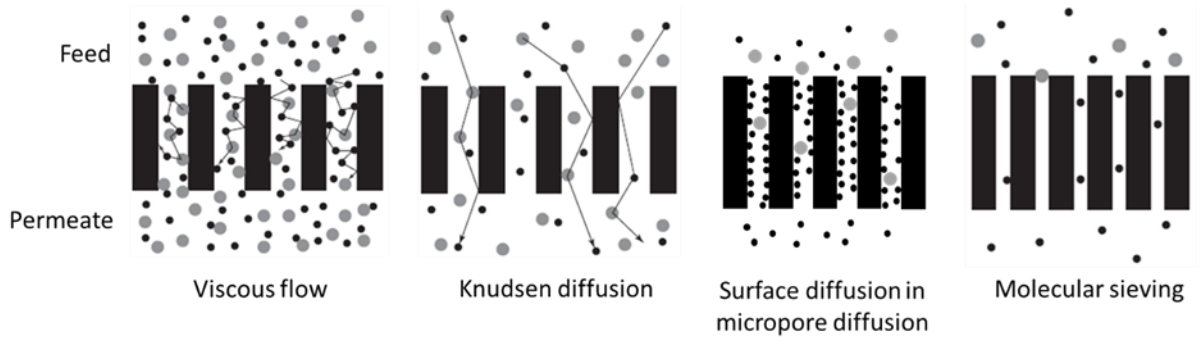

Figure 2.2: Illustration for the viscous flow, Knudsen diffusion, surface diffusion (micropore diffusion) and molecular sieving mechanisms [35]. Grey and black balls represent gas molecules with different sizes. Reproduced with permission of Elsevier.

Knudsen diffusion is predominant in macroporous (r_p>50nm) and mesoporous membranes (r_p between 2 and 50nm) [31, 35]. Gas transport follows Knudson diffusion mode when the mean free path of the gas molecules (λ) is much greater than the pore size of the membrane (r_p). In other words, the molecules-pore wall collisions are more frequent than the molecules-molecules collisions [31]. Knudsen diffusion coefficient D_k can be expressed as:

$$D_k = \frac{2}{3}\frac{\varepsilon}{\tau} r_p u = \frac{2\varepsilon r_p}{3\tau}\left(\frac{8RT}{\pi M}\right)^{1/2} \qquad (2.6)$$

In this equation, ε and τ are the porosity and the tortuosity of substrate pore structure; u is the mean molecular speed and M is the molecular weight of permeating gas. The Knudsen Equation for diffusive flow can describe the flux equation of this pore diffusion regime [36]:

$$J = -\frac{D_k}{RT}\left(\frac{dp}{dz}\right) \qquad (2.7)$$

It can be seen that the flux is proportional to the partial pressure gradient of permeating gas (dp/dz) as well as the Knudsen diffusion coefficient D_k, which is inversely proportional to the gas molecular weight. Based on this expression, the difference in gas molecular weight is the origin that makes Knudsen diffusion a selective transport mechanism. Lighter molecules tend to have higher mean molecular speed in Knudsen diffusion regimes hence higher flux through the porous medium.

When the pore size increases to the extent that it is much larger than the mean free path of the gas molecules, molecule-molecule collisions become more frequent and there is minimum interaction between the gas molecules and the pore walls. The gas molecules would form a bulk or laminar flow pattern if they were exposed to a drive force. The membranes lose selectivity in viscous flow regime, as the flux in this regime has no dependence on each individual gas components [31, 35]. Slip flow can be seen as a transition regime between Knudsen diffusion and viscous flow.

Microporous (1nm to 2nm) and nanoporous membranes have smaller pore sizes approaching or even similar to the size of permeating gas molecules. As a result, the diffusion coefficients of the two gases are strong functions of the molecular shape and size, the pore size, and the strength of the interactions between pore walls and molecules. In addition, molecules with stronger affinity to the membrane material will be adsorbed onto the pore walls and undergo surface diffusion along the walls. For small pore sizes this behaviour often obstructs other molecules with weaker interaction with the pore walls hence enhances the selectivity [34]. Molecular sieving is a similar mechanism as microporous diffusion. Membrane selectivity has even stronger dependence on the molecular size, as large molecules are often rejected from the entrance of porous network and retain on the feed side. Overall, the pore diffusion model suggests that inorganic porous membranes are molecular weight/size selective, with Knudsen diffusion and molecular sieving being the most important selection mechanism. The progression from Knudsen diffusion to molecular sieving is in parallel with increasing membrane selectivity [31].

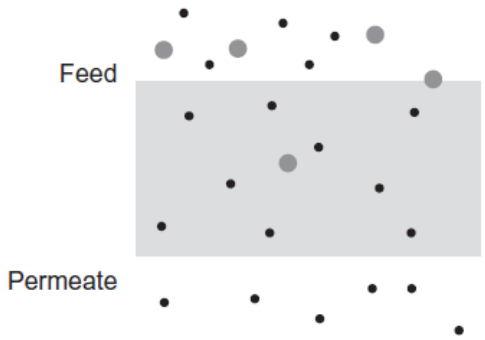

Figure 2.3: Illustration for the solution diffusion mechanism through homogeneous medium (grey box) [35]. Grey and black balls represent gas molecules with different solubility in homogeneous medium. Reproduced with permission of Elsevier.

Organic polymeric membranes generally have homogeneous and nonporous features. Gas transport through this type of membranes more likely occur via the solution diffusion mechanism. The mechanism involves dissolution of permeant on feed side interface, molecular diffusion through the homogeneous medium, and gas desorption on permeate side (Figure 2.3). Henry's law governs the solubility of the permeant and molecular diffusion through nonporous homogeneous medium follows Fick's law of diffusion [35, 37]. By combining the two concepts, the molar flux through the membrane via solution diffusion model can be expressed as:

$$J = -D\frac{dC_i}{dx} = -SD\frac{dp_i}{dx} \qquad (2.8)$$

$$J = -\frac{SD}{\delta}\int_{p'_i}^{p"_i} dp_i = \frac{SD}{\delta}(p'_i - p"_i) \qquad (2.9)$$

D represents gas diffusivity within the homogeneous medium and dC_i/dx represents the concentration gradient of the gas specie i across the membrane. The concentration of the gas can be written as $C_i = Sp_i$ based on Henry's law, where S is the solubility constant and p_i is the gas partial pressure. Integrating through the entire membrane thickness δ gives equation 2.9.

By comparing equation 2.9 with equation 2.2, gas permeability P can be written as a product of thermodynamic factor S (solubility coefficient), and kinetic parameter D (diffusion coefficient). The temperature dependence of D and S obeys the Arrhenius equation:

$$\mathrm{P} = \mathrm{S} \times \mathrm{D} = S_0 \exp\left(-\frac{\Delta H_s}{RT}\right) \times D_0 \exp\left(-\frac{E_d}{RT}\right) = P_0 \exp\left(-\frac{E_p}{RT}\right) \qquad (2.10)$$

E_p is activation energy of gas permeation; E_d is activation energy of diffusion and ΔH_S is the enthalpy of sorption. P_0, S_0 and D_0 are pre-exponential constants [38, 39]. Therefore, according to the solution diffusion mechanism, the permeability of each individual gas components is not only influenced by the gas solubility but also the molecular diffusivity in the membrane material. Relative values of both parameters for permeating gases determine the membrane selectivity at any specific temperature.

One important application of gas separation membranes is in the field of CO_2 capture processes. For example, membranes for CO_2/H_2 separation is associated with pre-combustion CO_2 capture; An O_2/N_2 separating membrane can also be utilised for ASU to deliver enriched O_2 to pre-combustion and oxy-fuel combustion systems. This chapter will primarily focus on reviewing various types of CO_2 permeable membranes.

2.1.3. Single phase membranes for CO_2 separation

Polymers were one of the first a few materials considered for membrane based CO_2 separation. Polysulfone and cellulose acetate are the earliest commercial membranes and they have been joined by more recent development on a variety of materials such as polyimides, polyamides, polycarbonates [40]. The operating temperature of non-facilitated polymeric membranes is typically above their glass transition temperature, making their behaviour liquid like [30]. However, as previously mentioned most polymeric membranes cannot withstand a temperature higher than 250°C. The application of polymeric membrane is therefore confined to low temperature CO_2 separation, for instance post-combustion with prior cooling and pre-combustion in association with LTS process. CO_2/N_2 or CO_2/H_2 selectivity is an important parameter for assessing the performance of polymeric membranes. Early work on polysulfone and cellulose acetate based polymeric membranes showed CO_2/N_2 selectivity of 20 to 30 with poor chemical stability. Later research found out polymers with polar functional groups including polyimides and polyethylene oxide (PEO) based membranes tend to have better affinity and solubility to CO_2 molecules, CO_2/N_2 selectivity could be improved to 40-60 [37]. Nevertheless, improvement on selectivity often accompanies with a drop in CO_2 permeability [41]. In general, polymeric membranes benefit from low cost, ease of synthesis, and good mechanical stability under low temperature whereas their temperature endurance and selectivity-permeability trade-off are the main drawbacks [42].

In contrast, most inorganic porous membranes exhibit high temperature endurance. In the context of CO_2/N_2 separation, the pore diffusion model suggests that macroporous and mesoporous inorganic membranes cannot have strong selectivity on CO_2 due to its similar molecular weight with N_2. Microporous and molecular sieving membranes have drawn attention to the researchers as they can potentially offer higher CO_2 selectivity. Inorganic materials including zeolite, carbon molecular sieves and microporous silica membranes fall into this category. Zeolites are well-defined crystalline materials with uniform pore microstructure. Micropore diffusion and molecular sieving likely dominate gas transport through porous zeolites. Selective adsorption of gas molecules on zeolites by molecular size and polarity makes CO_2 more favourable to permeate across the membrane at low temperature. At elevated temperature higher than 100°C, zeolites start to lose selectivity to CO_2 due to the decrease of adsorption capacity [43, 44]. Amorphous silica is a versatile material because the pore microstructure can be tailored by changing the preparation method and conditions. Although a few silica-based membranes showed reasonable CO_2 permeability up to 300°C, decreasing permeability and selectivity at higher temperatures remains a general trend [43]. Carbon molecular sieving membranes contain

narrower pores and tend to be more selective than silica and zeolite membranes. CO_2/N_2 selectivity of higher than 100 have been demonstrated in laboratory experiments, whilst these have been achieved only at very low permeability. Further research is also required to improve their mechanical strength to avoid thermal cracking [35].

2.1.4. Composite membranes for CO_2 separation

Purely polymeric or inorganic porous membranes exhibit clear advantages and shortcomings. In recent years, novel composite membranes that combine the advantages of fundamental gas transport mechanisms have been emerging. One example of them is facilitated transport membranes. These membranes normally comprise a porous support as well as active carrier material. The carrier can either be a top layer or incorporate within the porous structure and it is chosen to interact with CO_2 specifically. As shown in Figure 2.4, the inlet CO_2 on membrane feed side undergoes reversible chemical reaction with the carrier and form products such as complexes, followed by the facilitated transport across the membrane with the carrier. The complexes then dissociate CO_2 on membrane permeate side via the reverse reaction while the carrier is recovered. The active carrier itself can be mobile or fixed. Support liquid membranes (SLM) consist of a liquid phase containing a carrier species in the pores of a polymer support and they were the first developed facilitated transport membranes with mobile carrier [37]. On the other hand, polymer layer with active functional groups such as amine attached to the polymer backbone can be used as fixed carrier. CO_2 reacts with the active functional group and the products diffuse across the membrane between carrier sites along the polymer backbone [35].

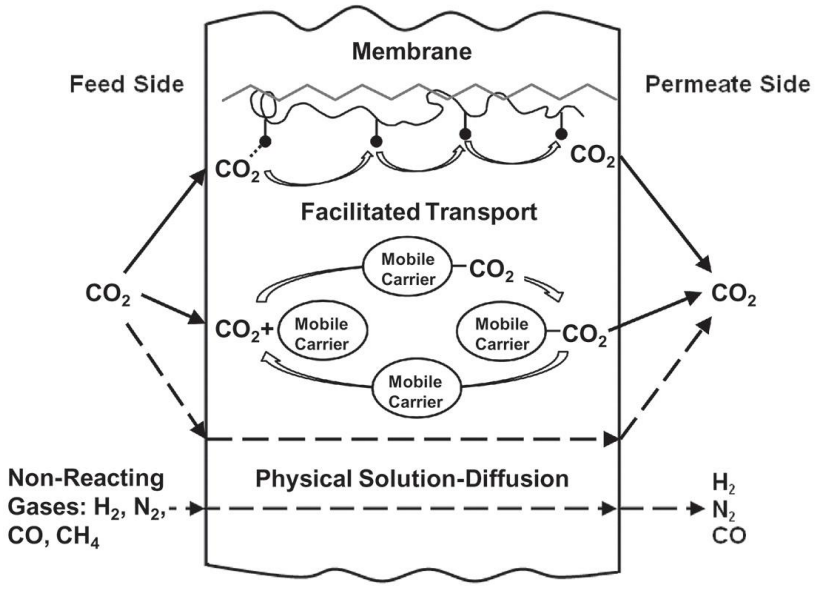

Figure 2.4: Active transport mechanisms through facilitated transport membranes. Top: fixed carrier transport; middle: mobile carrier transport; bottom: non-facilitated transport [45].

Having facilitated CO_2 transport mechanism activated, other gas species regardless their molecular sizes will not compete with CO_2 in this mechanism and can only transport in non-facilitated routes. The fixed-

site carrier can increase the membrane stability due to its polymeric nature and is stable inherently in the membrane. One typical fixed carrier facilitated transport membrane being widely studied is polyvinylamine (PVAm) carrier supported on crosslinked polyvinylalcohol (PVA). At room temperature this type of membrane can offer 10^{-8} mol·m^{-2}Pa^{-1}s^{-1} CO_2 permeance, with higher than 100 CO_2/N_2 selectivity and around 50 CO_2/CH_4 selectivity [45].

In supported liquid membranes, CO_2 transport takes place through the liquid in the pores following the CO_2 selective interfacial reaction. High selectivity and flux can be achieved because the liquid mobility in porous network allows large fluxes and liquid compounds in the pores offer high selectivity [42]. Ionic liquid is a common choice for the carrier liquid as they have high temperature durability and negligible volatility [37]. It has been demonstrated experimentally that at 100°C amino acid based ionic liquid membranes can achieve CO_2/N_2 selectivity of 100 while maintaining CO_2 permeability of 10^{-11} mol·m^{-1}Pa^{-1}s^{-1} [46]. An amine-functionalised ionic liquid encapsulated in a supported ionic liquid membrane has been shown thermally stable and operable at 300°C. The membrane selectivity dropped at higher temperature possibly due to higher complex dissociation rate. Nevertheless, the membrane showed potential for pre-combustion CO_2/H_2 separation [47].

Molten carbonate dual phase membrane is a special case of facilitated transport membranes in terms of gas transport mechanism. The concept (see Figure 2.5 and 2.6) is particularly similar to supported liquid membranes. Here the high temperature molten carbonate mixture acts as the liquid phase mobile CO_2 carrier. Solid phase ceramic support materials are responsible for bulk oxide ions/electrons transport, so that charged species can be delivered to feed side interface and undergo electrochemical reaction with inlet CO_2.

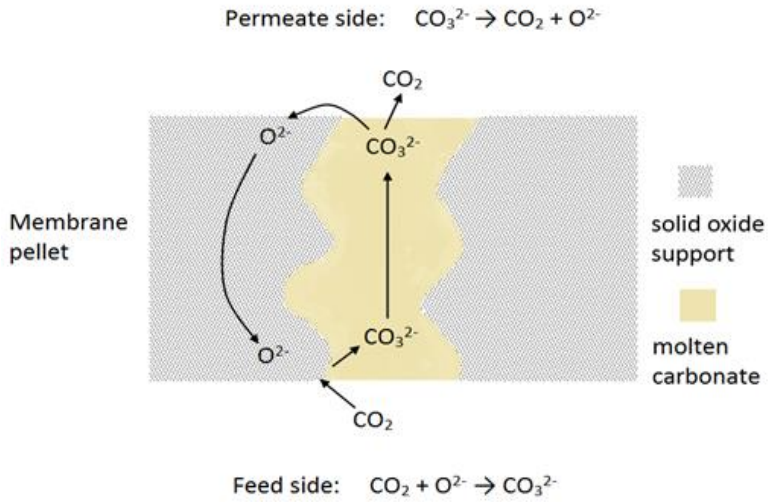

Figure 2.5: Proposed CO_2 transport mechanism through membranes with oxide ion (O^{2-}) conductive support. CO_2 molecules on membrane feed side react with O^{2-} on gas/solid/molten salts three-phase boundary and form CO_3^{2-} that in turn diffuse across the membrane. The reverse electrochemical reaction occurs on permeate side to release CO_2 and return O^{2-} to the bulk solid phase.

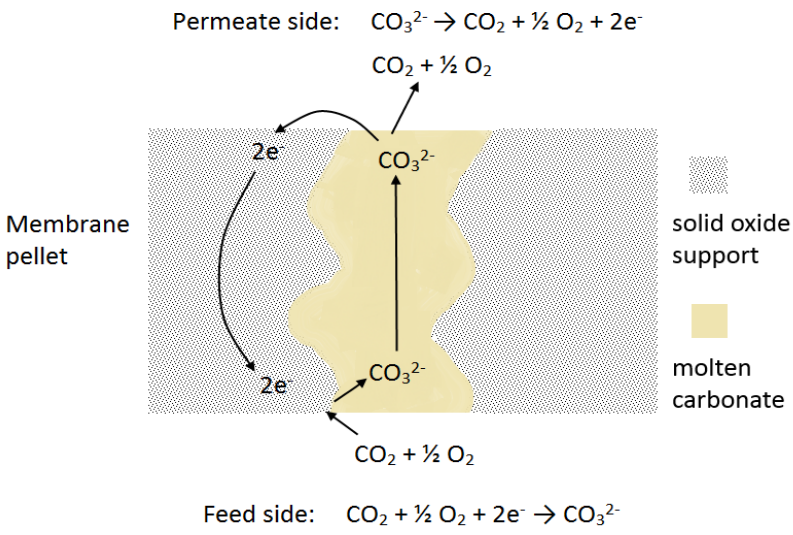

Figure 2.6: Proposed CO_2 transport mechanism through membranes with electronic conductive support. CO_2 molecules on membrane feed side react with O_2 and electrons on gas/solid/molten salts three-phase boundary and form CO_3^{2-} that in turn diffuse across the membrane. The reverse electrochemical reaction occurs on permeate side to release CO_2 and O_2 then return electrons to the bulk solid phase.

Two facilitated CO_2 transport mechanisms for molten carbonate dual phase membranes have been proposed. When the solid phase material is purely oxide ion conductive (Figure 2.5), CO_2 selective interfacial reactions are enabled on the three-phase boundary of gas, solid support and molten salt, making this transport pathway purely CO_2 selective. When solid phase is electronic conductive and co-feeding O_2 with CO_2 on membrane feed side (Figure 2.6), another CO_2 transport mechanism has been proposed involving O_2-CO_2 co-permeation. Additionally, both transport mechanisms would take place simultaneously if the solid phase material were mixed ionic/electronic conductive (MIEC).

Y. S. Lin et al. initialised the tests over molten carbonate dual phase membranes for CO_2 separation [48]. They first fabricated electronic conductive porous stainless-steel disk membranes and directly infiltrated them with ternary Li/Na/K carbonate mixture with a melting point of 397°C. They carried out permeation experiments using these membranes at 450 to 750°C and demonstrated that the membranes were CO_2-O_2 co-permeable and reached CO_2 permeance of 2.5×10^{-8} $mol \cdot s^{-1}m^{-2}Pa^{-1}$ with O_2 co-permeation at 650°C. Under the same condition, the separation factor of CO_2 over N_2 was approximately 16 and the CO_2/N_2 selectivity was roughly 25. They believed the mechanism shown in Figure 2.6 governed the observation they found out.

They also extended the experimental study to purely ionic conductive molten carbonate dual phase membranes, following the mechanism described in Figure 2.5. Perovskite like ceramic material $La_{0.6}Sr_{0.4}Co_{0.8}Fe_{0.2}O_{3-\delta}$ (LSCF6482) was selected as solid phase and the same fabrication method was adopted. Experimental CO_2 permeation data showed that the CO_2 permeance grew exponentially with increasing temperature in the range of 700 to 900°C. Although the CO_2 permeance of these disk

membranes was rather low at 700°C in the order of 10^{-9} mol·m^{-2}Pa^{-1}s^{-1}, the membrane with smallest thickness (0.375mm) reached 4.77×10^{-8} mol·m^{-2}Pa^{-1}s^{-1} at 900°C and A CO_2/Ar separation factor of at least 225 was achieved [49].

The inherent advantages of molten carbonate dual phase membranes are that they operate at high temperature (typically 600 to 900°C, which is above the melting point of carbonate mixture) and can achieve very high separation factors of CO_2 over N_2 by employing the principle of facilitated CO_2 transport. This temperature range overlaps with flue gas temperature that vary from a few hundreds of degrees Celsius to 1000°C, depending on the specific locations in the flue gas line in the power plant [48]. It means dual phase membranes is suitable for direct CO_2 separation from hot flue gas. As the membranes use the heat of the power plant efficiently, the process can potentially approach minimal energy requirement. Like most other classes of membranes, the CO_2 permeation flux needs to be enhanced as it is an imperative parameter for large scale CO_2 capture. In order to achieve higher flux, better understanding on the membrane behaviour must be obtained experimentally. Up to now researchers has been focusing on the investigation of the following areas:

- The physical and chemical properties of various solid support materials and the molten carbonate mixture, as well as the interaction of CO_2 with the molten carbonate mixture.
- Exploring different approaches for improving CO_2 flux through molten carbonate dual phase membranes, including modification of membrane geometry and porous microstructure, enhancing the solid phase conductivity and enhancing the thermodynamic driving force for CO_2 permeation.
- Experimental verification of CO_2 flux-driving force correlation models.

In the following subchapters, comprehensive review will be performed covering the above research topics. Previous work that closely match the aims and objectives of this project will be identified and further discussed.

2.2. Properties of molten carbonate dual phase membranes

2.2.1. The origin of molten carbonate dual phase membranes

The origin of molten carbonate dual phase membranes is from the concept of molten carbonate fuel cells (MCFC). The state-of-the-art MCFC consists of a porous nickel based alloy as anode (fuel electrode), a porous lithium-doped nickel oxide as cathode (oxidant electrode), as well as a liquid solution of lithium, sodium, and/or potassium carbonates soaked in a matrix as the electrolyte [50, 51]. The reactions at the anode, cathode, and the overall reaction for the MCFC are:

Anode: $H_2(g) + CO_3^{2-} \rightarrow H_2O(g) + CO_2(g) + 2e-$ (2.11)

Cathode: $1/2\ O_2(g) + CO_2(g) + 2e- \rightarrow CO_3^{2-}$ (2.12)

Overall: $H_2(g) + 1/2\ O_2\ (g) + CO_2\ (g) \rightarrow H_2O(g) + CO_2(g)$ (2.13)

Here an external electrical circuit is used to recirculate the electrons (Figure 2.7). On the anode, H_2 is normally used as the fuel, which could be supplied from an internal steam methane reforming process. Besides, MCFC can also use carbon monoxide (CO), natural gas or propane as the fuel [51].

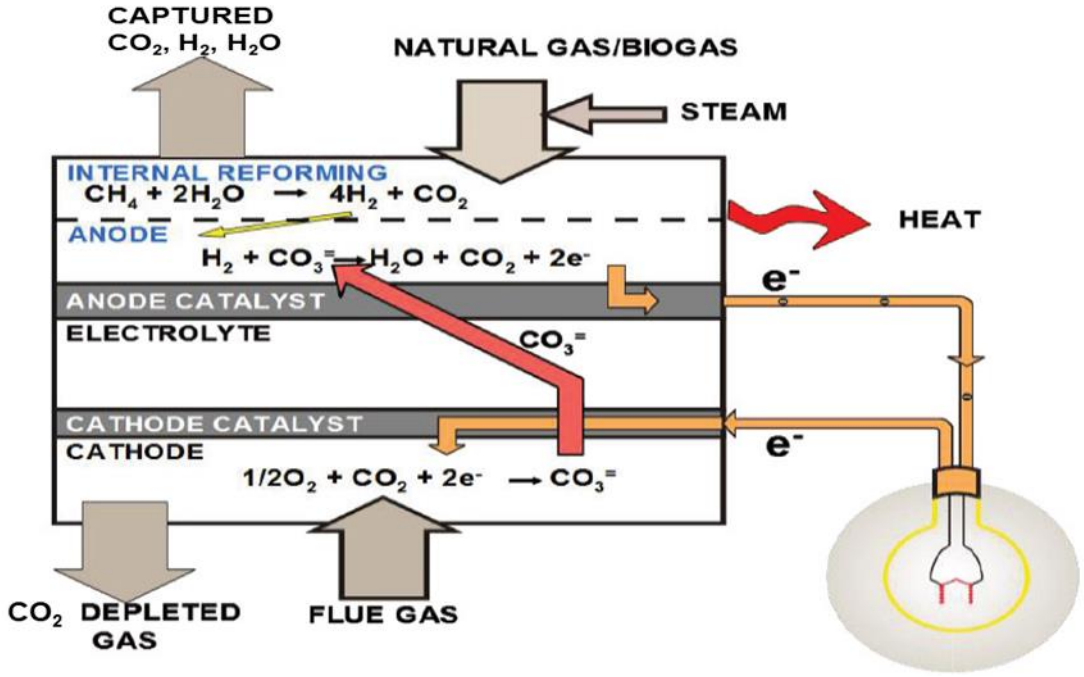

Figure 2.7: Schematic diagram of the MCFC system. This also illustrates the operating principle of electrochemical membrane (ECM) cell: CO_2 is used on cathode as an oxidant and transferred to anode via carbonate ions in electrolyte [52].

The modern MCFC system operates at high temperature (about 650 °C), it can be used for cogeneration (combined heat and power) and distributed electricity generation [51]. In principle, MCFC itself is also capable of CO_2 capture, making the concept of combined Electric Power and Carbon dioxide Separation (CEPACS) feasible. A principle of electrochemical membrane (ECM) technology derived from MCFC system has been constructed and operated with external circuit at bench scale [52]. With a total electrochemical membrane area of 11.7m^2, the test demonstrated the ability of ECM technology to selectively transfer CO_2 from the cathode to the anode of the cell, operating at a peak CO_2 flux of 180 $ml \cdot s^{-1} \cdot m^{-2}$, and achieving >90% of CO_2 removal from a simulated flue gas stream [52].

2.2.2. CO_2 transport pathways in practice

A molten carbonate dual phase membrane is a refined and simplified version of ECM technology focusing on the CO_2 separation step. Ionic/electronic conductive solid material interconnecting across the whole thickness of the membrane replaces the external circuit. Based on the proposed electrochemical transport mechanisms, rate of CO_2 transport is determined by four consecutive steps: interfacial electrochemical reaction on feed side, carbonate ion diffusion through molten salt, reversed

interfacial reaction on permeate side and ionic/electronic conduction through solid phase. Hence, interfacial reaction kinetic rate constant, carbonate conductivity of molten carbonate mixture, ionic/electronic conductivity of solid support could impact the CO_2 transport through dual phase membranes [53].

Kinetically, the CO_2 permeation flux J via electrochemical transport mechanisms can be written as:

$$J = A\ exp\left(\frac{-E_a}{RT}\right) \qquad (2.14)$$

In the equation Ea (J/mol) is the apparent activation energy for the overall gas permeation process, T is permeating temperature and A is a pre-exponential constant. Permeation experiments can be conducted by measuring CO_2 flux at various temperature under the same gas environment. By plotting ln J against 1/T, Ea can be determined experimentally and compared to activation energy for individual steps. If the rate of one particular step is much slower than other steps, then the overall Ea by measurement is approaching the activation energy of this individual step and it becomes rate limiting.

It has been proposed the electrochemical CO_2 transport mechanisms described in Figure 2.5 and 2.6 will be activated at above the melting point of the carbonate phase, only if the solid support material possesses oxide ion conductivity and/or electronic conductivity. At this point, the molten carbonate ideally fills most of the interconnected pores and the carbonate ion conductivity is largely increased. However, CO_2 transport through molten carbonate dual phase membranes is not restricted to the electrochemical transport mechanisms during experimental operation. Other physical gas permeation mechanisms are also possible, including Knudsen diffusion through unfilled pores as well as solution diffusion through the molten phase. These physical mechanisms could become predominant for inert or weakly conductive solid support. In addition, cracking on the bulk membrane surface or lose of molten carbonate (carbonate decomposition) could lead to trans-membrane leak. Defects or failure of sealant material that isolates the feed and permeate side reactor chambers may lead to cross-chamber leak. Gas flows would pass through the gaps directly and that implies the failure of membrane separation.

Disk shape and hollow fibre are the most common geometry for the solid support of dual phase membranes. Disk shaped membrane support can be fabricated using a simple powder pressing and sintering technology, forming a random packed pore network. The average pore diameter ranges from 0.1 to 10μm indicating a macroporous feature [48, 49]. Direct hot infiltration can be accomplished by placing carbonate powder on top of the membrane disk and elevating the temperature above the melting point of the carbonate mixture. When carbonate melts, the wettability of the support surface and the capillary forces of the pores drive the molten carbonate to distribute throughout the entire network. If the infiltrated membrane still contains unfilled interconnected pores, it is possible that gas will permeate through these pores. With a temperature just above the melting point of the carbonate mixture, the carbonate may not fully occupy the pores. Gas permeation through dual phase membrane is most likely governed by Knudsen pore diffusion [48]. At this stage, the membranes can hardly show any selectivity.

Furthermore, membranes may lose selectivity at higher temperature if they suffer thermal cracking or insufficient carbonate loading. In order to prevent this, it is necessary to achieve certain porosity while maintaining the mechanical strength during the fabrication of porous support. For ceramic materials with relatively lower densification temperature, pore formers such as graphite, carbon black and corn starch are blended with ceramic powers, followed by pressing and sintering [54]. Pore former will burn off while ramping up to the sintering temperature. Total pore volume must be estimated to ensure the amount of carbonate loading is adequate to occupy the interconnected porous network.

Once the carbonate mixture fully melts at higher temperature, it presents as liquid phase within pores of solid substrate. It is suggested that inlet gas on membrane feed side could possibly dissolve into molten carbonates as molecular species. If an inert support were used, any gas transport including CO_2 would more likely occur via solution diffusion [55]. When support material has ionic/electronic conductivity, electrochemical transport route is active for CO_2 whilst other gas species mainly transport via solution diffusion. Meanwhile solution diffusion is still a parallel but insignificant route for CO_2 transport. According to the solution diffusion mechanism, solubility and diffusivity of individual gas species in the molten carbonate mixture are important parameters that determine the membrane selectivity solely by this route. The values of the solubility constant S (the inverse of Henry's law constant H) for N_2 and CO_2 in the ternary carbonate melt (43.5 mol% Li_2CO_3, 31.5 mol% Na_2CO_3, 25.0 mol% K_2CO_3) at different temperatures are summarised in Table 2.2:

Table 2.2: Solubility constants of N_2 and CO_2 in ternary carbonate mixture between 560 and 850°C. Data measured by quenching saturated molten salt and allowing the gas to escape for analysis [56].

Temperature (°C)	**N_2 solubility constant $mol \cdot cm^{-3} \cdot Pa^{-1}$**	**CO_2 solubility constant $mol \cdot cm^{-3} \cdot Pa^{-1}$**
560	-	$(0.89 \pm 0.10) \times 10^{-12}$
700	$(0.68 \pm 0.08) \times 10^{-12}$	3.55×10^{-11}
750	$(1.24 \pm 0.07) \times 10^{-12}$	-
800	$(1.32 \pm 0.10) \times 10^{-12}$	-
850	$(1.69 \pm 0.11) \times 10^{-12}$	-

The solubility coefficients generally grow with temperature based on the above table. CO_2 solubility in ternary carbonate mixture is generally higher than N_2. However, the permeability of each gas specie still depends upon the gas diffusivity in the melt. As gas diffusivity data in molten ternary carbonates was scarce in literature, theoretical CO_2 selectivity by the solution diffusion mechanism is difficult to predict.

Gas transport through defects of membrane sealing is also governed by Knudsen diffusion [48], leading to the loss of CO_2 selectivity. The sealant materials must be carefully chosen and tested to prevent cross-

chamber leak and minimise the gas transport through any defect. The sealant for dual phase membranes must sustain high temperature in terms of mechanical strength and chemical stability. Ideally, they form a dense, robust and gas tight layer that adhesive to both the membrane material and the gas inlet tubing material. Metallic gold and silver sealants are investigated and proved that they are able to provide high temperature leak free sealing for metallic-carbonate membranes as well as perovskite-like ceramic-carbonate membranes [57, 58]. They can be applied between the gas inlet tubing and membrane surface either as a form of paste or silver/gold ring seal. The melting point of silver and gold are 962 and 1063°C respectively [58], indicating they remain solidified at usual operating temperatures of dual phase membrane. Besides, ceramic-based sealant and borosilicate glass sealant were also studied for ceramic membrane reactors. Gas tightness was difficult to achieve by ceramic sealants whilst the performance of glass-based sealant was not stable with frequent variation of temperature [59, 60]. It is also noticeable that double-layer sealing, for instance silver-ceramic double sealing and gold-glass double sealing were found to be reliable for high temperature gas separation using ceramic membranes [57, 61].

2.2.3. Properties of membrane support materials

Various studies in molten carbonate dual phase membranes suggest that the electrochemical CO_2 transport mechanism is relevant to the bulk oxide ion/electronic conductivity in solid support [48, 62-64]. This route of CO_2 transport is predominant only if the support material is charge conductive. Knowing the importance of the support material in dual phase membranes, it is necessary to review the structural, thermochemical properties as well as conductivities of a typical membrane support material with the following properties:

- Inert membrane support, taking α-alumina (α-Al_2O_3) as a typical example.
- Ionic conductive membranes, taking yttrium stabilised zirconia (YSZ) as a typical example.
- Mixed ionic/electronic conducting membranes, including perovskite-type Lanthanum Strontium Cobalt Ferrite (LSCF) membranes.

α-alumina is a naturally occurring mineral namely corundum. Its crystalline structure is a rhombohedral lattice system, with very high melting point of above 2000°C. Alumina is also considered as an inert material that neither chemically reactive nor electronic conductive. The electrical resistivity of alumina is 2×10^6 Ω·cm at 1000°C and is among the highest of ceramic materials [65]. The densification of powder pressed alumina pellets also occurs at relatively high temperature. In conventional heat sintering processes, the densification is achieved through fast growth on grain size, followed by shrinkage of pores. Research in the densification process during alumina sintering has shown that fast grain growth did not happen until 1350 to 1400°C and the pellet approached full densification above 1450°C [66], indicating the sintering temperature profile must be carefully controlled to obtain the desirable membrane support porosity.

Being an insulating material to both electrons and oxide ions, α-alumina support is often used for control experiment for CO_2 permeation against other oxide or electronic conducting membranes. Wade el al. conducted an isothermal CO_2 permeation experiment at 750°C using alumina as a support and infiltrated with molten ternary carbonates. During the 4000 minutes operation the CO_2 permeability never exceeded 8×10^{-13} $mol{\cdot}m^{-1}s^{-1}Pa^{-1}$ which is around one order of magnitude lower than oxide ion conducting YSZ supported membrane [53]. They further demonstrated the temperature effect on CO_2 permeability and CO_2/N_2 selectivity through alumina based dual phase membrane was insignificant. Across the temperature range from 500 to 900°C, CO_2 permeability was barely observable at 500-600°C. The permeability was increased at higher temperature however stayed within the order of magnitude of 10^{-13} $mol{\cdot}m^{-1}s^{-1}Pa^{-1}$ [53].

Yttrium stabilised zirconia (YSZ) is a well-known oxide ion conductor. Pure zirconium oxide (ZrO_2) itself has monoclinic lattice structure up to 1100°C and has very small ionic conductivity due to low concentration of oxygen vacancies on lattice sites [67]. Generally, doping metal oxides with lower-valence metal cation can create oxygen vacancies that facilitate the ionic conductivity throughout the lattices. Yttrium oxide (Y_2O_3) containing Y^{3+} cations is one of the most established dopants to stabilise zirconia. Figure 2.8 depicts the process on the formation of YSZ. When Y_2O_3 is incorporated into a ZrO_2 lattice, Y^{3+} cations replace Zr^{4+} thus breaking the charge balance and creating a negatively charged lattice site Y'_{Zr}, relative to the surrounding crystal lattice. As a compensation for the charge imbalance on the lattice site, a +2 charged oxygen vacancy Vö is created for every two Y'_{Zr} introduced. The remaining oxygen from Y_2O_3 go into the lattice structure as lattice oxygen O_o^x, which is neutral relative to the surrounding lattice [62, 68]. This process can be expressed using standard Kröger-Vink notation:

$$Y_2O_3 \longrightarrow 2Y'_{Zr} + V_o^{\bullet\bullet} + 3O_o^x \qquad (2.15)$$

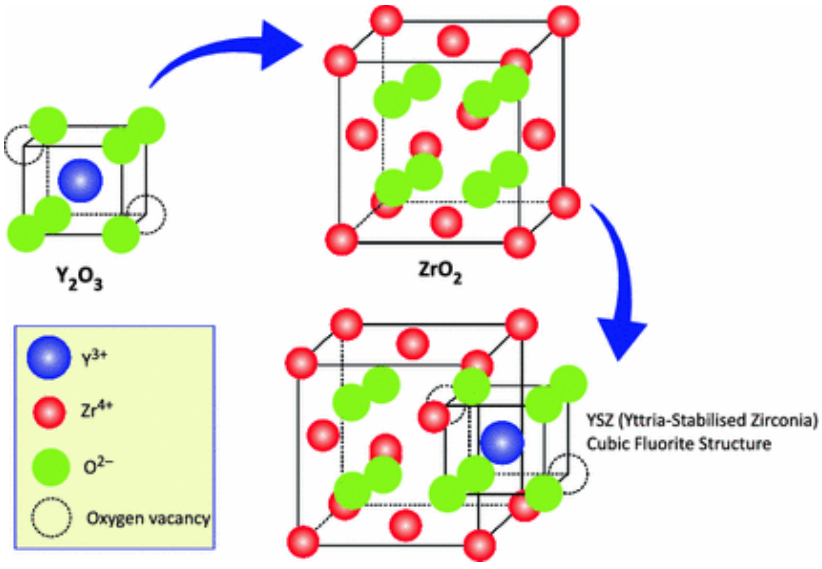

Figure 2.8: The formation of YSZ by adding Y_2O_3 dopant, creating thermodynamically stabilised cubic fluorite structure with oxygen vacancies on lattice sites [67]. Reproduced with permission of Springer Nature.

The ionic conductivity of YSZ is directly relevant to the concentration of oxygen vacancies. The concentration of the dopants is optimised because at lower dopant levels the oxygen vacancy concentration is insufficient whilst at higher dopant levels, the defect ordering, vacancy clustering or electrostatic interactions may decrease the ionic conductivity [67]. By adding 3 mol% Y_2O_3 the zirconia can be partially stabilised, a mixture of metastable tetragonal ZrO_2 and cubic phase is obtained due to this insufficient amount of dopant. Doping 8 mol% Y_2O_3 makes zirconia fully stabilised into an oxygen deficient cubic fluorite structure [67]. In the context of ionic conducting dual phase membranes, the mobility of oxygen vacancies allows the transport of lattice oxygen in the solid phase. Gas phase CO_2 on feed side of the membrane can therefore react with lattice oxygen and produce carbonate ions. After diffusing across the membrane via molten phase, carbonate ions then react with oxygen vacancies on membrane permeate side, releasing gas phase CO_2 and returning oxygen to the lattice, with further lattice oxygen back diffusion closing the loop (Figure 2.9) [68].

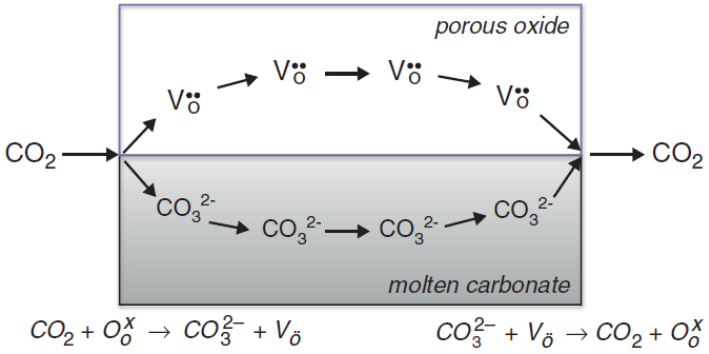

Figure 2.9: Schematic diagram showing a dual phase solid oxide-molten carbonate membrane transporting carbon dioxide. Interfacial reactions on both sides of the membrane are expressed with Kröger-Vink notation [68]. Note that O_o^x is equivalent to O^{2-} combining with Vö. Reproduced with permission of Elsevier.

Electronic conductivity can also arise in solid oxide materials. One major mechanism for their electronic conductivity is related to the surrounding oxygen atmosphere [62]. The oxygen partial pressure upon the material surface determine the generation of electrons (e^-) and electron holes ($h^\bullet$), as shown in equation 2.16 and 2.17 [69]:

$$\frac{1}{2}O_2(g) + V_o^{\bullet\bullet} \leftrightarrow O_o^x + 2h^\bullet \qquad (2.16)$$

$$O_o^x \leftrightarrow \frac{1}{2}O_2(g) + V_o^{\bullet\bullet} + e^- \qquad (2.17)$$

The equilibrium constants of these equations at a given temperature determine the tendency of electrons and holes formation within the YSZ structure. High oxygen partial pressure facilitates hole formation and p type electrical conductivity (mobility of holes). On the other hand, low oxygen partial pressure facilitates electron formation and n type electrical conductivity (mobility of electrons). Literature suggested that comparing with other solid oxides, stabilised zirconia ceramics exhibit a minimum electronic contribution to total conductivity in the oxygen partial pressure (pO_2) range from 10–20 MPa

down to 10^{-25} Pa within the temperature window of 700-900°C [62, 69, 70]. It means pO_2 needs to be extremely high to enable hole formation and extremely low to enable electronic formation. Thus, YSZ essentially is a purely ionic conductor within the oxygen partial pressure range for practical applications.

Another important chemical property of zirconia is the interaction with Li_2CO_3 under elevated temperature higher than 650°C and low CO_2 partial pressure. Under this condition, the decomposition of carbonate ions releases oxide ions into zirconia. When oxide ions and lithium ions incorporate into zirconia lattice, a new phase of zirconate is formed as a thin layer on the molten salt-zirconia interface. This is a reversible process and the overall equation can be written as equation 2.18 [53, 62, 71]:

$$Li_2CO_3 + ZrO_2 \leftrightarrow Li_2ZrO_3 + CO_2 \qquad (2.18)$$

The presence of non-ionic conductive lithium zirconate (Li_2ZrO_3) layer may interfere the interfacial reaction explained earlier in the electrochemical CO_2 transport mechanisms. However, Li_2ZrO_3 is a well-known CO_2 absorbent and the reverse reaction is particularly effective on Li_2ZrO_3-ternary carbonate interface. Wade et.al performed thermogravimetric analysis (TGA) for YSZ and carbonates mixtures, comparing the weight loss of YSZ mixing with individual Li/Na/K carbonates, YSZ mixing with unreactive binary Na/K carbonates and YSZ mixing with ternary Li/Na/K carbonates up to 900°C under 10% CO_2 atmosphere. The result (Figure 2.10) showed the weight loss of YSZ-Li_2CO_3 mixture was irreversible. Although the YSZ-ternary carbonate mixture started to lose weight at 765°C, the weight was mostly recovered upon cooling down to around 600°C [53]. They further showed the CO_2 downhill permeability through YSZ-binary carbonate and YSZ-ternary carbonate membranes were similar at 750°C, feeding 50% CO_2 in He [53]. The result indicated the interference of the zirconate phase on CO_2 permeation is only possible under higher temperature or low CO_2 partial pressure.

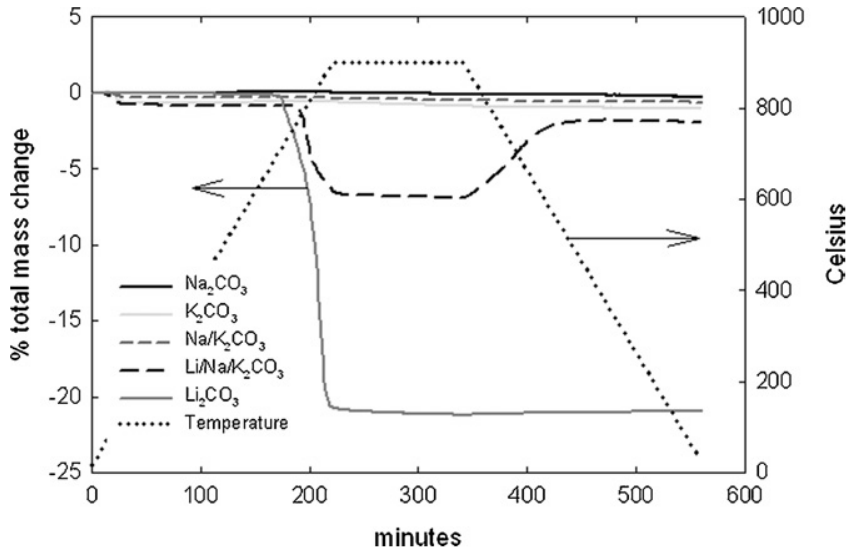

Figure 2.10: TGA curves of YSZ and alkali–metal carbonate mixtures in 10% CO_2 atmosphere. Temperature ramp of 4°C/min was applied up to 900°C where the sample was held for 3 hours before ramped down [53]. Reproduced with permission of Elsevier.

Lanthanum Strontium Cobalt Ferrite (LSCF or $La_{1-x}Sr_xCo_{1-y}Fe_yO_{3-\delta}$) is a ceramic material with a phase containing mixed lanthanum (III) oxide, strontium oxide, cobalt oxide and iron oxide. It is a perovskite-type rhombohedral or orthorhombic crystalline, which has a general formula of ABO_3 (Figure 2.11). Lanthanum Strontium Cobalt Ferrite is a mixed ionic-electronic conductor (MIEC). By modifying the proportion of the metal cations on A sites and B sites for the LSCF system, the concentration of the oxygen vacancy and electron/hole carriers is tuneable. Sr on the A site lattice of LSCF acts as an acceptor, enhancing the formation of oxygen vacancies due to the ionic compensation similar to YSZ. In parallel, electronic compensation by valence change of the B site ions is another way to maintain charge neutrality corresponding to the A site acceptor dopant (Sr^{2+}). [72, 73] This in turn generates electron vacancy (holes) and the mobility of p type carriers (holes) makes LSCF electronic conductive. In this case, Co (II) and Fe (III) ions induce the electronic conductivity in LSCF and the interaction between oxygen and solid oxides as in equation 2.16 and 2.17 is not necessary. Anderson and co-workers carried out studies in structure and electrical behaviours in LSCF system. They revealed that high Sr and Co content in LSCF such as $La_{0.2}Sr_{0.8}Co_{0.8}Fe_{0.2}O_{3-\delta}$ (LSCF2882) exhibited both higher ionic conductivity and higher p type electrical conductivity [72-74]. However, compositions having high Sr and Co content seemed susceptible to fracture due to their high thermal expansion coefficient as well as relatively low chemical stability [75]. $La_{0.6}Sr_{0.4}Co_{0.2}Fe_{0.8}O_{3-\delta}$ (LSCF6428) has been found to compromise the conductivity and stability and therefore the LSCF6428 composition was chosen for the experimental studies in this project.

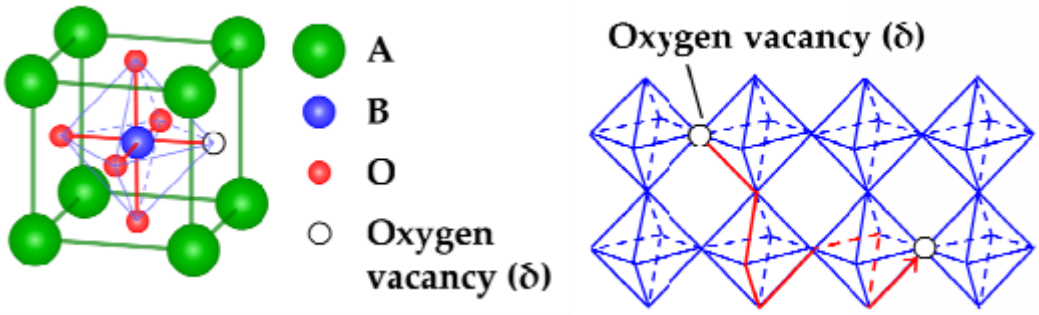

Figure 2.11: Crystalline structure (left) and oxygen vacancy migration path (right) in the polyhedrons of mixed conducting perovskites. A-sites are occupied by La (III) and Sr (II) ions, and the B-sites are occupied by Co (II) and Fe (III) ions that surrounded by oxygen ions, δ is the oxygen deficiency per unit cell [76].

Precisely, in LSCF system the chemical stability and oxygen nonstoichiometry (δ) are also associated with the variation of surrounding oxygen partial pressure (pO_2) and temperature. The dependency of oxygen nonstoichiometry (or the oxidation state of LSCF) upon the temperature in both reducing and non-reducing environments have been investigated by several researchers, leading to a change in ionic and electronic conductivities corresponding to the changing oxygen vacancy concentration. The general trend is that the degree of oxygen nonstoichiometry increased with increasing temperature, decreasing

oxygen partial pressure and increasing Sr or Co content [77], following the dissociation of lattice oxygen from LSCF in its oxidised state ($LSCFO_3$) as described in equation 2.19:

$$LSCFO_3 \overset{T,\ pO_2}{\longleftrightarrow} LSCFO_{3-\delta} + \frac{\delta}{2}O_2 \qquad (2.19)$$

For the effects of the Sr and Co content, pO_2 and temperature on LSCF chemical stability, researchers performed solid electrolyte coulometry (SEC) to study how δ related to changing pO_2 and temperature. LSCF2882 with high Sr and Co content became oxygen deficient at 300°C even in non-reducing atmosphere (log pO_2 = -2.9). In contrast, LSCF8228 and LSCF6428 became oxygen deficient only at higher than 600°C, whilst LSCF8228 is not as conductive as LSCF6428 under same environment. It was also reported that in temperature programmed reduction using 4% CO/He, LSCF 2882 began to lose crystallinity at 300°C, suffered from carbon deposition and severe degradation at 800°C [77, 78], δ against log pO_2 and temperature plots for LSCF6428 are shown in Figure 2.12.

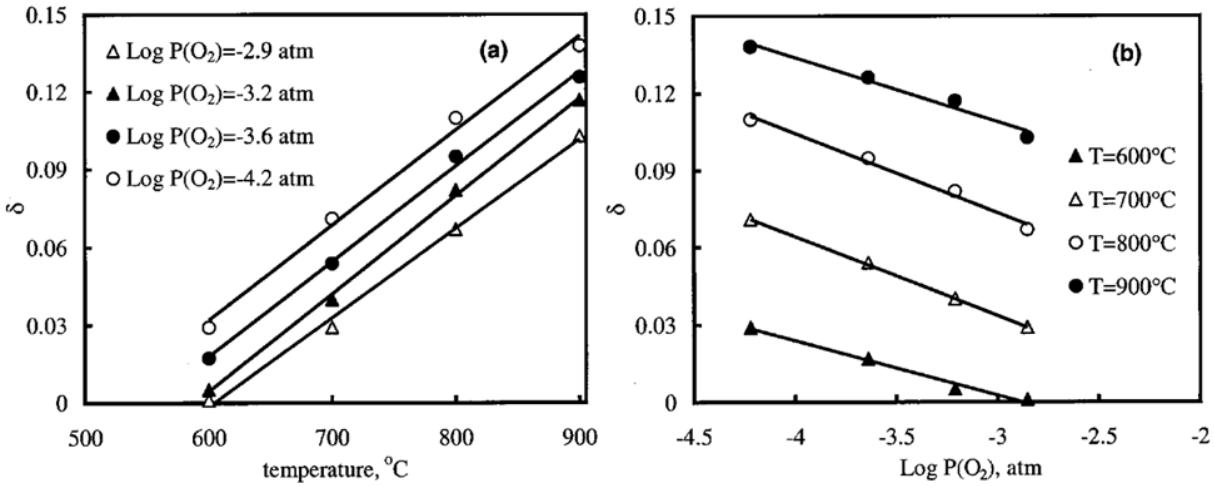

Figure 2.12: Oxygen nonstoichiometry as a function of (a) temperature, (b) pO_2 for LSCF6428 [78]. Reproduced with permission of Elsevier.

Upon a small change in temperature and oxygen partial pressure on the surface of LSCF, oxygen must be either lost or gained in order to re-establish equilibrium in response with the ambient gas environment and temperature. The Re-equilibration rate depends on pO_2 at a fixed temperature. With higher ambient pO_2 baseline, LSCF tends to re-equilibrate faster. However, at a fixed pO_2 the kinetics of the reverse surface reaction in equation 2.19 may be enhanced at higher temperature. As a result, re-equilibration was found to be faster at 600 and 900°C [78]. Although LSCF6428 exhibited greater regeneration efficiency comparing with LSCF8228 [77]. O_2 and/or CO_2 permeation flux via LSCF6428 based membranes may take a long time to reach steady state at high temperature due to the re-equilibration behaviour. It has been experimentally observed that oxygen permeation over LSCF6428 perovskite membranes under air/N_2 gradients at 850 °C requires 15-22 h to reach steady state. During this period, the oxygen flux increases 47-82% from its initial value due to the gradual development of an oxygen-deficient structure [79].

Because of the electronic conductive feature in the LSCF system, dense LSCF based membranes exhibit high selectivity to O_2 at 700-1000°C. By undergoing the interfacial electrochemical reactions described in Figure 2.13, O_2 molecules can permeate through the dense membrane driven by O_2 chemical potential gradient. Dense LSCF based membranes exhibited an oxygen permeation flux one or two orders of magnitude higher than that of stabilized zirconia [80]. This concept of oxygen permeable membranes has been extensively studied in the research areas of membrane based air separation, which separate out high purity O_2 from the air and can be potentially applied to pre-combustion carbon capture and oxy-fuel combustion processes.

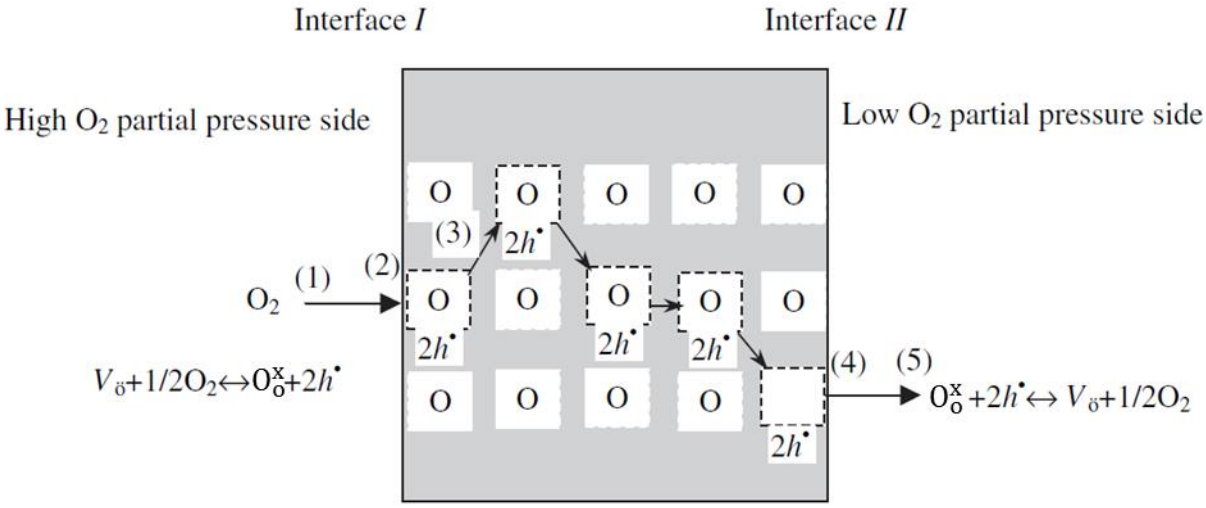

Figure 2.13: Schematic of oxygen migration in perovskite type MIEC membranes. O_2 permeate from high O_2 partial pressure to low O_2 partial pressure side in series: (1) Mass transfer of gaseous oxygen from the gas stream to the membrane surface (high pressure side). (2) Reaction between the molecular oxygen and oxygen vacancies at the membrane surface (high pressure side). (3) Oxygen vacancy bulk diffusion across the membrane. (4) Reaction between lattice oxygen and electron hole at the membrane surface (low pressure side). (5) Mass transfer of oxygen from the membrane surface to the gas stream (low pressure side) [31]. Reproduced with permission of John Wiley and Sons.

Going back to the concept of LSCF-carbonate dual phase membranes that are utilised for CO_2 separation and CO_2-O_2 co-permeation, proposed mechanisms were briefly outlined in Chapter 2.1.4 (see Figure 2.5 and 2.6). For downhill CO_2 permeation alone, the electronic conductivity of LSCF is not exploited. Therefore, it is true that the mechanism described in Figure 2.5 is the only major electrochemical transport mechanism. Considering the LSCF as a dense solid phase is oxygen permeable, the CO_2-O_2 co-permeation needs to be described more comprehensively. As a MIEC material, parallel pathways for electrochemical transport may be available for CO_2-O_2 co-permeation when the chemical potential difference of O_2 between feed and permeate sides is positive (Figure 2.14). O_2 itself can transport as lattice oxygen via the solid phase (i), and co-permeate with CO_2 through the melt (ii) simultaneously [68]. These combined mechanisms also apply to the uphill CO_2 permeation when CO_2 chemical potential difference is slightly negative across the membrane. If the feed side CO_2 chemical potential is

also higher (downhill CO_2 and O_2 co-permeation), the electrochemical pathway in Figure 2.5 utilising the oxide ion conductivity of LSCF may superimpose on top of the two pathways in Figure 2.14.

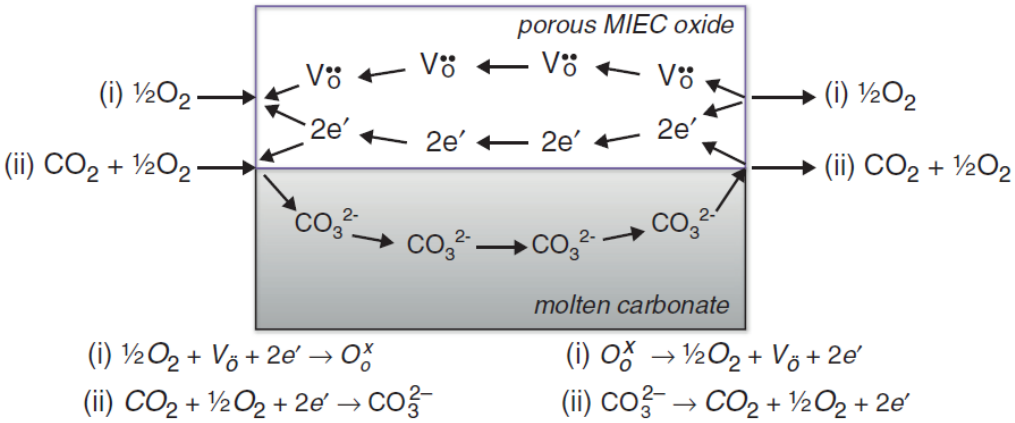

Figure 2.14: Parallel pathways available when using an MIEC instead of a pure oxygen-ion conducting host porous oxide. It is possible to transport oxygen alone (i) or in combination with carbon dioxide (ii). The reactions at both membrane surfaces are also shown in Kröger-Vink notation [68]. Here the reaction (i) on the left is equivalent to the reaction on interface I in figure 2.13. When two electrons (represented here as e') fill the two holes associated with the lattice oxygen, a full lattice oxygen is generated. Reproduced with permission of Elsevier.

2.2.4. Properties of molten carbonate

Molten carbonate is the active phase that facilitate the electrochemical transport of CO_2 across dual phase membranes. It is also important to study the properties of the molten carbonate as this may directly influences the CO_2 permeation flux and selectivity. In this section the following major properties of ternary molten carbonate mixture are reviewed:

- The carbonate ion conductivity through molten carbonate phase.
- The chemical stability of molten carbonate, particularly the thermodynamics of molten carbonate decomposition and the equilibrium with gas phase environments.
- Complexity of gas phase-molten phase chemical interaction and formation of new ionic species in the melt.

Table 2.3: Compositions and melting points of the alkali metal carbonate mixtures investigated by Wade et al. [53].

Carbonate composition (mol %)	Melting point (°C)
100% Li_2CO_3	726
100% Na_2CO_3	858
100% K_2CO_3	899
41% Na_2CO_3, 59% K_2CO_3	710
43% Li_2CO_3, 31% Na_2CO_3, 25% K_2CO_3	397

Molten carbonate is a special form of ionic liquid with much higher melting point. The melting points of pure carbonates of Li, Na and K are higher than 700°C. Interestingly, binary mixture of Na/K carbonates has slightly lower melting points and ternary carbonate mixture of Li, Na and K has significantly lower melting point (Table 2.3). The ternary mixture would be beneficial particularly for applications such as pre-combustion CO_2 separation. Therefore, this composition is widely employed for laboratory scale research for CO_2 separation using molten carbonate dual phase membranes.

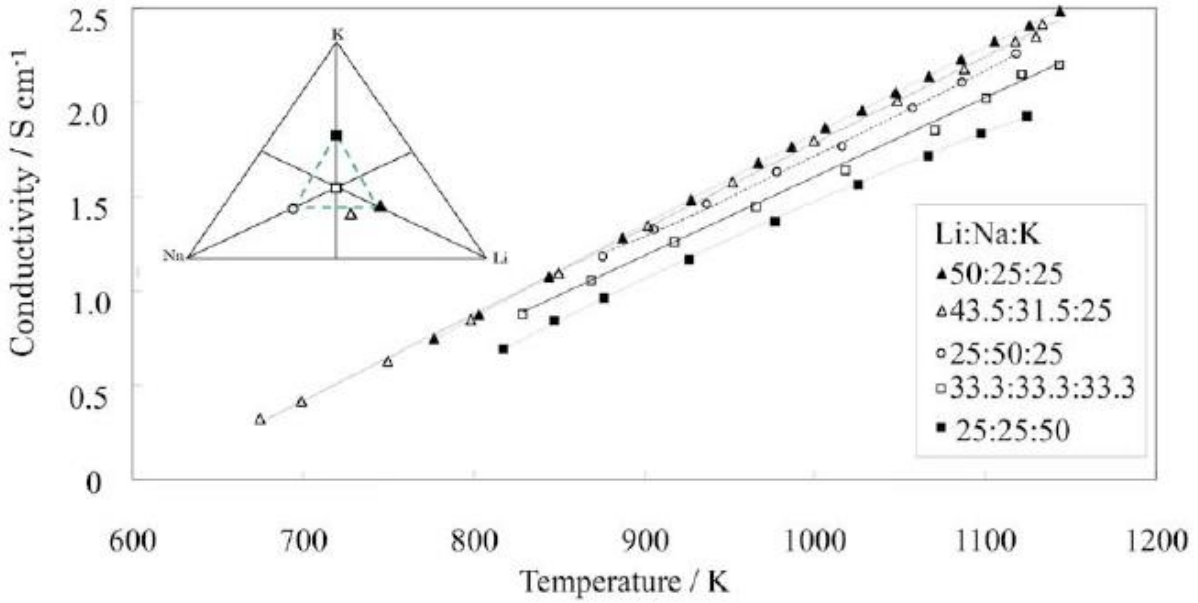

Figure 2.15: Temperature dependence of the molten $Li_2CO_3/Na_2CO_3/K_2CO_3$ ternary carbonates conductivity. The compositions lie within the centre area of the triangular phase diagram, enclosed by a dashed line boundary near central equimolar composition [81]. Reproduced with permission of Electrochemical Society.

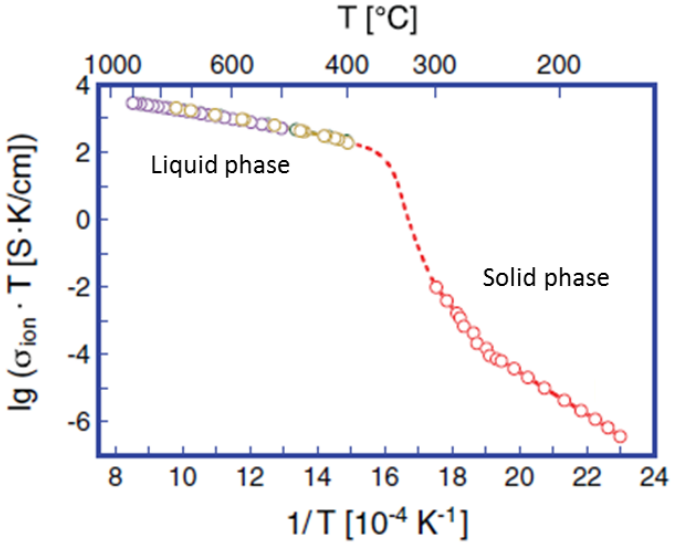

Figure 2.16: Temperature dependence of the electrical conductivity of a ternary eutectic carbonate mixture comprising Li_2CO_3, Na_2CO_3 and K_2CO_3 of the molar ratio 41:37:22 in the solid and liquid state [82]. Reproduced with permission of Electrochemical Society.

Kojima and co-workers measured the carbonate ion conductivity of ternary carbonate mixtures with various compositions [81]. The measurements were made using impedance spectroscopy. It turned out that for carbonate mixtures not far from equimolar compositions, the carbonate ion conductivity is not strongly affected by the variation of compositions (Figure 2.15). Conductivities were measured from just above the melting point of each composition up to around 850°C. The values tend to stay on the same order of magnitude for all the compositions and across the whole range of temperature. They also established an empirical quadratic function which reflects the temperature dependants of carbonate ion conductivity:

$$\sigma_c = a + bT + cT^2 \qquad (2.20)$$

Here, a (S m^{-1}), b (S m^{-1} K^{-1}), and c (S cm^{-1} K^{-2}) are experimentally determined constants and σ_c is the carbonate ion conductivity in S/cm. For the 43.5:31.5:25.0 composition the c coefficient is close to zero. Hence the carbonate ion conductivity is essentially close to a linearly dependency to temperature. In another measurement taken by Ward and Janz [83], an exponential model was proposed because their measurement values at temperatures above 600°C were slightly higher comparing with Kojima and co-workers. Anyhow, the carbonate ion conductivity presented from various literatures agreed reasonably well. Furthermore, a plot of log (σ_cT) against 1000/T comprised several measurements from literatures also included the carbonate ion conductivity of 41:37:22 composition below its melting point (Figure 2.16). It is worth pointing out that the carbonate ion conductivity dropped significantly by at least four order of magnitude upon the solidification of molten carbonate. It indicates the carbonate mixture almost lose the conductivity in solid state [82].

The most important thermochemical behaviour of the molten carbonate mixture is the CO_2 dissociation under high temperature. The thermodynamics of CO_2 dissociation directly affects the measurement for membrane permeate side CO_2 content. Accordingly, high CO_2 partial pressure upon permeate side membrane surface may inhibit the carbonate decomposition as well as the CO_2 transport. The dissociation of CO_2 can be expressed as:

$$M_2CO_3 \rightleftharpoons M_2O + CO_2 \qquad (2.21)$$

Here, M_2CO_3 represents the Li, Na, K mixture of the ternary eutectic carbonate. M_2O stands for the Li, Na, K mixture of alkali metal oxides. When this reaction reaches thermodynamic equilibrium at a specific temperature T, the equilibrium constant or equilibrium dissociation constant K_d can be related to the standard Gibbs free energy of reaction ($\Delta_r G^{\ominus}$) shown in equation 2.22:

$$\Delta_r G^{\ominus} = -RTlnK_d \qquad (2.22)$$

$$K_d = \frac{a_{CO_2} a_{M_2O}}{a_{M_2CO_3}} = \frac{p_{CO_2} X_{M_2O}}{X_{M_2CO_3}} \qquad (2.23)$$

The definition of the equilibrium dissociation constant K_d is shown on equation 2.23, where a is the activity of relevant species. The alkali metal oxides produced can dissolve into the molten carbonate mixture forming a solution. However, the alkali oxides content was considerably low even at high temperature. The mole fraction of oxides (X_{M2O}) in the melt was determined as low as 10^{-3} to 10^{-5} in literature [84-86]. As $X_{M2CO3} \rightarrow 1$ and $X_{M2O} \rightarrow 0$ in this system, this can be treated as an ideal dilute solution and the activity can be replaced by mole fraction for simplification. On the other hand, activity of CO_2 can be replaced by partial pressure assuming it is an ideal gas.

It is difficult to calculate the standard Gibbs free energy of reaction 2.21 from the Gibbs free energy of formation of individual carbonates, since the carbonate mixture is in solid phase at standard state and individual carbonates are immiscible. The values of K_d and the equilibrium CO_2 partial pressure were often determined by experimental measurements. Spedding and Mills measured the dissociation pressures of carbonate melts from 750 to 950°C using static mercury manometric techniques, in which sweep gas was not present. Equilibrium pCO_2 were between 1.4×10^3 to 1.4×10^4 Pa [87]. Lorenz and Janz later used emf-concentration-cell principle, in which the potential between two inert electrodes in the carbonate melt is monitored. The potential is dependent on the CO_2 partial pressure over the test electrode. Their values were about 5 times smaller than Spedding and Mills. The carbonate decomposition probably did not approach true thermodynamic equilibrium under the conditions of dynamic flow for the emf approach. Constant flow may sweep some of the CO_2 away before full equilibrium is attained [88].

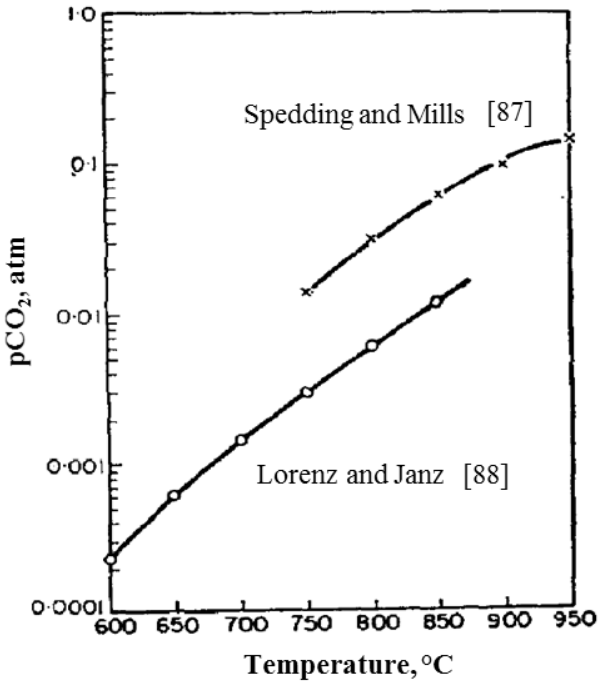

Figure 2.17: Equilibrium CO_2 dissociation pressures for the ternary eutectic carbonate of Li, Na, K (43.5:31.5:25.0 mole %) from 600 to 950°C [87, 88]. Reproduced with permission of Elsevier.

The chemical interaction between CO_2 and molten carbonate is not limited to the CO_2 dissociation. CO_2 molecules can react with molten carbonate directly on membrane surface if they are in contact with the molten phase. This is regarded as chemical solubility of CO_2 in the molten phase. The product species, namely dicarbonate ions ($C_2O_5^{2-}$), has been spectroscopically identified in a supported molten carbonate membrane for CO_2 permeation [89]. CO_2 also involves in the chemical interactions between molten carbonate and oxygen, forming various carbon and/or oxygen containing ionic species incorporated into the molten carbonate, including peroxide ions (O_2^{2-}), superoxide ions (O_2^-), peroxycarbonate ions (CO_4^{2-}) and superoxycarbonate ions (CO_5^{2-}). Some possible reactions are listed below [90-92]:

CO_2 addition: $CO_2 + CO_3^{2-} \leftrightarrow C_2O_5^{2-}$ (2.24)

Peroxide formation: $1/2O_2 + CO_3^{2-} \leftrightarrow O_2^{2-} + CO_2$ (2.25)

Superoxide formation: $3/2O_2 + CO_3^{2-} \leftrightarrow 2O_2^- + CO_2$ (2.26)

Oxygen incorporation: $1/2O_2 + CO_3^{2-} \leftrightarrow CO_4^{2-}$ (2.27)

Superoxycarbonate ions formation: $O_2 + CO_3^{2-} \leftrightarrow CO_5^{2-}$ (2.28)

The complexity of molten salt chemistry and the detailed mechanisms about reactions 2.24-2.28 are beyond the scope of this research. Nevertheless, when these reactions take place in parallel with the proposed interfacial electrochemical reaction (Figure 2.14), each one of the reactions could also be the rate-limiting step of the CO_2 transport across the molten carbonate dual phase membrane. The existence of these surface reactions cannot be ignored while carrying out the mechanistic studies of the membranes. (See details in Chapter 2.4)

Having reviewed the properties of both membrane support materials and molten carbonate, it is important to study how those properties influence the CO_2 permeation flux and selectivity of the membrane. The next stage will be looking at the experimental studies that investigate the functionalities and applications of molten carbonate dual phase membranes into CO_2 separation.

2.3. Enhancing CO_2 permeation flux through dual phase membranes

High CO_2 selectivity is the inherent advantage of the molten carbonate dual phase membranes due to their facilitated electrochemical CO_2 transport feature. This transport mechanism theoretically offers infinite CO_2 selectivity. However, in practical membrane operation many other factors may influence the membrane selectivity including the gas tightness of the sealant, membrane cracking and physical transport of other gas species through the molten phase. On the other hand, CO_2 permeation flux through molten carbonate dual phase membranes is an important parameter to be improved from the practical point of view, especially for post-combustion CO_2 separation. Chapter 1 has shown that the volumetric flow rate of flue gas emission from a typical coal fired power plant is of the order of 500m^3/s, equivalent to 11000 ton CO_2 per day [93]. Compact membrane separation units with high permeation flux are

desirable as this avoids the necessity for high membrane surface area which leads to high capital cost. Merkel et al. pointed out that for CO_2/N_2 selectivity above 30, increases in membrane CO_2 permeance are more important than further increases in selectivity. In practical post-combustion CO_2 separation applications, feed-to-permeate pressure ratio is usually between 5 and 15 and this poses a limitation on CO_2 enrichment within the permeate stream. Increasing membrane permeance will help reduce the required membrane area and capital cost, but further increasing selectivity has only a small impact on product purity [93]. Various approaches can be employed to improve the CO_2 permeation flux through molten carbonate dual phase membranes. This section reviews the experimental studies to find out effective methods for CO_2 permeation flux enhancement. Membrane functionalities, particularly CO_2 selectivity, will also be discussed.

2.3.1. Modifying pore microstructure and membrane geometry

The CO_2 permeation flux can simply be enhanced by modifying the physical properties of the dual phase membranes, including the pore microstructure as well as the geometry of the support material. Membrane support microstructure can be described in terms of porosity φ, tortuosity τ and average pore diameter of solid substrate r_p. It has been reported that with same membrane support material, porosity, tortuosity and average pore diameter of solid substrate are important factors for CO_2 permeation. Ortiz-Landeros et al. [94] prepared six porous LSCF6482 ($La_{0.6}Sr_{0.4}Co_{0.8}Fe_{0.2}O_{3-\delta}$) disks using pressing and sintering methods. The disks were sintered within a temperature range of 900 to 1200°C, resulting average pore diameter from 0.4mm to 0.8mm and open porosity from 0.528 to 0.079. The volumetric carbonate fraction of the fully infiltrated support disks was close to these values. They proposed that sintering temperature of solid support LSCF6482 controls solid fraction to tortuosity ratio $(\varphi/\tau)_s$ and carbonate fraction to tortuosity ratio $(\varphi/\tau)_c$, the two ratios further control the apparent measured conductivities of solid material and the melt respectively. The ratios were introduced as correction factors for the intrinsic dense solid conductivities and molten carbonate conductivities within their empirical formula for CO_2 permeation flux. It turned out that an optimum sintering temperature exists for maximum CO_2 permeation. 1000°C sintering temperature showed the highest CO_2 permeance across all operating temperatures from 750 to 900°C (Figure 2.18). They also confirmed the membrane microstructure changed as a function of sintering temperature. At sintering temperatures higher than 1000°C, CO_2 permeation dropped because densification becomes preeminent, yielding a denser support that lacks pore interconnectivity.

Apart from sintering temperature, specific membrane support fabrication methods can also help modify pore structure under similar membrane geometry. Zhang et al. [95] co-precipitated solid oxide material $Ce_{0.8}Sm_{0.2}O_{1.9}$ (SDC) with NiO from the nitrates of the constituents forming nanocomposite powder, followed by pressing and sintering. Membrane support had highly interconnected pores and narrow pore size distribution (600nm median pore size). Downhill CO_2 permeability was two orders of magnitudes higher than Anderson and Lin's work using LSCF6482 (sol-gel methods) and Wade et al.'s

work using YSZ (tape casting technique) [49, 53]. The intrinsic ionic conductivity of the three materials is not vastly different and the three membrane disks had similar thickness.

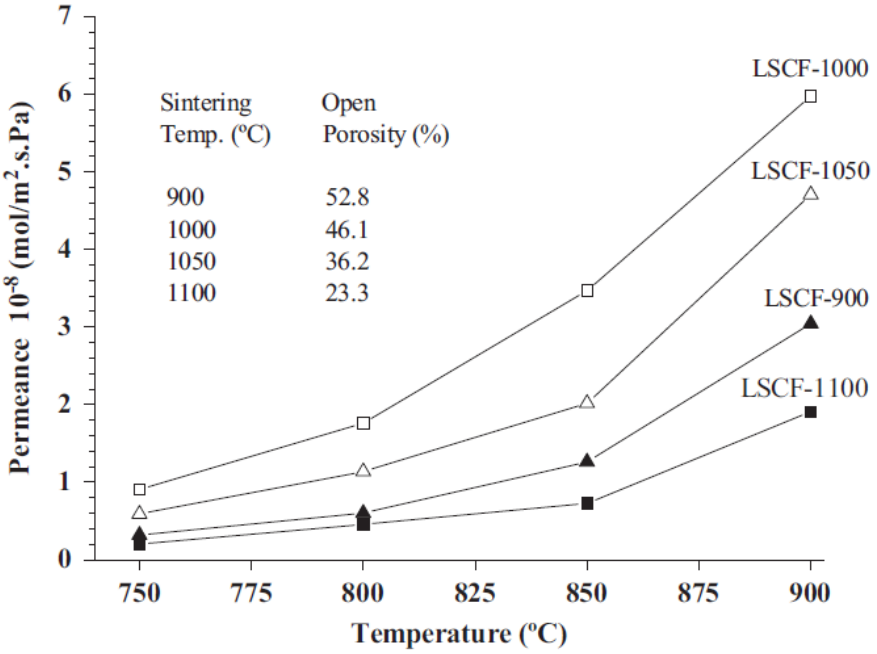

Figure 2.18: High temperature CO_2 permeance of the dual phase membranes against operating temperatures (750-900°C), with supports prepared at different sintering temperatures. LSCF-1000 represents the LSCF 6482 support sintered at 1000°C. Nomenclatures are the same for other sintering temperatures [94]. Reproduced with permission of Elsevier.

Changing the thickness of the membrane is another way to enhance the CO_2 permeation flux since it shortens the diffusion paths and reduces the resistance of ion/electron transport. Based on equation 2.9, thinner membrane thickness δ can improve the CO_2 permeation flux J under similar driving force, even though same solid phase material with same CO_2 permeability is used. Anderson and Lin [49] were one of the pioneers who experimentally investigated the effect of membrane thickness on CO_2 permeance. They carried out downhill CO_2 permeance experiment across LSCF6482-carbonate membranes with thickness of 3 mm down to 0.375 mm. CO_2 permeance increased with decreasing membrane thickness for every operating temperature as seen in Figure 2.19. Arrhenius plots were produced for the four membranes based on these results. The apparent activation energy of CO_2 permeation (see equation 2.14) was between 86.4 and 89.9 kJ/mol. As the thickness approaching 0.375 mm, the activation energy levelled off at 89.9 kJ/mol and the rate of permeance improvement gradually diminished (Figure 2.19). They suggested that both behaviours indicated the bulk ionic diffusion in solid phase was no longer rate limiting for thinner membranes and the rate of interfacial reactions may become an important rate determining factor for CO_2 permeation. It is possible that interfacial reaction will become rate limiting if the thickness is further reduced. In another noticeable research by Lu and Lin [96], they attempted to fabricate ultrathin 10 μm disks of YSZ-carbonate membranes with non-wettable porous $Bi_{1.5}Y_{0.3}Sm_{0.2}O_{3-\delta}$ (BYS) base layer. The CO_2 flux is one order of magnitude higher than 200-400 mm

thick YSZ-carbonate membrane [96]. Apparent activation energy for CO_2 permeation through the thin YSZ-carbonate membrane is 106 kJ/mol. The value is larger than the activation energy for CO_2 permeation through thicker YSZ-carbonate membrane (84 kJ/mol) [53], which is closer to oxide ion conduction in YSZ electrolytes reported in literature (81 kJ/mol) [97]. Conductivity data (Table 2.4) of solid materials revealed that bulk O^{2-} diffusion rate is much lower than CO_3^{2-} transport through molten carbonate, indicating CO_2 permeation through thin molten carbonate dual phase membranes is more likely to be interfacial reaction limiting.

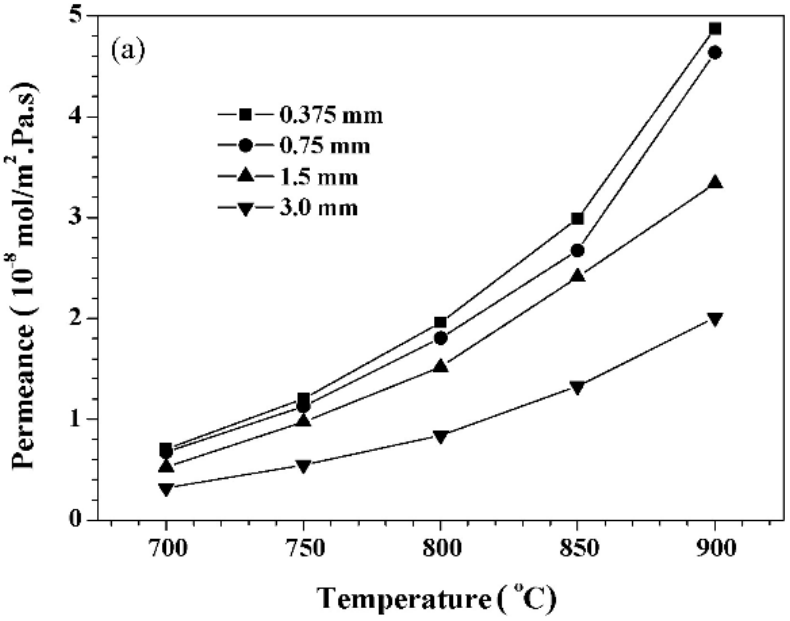

Figure 2.19: High temperature downhill CO_2 permeance of the LSCF6482-carbonate dual-phase membrane for various membrane thicknesses as a function of temperature [49]. Reproduced with permission of Elsevier.

Porous solid oxide membrane disks made by powder pressed and sintering method tend to have random packed pore network (Figure 2.20 a) [98]. Alternatively, phase inversion techniques can be utilised to fabricate porous hollow fibre membrane support [97]. The resultant porous membrane support is in a thin tubular geometry with an outer shell diameter of around 2 mm and a wall thickness of a few hundred μm. The hollow fibre support fabricated by phase inversion has large finger-like straight channels and denser sponge-like top layer with random packed pore networks (Figure 2.20 b). Hence the phase inversion technique can modify the pore microstructure simultaneously with lowering the membrane thickness. The incorporation of molten carbonate is normally achieved by impregnation of ternary carbonate suspension. In general, hollow fibre membranes are operated in shell and tube configuration. Gas permeates across the membrane through the wall of the fibre from shell side to tube side or vice versa, with both ends of the fibre sealed. The advantages of hollow fibre molten carbonate membranes are that both thickness and pore microstructure can be tailored and optimised during the fabrication. The effective surface area for gas permeation is also largely increased comparing with disk membranes. Zuo and co-workers [97] fabricated YSZ-carbonate hollow fibre membranes and carried out high

temperature downhill 1:1 CO_2/N_2 separation experiments. Across 550 to 950°C, CO_2 permeation flux ranged from 0.022 to 0.22 ml·cm^{-2}min^{-1} [97]. Converting to CO_2 permeance it was roughly 1.94×10^{-8} mol·m^{-2}s^{-1}Pa^{-1} at 850°C. This is approximately three times higher than a thicker disk shaped YSZ-carbonate membrane fabricated by Ahn and co-workers [98]. The CO_2/N_2 selectivity of this hollow fibre membrane was considerable since the N_2 concentration on permeate side was on 10^2 ppm scale. Chen et al. developed 0.1-0.15 mm thick SDC-carbonate hollow fibre membranes by phase inversion. With a 50% CO_2/50% N_2 feed condition, their membranes achieved stable 7.0×10^{-7} mol·m^{-2}s^{-1}Pa^{-1} CO_2 permeance for 85h at 700°C [99], remarking a further improvement to the SDC disk membranes [95].

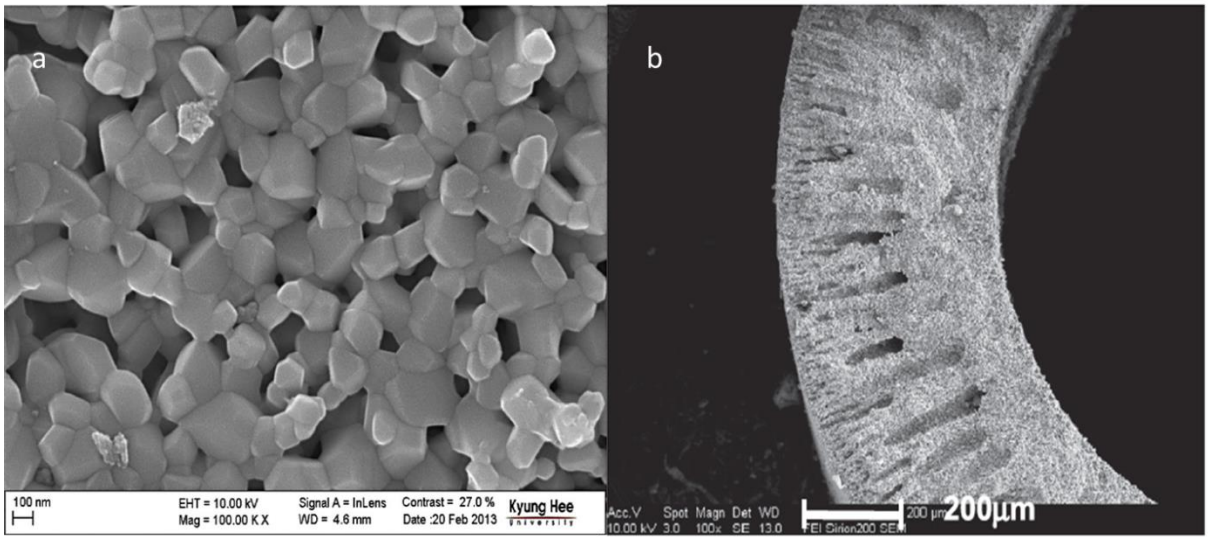

Figure 2.20: (a) Surface scanning electron microscope (SEM) image of disk shaped YSZ membrane support with random packed pore network [98]. (b) Cross-sectional SEM image of phase inverted YSZ hollow fibre with finger-like channels and packed pore top/bottom layer [97]. Reproduced with permission of Elsevier.

2.3.2. Enhancing bulk ion/electron transport in solid phase

Along with physical microstructure and geometry modification, studies widely agreed that chemical properties of the molten carbonate dual phase membranes directly related to the CO_2 permeability based on the proposed electrochemical mechanisms. Bulk ionic/electronic conductivities in solid phase may influence the CO_2 permeability strongly. For downhill CO_2 permeation alone, purely oxide ion conductive and MIEC materials have been widely employed as solid support. CO_2 permeation can be limited by bulk oxide ion diffusion, interfacial electrochemical reactions or carbonate ion diffusion in the melt. For thick membranes (~1mm) the rate-limiting step is more likely to be bulk oxide ion diffusion [49]. One straightforward way to enhance ion transport is choosing alternative solid material with higher ionic conductivity. Whilst for thin membranes that are no longer bulk oxide ion diffusion limiting, changing solid material probably cannot be effective no matter how high the conductivity is. Similarly, for downhill O_2-CO_2 co-permeable MIEC membranes which are bulk oxide ion/electron diffusion limiting, switching to a highly ionic and electronic conductive solid material is also expected

to promote the permeation flux of both O_2 and CO_2. This section will compare the CO_2 flux of molten carbonate dual phase membranes fabricated using various solid phase material. To exclude the effect from physical modification and driving force, membranes with similar geometry and microstructure were chosen. Preferably the experiments were conducted under similar feed CO_2 concentration to ensure the CO_2 partial pressure differences across the membranes were similar. It is also clearer to compare in terms of the CO_2 permeability of different support materials as permeability reflects the properties of membrane materials themselves regardless of membrane thickness and driving forces.

Currently the most common ionic conductive and MIEC solid material being studied for downhill CO_2 separation out of inert gases are YSZ, LSCF, samarium doped ceria (SDC), doped bismuth oxide (BYS) and gadolinium-doped ceria (CGO). A cross comparison can be made from Anderson and Lin's work [49] on LSCF6482-carbonate membrane and Ahn's work [98] on YSZ-carbonate membrane. They both used thick disk membranes (δ>1mm) and 50% CO_2 feeding gas at ambient pressure. They obtained downhill CO_2 permeance of 0.3×10^{-8} and 0.1×10^{-8} $mol\cdot m^{-2}s^{-1}Pa^{-1}$ respectively at 650°C. The materials have similar solid ionic conductivity, resulting CO_2 permeance values on the same order of magnitude.

Besides, downhill CO_2 permeation thorough dual phase membranes using $Bi_{1.5}Y_{0.3}Sm_{0.2}O_{3-\delta}$ (BYS), $Ce_{0.9}Gd_{0.1}O_{2-\delta}$ (CGO), $Ce_{0.8}Sm_{0.2}O_{2-\delta}$ (SDC) substrates were studied extensively because of their higher ionic conductivities. It is noteworthy that the downhill experiment carried out by Patrício et al. using 0.92 mm disk shaped CGO-carbonate membranes achieved CO_2 permeance of 4.9×10^{-8} $mol\cdot m^{-2}s^{-1}Pa^{-1}$ [100]. In terms of permeability it was 4.51×10^{-11} $mol\cdot m^{-1}s^{-1}Pa^{-1}$, which was a significant improvement comparing with YSZ and LSCF6482 membranes [100] because the CGO substrates have higher ionic conductivity than YSZ and LSCF6482.

For CO_2-O_2 co-permeation, electronic conductivity of solid oxide material is more important than the oxide ion conductivity. Early experiment carried out by Chung et al. [48] intended to justify the co-permeation mechanism described in Figure 2.6 using purely electronic conductive stainless steel as solid support. They successfully demonstrated that electronic conductive solid support allowed CO_2-O_2 co-permeation. However, the experiment required CO_2/O_2 atmosphere, which oxidised the metal support and reduced its electronic conductivity.

More chemically stable support metals under O_2 atmosphere have been tested for metallic-carbonate dual phase membranes. One typical example is highly electronic conductive silver (Ag). Huang's research group developed silver-carbonate dual phase membrane (Ag-MC) for CO_2-O_2 co-permeation. They fabricated powder pressed and sintered Ag-MC pellets with 1.67mm thickness and obtained downhill CO_2 flux of 0.82 $ml\cdot cm^{-2}min^{-1}$ and O_2 flux of 0.43 $ml\cdot cm^{-2}min^{-1}$ at 650°C. This indicated the CO_2/O_2 ratio on permeate side was close to 2:1 as depicted on the co-permeation mechanism (see electrochemical reaction on membrane permeate side in Figure 2.6). Since the silver support is not ionic conductive, electrochemical CO_2 transport alone (Figure 2.5) is not expected. The equivalent CO_2

permeance reached 1.4×10^{-7} $mol \cdot m^{-2}s^{-1}Pa^{-1}$ which was six times higher than the stainless steel-carbonate membrane reported by Chung, even though the overall CO_2/O_2 partial pressure difference in Huang's study was only half of Chung's. They concluded that the high level of permeation performance exhibited by the Ag–MC membrane was attributed to better chemical compatibility of MC with Ag; better catalytic activity over CO_2 and O_2 activation processes and better electronic conductivity of Ag in oxidising atmosphere [101].

Overall, the effect of highly ionic and/or electronic conductive solid supports on CO_2 permeation can be seen from the literature for both CO_2 selective and CO_2-O_2 co-permeable membranes. As different researchers had different fabrication methods, consistency of membrane geometry and microstructures cannot be guaranteed. Therefore, the cross comparison of CO_2 permeance in various studies was not always representing the pure effect of solid phase conductivity. Anyhow, a summary table (Table 2.4) is produced to compare the ionic conductivity and electronic conductivity of various materials, as well as a summary table cross comparing CO_2 permeance through various ceramic-carbonate and metallic-carbonate dual phase membranes at the end of Chapter 2.3 (Table 2.5 and 2.6).

Table 2.4: Ionic conductivities and electronic conductivities data of solid oxide materials at 900°C (650°C for silver and stainless steel). Here the correction factor for carbonate ion conductivity due to membrane microstructure is ignored [48, 53, 63, 68, 101-104].

	Ionic conductivity (S/cm)	**e- conductivity (S/cm)**	**Tertiary CO_3^{2-} conductivity (S/cm)**
YSZ	0.106	~0	3.5
$Ce_{0.8}Sm_{0.2}O_{2-\delta}$ (SDC)	0.18	~0	3.5
$Bi_{1.5}Y_{0.3}Sm_{0.2}O_{3-\delta}$ (BYS)	0.94	~0	3.5
Gadolinium-doped ceria (CGO)	0.27	~0	3.5
LSCF6428 ($La_{0.6}Sr_{0.4}Co_{0.2}Fe_{0.8}O_{3-\delta}$)	0.23	252	3.5
LSCF6482 ($La_{0.6}Sr_{0.4}Co_{0.8}Fe_{0.2}O_{3-\delta}$)	0.091	1217	3.5
Stainless steel	~0	~10^4 at 650°C	3.5
Silver	~0	6.3×10^5 at 650°C	3.5

2.3.3. Enhancing thermodynamic driving force

It is possible to promote the CO_2 flux by enhancing the overall chemical potential difference for the CO_2 permeation. The general approach is to incorporate other gas species into the molten carbonate dual phase membrane system, such that they participate the transport mechanisms across the membrane. Thermodynamically, higher overall chemical potential difference across the membrane offers higher

driving force upon gas permeation. If the new gas species contributes to increasing the overall chemical potential difference of CO_2 permeation based upon the permeation mechanism, CO_2 permeation flux may well be enhanced as a response to higher driving force.

It has been shown in Chapter 1 that the concept of CO_2-O_2 co-permeation is ideal for post-combustion CO_2 separation out of flue gas. Although silver has very high electronic conductivity, the application of this type of membranes is limited because oxygen must be in the feed stream to allow CO_2 permeation. Operating silver-carbonate membranes at high temperature may also affect the membrane stability [104]. LSCF based membranes are more flexible and stable comparing with silver. Lin's group demonstrated experimentally that high temperature downhill CO_2 separation with O_2 co-permeation through LSCF 6482-carbonate membranes largely facilitated CO_2 permeation flux comparing with CO_2 permeation alone [105]. They selected a perovskite-like MIEC material as the solid support because MIEC is capable of both CO_2-O_2 co-permeation and CO_2 permeation without O_2. This means CO_2 permeation flux can be compared directly by alternating O_2 containing feed stream and O_2 free feed stream. To demonstrate a clear comparison, large CO_2 and O_2 concentrations were used for feeding gas. When feeding 50% CO_2 and 50% N_2 at 900°C the CO_2 permeation flux stabilised at 0.03 $ml \cdot cm^{-2}min^{-1}$. Once O_2 was present in feed stream (feeding 50% CO_2 and 25% O_2 with inert balance gas), CO_2 permeation flux increased to 3.4 $ml \cdot cm^{-2}min^{-1}$. This observation demonstrated the co-permeation of O_2 provided such large driving force for CO_2 transport that the CO_2 permeation flux was enhanced by more than two orders of magnitude. More recently, Zhuang et al. also reported the effect of O_2 existence in feeding gas for promoting the CO_2 permeation flux using LSCF6428-carbonate membranes [106]. Referring to Table 2.4, bulk charge diffusion through LSCF6482 substrate is much faster via electronic conduction mechanism. Hence in this case carbonate ion diffusion through molten phase would become rate limiting if the interfacial reaction was assumed to be very fast.

Thermodynamic analysis on this membrane system is required to interpret how the driving force is enhanced by co-feeding O_2. For a downhill separation which involves solely CO_2 permeation (Figure 2.5), the condition that feed side CO_2 partial pressure (p'_{CO_2}) > permeate side CO_2 partial pressure (p''_{CO_2}) has to be satisfied according to thermodynamics of CO_2 driving force as discussed in Chapter 1.3. In contrast, for CO_2/O_2 co-permeation the addition of oxygen offers extra chemical potential on feed side. The thermodynamic driving force can be derived from the first principle of the reversible reaction Gibbs free energy on both sides of the membrane:

$$\Delta_r G' = \left(\frac{\partial G'}{\partial \xi}\right)_{p,T} \qquad (2.29) \qquad\qquad \Delta_r G'' = \left(\frac{\partial G''}{\partial \xi}\right)_{p,T} \qquad (2.30)$$

$\Delta_r G'$ is the reaction Gibbs free energy of feed side electrochemical reaction. $\Delta_r G''$ is the reaction Gibbs free energy of permeate side electrochemical reaction. ξ is the extent of the interfacial reaction with a unit of moles. Here, the reaction Gibbs free energy for reversible reactions is defined as the slope of

curve that describes how total Gibbs free energy of the reaction mixture (G' and G" comprising all reactants and products) changes against the extent of reaction [86].

Assuming the mechanism in Figure 2.6 is the only dominating mechanism, when the feed side reaction advances by dξ, the corresponding change in total Gibbs free energy can be written as equation 2.31. Hence the reaction Gibbs free energy of feed side electrochemical reaction can be written as equation 2.32, similarly for permeate side (equation 2.33).

$$dG' = -\mu'_{CO_2} d\xi - \frac{1}{2}\mu'_{O_2} d\xi - 2\mu'_{e} d\xi + \mu_{CO_3^{2-}}{}' d\xi \qquad (2.31)$$

$$\Delta_r G' = \left(\frac{\partial G'}{\partial \xi}\right)_{p,T} = \mu'_{CO_3^{2-}} - \mu'_{CO_2} - \frac{1}{2}\mu'_{O_2} - 2\mu'_{e} \qquad (2.32)$$

$$\Delta_r G'' = \left(\frac{\partial G''}{\partial \xi}\right)_{p,T} = \mu''_{CO_2} + \frac{1}{2}\mu''_{O_2} + 2\mu''_{e} - \mu''_{CO_3^{2-}} \qquad (2.33)$$

In order to make the forward CO_2 permeation from membrane feed to permeate side proceed spontaneously, it must satisfy that $\Delta_rG'+\Delta_rG''< 0$. The chemical potential difference of the carbonate ion and electron are both zero when the system is at equilibrium (i.e. $\Delta_rG'+\Delta_rG'' = 0$). At this point, the system is in no flux condition and no CO_2 uphill permeation is observable. Once the overall chemical potential difference of CO_2 and O_2 between membrane feed and permeate side start increasing, the equilibrium is perturbed allowing uphill CO_2 permeation to take place. Replacing chemical potential of gas species in terms of partial pressure, this relation can be written as equation 2.34. By rearranging this, equation 1.4 in Chapter 1.3 can be obtained which describes the requirement for forward CO_2 permeation when O_2 co-permeate with it.

$$RTln\left(\frac{p''_{CO_2}}{p^{\ominus}_{CO_2}}\right) + RTln\left(\frac{p''_{O_2}}{p^{\ominus}_{O_2}}\right)^{1/2} < RTln\left(\frac{p'_{CO_2}}{p^{\ominus}_{CO_2}}\right) + RTln\left(\frac{p'_{O_2}}{p^{\ominus}_{O_2}}\right)^{1/2} \qquad (2.34)$$

This relation suggests that p'CO_2 is not necessarily larger than p"CO_2 given that p'O_2 is a lot higher than p"O_2. It indicates CO_2 could be able to permeate against its own chemical potential difference with O_2 co-permeation. E. Papaioannou et al. investigated uphill CO_2 permeation using LSCF6428 membranes [28]. The gas flows were shifted between asymmetrical operation (feed side 0.99% CO_2, 1.03% N_2, 19.45% O_2 in Ar, permeate side 1.03% CO_2 in Ar) and symmetrical operation (1.03% CO_2 in Ar both sides). The symmetrical condition was also a non-permeating condition in which the driving force for CO_2 permeation is negligible. It set up a reference CO_2 concentration and the variation of permeate and feed side CO_2 concentration can be monitored once switching to asymmetrical condition. At 600°C CO_2 permeation flux of $(1.8 \pm 0.3) \times 10^{-4}$ mol·m^{-2}s^{-1} was observed with asymmetrical operation. Following this work, the CO_2 concentration in feed gas was halved and CO_2 permeation flux still stabilised at $(1.5 \pm 0.3) \times 10^{-4}$ mol·m^{-2} s^{-1}. This work validated the theory of uphill permeation based on the above thermodynamic analysis.

Table 2.5: Summary of CO_2 permeance for downhill CO_2/inert gas separation experiments in literature, varying solid materials and thickness. Sweep gas were pure inert gas.

Ref.	Solid phase	Feed	Thickness mm	Temperature °C	Permeance mol m^{-2} s^{-1} Pa^{-1}
[53]	YSZ	50% CO_2	0.25mm disk	650	0.32×10^{-8}
[98]	YSZ	50% CO_2	Thick disk	650	0.1×10^{-8}
[97]	YSZ	50% CO_2	0.2mm hollow fibre	650	$\sim0.91\times10^{-8}$
[96]	YSZ-BYS	25% CO_2	0.01mm disk	650	$\sim7.7\times10^{-8}$
[49]	LSCF6482	50% CO_2	0.375mm disk	700	0.8×10^{-8}
[95]	SDC	48% CO_2	1.2mm disk	650	2.25×10^{-7}
[99]	SDC	50% CO_2	0.1mm hollow fibre	700	$\sim7.0\times10^{-7}$
[97]	BYS	50% CO_2	0.05mm disk	650	1.1×10^{-8}
[100]	CGO	50% CO_2	0.92mm disk	650	4.9×10^{-8}

Table 2.6: Summary of CO_2 permeation flux for CO_2-O_2 co-permeation experiments in literature, using various solid materials with different thermodynamic driving forces. The work by E. Papaioannou et al. [28] represents a condition for 'uphill' CO_2 permeation.

Ref.	Solid phase	Feed	Permeate (sweep gas)	Temperature °C	Flux mol m^{-2} s^{-1}
[48]	Stainless steel	66.7% CO_2, 33.3% O_2	Inert gas	650	1.68×10^{-3}
[101]	Ag	42% CO_2, 42% O_2, 16% N_2	99.999% He	650	6.1×10^{-3}
[105]	LSCF6482	50% CO_2, 50% N_2	100% Ar	900	2.23×10^{-4}
[105]	LSCF6482	50% CO_2, 25% O_2, 25% N_2	100% Ar	900	2.53×10^{-2}
[28]	LSCF6428	0.99% CO_2, 1.03% N_2, 19.45% O_2 in Ar	1.03% CO_2 in Ar	600	1.8×10^{-4}
[28]	LSCF6428	0.51% CO_2, 0.57% N_2, 19.45% O_2 in Ar	1.03% CO_2 in Ar	600	1.5×10^{-4}

Overall, the concept of CO_2-O_2 co-permeation could be a more promising method to enhance CO_2 permeation flux in terms of practical application, since the CO_2 permeation flux at lower temperature (i.e. 600°C) could outperform the downhill CO_2 permeation alone at high temperature (i.e. 900°C). The uphill CO_2 permeation would be able to overcome its own chemical potential gradient without compression, making post combustion CO_2 separation process less energy intensive. Moreover, a few studies have shown the CO_2 flux had certain correlations with its driving force, depending on the permeation mechanisms [28, 105, 107]. Nevertheless, CO_2 transport mechanism through ceramic-

molten carbonate dual phase membrane has not been fully understood and new surface reaction mechanisms involving various ionic species in the melt (see equation 2.24-2.28) was proposed recently [92]. The CO_2-O_2 co-permeation can be rate limited not only by bulk ionic/electronic diffusion but also by various electrochemical reactions. The flux would correlate with the driving force differently if the rate-limiting step were different. Therefore, a study on flux-driving force correlation for CO_2-O_2 co-permeable dual phase membranes can help gain mechanistic insight and predict how well they can perform under the operating condition of practical application.

2.4. CO_2 flux-driving force models

2.4.1. CO_2-O_2 co-permeation models

A number of studies have suggested semi-empirical formulae that describe the downhill CO_2 flux-driving force relationships for oxide ion conducting dual phase membranes [53, 62, 63, 94]. It has been widely agreed that the downhill CO_2 flux J_{CO_2} is proportional to ln (p'_{CO_2}/ p''_{CO_2}), the pre-exponential factors comprise the solid and molten phase ionic conductivities as well as membrane pore properties. Unlike the downhill CO_2 permeation alone, CO_2-O_2 co-permeation through electronic conductive membranes involves electron transport in the solid and ionic transport in the melt. More complex transport mechanisms are expected. As a result, the rate-limiting step of CO_2 transport have more possibilities. Different rate-limiting steps yield different CO_2 flux-driving force correlation models. So far, only Zhang et al. and Chung el al. have suggested models for CO_2 flux-driving force correlation on the basis of CO_2-O_2 co-permeation [48, 92].

As the charge transport in this membrane system forms a closed loop without external current, the overall charge flux balance can be written as equation 2.35. Based on the electrochemistry equation 2.36 for diffusive carbonate ion flux (likewise for the equation of electron), equation 2.37 expresses the flux of carbonate ion, ignoring the static potential across the membrane whilst preserving the chemical potential. In these equations, z_e and z_c are the charge numbers of electron and carbonate ion respectively, J_e and $J_{CO_3^{2-}}$ are the flux of electron and carbonate ion. σ_c and σ_e are the carbonate ion conductivity in molten phase and electron conductivity in solid phase. ∇ denotes gradient across the membrane, μ denotes chemical potential and ϕ denotes static potential. F in equation 2.36 and 2.37 represents the Faraday constant.

$$z_e J_e + z_c J_{CO_3^{2-}} = 0 \tag{2.35}$$

$$J_{CO_3^{2-}} = -\frac{\sigma_c}{z_c^2 F}\left(\nabla \mu_{CO_3^{2-}} + z_c F \nabla \phi_c\right) \tag{2.36}$$

$$J_{CO_3^{2-}} = -\frac{\sigma_c \sigma_e}{(\sigma_c + \sigma_e) z_c^2 F^2}\left(\nabla \mu_{CO_3^{2-}} - \frac{z_c}{z_e}\nabla \mu_e\right) \tag{2.37}$$

Considering $CO_2 + 1/2O_2 + 2e^- \leftrightarrow CO_3^{2-}$ as the global electrochemical reaction occurring at the feed side interface of the membrane, when this reaction reaches local thermodynamic equilibrium, the local Δ_rG' associated with the global electrochemical reaction becomes zero, giving equation 2.38 for membrane feed side. Substituting this relation into equation 2.37, a theoretical correlation between steady state CO_2 flux and chemical potential gradient of CO_2 and O_2 can be obtained (equation 2.39).

$$\nabla\mu_{CO_3^{2-}} - 2\nabla\mu_e = \nabla\mu_{CO_2} + \frac{1}{2}\nabla\mu_{O_2} \qquad (2.38)$$

$$J_{CO_2} = J_{CO_3^{2-}} = -\frac{\sigma_c\sigma_e}{4(\sigma_c+\sigma_e)F^2}\left(\nabla\mu_{CO_2} + \frac{1}{2}\nabla\mu_{O_2}\right) \qquad (2.39)$$

This flux-driving force model for CO_2-O_2 co-permeation was proposed based on silver-carbonate dual phase membranes [92]. In this case, carbonate ion conductivity σ_c was five orders of magnitude smaller than electronic conductivity of silver σ_e, so the $\sigma_c + \sigma_e$ term in equation 2.39 was approximately σ_e. Although LSCF6428 being used for this project has smaller electronic conductivity than silver, this approximation is still valid. The chemical potential gradient terms can be replaced by partial pressure gradient. Microstructural correction factors (see Chapter 2.3.1) comprising membrane porosity ε, carbonate volumetric fraction φ and tortuosity τ are also included. By integrating over the whole length of membrane thickness (δ) as well as the entire partial pressure difference, equation 2.40 can be obtained.

$$J_{CO_2} = -\frac{\varepsilon\varphi}{\tau}\frac{RT\sigma_c}{4F^2\delta}\int_{p'CO_2,p'O_2}^{p''CO_2,p''O_2}\left(dlnp_{CO_2} + \frac{1}{2}dlnp_{O_2}\right) \qquad (2.40)$$

This model was built up based upon several assumptions:

- $CO_2 + 1/2O_2 + 2e^- \leftrightarrow CO_3^{2-}$ is the global electrochemical reaction occurring on the gas-solid-carbonate interface. CO_2 transport is facilitated by the counter diffusion of e^- and CO_3^{2-} in the solid and melt respectively.
- This electrochemical transport is the only dominating route to transport CO_2 (i.e. through metallic-carbonate membrane). For MIEC the electrochemical transport involving oxide ions is not included.
- Assuming the microstructural correction factors term is always a constant, because in our research same material, fabrication method and sintering temperature will be employed. Since we focus on studying the effect of changing driving force to CO_2 flux, it is important to control other variables including temperature, membrane thickness and membrane microstructure.
- Assuming that σ_c and σ_e are both pCO_2 and pO_2 independent [108].

There are several different possibilities for the dominating rate-limiting step. For each individual possible rate-limiting step, a unique CO_2 flux-driving force relationship can be derived followed by further assumptions based on equation 2.40. In the case that interfacial electrochemical reaction $CO_2 + 1/2O_2 + 2e^- \leftrightarrow CO_3^{2-}$ is very fast, formation of CO_3^{2-} is instantaneous on membrane feed side surface.

The rate of CO_2 transport through the membrane solely depends on carbonate ion conductivity in the melt. Zhang et al. proposed that the feed side carbonate ion conductivity is proportional to surface concentration of CO_3^{2-} (or $[CO_3^{2-}]_S$) and has no dependence with surface partial pressure of CO_2 and O_2 [92]. Since the formation of CO_3^{2-} is instantaneous and CO_3^{2-} transport is slower, there could be an accumulation of carbonate ions upon membrane feed side surface. Consequently, a chemical potential gradient of CO_3^{2-} across the membrane in molten phase is formed. Integrating 2.40 gives equation 2.41, which represent the semi-empirical CO_2 flux-driving force relationship for bulk carbonate ion diffusion limiting case. In other words, CO_2 flux would have logarithm dependency with feed side and permeate side CO_2 and O_2 partial pressures.

$$J_{CO_2} = -\frac{\varepsilon\varphi}{\tau}\frac{RT\sigma_c}{4F^2\delta}\ln\left(\frac{p"CO_2 p"O_2^{1/2}}{p'CO_2 p'O_2^{1/2}}\right) = \frac{\varepsilon\varphi}{\tau}\frac{RT\sigma_c}{4F^2\delta}\ln\left(\frac{p'CO_2 p'O_2^{1/2}}{p"CO_2 p"O_2^{1/2}}\right) \qquad (2.41)$$

On the other hand, interfacial reaction rate could be much slower than bulk carbonate ion diffusion. If the global interfacial electrochemical reaction $CO_2 + 1/2O_2 + 2e^- \leftrightarrow CO_3^{2-}$ is the only step involved in charge transfer, this reaction becomes rate limiting and $[CO_3^{2-}]_S$ becomes dependent on surface partial pressure of CO_2 and O_2. Zhang et al. expressed the rate equation as $r = kpCO_2pO_2^{1/2}$ where k is the rate constant. Following the integration over partial pressure gradient, a relation of $[CO_3^{2-}]_S = k_1pCO_2pO_2^{1/2}$ can be obtained, where k_1 is a proportionality constant. As σ_c is always proportional to $[CO_3^{2-}]_S$, the dependence of σ_c and surface partial pressure of CO_2 and O_2 can be expressed as $\sigma_c = K_1pCO_2pO_2^{1/2}$ where K_1 is an overall proportionality constant. In this case, σ_c term in equation 2.40 needs to be included within the integral. Therefore, in the case of interfacial reaction $CO_2 + 1/2O_2 + 2e^- \leftrightarrow CO_3^{2-}$ limiting, CO_2 flux-driving force relationship can be expressed as equation 2.42. In other words, CO_2 flux has linear dependency with feed side and permeate side CO_2 and O_2 partial pressures.

$$J_{CO_2} = -\frac{\varepsilon\varphi}{\tau}\frac{RTK_1}{4F^2\delta}\left(p"CO_2 p"O_2^{1/2} - p'CO_2 p'O_2^{1/2}\right) \qquad (2.42)$$

Surface charge transfer has more possibilities according to the molten carbonate chemistry described in reactions 2.24-2.28. Various gas-liquid electrochemical reactions are possible on the surface of molten carbonate. It implies that global interfacial reaction may involve more sub steps, forming various active intermediate species including peroxide ions (O_2^{2-}), superoxide ions (O_2^-), peroxycarbonate ions (CO_4^{2-}) and superoxycarbonate ions (CO_5^{2-}) [92]. When any of these sub reactions is rate limiting, overall CO_2 flux though the membrane could slow down. For instance, when peroxide formation (reaction 2.25) is rate limiting, the peroxide ion concentration $[O_2^{2-}]_S$ was expressed as $k_2pCO_2^{-1}pO_2^{1/2}$. $[CO_3^{2-}]_S$ also followed the same dependence on pCO_2 and pO_2 therefore carbonate ion conductivity was expressed as $\sigma_c = K_2pCO_2^{-1}pO_2^{1/2}$ [92]. Likewise, when the formation of any other intermediate ions is rate limiting, unique CO_2 flux-driving force relationship can be obtained followed by integration. The relationships obtained from intermediate surface reaction limiting scenarios are listed below.

Peroxide formation limiting: $J_{CO_2} \propto (p'CO_2^{-1}p'O_2^{1/2} - p"CO_2^{-1}p"O_2^{1/2})$ (2.43)

Superoxide formation limiting: $J_{CO_2} \propto (p'CO_2^{-1}p'O_2^{1/2} - p"CO_2^{-1}p"O_2^{1/2})$ (2.44)

Peroxycarbonate formation limiting: $J_{CO_2} \propto (p'O_2^{1/2}\ln p'CO_2 - pO_2^{1/2}\ln p"CO_2)$ (2.45)

Superoxycarbonate formation limiting: $J_{CO_2} \propto (p'O_2\ln p'CO_2 - p"O_2\ln p"CO_2)$ (2.46)

2.4.2. Further enhancement of thermodynamic driving force

In the context of membrane based post-combustion CO_2 separation, vacuuming permeate side gas stream has been the most common option for generating a more concentrated CO_2 stream. This option lowers the total pressure on membrane permeate side. Its energy consumption is in accordance with higher desired CO_2 concentration in permeate stream, as well as higher desired thermodynamic driving force (CO_2 partial pressure difference). So far, the concept of uphill CO_2-O_2 co-permeation through MIEC-carbonate dual phase membranes seems to be a possible alternative. Merkel et al. suggested that if high permeance membranes can be developed up to 1.34×10^{-6} mol·m^{-2}s^{-1}Pa^{-1} or more, no compression/vacuuming will be the preferred approach from energy and cost standpoints [93]. Although the uphill CO_2 permeance with O_2 has the potential to approach this figure, further enhancement on CO_2 flux and its thermodynamic driving force is clearly required.

Considering the CO_2 content is relatively low at 10-15% by volume within the flue gas, enriching feed side O_2 content is an option to achieve higher CO_2 flux. Based on equation 2.41-2.46, if feed side oxygen partial pressure p'O_2 is higher whilst controlling other parameters, the driving force term involving CO_2 and O_2 partial pressures will be higher no matter what relationship holds between CO_2 flux and driving forces. In practice, flue gas would be blended with high concentration O_2 supplied from an ASU. The drawback of this option is that there is a limitation in term of the flux enhancement. Firstly, the production of purified O_2 from ASU could be very energy intensive. Secondly, it is impractical to blend massive flow rate of O_2 comparable to the rate of flue gas emission.

Removing membrane permeate side O_2 seems to be more promising than O_2 enrichment on feed side. According to the uphill CO_2-O_2 co-permeation through LSCF6428-carbonate membranes [28], permeate side O_2 content at steady state due to transport through the membrane ranged from 0.2 to 0.3%. If permeate side O_2 content p"O_2 can be decreased to nearly zero, the driving force term in equation 2.41 will be vastly increased for a logarithm dependency between CO_2 flux and driving force. The CO_2 flux can theoretically approach infinity. However, for a linear dependency (i.e. equation 2.42-2.46), there will be a maximum limit on the driving force term, therefore the flux cannot approach infinity. Anyhow, the O_2 removal on membrane permeate side also separate O_2 out of CO_2 in permeate stream, allowing two processes being completed simultaneously. Figure 2.21 (a) and (b) visualise the logarithm and linear CO_2 flux-driving force relationships proposed by Zhang et al.

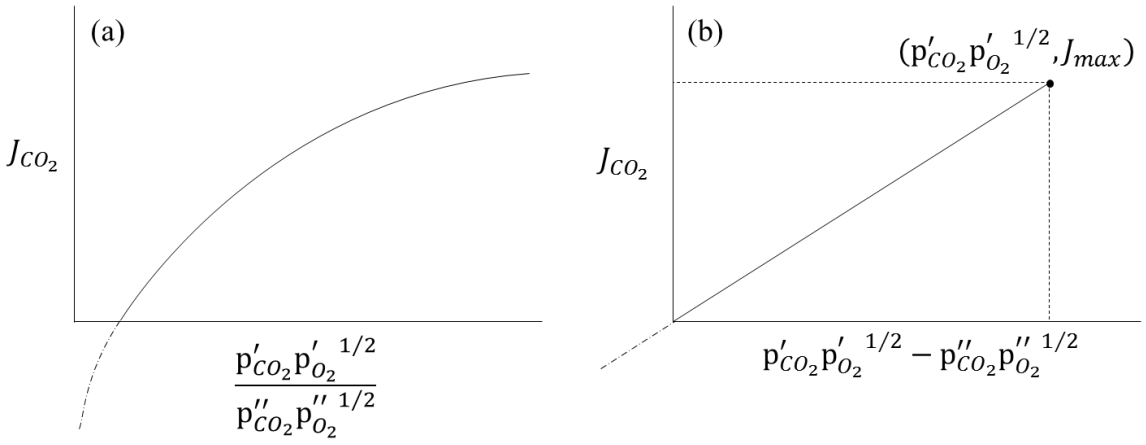

Figure 2.21: Graphic illustration of the CO_2 driving force (J_{CO_2}) and driving forces dependency. (a) Bulk diffusion limiting. CO_2 driving force has logarithmic relationship with driving force (product of partial pressures). Maximum flux: infinity; zero flux: product of partial pressures goes to 1; minimum flux: negative infinity. (b) Global interfacial reaction limiting. CO_2 driving force has linear relationship with driving force. Maximum flux: at the black dot when $p''CO_2\ p''O_2^{1/2}=0$; zero flux: difference of partial pressures goes to 0; minimum flux: when driving force is $-p''CO_2\ p''O_2^{1/2}$ and $p'CO_2p'O_2^{1/2}=0$.

One approach of doing this is removing permeate side O_2 by chemical reaction with reducing gas continuously. H_2 is the primary choice as they react with O_2 at high temperature and produce water vapour. The product can be separated out of CO_2 easily by condensation. Using CO as reducing gas is also feasible as it can be oxidised directly to CO_2. However, this may interfere the measurement of actual CO_2 permeation flux as well as induce carbon deposition on the LSCF based solid support. For safety and practical consideration, only small content of H_2 (0.5 to 1%) is required in sweep gas in order to carry out O_2 removal, as O_2 content on membrane permeate side is expected to be low for uphill CO_2-O_2 co-permeation. Since this reaction is both spontaneous and exothermic at 600°C, no energy input to the system is needed. Huang et al. tested this approach using a silver-carbonate membrane for downhill CO_2-O_2 co-permeation feeding a model flue gas [109]. They explored the effect to CO_2 and O_2 fluxes with changing concentration of H_2 in sweep gas. The experimental results are summarised in Table 2.7. They concluded that the addition of H_2 in sweep gas increases the chemical potential gradient of O_2 across the membrane, thus enhancing downhill permeation fluxes of CO_2 as well as O_2 because of the coupled CO_2-O_2 transport. However, they did not specify how much O_2 was removed by H_2, nor did they mention an explicit link between CO_2 flux and O_2 chemical potential gradient.

Although incorporating H_2 in sweep gas enabled continuous removal of O_2 and performed well on silver-carbonate membranes, the interaction between LSCF based materials and hydrogen in conjunction with the presence of water vapour could possibly shorten the lifetime of LSCF, due to the increase of oxygen non-stoichiometry or even loss of crystalline structure mentioned in Chapter 2.2.2. Although this has not been tested on LSCF6428-carbonate system, to avoid the complexity another

approach for O_2 removal is considered in this research, which is removing membrane permeate side O_2 by oxygen carrier material (OCM). OCM in reduced state consists of porous metal particles incorporated into support materials. Once O_2 molecules diffuse into the OCM, metal particles will react with oxygen, with themselves being oxidised. Any interaction between the membrane and the OCM is unlikely as long as they are not physically in contact. The drawback is when the OCM reaches maximum oxygen capacity, metal particles are converted to metal oxides and they must be reduced back. As a result, this process is cyclic and cannot operates continuously. Chapter 6 will focus on studying CO_2 flux-driving force correlations for uphill permeation, and the application of OCM for generating larger chemical potential gradient of O_2 across the membrane.

Table 2.7: The effect of H_2 concentration in the sweep gas on CO_2 and O_2 permeation fluxes. Feed gas: 15% CO_2, 10% O_2 and 75% N_2 [109].

Feed gas	**Sweep gas**	**CO_2 flux** **ml min^{-1} cm^{-2}**	**O_2 flux** **ml min^{-1} cm^{-2}**
15% CO_2, 10% O_2 and 75% N_2	100% Ar	0.55	0.32
	4.35% H_2 in Ar	0.74	0.55
	9.41% H_2 in Ar	1.13	0.74

3. Methodology

In this research, the experimental methods consist of four steps: membrane fabrication (Chapter 3.1), membrane sealing (Chapter 3.3), main CO_2 separation experiments (Chapter 3.4) and effluent gas analysis (Chapter 3.5). Membrane characterisation was also performed separately once they were fabricated. (Chapter 3.2). This chapter gives detailed explanation on how the experimental and analytical works were carried out.

3.1. Membrane fabrication

3.1.1. Sintering solid substrates

Powder pressing and sintering method was used coherently followed by hot infiltration of mixed ternary carbonate powder. This effective fabrication method for making disk shaped membrane supports was previously established [110]. The first step was to fabricate robust porous alumina, YSZ and LSCF6428 solid substrates that are suitable for high temperature CO_2 separation experiments. For an alumina membrane substrate, commercial alpha-phase aluminium oxide powder (99.9% purity, metals basis, 20-50 microns particle sizes) was purchased from *Alpha Aesar*. 1 or 2 drops of 10 mol% polyvinyl alcohol (PVA) was added into 1g powder and well mixed with pestle and mortar. PVA has a function of binding particles, it helps achieve better packing of powders after pressing and keep the pellet in good shape during pressing and sintering. On the other hand, powder grinding may help achieve more uniform particle size distribution. The powder was subsequently transferred to an automatic *ATLAS* T25 hydraulic press and pressed using 3 MPa pressure for a duration of 30s, forming pellet shape with loosely packed particles. A batch of 7 to 8 pellets were placed on a ceramic crucible followed by sintering in the air at 1400°C to 1500°C for 24 hours. Since the densification temperature of alumina pellets is relatively high, 1400°C to 1500°C sintering temperature can produce alumina pellets with 30% to 40% porosity. For ceramic membranes, this porosity would have the best compromise between mechanical strength and pore interconnectivity. A high temperature box furnace was used for sintering. The ramping rate of heating and cooling were both 1°C/min, starting and finishing at room temperature. Low ramping rate can avoid rapid thermal expansion of particle grain boundaries, which leads to cracks on pellet surface or interior. Due to grain growth, the pellet after sintering was tightly packed with much higher mechanical strength, the void fraction (porosity) was reduced but the pellet remained porous.

Sintering process for YSZ substrate was similar to alumina, but the sintering temperature and the temperature dwelling time was different. 8mol% Yttria stabilised Zirconia powder (*PI-KEM Ltd*) was used. Generally, YSZ pellets were sintered between 1150°C to 1200°C, with 1°C/min ramping rate and 4 hours dwell time. YSZ is ionic conductive, its ionic diffusion coefficient is larger than inert alumina. This property contributes to higher grain growth rate and void shrinking rate. Higher sintering temperature would close most interconnected pores whilst lower sintering temperature would not offer satisfactory pellet hardness and mechanical strength. However, the 1150-1200°C sintering temperature

window, which gives a membrane porosity of 30-40%, cannot offer satisfactory membrane mechanical strength. Membranes with micro-cracking formation upon sintering was prone to bulk cracking under high operating temperature. In order to strengthen YSZ pellet without sacrificing porosity, 20wt% corn starch as pore former can be added to YSZ powder. Ball mixing of the YSZ and corn starch powders was carried out using *FLUXANA* mixer for 0.5-1 hour. Thereafter, homogeneous mixture of YSZ and corn starch was ready for pressing. The sintering program was adjusted to dwell 2 hours at 200°C allowing corn starch to burn off and create pores. Furthermore, the addition of corn starch allowed higher sintering temperature at 1400 to 1450°C while maintaining membrane porosity at 30-40%.

The grain growth and void shrinking rate for LSCF6428 is comparable to YSZ. The use of pore former would also be necessary. Typically, 20-25wt% corn starch in conjunction with 1200-1250°C sintering temperature were employed giving robust membrane support pellets with 30-40% porosity. Commercial powders of LSCF6428 (*Praxair*) and practical grade corn starch supplied by *Sigma-Aldrich* were used. The LSCF6428 powder had an average particle size of 2.73μm measured by the Malvern Zetasizer Nano instrument. Due to the high amount of LSCF6428 pellets required, 15g raw LSCF powder was mixed with 4 to 5 drops of PVA by using automatic *Retsch* Mortar Grinder, followed by 1-2 hours ball mixing with 5g corn starch. The mixed powder was produced batchwise for pressing and sintering.

3.1.2. Mixing ternary carbonates

The composition of molten ternary carbonate phase was 32.1wt% Li_2CO_3 (99.0% purity powder), 33.4wt% Na_2CO_3 (99.5% purity granular), and 34.5wt% K_2CO_3 (99.0% purity granular). Individual chemicals were purchased from *Alpha Aesar*. This specific formulation of ternary carbonate mixture was chosen as the mixture has lower melting point (around 400°C) comparing with individual carbonate (723°C for Li_2CO_3, 851°C for Na_2CO_3 891°C for K_2CO_3, data extracted on chemical container label and safety data sheet by *Alpha Aesar*). Any binary mixture has melting point within a range of 700 to 800°C, which cannot offer a broad operating temperature window for molten carbonate membrane CO_2 separation purposes. Na_2CO_3 and K_2CO_3 were grinded to fine powder in turn using pestle and mortar firstly. Around 4g of each powder was placed in three individual ceramic cups and dehydrated at 300°C for 24 hours. Dehumidified powders of 3.21g Li_2CO_3, 3.34g Na_2CO_3, and 3.45g K_2CO_3 were measured and mixed using *FLUXANA* mixer for 0.5-1 hour. The resultant carbonate mixture consisted of similar weight of Li_2CO_3, Na_2CO_3 and K_2CO_3 and 0.433:0.312:0.255 in terms of molar ratio, which was close to the Eutectic mixture commonly used in the literature.

3.1.3. Membrane infiltration

Dual phase ceramic membranes were fabricated by direct infiltration of tertiary carbonates into porous network of solid substrates. Trial infiltration tests were carried out for alumina, YSZ and LSCF6428 pellets with similar porosity. It turned out alumina pellets absorb the least amount of molten salt after infiltration. For alumina substrates, excess amount of ternary carbonates powder was spread

homogeneously on the upper surface of the pellet, followed by heating up at 1°C/min to 600°C within a tubular furnace and maintaining the temperature for 2 hours. During this period molten carbonates mixture was fully melted and sucked into the entire porous network by capillary force. Excess carbonate passed through the interconnected pores and impregnated into porous sacrificial alumina crucible underneath holding the pellet. After the first infiltration, generally the pellet was flipped and loaded a smaller weight of carbonates for the second infiltration to ensure majority of the pores were filled. When the dual phase pellet was cooled down, excess carbonates may accumulate on membrane surface and coat an extra carbonate layer. This carbonate layer can be polished off using 1200 grits sandpaper. YSZ and LSCF6428 tended to absorb molten carbonate easily. The amount of carbonate powder needed can be estimated from the geometrical measurements of the pellets (equation 3.2). The molten carbonate power was pelletised to a small disk and put on top of the membrane support (Figure 3.1), followed by the same heating/cooling procedure as the alumina pellets. The weight change of the support pellet would be the weight of carbonate absorbed. Empirically, vast majority of the interconnected pore will be filled if the absorbed carbonate weight is above 80% of the maximum carbonate loading.

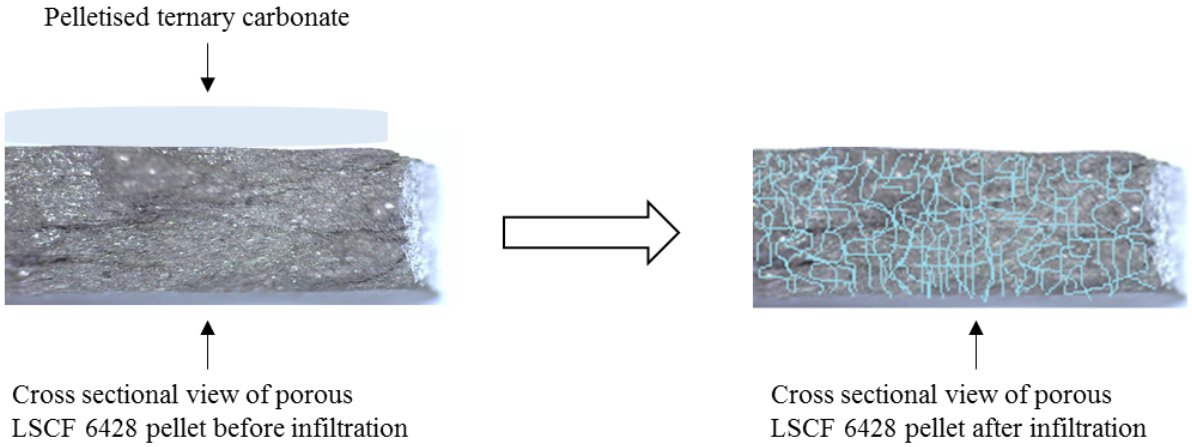

Figure 3.1: Illustration of the hot infiltration process of LSCF6428 membrane support pellet. The pelletised carbonate melted at 600°C and was sucked thoroughly into the random packed pore network of the support (molten carbonate residing within the pores is represented by the blue lines).

3.2. Membrane characterisation methods

3.2.1. Scanning electron microscope (SEM) and Energy-dispersive X-ray spectroscopy (EDS)

Scanning electron microscopy (SEM) enables imaging of solid phase material surface using an electron beam. The incident beam electrons interact with the specimen atoms through a variety of physical processes collectively referred to as ‘scattering events’ [111]. These beam electron–sample interactions generate the following products. The detector can transform these signals produced from the sample and capture enlarged images.

- Secondary electrons (SE): inelastic collision between primary incident electron and the sample, incident electrons knock out electrons out of the sample atoms. Image obtained from SE reflects the topography of the sample's surface [112].
- Backscattered electrons (BSE): elastic collision between primary incident electron and the sample, incident electrons are deflected upon striking the sample atoms. Larger atoms tend to scatter more incident electrons and produce stronger BSE signal, therefore image obtained from BSE reflects the compositional distribution on the sample surface [112].
- Characteristic X-rays: following knocking out inner shell electrons from sample atoms by incident beam, outer shell electrons may move to inner shell and release x-ray with an energy spectrum that conveys the composition information about the sample. Energy dispersive X-ray detector can be mounted to the SEM for conducting elemental analysis [112].

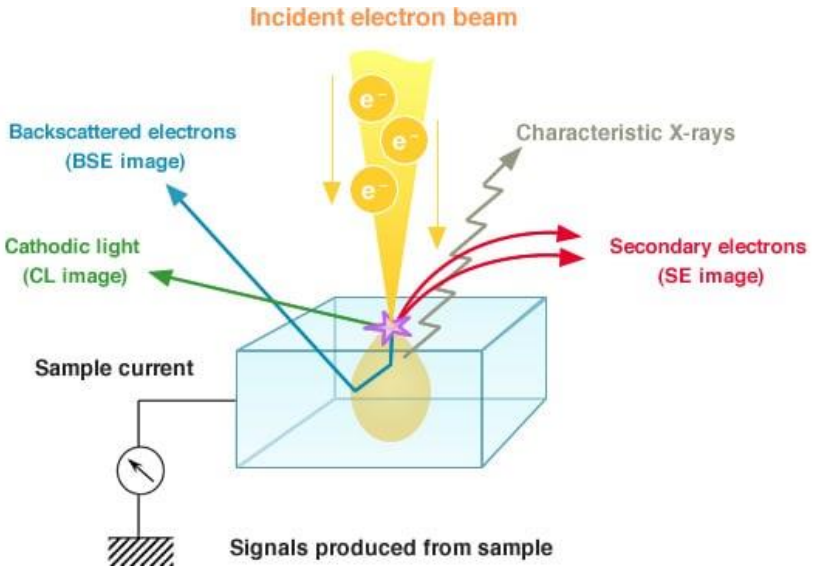

Figure 3.2: Schematic diagram showing all possible 'scattering events' upon incident elections-sample atoms interaction [112].

Surface and cross-sectional microstructures of the membrane support material can be used to assess the reliability and reproducibility of the fabrication methods. A *Hitachi* TM3030 benchtop SEM was used for surface characterisation of alumina, YSZ and LSCF6428 dual phase membranes under vacuum. The machine offers high magnification from 15 up to 60000 and employs built-in image processing to enhance image quality and resolution. Energy dispersive X-ray detector has also been installed, allowing EDS elemental analysis on membrane surface as well as the cross sections. Besides, it will reveal two-dimensional carbonate distribution within the porous network after infiltration. For this purpose, we chose a *Tescan Vega 3LMU* scanning electron microscope fitted with a *Bruker XFlash® 6 | 30* detector for EDS analysis, run by the Electron Microscopy Research Services at Newcastle University. The images offered excellent resolution, which may help determine how the carbonates reside within the pores and probe the gas tightness of an infiltrated pellet.

Figure 3.3 shows an example of SEM image for the top surface of porous alumina support disk. Image was magnified 6000 times on the scale of 5 μm. The support material was not infiltrated with carbonate thus dense and porous regions can be observed. The light grey particles represented solid phase alumina and the black background represented the pores. Whereas in the darker grey area, grain boundaries can be observed, indicating some degree of densification. The pore sizes on this image varied from a few microns to submicron scale. This example demonstrated that the SEM image was adequate such that the surface morphology and microstructure of the dual phase membrane disks can be identified.

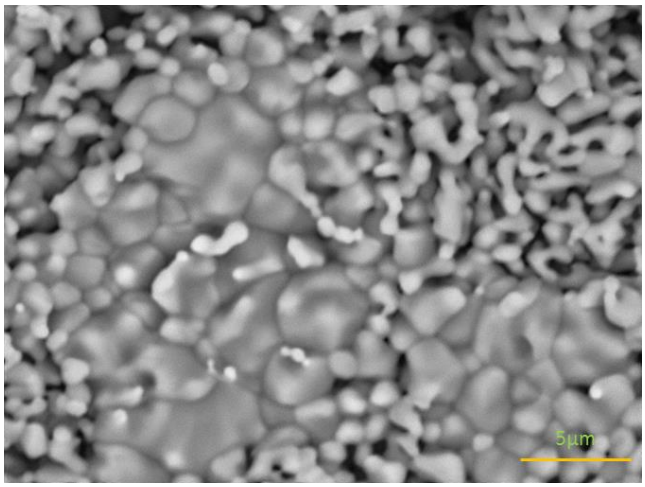

Figure 3.3: SEM image for the top surface of a fresh porous alumina support disk. Image was taken using the *Hitachi* TM3030 benchtop SEM hosted by NEXUS at Newcastle University.

3.2.2. X-ray diffraction (XRD)

The ceramic materials and carbonates being employed for dual phase membranes fabrication mostly have well defined crystalline phases. The unit cell crystalline lattice for YSZ and LSCF (see Figure 2.8 and 2.9) that consist of various lattice planes have been introduced in Chapter 2. During the CO_2 permeation experiments, the crystalline structure of membrane materials may undergo some subtle change. For example, new phases may form within the molten salt; oxygen nonstoichiometry of LSCF based ceramic support may change depending on the experimental conditions. These changes cannot be easily identified using SEM and EDS. X-ray diffraction (XRD) is a robust and non-destructive technique to identify crystalline phases and characterise crystalline materials. This analytical method can be used to evaluate how the crystalline structure of membrane materials changed within the pellets before and after a CO_2 permeation experiment. It is also possible to carry out phase quantification of those crystalline compounds within the dual phase membranes.

XRD is an application of the Bragg's law; a simplified explanation is that it describes the principle of X-ray diffraction in terms of a reflection of X-rays by sets of lattice planes. A single-phase polycrystalline material normally contains various sets of differently orientated planes with respect to the incident X-ray beam, depending on its crystal structure. Ideally, parallel planes within a crystalline phase are equally spaced, separated by the distance d. The incident X-ray was not only reflected on the

first plane of crystalline structure, it also penetrated deep inside the material where additional reflections occur at consecutive parallel planes. From Figure 3.4, it follows that the second wave travels a longer distance PN+NQ than the first after being reflected to the surface. The superposition of the reflected rays produces a sharp intensity maxima at angle 2θ, also known as 'constructive interference', occurs only if PN+NQ is a multiple of the X-ray wavelength λ, as shown in equation 3.1 [113]. When a crystalline specimen is exposed to X-ray beam of known wavelength covering a range of incident angles, XRD pattern unique to each crystalline phase is generated. Each set of parallel planes produces a peak at a specific diffraction angle, which corresponds to the superposition of diffracted X-ray reaching the detector. The XRD pattern is used to identify and characterise each crystalline phase present.

$$n\lambda = 2d \sin\theta \qquad (3.1)$$

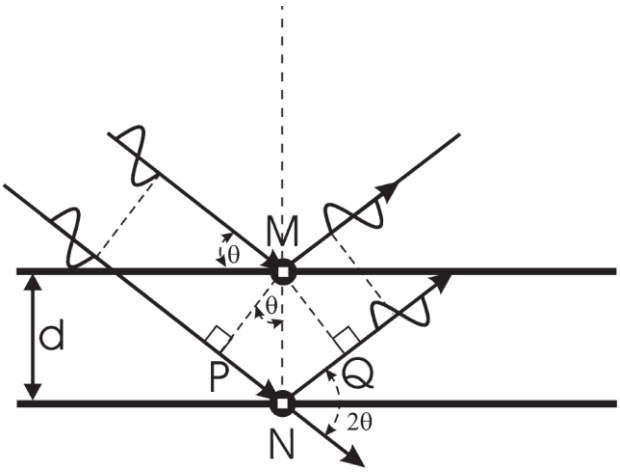

Figure 3.4: Illustration of the geometry used for the simplified derivation of Bragg's law. M and N are atoms on their associated planes [113]. Reproduced with permission of Royal Society of Chemistry.

Some subtle changes of the crystalline structure of membrane materials can be probed from the features of the XRD pattern. This includes peak intensity, peak position shift and peak width. The maximum peak intensity is often governed by the quantity of a specific crystalline substance in the sample. Higher amount of substance leads to more parallel planes that generate more intense X-ray diffraction. Thermal and chemical effects to the membrane materials during permeation experiments may cause slips on their grain boundaries by some residual strain. Ultimately, lattices are left in an elastically bent or twisted condition such that plane spacing has been modified. A shift on peak position often arises when all crystal grains receive a 'uniform strain', which means plane spacing changes uniformly. However, for 'non-uniform' strain, spacing between adjacent planes varies slightly, making the diffraction peak broad. In addition, a change on crystallite size may also cause peak broadening [114].

The instrument used here is a PANalytical X'Pert Pro MPD, powered by a Philips PW3040/60 X-ray generator and fitted with an X'Celerator detector. Diffraction data is acquired by exposing powder samples to Cu-Kα X-ray radiation with characteristic wavelength of 0.15 nm. X-rays were generated from a Cu anode supplied with 40 kV and a current of 40 mA. Phase identification was carried out by

means of the X'Pert accompanying software program PANalytical High Score Plus in conjunction with the ICDD Powder Diffraction File 2 Database (1999), ICDD Powder Diffraction File 4 - Minerals (2012), the American Mineralogist Crystal Structure Database (March 2010) and the Crystallography Open Database (February 2012; www.crystallography.net). Phase quantification was available to be performed using Rietveld refinement method.

3.2.3. Geometrical measurements

It is essential to characterise the membrane geometrical properties in order to understand how these membrane properties affect the CO_2 separation performance. Porosity, membrane thickness and carbonate loading are the most important parameters. Here, a simple method for estimating solid support porosity and maximum carbonate loading has been established based on the geometrical measurements of the fresh porous membrane pellets.

Once a fresh pellet was sintered (Figure 3.5), the pellet weight (m_{pellet}), diameter (d) and thickness (t) were measured. Apparent volume of the pellet V can be estimated based upon its geometry, whilst real volume of YSZ (V_{YSZ}, void volume not included) can be estimated using weight of pellet (m_{pellet}) divided by YSZ density (ρ_{YSZ}). Porosity of this pellet can be calculated as:

$$\varepsilon = \frac{V_{pore}}{V} = 1 - \frac{V_{YSZ}}{V} = 1 - \frac{\frac{m_{pellet}}{\rho_{YSZ}}}{0.25\pi d^2 t} \qquad (3.2)$$

Assuming all pores are interconnected, maximum weight of carbonates that can be infiltrated into solid substrate can be estimated as:

$$m_{max} = (V - V_{YSZ}) \times \rho_{molten} \qquad (3.3)$$

In equation (3.3) ρ_{molten} denotes the density of molten tertiary carbonates. A generalised density at 750°C (1.96 g/cm^3 [53]) has been used for the calculation.

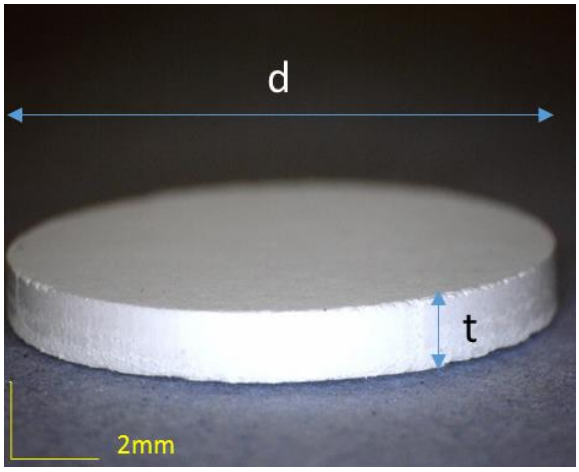

Figure 3.5: Geometry of a fresh disk shaped YSZ pellet under digital microscope. In this picture, d represents pellet diameter and t represents pellet thickness.

3.2.4. Mercury intrusion porosimetry (MIP)

The best analytical technique to quantify the total pore volume, total pore surface area and pore size distribution of the membrane support is presumably mercury intrusion porosimetry. Mercury is a non-wetting liquid with contact angles greater than 90° for vast majority of solid materials. It will only intrude capillary pores by applying external pressure. The intruding pressure rises by several increments during the analysis until the point that the mercury intrusion reaches equilibrium with the applied pressure and no longer fills the pores (Figure 3.6). Washburn equation (equation 3.4) describes the relationship between intruding pressure (p) and pore diameter (d_p), where γ is the surface tension of mercury and θ_C is the contact angle of the mercury on solid material surface. The pore size distribution is determined from the volume intruded at each pressure increment [115].

$$d_p = \frac{-4\gamma \cos \theta_c}{p} \qquad (3.4)$$

MIP is suitable for pore size measurement of the pressed and sintered membrane supports as it covers a wide range of pore diameter from 3 nm to 350 µm. Moreover, the mercury intrusion starts from larger pores, indicating the total intruded mercury volume can be a good approximation of the total opened pore volume of the membrane supports. The porosity of the membrane support can then be estimated using the same principle as equation 3.2. The MIP results are by no means accurate as the mercury cannot access all the pores within the membrane support, particularly closed pores. In some occasions large internal pores are accessible by very narrow throats. The technique misrepresents the size of these pores as having the diameter of their throats [115]. Nevertheless, the MIP results can be compared with the geometrical estimation to see whether they reach agreement.

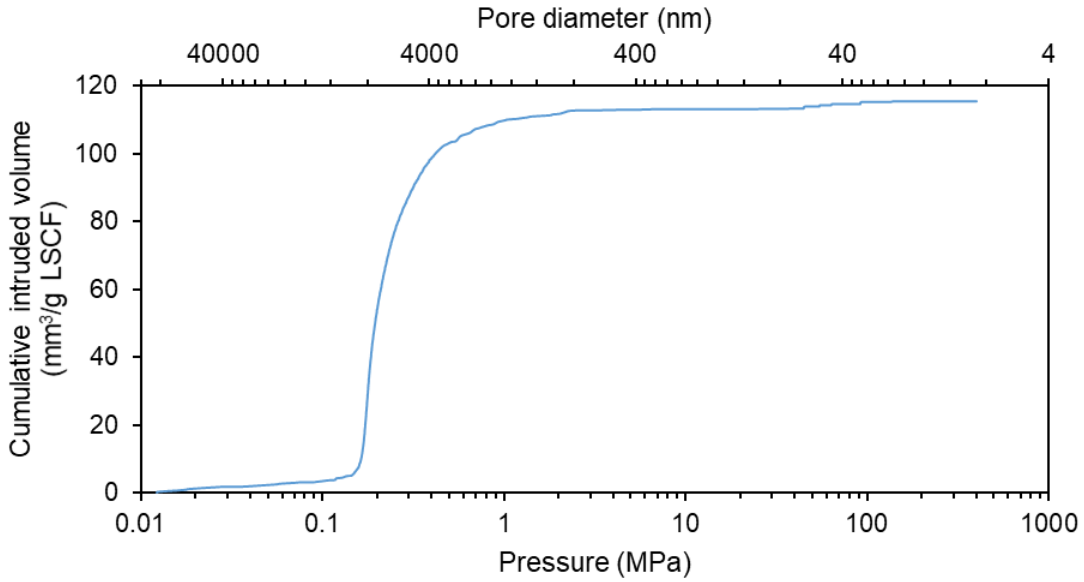

Figure 3.6: Curve of cumulative intruded volume versus incremental applied pressure and pore diameter being accessed. This plot represents a typical porous LSCF6428 support used in this project.

3.3. Membrane sealing techniques

Open-ended alumina tube with 230mm length, 12mm outside diameter, and 8mm inside diameter was used to hold the membrane pellet during CO_2 permeation experiment (Figure 3.7). The alumina tube can be mounted to membrane reactor (Figure 3.8). Any area exposed to feeding gas apart from effective permeation area (the circle with 8mm diameter, enclosed by inner diameter of alumina tube) must be sealed by gas tight sealant. Ceramic or silver/gold based sealant was chosen according to their effectiveness on particular membrane support material.

3.3.1. Silver/Gold paste sealants

Single layer silver sealing was adopted for LSCF6428-carbonate membranes. Silver paste purchased from *Fuelcellmaterials* was spread homogeneously onto the ring-shaped cross-sectional area of an open-ended alumina supporting tube (Figure 3.7a). Membrane was gently placed on top of sealant layer. Silver paste contains 70% silver and 30% organic solvent. Before the experiment starts, the sealant was firstly air-dried for one hour until the sealant hold the membrane firmly, followed by curing the sealing at 110°C overnight (12-24 hours). At this point, most solvent and moisture had evaporated, leaving a solid silver layer that attached membrane onto the alumina tube. Occasionally some small sealing defects can be observed after the curing procedure. Additional 'touch up' can be done by applying small amount of silver paste to fill any defect. The alumina tube with sealing membrane was installed into the membrane reactor for CO_2 permeation experiment.

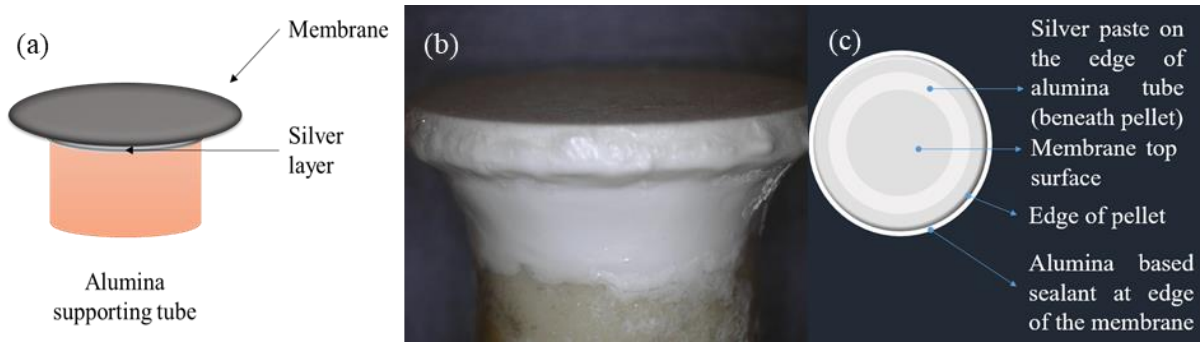

Figure 3.7: (a) A sketch of silver sealing for LSCF6428-carbonate membrane. (b) Appearance of silver-ceramic double-layer sealing for YSZ-carbonate membrane. (c) Top view sketch of the sealing in (b).

3.3.2. Metal-ceramic double sealing

The adhesion between silver and YSZ or alumina is not as good as LSCF6428. Silver sealed alumina-carbonate membrane very likely suffered sealant failure and cross-chamber leak under high operating temperature. On top of silver or gold paste, a layer of ceramic sealant can be applied to cover all area around the edge of pellet and entirely fill the gap between pellet edge and alumina tube (Figure 3.7b). Ceramic paste was well mixed with silicate based thinner (*Aremco*) in approximately 5:1 ratio by volume prior to the application. This layer of sealing was normally air dried 1-2 days followed by

coating silicate thinner as a protective layer. Sealing was further air dried 1-2 days for moisture removal before it was ready for experiment.

3.4. Experimental methods

3.4.1. High temperature membrane reactor for CO_2 separation

CO_2 separation experiments were performed using a high temperature membrane reactor (Figure 3.8). Alumina support tube (12mm OD × 8mm ID × 235mm L) with sealed membrane was mounted into a hole with an O-ring attaching on the centre bottom of the reactor. Reactor space is divided by the membrane into feed side chamber (enclosed by inner surface of the alumina supporting tube) and permeate side chamber (enclosed by quartz tube and outer surface of the alumina supporting tube). Chamber outlets locate on the bottom of each chamber. Two thin alumina tubes deliver inlet gas streams into corresponding chambers. Another thin alumina tube with closed top end could also be installed into the permeate side chamber such that a wire probe of K type thermocouple can be inserted, allowing real time temperature monitoring close to the membrane during CO_2 permeation experiments. The quartz tube (closed top end, 35mm OD × 32mm ID × 230mm L) separates the permeate side chamber with the surrounding atmosphere. Quartz tube is fitted with an O-ring and a stainless-steel screw-on gasket. By screwing the gasket that holds the O-ring underneath, gas tight sealing of the permeate side chamber can be achieved. The sealing of feed side chamber relies on the O-ring on the centre bottom of the reactor. In addition, vacuum grease manufactured by *Dow Corning* was spread evenly on the bottom of alumina supporting tube before mounting on to the reactor. This provides smoother insertion as well as an extra layer of heat/chemical resistance sealing between the two chambers.

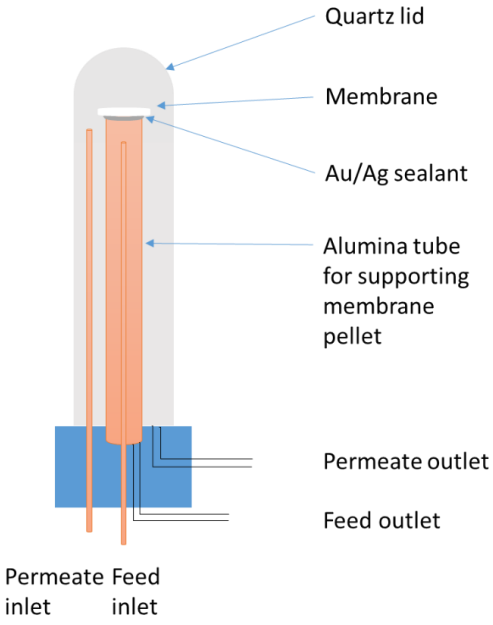

Figure 3.8: Illustration of the detailed design in membrane reactor.

A tubular furnace with CAL 9400 temperature controller brought the reactor to desired operating temperature. The temperature controller can be programmed to set the ramping and cooling rate of the furnace at 1°C per minute in general, as gradual ramping rate can minimise the possibility of membrane cracking due to the thermal expansion. The furnace is placed carefully around the quartz tube to ensure the membrane can be positioned into the isothermal zone of the furnace. Finally, the top end of furnace is blocked by quartz wool to avoid the convective heat loss to the surroundings.

3.4.2. Experimental rig design and operation

The configuration of the high temperature CO_2 separation rig was built up as shown in Figure 3.9. The rig consists of three parts: the gas flow system on the left, the membrane reactor enclosed by *Vecstar* furnace and the on-line gas analysis on the right. The entire system resided within ventilating fume hood. Figure 3.9 illustrate the simplest configuration for downhill CO_2 permeation experiments. They were carried out by feeding 20ml/min 50% N_2, 50% CO_2 mixture to the molten carbonate dual phase membrane at ambient pressure and 600-900°C temperature. At the same time, 20ml/min pure Argon flowed on the membrane permeate side as sweep gas.

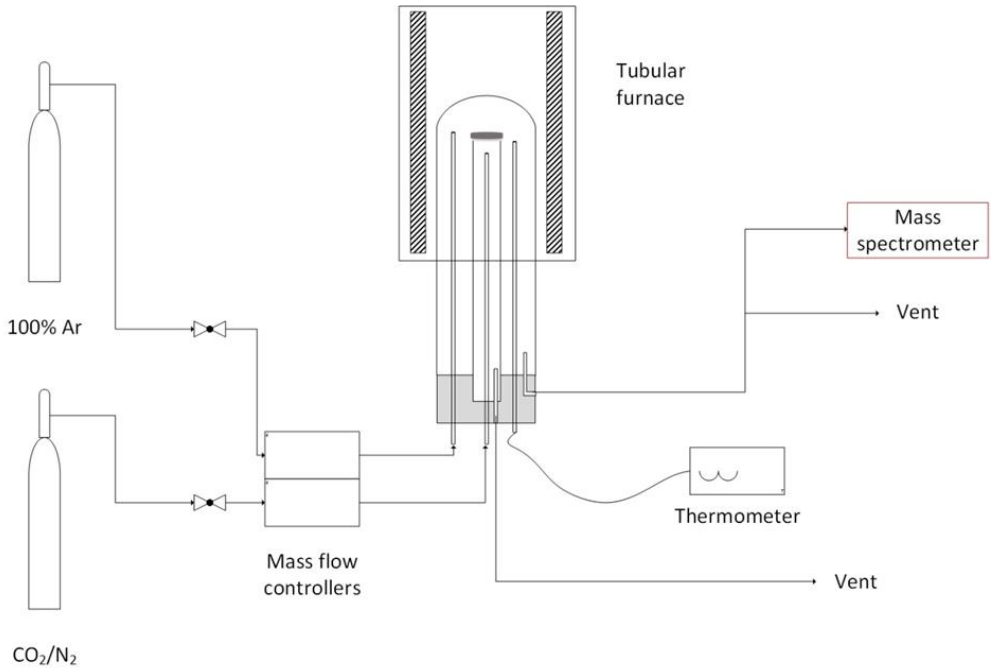

Figure 3.9: Flow diagram of high temperature downhill CO_2/N_2 separation system. This diagram incorporated all elements of the CO_2 separation rig: gas cylinders supplying relevant gas composition to membrane feed and permeate chambers, mass flow controllers regulating the flow rate into the membrane reactor, the membrane reactor located within the furnace and the mass spectrometer for outlet gas analysis.

An on-off valve was installed between the gas cylinder outlet and the mass flow controller on each line. The gas pressure out of the cylinders was set to 4×10^5 Pa. Mass flow controllers not only regulate the gas pressure to 10^5 Pa, but also the desired gas flow rates into the reactor. The flow rates of both feed and permeate inlets are adjustable using computer-controlled software. The values of flow rate were

calibrated by *Agilent* digital flow meter. For long CO_2 permeation experiments lasting over several days, more reliable flow rates with error bars needed to be obtained considering the time variation of the readings. In this case, the reading from the flow meter can be logged on to a computer using *PuTTY* for 1-2 hours. The average reading can be calculated, and the variation can be used to determine the error bar of the mean flow rate.

For downhill CO_2 permeation experiments, the feed outlet gas composition was not analysed and was diverted to the vent in the fume hood. The permeate side outlet that required gas composition analysis was diverted to gas analyser such as mass spectrometer (MS), gas chromatography (GC) or infrared CO_2 analyser (IR). The methods of gas analysis will be introduced in Chapter 3.5. For CO_2-O_2 co-permeation and uphill CO_2 permeation experiments, both the gas flow and the gas analysis methods were updated in accordance with the experimental standard operating procedure. The details will be given in associate with the experimental results in the following chapters.

3.5. Downstream gas analysis

3.5.1. Mass spectrometer (MS) measurements

Hiden QIC 20 and *Hiden* QGA models were both used for downstream gas analysis (i.e. membrane feed side and permeate outlets) during the membrane CO_2 permeation experiments. They possess the same working principle but a slightly different configuration. Nevertheless, they can generate comparable analytical results because their core unit are the same, which is The *Hiden* RGA Mass Spectrometer (Figure 3.10). It consists of an ion source, a quadrupole mass filter and detector. This analyser uptake around 15ml/min gas flow through a capillary sampling line, 99% of them bypass the detection chamber and 1% is used for analysis. The working principle of The *Hiden* RGA Mass Spectrometer is that all gas constituents within the inlet sampling gas collide with the electron beam generated by the filament located in the ion source. This ionises the gas molecules into positively charged ions. Next, a focus plate with negative electrical potential extracts all positively charged ions towards the mass filter and repels the electrons. The mass filter has radio frequency (RF) and direct current (DC) voltages applied to it thus enabling mass separation by the mass to charge ratio (m/z) of various gas constituents. Each m/z number has a specific RF and DC voltage on the mass filter allowing it to pass through to the detector [116]. The ions in turn hit Faraday Bucket and Secondary Electron Multiplier (SEM) detector walls and create ion current intensity. Higher concentration leads to higher rate of hitting and higher intensity. Faraday Bucket is the simplest detector that is essentially a passive conductor in the shape of a cup, which collects the positively charged ions passing through the mass filter. The ions generate a current when they hit the Faraday Bucket equivalent to 7.5×10^{-7} Amps/Pa of Nitrogen. The Faraday detector cannot be sensitive enough for low gas partial pressure measurements. The other detector, namely Secondary Electron Multiplier (SEM) detector is ideal for low gas partial

pressure measurement while offering higher sensitivity in terms of compositional analysis. The Electron Multiplier has a surface that is designed to generate secondary electrons once hit by an ion. A voltage is applied to the SEM allowing cascade electrons generation. By this way, the ion current can be magnified by a factor of 1000 thus facilitating low ion current detection [116].

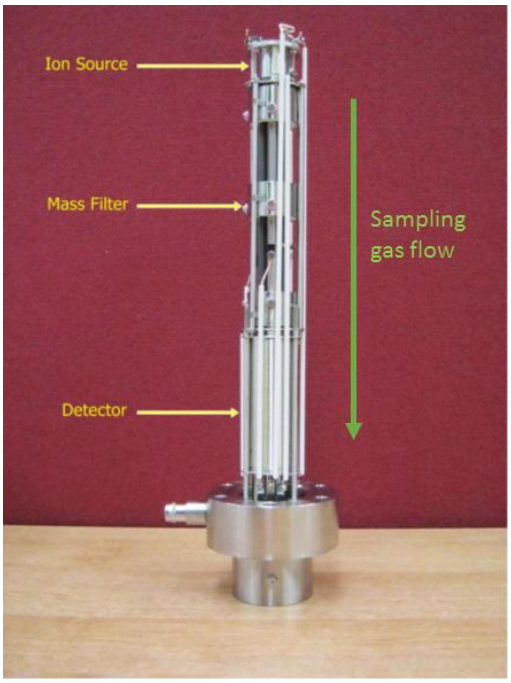

Figure 3.10: A picture of the MS Gauge Head consists of ion source, mass filter and detectors [116].

In this project, the major gas species of interest are N_2, CO_2, O_2 as well as Argon (balance gas). Mass spectrometer can detect them through various mass to charge ratio, because each element may have various isotopic masses in nature, and each molecule has a unique cracking pattern when it is ionised. Table 3.1 lists the isotopic masses and the natural abundances for each element of interest.

Table 3.1: The list of the isotopic masses and the natural abundances for carbon, nitrogen, oxygen and argon atoms. Data retrieved from [117].

Name	symbol	Mass (atomic mass unit)	% abundance
Carbon	^{12}C	12	98.93
	^{13}C	13	1.07
Nitrogen	^{14}N	14	99.63
	^{15}N	15	0.37
Oxygen	^{16}O	16	99.76
	^{17}O	17	0.04
	^{18}O	18	0.20
Argon	^{36}Ar	36	0.34
	^{38}Ar	38	0.06
	^{40}Ar	40	99.6

Table 3.2 lists all the fragmentations and m/z ratio for each gas specie of interest. In general, for each gas species the m/z number associated with the strongest intensity are selected for measurements. For instance, CO_2-44, N_2-28, O_2-32 and Ar-40 may be selected for on-line gas analysis during a permeation experiment. In case that two gas species have the same m/z number, other fragmentation must be chosen in order to avoid the clash on m/z number.

Table 3.2: Fragmentations of CO_2, N_2, O_2 and Ar molecules with top three relative sensitivities on their mass spectrum. Data retrieved from tech data on *Hiden Analytical* website.

Molecule	m/z	Relative intensity %
CO_2	44	100
	28	11.4
	16	8.5
N_2	28	100
	14 (double ionisation)	7.2
	29	0.8
O_2	32	100
	16 (double ionisation)	11.4
	34	0.4
Argon	40	100
	20 (double ionisation)	10.7
	36	0.3

The raw data from MS is the intensity signal corresponding to gas partial pressure. Due to the fast response of the detectors, a full scan of a range of gas constituents typically took only 30 to 60s, indicating data points can be produced every half to one minute. This is beneficial for a monitoring a rapid change in gas partial pressure, such as a fast reaction. The raw intensity was calibrated by feeding calibration gas, which contained a known composition of 1% N_2, 1% CO_2, and 20% O_2 in Ar. Gas calibration was typically run for 4-5 hours until the intensities for all gas species stabilised. Here, the calibration factor method (i.e. single point calibration) was employed [116, 118]. Average values of the last 30 intensity readings for N_2, CO_2, O_2 and Ar were assigned as their raw intensities I_{N_2}, I_{CO_2}, I_{O_2} and I_{Ar} corresponding to their concentration in calibration gas. The intensity ratio of N_2, CO_2 and O_2 to balance gas (Ar) was calculated respectively. Using these measured intensity ratios to compare with the known concentration ratios between individual gas specie and Ar, the calibration factor of specie 'i', also known as the relative sensitivity (RS), can be calculated as shown in equation 3.5:

$$CF_i = \frac{I_i/I_{Ar}}{y_i/y_{Ar}} \qquad (3.5)$$

In this equation, y_i represents the mole fraction of gas specie 'i' (O_2, CO_2 or N_2) in calibration gas and y_{Ar} represents and argon mole fraction in calibration gas. The calibration factor (CF) essentially corrects the raw intensity of species 'i' with respect to argon, according to the known mole fraction ratio that represents the ratio it should be. Using this method, calibration factors for all gas species in the calibration gas were obtained. The CF for Ar was always 1. This method assumed that the relative sensitivity or the calibration factor between specie 'i' and Ar stayed constant, at least within the period of calibration and permeation experiment. Therefore, CF values were used to correct the corresponding gas intensity measured during permeation experiment. The unknown gas composition including a mixture of N_2, CO_2, O_2 in Ar from the membrane reactor outlet can be determined using equation 3.6. The symbols with a prime represents the values for experimental measurements rather than calibration.

$$y_i' = \frac{I_i'/CF_i}{\sum_i I_i'/CF_i} \qquad (3.6)$$

Some minor corrections are required for the calculation such that more accurate gas composition analysis can be achieved. For this calibration method, generally zero gas calibrations (flowing pure Ar) were carried out before and after CO_2 permeation experiments to measure the baseline concentration of N_2 and O_2 that came from air leak at any point of the rig. Stabilised baseline concentration was subtracted from corresponding concentration calculated by equation 3.6, this is particularly important when the expected N_2 and O_2 concentration from reactor outlet is close the background baseline concentration.

During the ionisation process before sample detection in MS, fragments of high mass number molecules may overlap with lower mass number molecules. For instance, in this Mass Spectrometer 11.4% of CO_2 molecules in the sample can be fragmented to m/z ratio of 28, which clashes with singly ionised N_2. Consequentially a proportion of measured intensity for N_2-28 (m/z=28) comes from the fragmentation of CO_2-44. As this cracking factor is known, it is important to subtract the fragment proportion off the raw intensity of m/z=28 from both calibration gas data and experimental data, so that the subtracted intensity purely represent N_2.

3.5.2. Gas Chromatography (GC) analysis

As mentioned earlier, the accuracy of Mass Spectrometer analysis highly relies on stable relative sensitivity value for each gas species. In practice, it often suffers signal instability, commonly referred as 'drift'. The electrical system within the gauge head (see Figure 3.10) may perturb the signal intensity. The key parts that are responsible for the signal instabilities are those that regulate the ion beam toward the mass filter. The voltage of the focus plate was found to have a major influence on the signal stability [119]. If any gas species had a different signal drift rate from the balance gas Ar, the RS value wound not stay constant throughout the experiment.

Considering this drawback, gas outlet streams from the membrane reactor can also be analysed by gas chromatography (GC). A *Varian* 3800 GC coupled with thermal conductivity detector (TCD) was used for gas analysis. The GC is fitted with a molecular sieve 5A column connected (for separating out O_2 and N_2) in series with Shincarbon column (for separating out CO_2). They are packed with zeolite and carbon respectively inside their column channels. Before sample injection, only carrier gas (Ar) flow through the column to the detector. During injection, air push the sample gas into column where the pressure was kept at 3.3×10^5 Pa. Due to the molecular sieve property of packed column, gas molecules are separated by molecular weight. Lighter molecules will travel through columns faster and reach detector earlier. When a new gas component other than the carrier gas is involved, thermal conductivity of column effluent is changed, resulting a temperature change in detector filament, which in turn produces voltage peaks when each gas specie reaches the detector.

The GC method set column temperature at 100°C and detector temperature at 150°C. Each sample was injected twice, and GC required 10 minutes analysis time per injection. The first injection went through Shincarbon column and bypass molecular sieve 5A column, giving a CO_2 peak with retention time of 7 minutes. The second injection went through both columns, giving a N_2 peak with retention time of 16.7 minutes (Figure 3.11). After 20 minutes, GC took the second sample for injection. In principle, Shincarbon column can separate out O_2, N_2 and CO_2 under specifically designed GC method with ramping column temperature. However, this led to an inclined baseline for the voltage signal, making the peak area calculation more complex and less accurate. Therefore, two columns were utilised in series and kept an isothermal column environment in GC method. Comparing with MS, the time intervals between two measurements are much longer. The on-line GC analysis can only produce discrete measurements every 20 minutes rather than a continuous signal. For a long-term downhill CO_2/N_2 permeation experiment lasting 3-5 days, no rapid changes on membrane permeate side gas mole fractions were expected and the GC technique perfectly fit the purpose of on-line gas analysis.

GC can also be calibrated using one-point calibration method, which is by feeding calibration gas of 2% N_2 and 2% CO_2 in Ar. For a stable detector, peak area has linear proportionality with gas concentration. In other words, for the same gas species the peak area ratio equals the concentration ratio. For the analysis of CO_2 concentration that is:

$$\frac{A_{CO_2}}{A_{CO_2,cal}} = \frac{C_{CO_2}}{C_{CO_2,cal}} = \frac{C_{CO_2}}{2\%} \qquad (3.7)$$

Here, A_{CO_2} and $A_{CO_2,cal}$ are peak area of CO_2 concentration within the injected sample and calibration gas respectively, C_{CO_2} and $C_{CO_2,cal}$ are unknown CO_2 concentration and CO_2 concentration in calibration gas respectively. By feeding calibration gas, corresponding peak area of the known CO_2 concentration can be obtained, hence the proportionality factor between peak area and concentration for CO_2 can be calculated, likewise for all other gas species. Gas chromatograph of the sampling gas from membrane reactor outlets with unknown CO_2 and N_2 composition can then be analysed and determined.

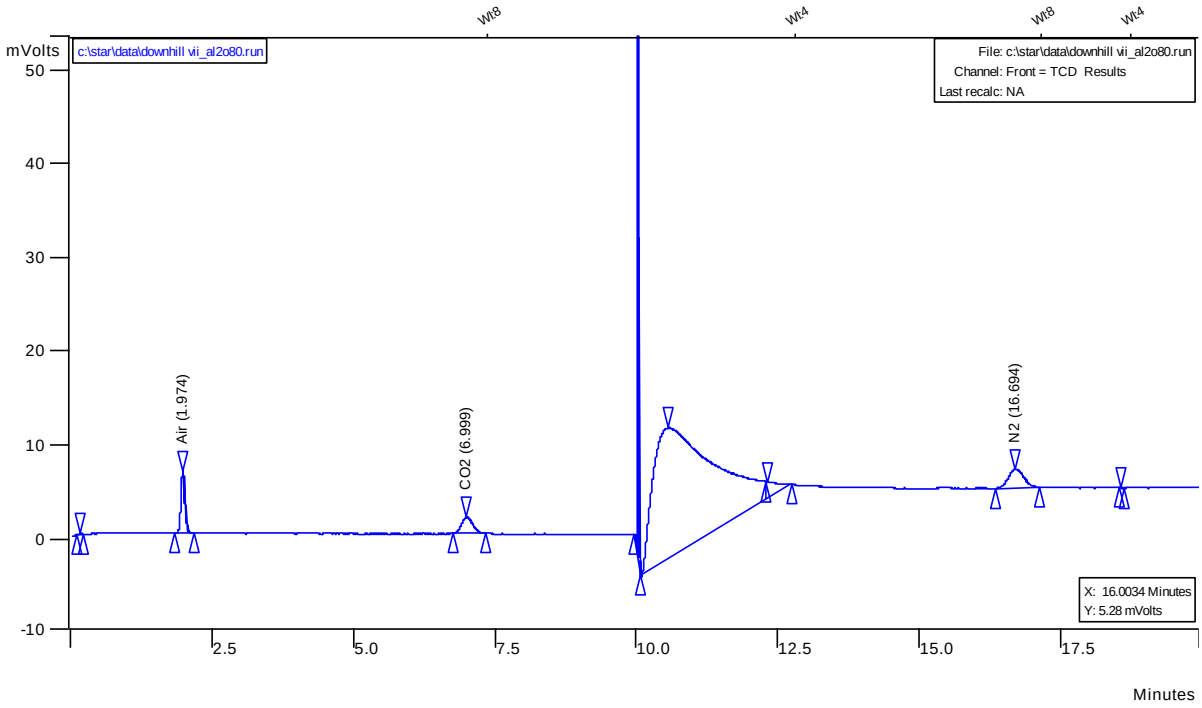

Figure 3.11: A gas chromatograph produced showing CO_2 and N_2 peaks. The first 10 minutes represents the chromatograph from Shincarbon column. An 'air' peak comprising both O_2 and N_2 shows up at approximately 2 minutes retention time. The last 10 minutes represents the chromatograph from molecular sieve 5A column, following an elevation of baseline due to switching column.

3.5.3. Infrared (IR) CO_2 analyser

The CO_2 permeation put great emphasis on the accuracy of CO_2 quantitative analysis. Stable, sensitive and high-resolution CO_2 signal for continuous monitoring is essential especially in the occasion of uphill CO_2 permeation, where a small change of CO_2 concentration needs to be identified. Infrared (IR) CO_2 analyser may provide the benefit from both MS and GC, with relatively stable calibration factors as well as instantaneous on-line monitoring.

During the uphill experiments discussed in Chapter 5 and 6, a *LI-COR* LI-840A CO_2/H_2O Gas Analyser was used in conjunction with MS to monitor the membrane permeate side CO_2 concentration. This instrument offered CO_2 measurement range of 0-20000 ppm and data logging rate of up to one measure per second. The signal noise at 370 ppm CO_2 was only ± 1 ppm [120]. The surrounding atmospheric pressure was the most significant factor that influenced the stability of the measurements. Given that the atmosphere pressure remained stable, the random error of the measurements can be controlled within ± 1%. This indicated the analyser can detect a 50-100 ppm change of CO_2 concentration even on a baseline of 10000 ppm concentration. Moreover, the analyser is reliable for measuring low concentration < 100 ppm.

The working principle of this CO_2 IR analyser is based on Beer-Lambert law, which states the absorbance of IR energy after traveling through the CO_2 containing optical path (Figure 3.12) is

proportional to CO_2 concentration in the optical path. This relation can be expressed as equation 3.8, where A_{IR} = Absorbance of the IR energy; I_0 = Initial IR intensity from the IR source; I = The IR intensity reaching the detector after partial absorption by CO_2 in the optical path; ε_a = Absorption coefficient of CO_2 molecules; l = Length of the optical path; C_{CO_2} = Concentration of CO_2 on the optical path which the IR transmitted through.

$$A_{IR} = -\log\left(\frac{I}{I_0}\right) = \varepsilon_a l C_{CO_2} \qquad (3.8)$$

This IR instrument has very simple configuration based upon the Beer-Lambert theory (Figure 3.12). The core elements only contain a few parts including a straight column of optical path with IR source and detector on both ends. The sampling gas flow from the source side to the detector side through the column before leaving the instrument to the vent.

Three-point calibration method was used for the IR analyser. Zero grade argon with little CO_2 content, 400 ppm CO_2 and 11000 ppm CO_2 were fed into the analyser in turn. The known CO_2 concentration of the above calibration gas compositions, namely 'zero', 'span' and 'span 2' respectively, were input into the analyser software. The software automatically generated a linear fitted line relating its measured IR absorbance with the actual CO_2 concentration, as well as the coefficients that link the two values. These coefficients do not have to be re-calibrated frequently. Unlike the MS that manipulates relative sensitivity, the CO_2 concentration obtained from the IR analyser would be independent on any other gas specie presenting along with CO_2.

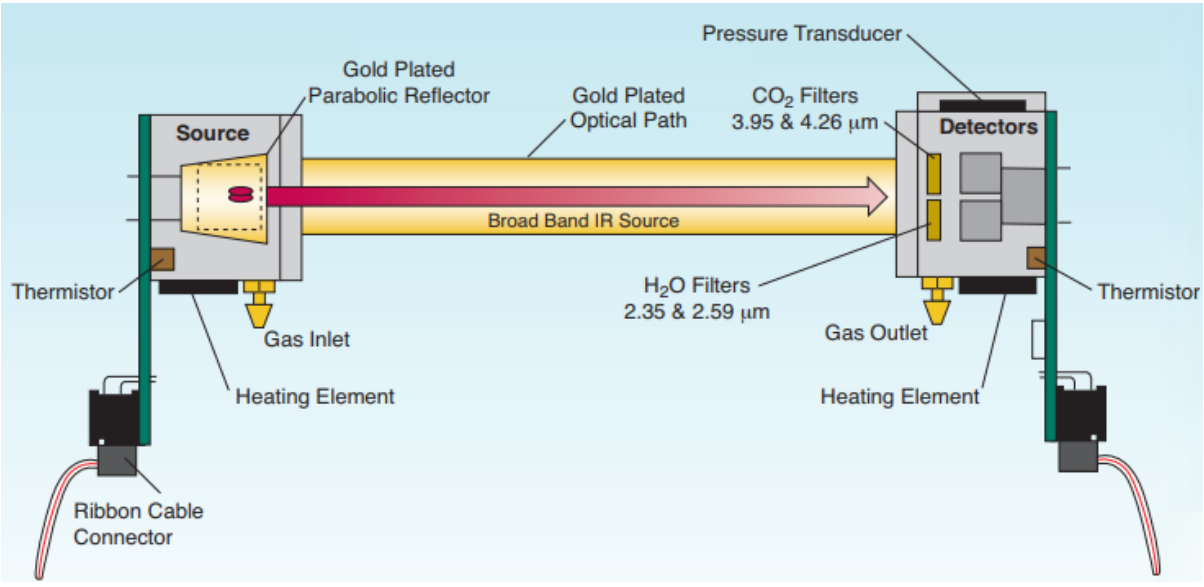

Figure 3.12: Schematic diagram of the LI-840A optical bench [120].

4. Membrane characterisation and selection

4.1. Introduction

Developing highly CO_2 permeable molten carbonate dual phase membranes has been an important research topic for potential applications in CO_2 capture. CO_2 permeance through these membranes can be affected by membrane geometry, membrane microstructure, properties of support materials and the molten salt chemistry. Up to now, many studies have been focussing on the optimisation of membrane porous network and conductivity in order to promote the CO_2 permeance. Whilst the relative importance of the above influence factors, as well as the CO_2 transport mechanisms, have not been well understood. This would require systematic comparisons of CO_2 permeance from mechanistic viewpoints.

This chapter intended to characterise and select membrane support materials with distinct conductivity properties, in order to clearly verify the link between CO_2 permeance and relevant transport mechanisms. Meanwhile, optimised membrane geometry, porosity and pore microstructure were found and controlled through this study. Standard experiments were designed to perform downhill CO_2 permeation through molten carbonate dual phase membranes using three types of support materials: alumina, YSZ and LSCF6428, representing inert, purely ionic conductive and mixed ionic/electronic conductive solid phase properties respectively. The three distinctive properties in turn represented three different CO_2 permeation mechanisms. It has been proposed that ionic conductive support facilitated electrochemical CO_2 transport mechanism (Figure 2.5) and electronic conductive support facilitated electrochemical CO_2-O_2 co-permeation mechanism (Figure 2.6). These mechanisms are not expected for inert alumina membranes. It would be interesting to put the membranes under relevant gas atmospheres and examine whether their performance followed the proposed mechanisms. Various characterisation techniques including geometrical measurements, MIP and high-resolution SEM has been utilised to find the optimised membrane morphology and ensure their consistency. Moreover, membrane characterisation assisted the establishment of appropriate and reproducible fabrication procedures, producing membranes with random packed pore network and homogeneously distributed ternary carbonate throughout the porous network.

The initial objective was to investigate the importance of permeation mechanisms on high temperature CO_2 permeance and CO_2/N_2 selectivity, by comparing the performance of alumina-carbonate, YSZ-carbonate and LSCF6428-carbonate membranes under two sets of conditions: (1) Downhill CO_2 separation feeding a fixed large CO_2 concentration, which simulates the condition of pre-combustion CO_2 capture. (2) Downhill CO_2 separation with O_2 co-permeation, feeding fixed but much smaller CO_2 concentrations, which simulates the condition of post combustion CO_2 capture. These fundamental permeation experiments were essential for validating the membrane functionality. They would also build up basic mechanistic knowledge that could be expanded in the later chapters.

4.2. Dual phase membranes characterisation: microstructural, compositional and geometrical properties

4.2.1. Membrane support geometry and porosity

Diameter and thickness of freshly sintered membrane support disks were measured using Vernier calliper and micrometer set. Average value of 3-5 repeating measurements were taken and the errors were estimated by looking at the deviation to the average. Weight of the membrane supports were also measured using a balance with an accuracy of 1mg. With the above measured parameters and the skeletal densities of corresponding solid materials, membrane support porosity and its maximum carbonate loading can be calculated according to equation 3.2 and 3.3. Skeletal density of solid phase materials and molten ternary carbonate density were taken from literature: ρAl_2O_3 = 3.98 g/cm^3 [121], ρ_{YSZ} = 5.9 g/cm^3 [122], $\rho_{LSCF6428}$ = 6.31 g/cm^3 [123], $\rho_{molten,750°C}$ = 1.96 g/cm^3 [53]. Carbonate density at liquid state was used due to its volume expansion during the phase transition.

Table 4.1: Geometrical properties and porosity estimation of the membranes used for downhill CO_2 permeation alone. As shown in the table the membrane porosities by geometrical estimation were close. The membrane thickness was harder to control but kept as close as possible.

Membranes	Al_2O_3-carbonate	YSZ-carbonate	LSCF6428-carbonate
Sintering temperature	1450°C	1300°C	1250°
pore former wt% in raw powder	0 wt%	20 wt%	20 wt%
Weight of solid phase	1.039 g	1.479 g	1.174 g
Weight of carbonate phase	0.292 g	0.238 g	0.218 g
Pellet mean diameter	1.752 cm	1.545 cm	1.174 cm
Pellet mean thickness	0.175 cm	0.211 cm	0.146 cm
Estimated porosity	0.38	0.38	0.37
Max carbonate loading	0.311 g	0.295 g	0.22 g
% max carbonate loading	93.9%	80.1%	99.1%

Mercury intrusion porosimetry (MIP) was performed for two porous LSCF6428 supports without carbonate loading. Their bulk porosity values were 32% (MIP_1 sample) and 41% (MIP_2 sample) by geometrical estimation. The MIP measured the total mercury intrusion volume as an estimation of total pore volume of the samples (volume of intruded mercury per unit sample weight), as well as the sample bulk density (sample weight divided by apparent sample volume). The porosity would be the product of the two times 100%. The measured bulk porosity values of MIP_1 and MIP_2 were 24% and 42% respectively, indicating a general agreement to the geometrical estimation. It is noteworthy that the porosimeter measured a smaller value than the geometrical estimation for MIP_1, possibly due to the presence of inaccessible closed pores at this porosity (see microstructure in Figure 4.2 and 4.3).

Membranes in Table 4.1 were chosen for downhill CO_2 permeation. For the same material under the same sintering profile, the geometry of sintered disks was highly consistent and reproducible. Here, the most important parameters to control are the membrane porosity and thickness. The three samples listed in Table 4.1 had very similar porosity, controlled by sintering temperature and pore former addition. However, some differences in membrane thickness were expected. The YSZ membrane required silver-ceramic double sealing. A thicker disk was preferred to prevent the thermal explanation of ceramic sealant from cracking the membrane. The actual weight of carbonate phase divided by the maximum carbonate loading estimated from geometrical measurements was shown as '% max carbonate loading'. Normally, a figure of higher than 80% tended to eliminate trans-membrane leak, which describes gas leak through uninfiltrated porous network. Whereas a figure of more than 100% would indicate carbonate accumulation on membrane top surface.

4.2.2. Membrane microstructure on SEM

SEM images provided basic surface characterisation of the membranes used in this project. Top surface SEM images of sintered porous alumina, YSZ and LSCF6428 porous support disks were firstly analysed using the Hitachi TM3030 model (Figure 4.1). Disks with comparable estimated bulk porosity (37-38%) were chosen for the analysis. In general, for a porous disk, the light grey region represents the solid material and the black background represents the void. For all analysed materials, randomly packed pores can be observed, as well as grain boundaries of adjacent crystallites representing densified region. Alumina membrane was sintered without adding pore former, whilst YSZ and LSCF6428 disks were fabricated by blending raw ceramic powers with corn starch powder as pore former. From the local surface images, it seemed the addition of pore former created larger pore diameter for YSZ and LSCF6428 comparing with alumina, although the three disks had very similar porosity. Larger porous channel may lead to better chance of forming highly interconnected porous network after sintering.

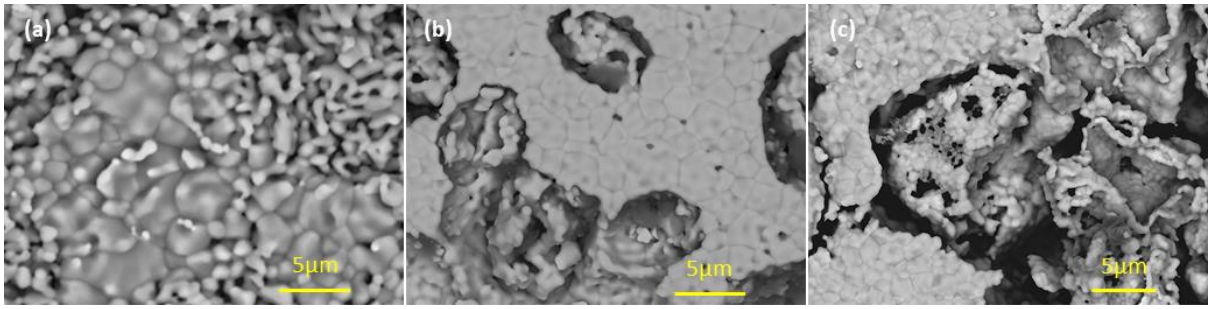

Figure 4.1: Top surface SEM of (a) porous alumina support with 38% porosity, sintered at 1450°C. (b) Porous YSZ support with 38% porosity, powder pressed with 20wt% corn starch, sintered at 1450°C. (c) Porous LSCF6428 support with 37% porosity, powder pressed with 25wt% corn starch, sintered at 1250°C.

The work in this chapter required a good control of membrane porosity with good mechanical strength in the meantime. Without changing the particle sizes of the raw ceramics powder, both sintering temperature and corn starch content can control the porosity of membrane support disks. For alumina

disks fabrication, various sintering temperatures have been employed, such that best compromise between membrane porosity and mechanical strength can be found. Table 4.2 summarised the dependency of the estimated membrane porosity against increasing sintering temperature. It has been found membrane disks sintered at below 1400°C were prone to micro cracking during CO_2 permeation experiments. Whilst membrane porosity reduced significantly above 1500°C. It appeared that the alumina disks with porosity within the range of 30-40% are the most useable.

In contrast, YSZ and LSCF6428 disks tended to densify at lower temperature. Various sintering temperature in conjunction with different corn starch content have been attempted. In order to maintain membrane mechanical strength, the best option was to add pore former such that the sintering temperature can be higher. Disks with porosity of 35-45% adding 20-25 wt% corn starch powder were the most useable. This was coherent with previous researchers particularly for LSCF6428 membrane support [110]. It is worth noting that the addition of pore former inevitably modified the pore microstructure, making the porous network of YSZ and LSCF6428 different from alumina in terms of pore size and tortuosity. However, they were all fabricated using the powder pressed method and exhibited random packed pore network, which indicated they have some degree of consistency.

Table 4.2: Estimated membrane support porosity ε versus sintering temperature and corn starch content for all three ceramic materials. Ceramic powders weighed between 1-2 g and did not strongly affect the membrane porosity. Ramping and cooling rates of the sintering furnace were either 1°C/min or 2°C/min.

Sintering temperature	Al_2O_3 (no pore former)	YSZ (no pore former)	YSZ (20wt% corn starch)	LSCF6428 (20wt% corn starch)	LSCF6428 (25wt% corn starch)
1100°C		ε ≈ 45%			
1170°C		ε ≈ 35%			
1185°C		ε ≈ 27%			
1200°C	ε ≈ 58%	ε ≈ 25%			ε ≈ 46%
1250°C				ε ≈ 37%	ε ≈ 41%
1270°C	ε ≈ 54%	ε ≈ 13%		ε ≈ 32%	
1300°C		ε ≈ 10%	ε ≈ 42%		
1335°C	ε ≈ 53%				
1450°C	ε ≈ 38%		ε ≈ 37%		
1500°C	ε ≈ 32%	ε ≈ 9%			

SEM images can be useful to visualise and compare any change of microstructure and porosity. In this way, the images can assist in selecting the optimised membrane microstructure and porosity. Two top surface images of LSCF6428 disks with different bulk porosity were taken shown in Figure 4.2. The bulk porosity of the disk on the left was roughly 32%. It was sintered at higher temperature with less corn starch content. The disk on the right had a bulk porosity of 10% higher. Local SEM showed porous

area were significantly increased and the pore diameter became larger. The higher corn starch content may provoke better pore interconnectivity, which is imperative for their performance on CO_2 permeability, given that the corn starch powder is homogeneously mixed with ceramic powder and agglomeration of corn starch particles during heating up was minimised.

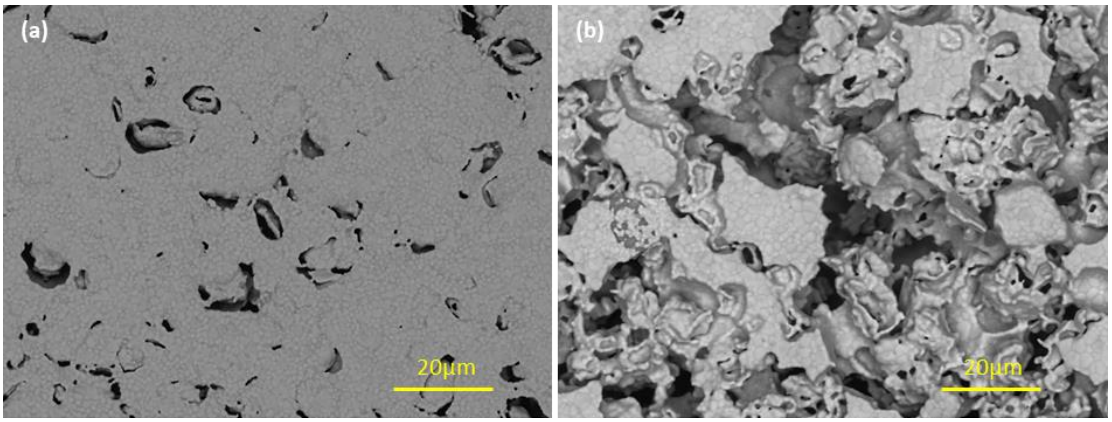

Figure 4.2: Top surface SEM of two porous LSCF6428 supports with different porosity. (a) Powder pressed with 20 wt% corn starch and sintered at 1270°C. Porosity was 32% by geometrical estimation. (b) Powder pressed with 25 wt% corn starch and sintered at 1250°C. Porosity was 42% by geometrical estimation.

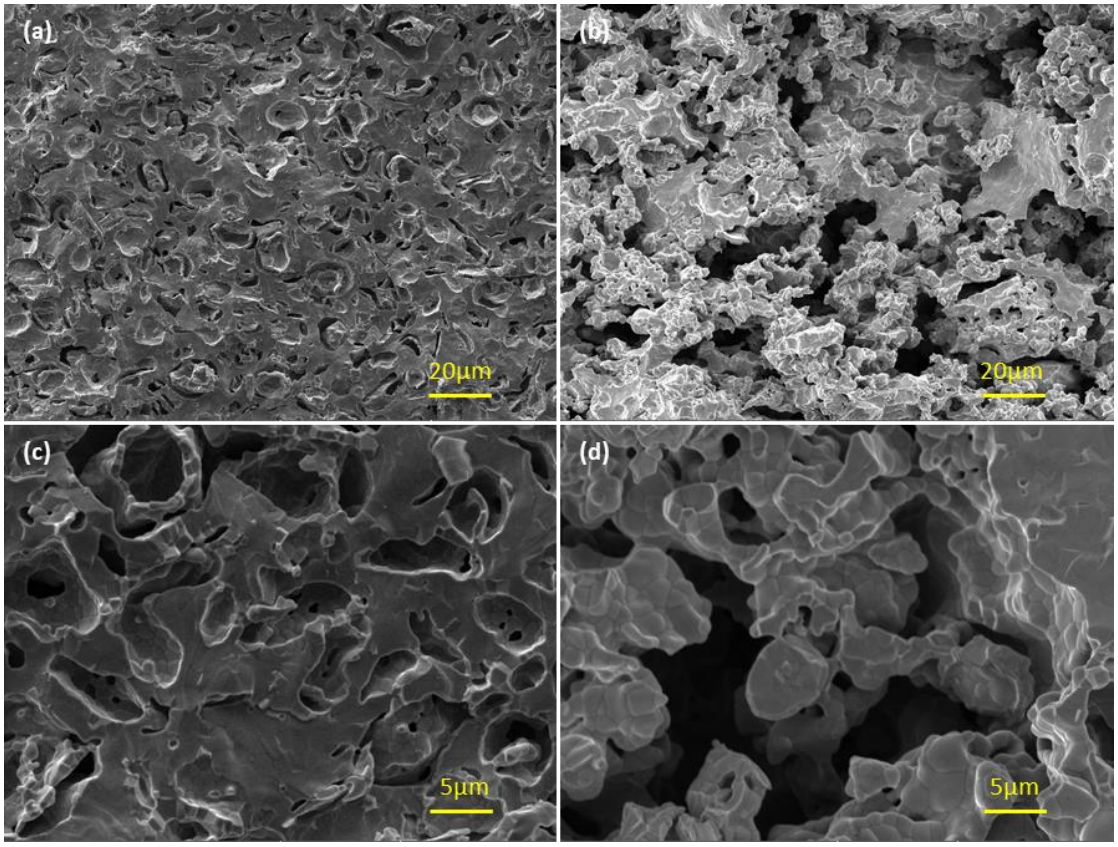

Figure 4.3: Cross-sectional SEM of two porous LSCF6428 supports. (a) and (c): Powder pressed with 20 wt% corn starch and sintered at 1270°C. Porosity was 31% by geometrical estimation; (b) and (d): Powder pressed with 25 wt% corn starch and sintered at 1250°C. Porosity was 41% by geometrical estimation.

The surface SEM images offered limited information about pore interconnectivity as the incident electron beam could not penetrate through deeper layers beneath the membrane surface. Therefore, cross-sectional SEM analysis on the membrane disks was necessary. Figure 4.3 compares the cross-sectional SEM images of two LSCF disks with 31% and 41% bulk porosity respectively. The more porous support seemed to have wider pore channels and better interconnected pore network. The pore size distribution from MIP further confirmed that the 42% porous MIP_2 held a modal pore diameter of 8.4μm, comparing with 0.8μm for MIP_1. To analyse the pore interconnectivity of the bulk membrane disk, three-dimensional imaging such as Computed Tomography (CT) is required. Nevertheless, the cross-sectional SEM determined that membrane disks with around 40% bulk porosity would be more suitable for carbonate infiltration and CO_2 permeation experiments.

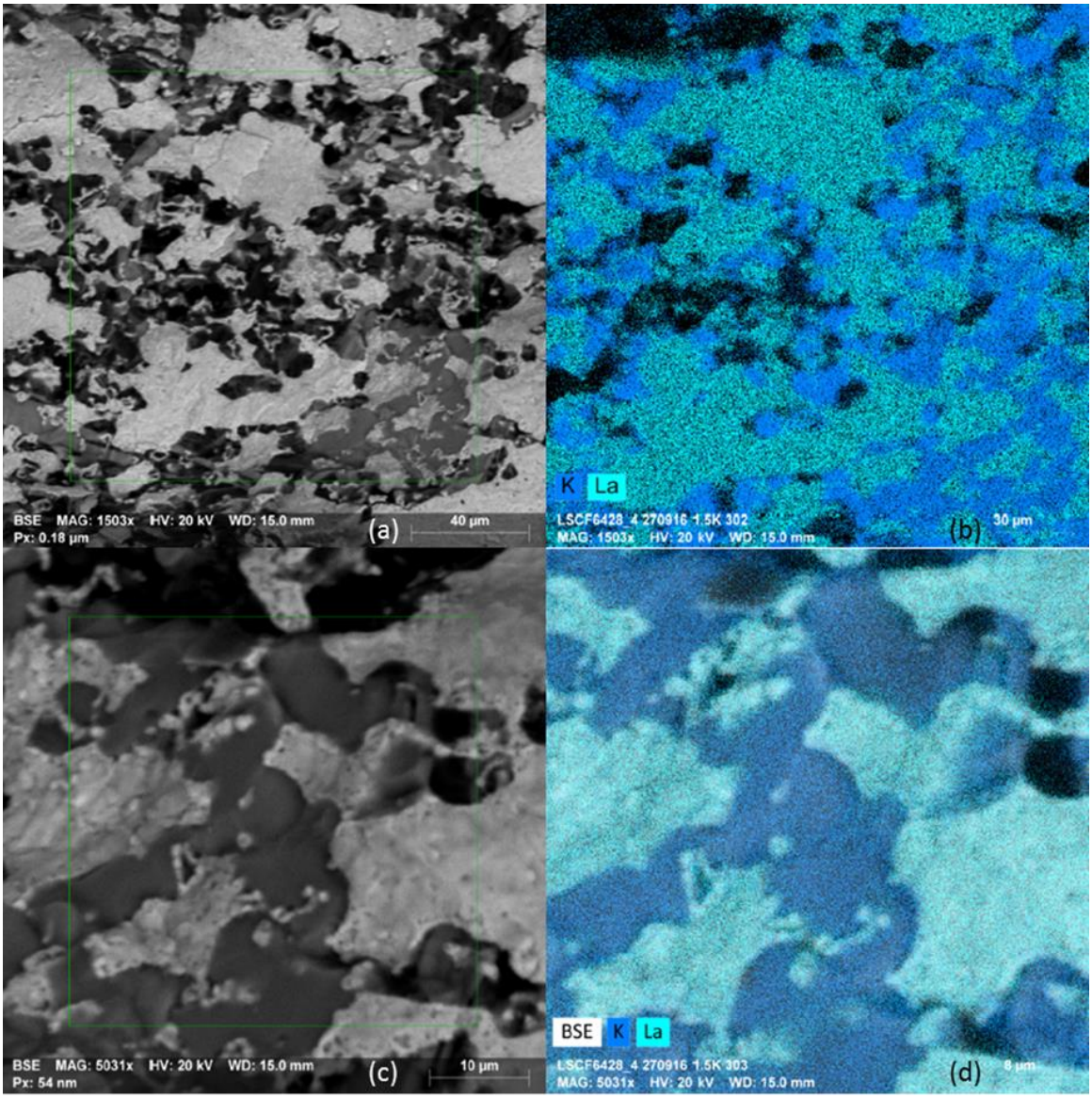

Figure 4.4: Cross-sectional SEM (a and c) and EDS mapping (b and d) of an infiltrated LSCF6428-carbonate dual phase membrane. The bulk porosity of the solid support disk was around 40%. Carbonate loading reached 95% of theoretical maximum. The membrane top surface is towards the top of the image.

An ideal dual phase membrane after hot carbonate infiltration must contain appropriate amount of carbonate so that most of the pores are filled without carbonate accumulation on the membrane surface. A good way to analyse how frozen carbonate resides within the membrane support is to use SEM combined with EDS. The cross-sectional image of an infiltrated LSCF6428 membrane disk at room temperature (Figure 4.4 a and c) were taken using backscattered electrons (BSE). BSE were generated deeper below the surface layer of the sample, the signal strength from BSE were also more sensitive to the material density. This made the carbonate phase and solid phase more distinguishable. It can be observed that the majority of pores originally represented by black background was replaced by dark grey area that represented the carbonate. There were some void volume remaining since the volume of the carbonate reduced once solidified. For the EDS analysis of this membrane (Figure 4.4 b and d), metallic element lanthanum (light blue area) was chosen to represent solid ceramic material, potassium (blue area) were chosen to represent the ternary carbonate. The carbonate phase homogeneously distributed within the random packed pore network on the scanned slice (Figure 4.4 a), which showed 1/8 of the entire membrane thickness. More importantly, interconnected carbonate channels can be easily found out on the EDS mapping.

Figure 4.5 showed the top surface SEM and EDS of another infiltrated LSCF6428 membrane. The overlapping of carbonate with LSCF6428 was minimal, indicating that no carbonate layer covered the membrane top surface and the carbonate loading within the membrane were unlikely in excess of the theoretical maximum. Therefore, SEM and EDS helped confirm these membranes achieved appropriate carbonate loading and carbonate distribution. Hence, SEM and EDS analysis were important before performing CO_2 permeation experiment to ensure consistent membrane functionality.

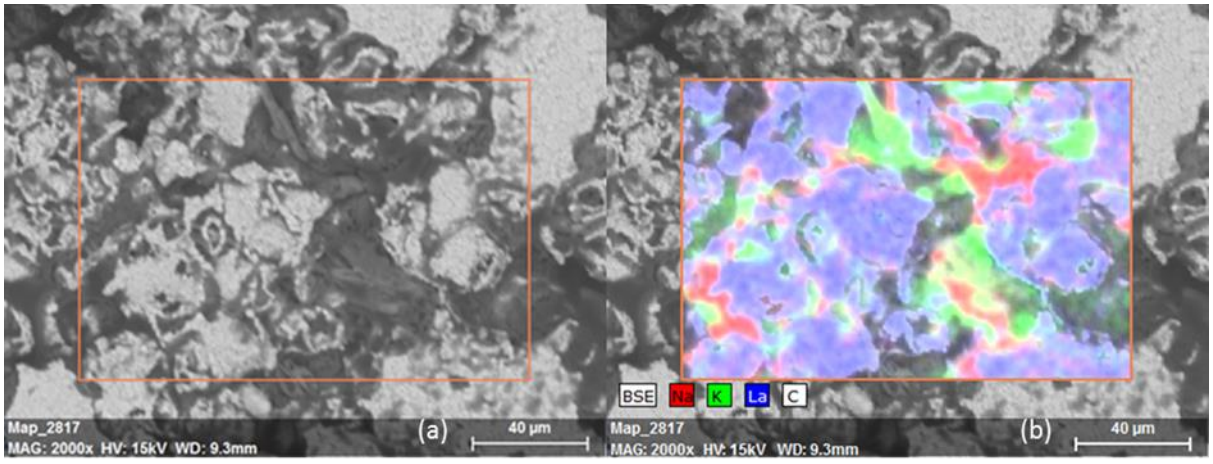

Figure 4.5: Top surface SEM (a) and EDS mapping (b) of an infiltrated LSCF6428-carbonate dual phase membrane, with around 40% bulk porosity and 88% of theoretical maximum carbonate loading. The light grey area on SEM represented solid phase LSCF6428 and darker grey area represented ternary carbonate.

4.3. Downhill CO_2 permeation experiments

4.3.1. Experimental design and procedure

Downhill CO_2 permeation experiment with 50% CO_2 and 50% N_2 as feeding gas has been the first step to assess the membrane performance in terms of CO_2 permeance and CO_2/N_2 selectivity. Although this is not a practical composition of pre-combustion CO_2 capture that targets on CO_2/H_2 separation, applying this experimental condition on various types of membranes provides a good way to compare the inherent performance of different membrane materials. In our downhill CO_2 permeation experiments, 50% CO_2 and 50% N_2 feeding gas were adopted consistently. Best effort has also been given to control the membrane porosity and thickness. In this way the comparison of CO_2 permeance and selectivity can be focused on the intrinsic properties of membrane support materials.

Three different types of powder pressed membrane support materials, including alumina – a representative of insulator, Yttria-stabilised zirconia (YSZ) – a representative of oxide ion conductor, and LSCF6428 – a representative of mixed ionic and electronic conductor, were fabricated followed by hot infiltration of ternary carbonates mixture (33 wt% Li_2CO_3, 32 wt% Na_2CO_3, 35 wt% K_2CO_3) at 600°C. Bulk porosity of 37%-38% has been chosen for all porous support materials. Furthermore, they all exhibited random packed pore network following the same fabrication method, although the pore sizes may vary due to the addition of corn starch for YSZ and LSCF6428. Membrane thickness of 1.5 to 2mm were used coherently for this study.

The experimental rig used here was identical to the one displaced in Chapter 3.4. A dual-chamber high temperature membrane reactor (Figure 3.8) is used in combination with the flow diagram showed in Figure 3.9. Flow rate of inlet gas streams to both reactor chambers were set to 20 ml/min delivered at 10^5 Pa. Membranes were heated up at 1°C/min under operating gas condition, which means the gas flow remained 50% CO_2 and 50% N_2 for membrane feed side and 100% Ar for membrane permeate side from the starting point of operation. The mole fraction of CO_2 and N_2 on membrane permeate side is analysed on-line by mass spectrometer or GC. Measurements were taken at steady state CO_2 permeation from 600 to 850°C, with 50°C temperature intervals. CO_2 and N_2 concentration within feed side inlet was so high that a small decrease on CO_2 and N_2 concentration within retentate stream cannot be measurable on existing gas analysers. Because of this, retentate stream was directly discharged to the vent without gas analysis.

4.3.2. CO_2 permeance and selectivity calculation

In theory, CO_2 permeance can then be calculated using the following relationship, which is a rearrangement of equation 2.2.

$$B_{CO_2} = \frac{J_{CO_2}}{\left(p"_{CO_2} - p'_{CO_2}\right)} = \frac{F y_{CO_2}}{A\left(p"_{CO_2} - p'_{CO_2}\right)} \qquad (4.1)$$

J_{CO_2} is the permeation flux of CO_2; F is sweep gas flow rate; y_{CO_2} is the measured permeate side CO_2 mole fraction; A is the effective permeation area; B is the CO_2 permeance; p"CO_2 and p'CO_2 are membrane permeate and feed side CO_2 partial pressure respectively. Note that p'CO_2 represents the CO_2 partial pressure of retentate stream instead of CO_2 partial pressure within feed side inlet. As the feed side gas composition was not measured, CO_2 partial pressure of retentate stream was calculated according to the CO_2 mass balance equation across the membrane depicted in equation 2.1. Effective membrane area in this equation is defined as the total membrane area exposed to feed inlet gas, including both solid phase and molten phase. This is equivalent to the total membrane area enclosed by the inner boundary of membrane sealing. Typical value of A for this reactor configuration is 0.5 cm^2. The area that feed inlet gas in contact with on membrane surface consisted of both solid phase and molten carbonate due to the porous feature of membrane support. Although electrochemical CO_2 transport was via the packed pore networks filled with molten carbonate, the area of solid phase was also inclusive, as solid phase ion transport was not confined along the pore walls but throughout the bulk solid. The permeance of N_2 can be calculated based on the same principle.

In practice, the measured CO_2 mole fraction also included other two possibilities: trans-membrane leaks due to unfilled pores or cracking and cross-chamber leak through sealant defect. These two gas transport processes are likely governed by size selective mechanisms. Since N_2 and CO_2 molecules have similar molecular sizes, N_2 also played a role of leak indicator during the downhill experiments. Ideally, trans-membrane leaks and cross-chamber leak should be negligible in order to obtain reliable CO_2 permeance. However, in case of a minor leak, it had to assume the amount of CO_2 leak was the same as N_2, thus permeate side CO_2 mole fraction was corrected by subtracting observed N_2 mole fraction from observed CO_2 mole fraction. Leak subtracted CO_2 mole fraction was subsequently used for permeation flux calculations. However, the leak must have reduced the driving force for CO_2 permeation to some extent and determination of CO_2 permeance through a leaking membrane is subjected to large uncertainty.

Permeate side N_2 mole fraction may have a background due to the fittings associated with permeate side chamber, as well as the mass spectrometer inlet lines. An in-situ zero gas calibration feeding pure Ar into both reactor chambers could be performed to measure this background. By subtracting the background off the observed N_2 mole fraction, a more reliable membrane CO_2 selectivity can be obtained by calculating the ratio of CO_2 permeance to N_2 permeance with background subtraction.

4.3.3. Alumina-carbonates membrane

Downhill CO_2 permeation experiment using alumina-carbonate dual phase membrane were conducted at 600°C, 700°C, 750°C and 800°C successively. The membrane was sealed by gold paste, which was the best option for alumina membranes. At 600°C, permeates side CO_2 mole fraction stayed at 0.04% for roughly one hour before an increase of both N_2 and CO_2 mole fractions, indicating a minor leak. Although the membrane was resealed upon heating up to 700°C, N_2 and CO_2 mole fractions could not be sustained at steady state at any specific temperature. This experiment offered rough estimate of CO_2

permeance through alumina-carbonate membrane at 600, 700 and 750°C (a, b and the beginning of c in Figure 4.6). During the heat up process, peaks of CO_2 permeate side mole fraction appeared at 700 to 750°C but they were not accounted as CO_2 permeation. This was probably due to the re-establishment of the thermodynamic equilibrium of carbonate decomposition (equation 2.21) for each temperature, leading to a compositional change of the molten salt. If this were the case, 6×10^{-5} mol of alkali oxide would be formed at 700°C by integrating the CO_2 peak, corresponding to an increase of oxide mole fraction (X_{M_2O}) by 0.02. This value was significantly larger than the theoretical X_{M_2O} (2×10^{-4}) calculated using the equilibrium dissociation constant K_d under this experimental condition, indicating the existence of other CO_2 source such as dissolution in the melt. At higher temperatures the leaking rate started to increase before reaching new equilibrium position. Steady state CO_2 permeation was barely observed. The leaking significantly affected the driving force of downhill CO_2 permeation at 800°C; CO_2 permeance calculated by leak subtraction no longer reflected the real membrane permeance.

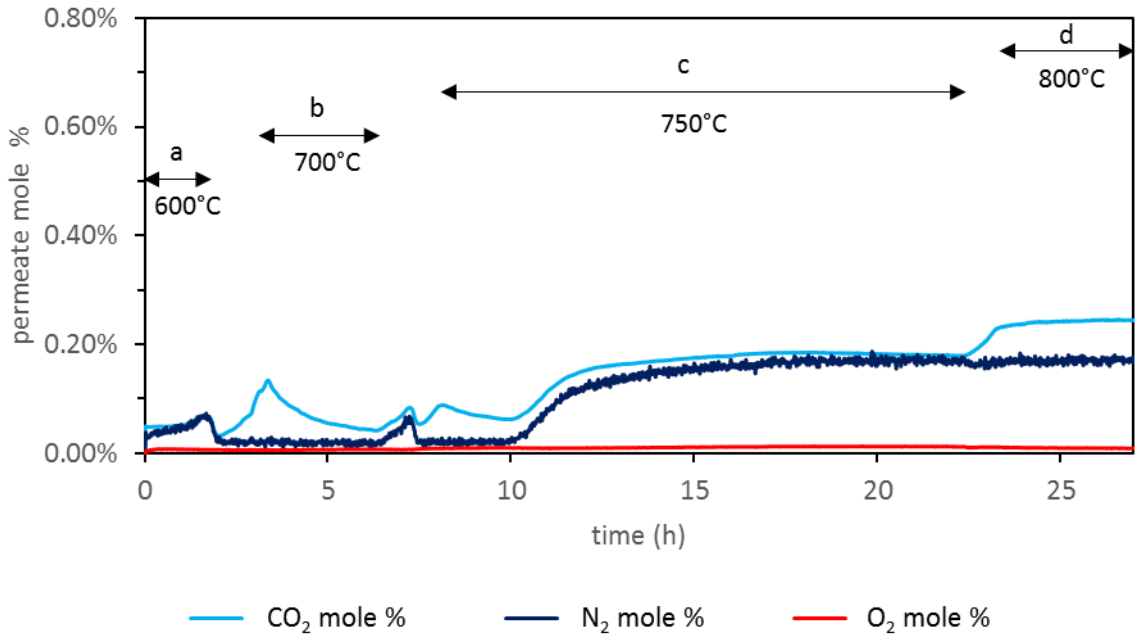

Figure 4.6: Permeate side outlet gas composition against time with alumina-carbonate membrane, analysed on-line using mass spectrometer. The figure consists of four regions: (a) operating temperature at 600°C; (b) operating temperature at 700°C; (c) operating temperature at 750°C; (d) operating temperature at 800°C. 50% CO_2, 50% N_2 feeding gas and 100% Ar sweep gas were used throughout the experiment.

Alumina is an inert material thus the proposed electrochemical transport routes for CO_2 are not valid. It is possible that solution diffusion mechanism was the major route of CO_2 and N_2 permeation. CO_2 and N_2 permeability would therefore be determined by their solubility and diffusion coefficient in molten carbonate. Experimentally determined solubility data at 700°C for CO_2 and N_2 are available in literature (Table 2.2) but diffusion coefficients are unavailable. Nevertheless, a few literatures reported estimated diffusion coefficients of CO_2 in molten carbonate based on MCFC electrode modelling

studies. The values ranged from 10^{-6} to 10^{-5} cm^2/s [124, 125]. Hence the CO_2 permeance via solution diffusion mechanism tends to be within the range of 10^{-10} to 10^{-9} $mol \cdot m^{-2} \cdot s^{-1} \cdot Pa^{-1}$ for a 1mm thick disk membrane, which is comparable to the calculated CO_2 permeance in this experiment at 700°C (2×10^{-9} $mol \cdot m^{-2} \cdot s^{-1} \cdot Pa^{-1}$). Besides, the molten salt chemistry implied possible chemical interaction between CO_2 and ternary molten carbonates (reaction 2.24). This could enable facilitated CO_2 permeation routes through the molten carbonate directly. Alumina has been used as a reference support material. Comparing CO_2 permeance of molten carbonate membranes with ionic or mixed conductive supports with alumina-carbonate membranes may provide an insight on the significance of the proposed electrochemical transport mechanism. The CO_2 permeances through alumina-carbonate membrane obtained above 750°C were not accurate due to leaking. Therefore, comparison with literature data was necessary before any discussion on how the property of support materials affected CO_2 permeance.

4.3.4. YSZ-carbonates membrane

Downhill CO_2 permeation experiment using YSZ-carbonate membrane was performed following very similar operating procedure. The membrane was sealed using silver-ceramic double sealing techniques. This type of sealant was prone to cracking under normal 1°C/min ramping rate, 0.5°C/min ramping rate was used for heating up instead. In addition, the sealants did not provide excellent sealing at below 700°C, thus only CO_2 permeance at 700°C, 750°C and 800°C were measured. Permeate side gas analysis was carried out using on-line GC in series with mass spectrometer. Due to slower ramping rate as well as the large CO_2 peak possibly caused by carbonate decomposition (Figure 4.7), the stabilisation towards steady state permeation required longer time scale. GC had the advantage of stable measurements for long term experiments whilst mass spectrometer signal suffered drift at the time of carrying out this experiment. Thus, the GC data for this experiment was considered as highly reliable. The membrane achieved good gas tightness once the temperature reached 700°C and sustained around 45 hours, before a minor leak initiated at 800°C.

The YSZ-carbonate membrane and alumina-carbonate membrane used in this work were fundamentally different in terms of support material properties. YSZ support was oxide ion conductive while alumina was inert. Proposed interfacial electrochemical reaction $CO_2 + O^{2-} \leftrightarrow CO_3^{2-}$ was thought to facilitate CO_2 transport across YSZ-carbonate membrane whilst there was no such facilitated transport mechanism for N_2. The facilitated electrochemical transport was believed to promote both CO_2 permeance and selectivity. In this experiment, N_2 mole fraction on membrane permeate side was recorded as zero as the amount of N_2 must be below the 100-ppm detection limit of the GC detector. Steady state CO_2 permeance were obtained at all three temperatures, reaching 0.68×10^{-8}, 1.1×10^{-8} and 1.6×10^{-8} $mol \cdot m^{-2} \cdot s^{-1} \cdot Pa^{-1}$ at 700, 750 and 800°C respectively. The maximum CO_2/N_2 selectivity reached at least 19 at 800°C during this experiment, assuming the permeate side N_2 concentration was close to 100 ppm. In general, the CO_2 permeance in this work has shown good agreement with recent YSZ-carbonate dual phase membrane research [53, 97, 98].

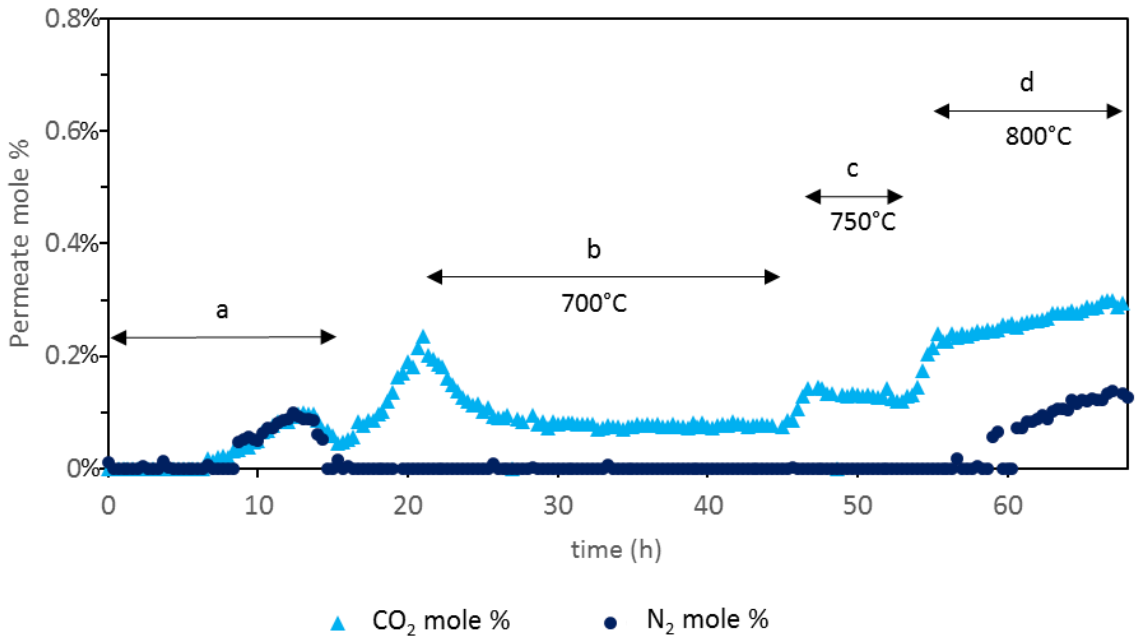

Figure 4.7: Permeate side outlet gas composition against time with YSZ-carbonate membrane, analysed on-line using GC. Injections were taken every 15 minutes. The figure consists of four regions: (a) initial heating up period with a ramping rate of 0.5°C/min; (b) operating temperature at 700°C; (c) operating temperature at 750°C; (d) operating temperature at 800°C. 50% CO_2, 50% N_2 feeding gas and 100% Ar sweep gas were used throughout the experiment.

The logarithm of CO_2 permeation flux against the reciprocal of operating temperature was plotted using the steady state permeation fluxes obtained at 700, 750 and 800°C (Figure 4.8). According to the Arrhenius equation depicted in equation 2.14, the gradient of the linear fit line is $-E_a/R$, where R is the gas constant and E_a is the apparent activation energy of downhill CO_2 permeation in kJ/mol. It turned out that the apparent activation energy for this specific YSZ-carbonate dual phase membrane is 76.7 kJ/mol, which is not far below the activation energy of oxide ion conduction in YSZ electrolyte (81 kJ/mol) [97]. Errors for operating temperature and CO_2 flux were evaluated following the error propagation rules. The operating temperature was monitored using a thermometer and the random error for temperature reading was small, leading to narrow error bars for the horizontal axis. The flux axis incorporated errors from GC measurements of gas mole fraction, flow rate measurements and effective permeation area calculation. In this experiment, stable GC analysis made both systematic and random error low, and the uncertainty of flow rate and effective permeation area were the major contribution of the error of CO_2 permeation flux. The standard error for the apparent activation energy was approximately ±5.0 kJ/mol.

In order to obtain better estimation of the activation energy, more data points over a wider range of operating temperature are required. However, gas tight sealing was challenging to achieve below 650 and above 800°C. Despite the slight deviation from 81kJ/mol, the apparent activation energy was still

comparable to other disk shaped YSZ-carbonate membranes in the literature [53]. It indicated that oxide ion conduction in YSZ phase is likely to be the rate limiting step of CO_2 permeation for a thick YSZ-carbonate membrane (~2mm). This also confirmed that for molten carbonate dual phase membranes, oxide ionic conductivity of solid support materials could be pivotal for improving their downhill CO_2 permeance.

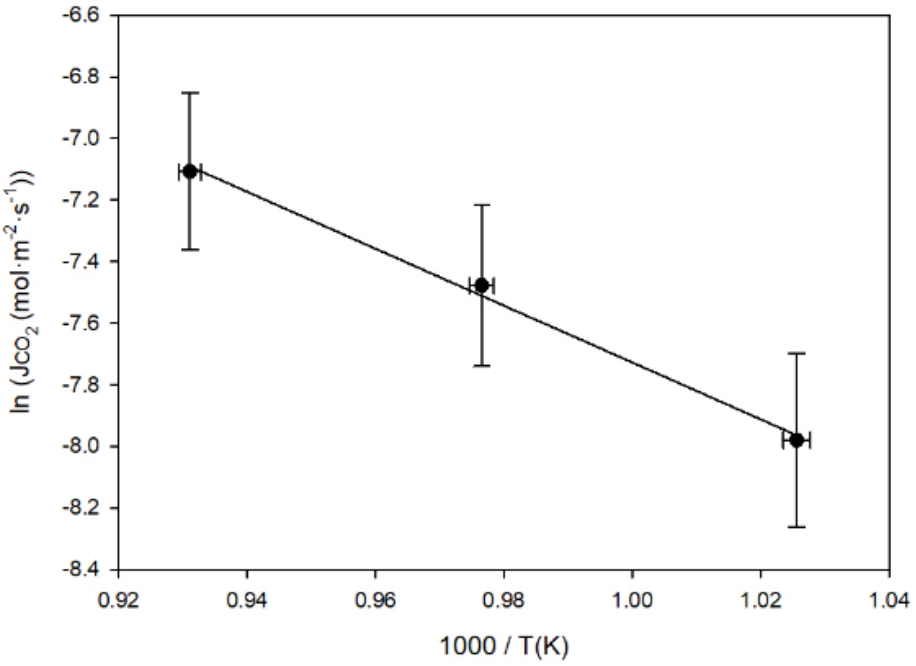

Figure 4.8: Arrhenius plot showing logarithm of CO_2 permeation flux against 1000/T for downhill CO_2 permeation experiment using YSZ-carbonate membrane.

4.3.5. LSCF6428-carbonates membrane

The LSCF6428 is an MIEC membrane support material that offers excellent electronic conductivity as well as good ionic conductivity. Nevertheless, the proposed electrochemical transport mechanisms suggested that only the ionic conducting property of LSCF6428 was utilised when feeding 50% CO_2 and 50% N_2. Ultimately the comparison of CO_2 downhill permeation between YSZ-carbonate membrane and LSCF6428-carbonate membrane would be based on the same mechanisms but different support materials.

Silver paste has been a common choice for sealing LSCF based membranes. The LSCF6428-carbonate membrane reached leak-free condition at 600°C (region b in Figure 4.9) after the initial heating up process. There were small increments of CO_2 permeance at 650, 700 and 750°C respectively. Unlike alumina and YSZ based membranes, CO_2 permeance at lower temperature showed fast stabilisation for LSCF6428-carbonate membrane (region c to e in Figure 4.9). However, once heating up to 800°C a CO_2 peak appeared followed by a gradual stabilisation of CO_2 permeation that lasted longer than 40 hours. Similarly, a CO_2 peak also appeared during heating up to 850°C. The CO_2 permeance gradually stabilised at 2.01×10^{-8} $mol \cdot m^{-2} \cdot s^{-1} \cdot Pa^{-1}$ at 850°C. The permeate side N_2 concentration was coherently

below 0.04% up to 800°C. It indicated successful and robust sealing by silver paste considering the background N_2 level of the permeate side chamber was 0.02-0.03% (Figure 4.10). At 850°C, permeate side N_2 concentration increased slightly but stabilised at 0.06%. This could be due to a minor leak or higher N_2 permeation via solution diffusion mechanism. After subtracting the N_2 background of 0.03%, CO_2/N_2 selectivity of 18 at 800°C and 12 at 850°C were achieved.

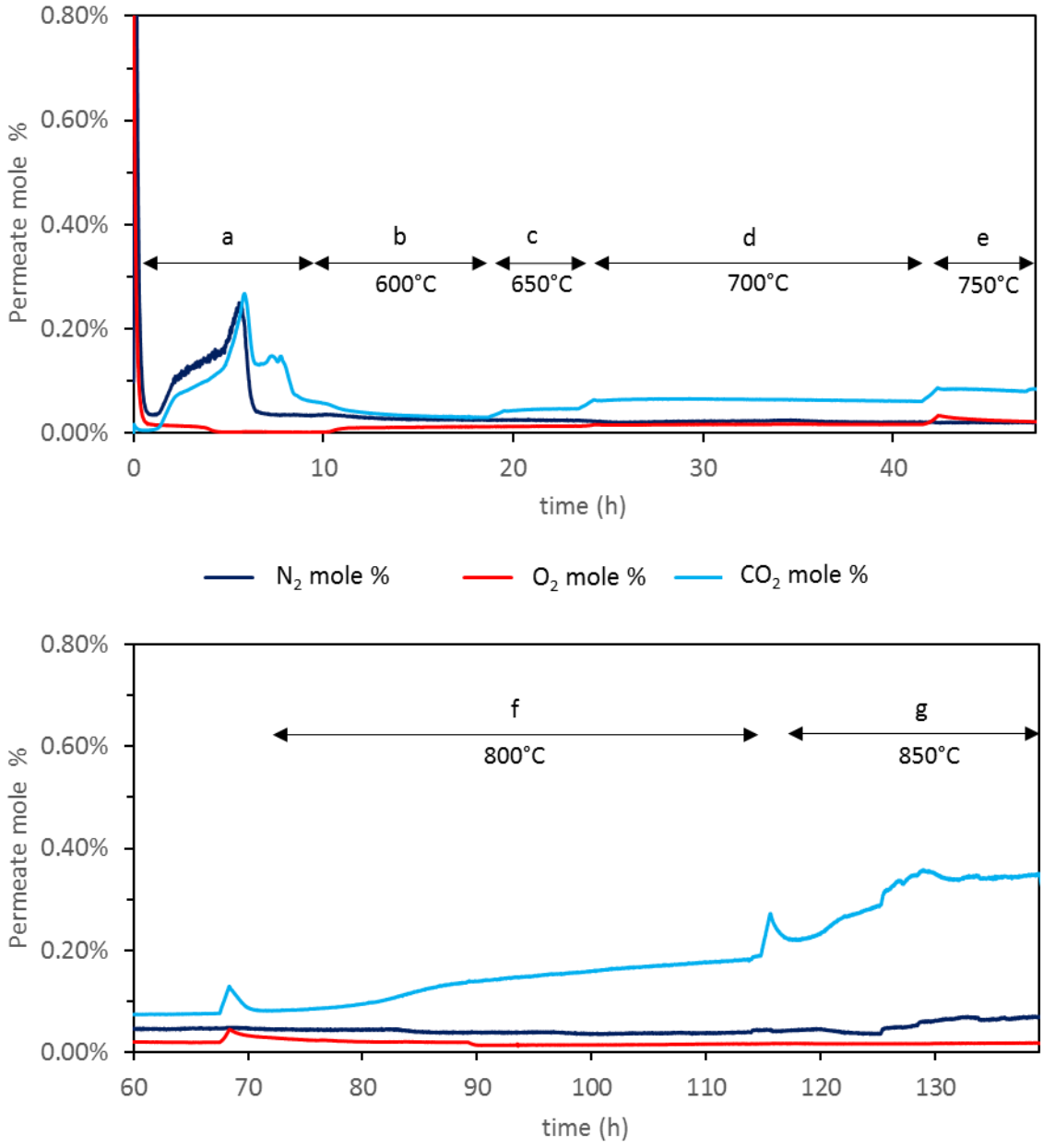

Figure 4.9: Permeate side outlet gas composition against time with LSCF6428-carbonate membrane, analysed on-line using mass spectrometer. The figure consists of seven regions: (a) heating up at 1°C/min; (b) operating temperature at 600°C; (c) operating temperature at 650°C; (d) operating temperature at 700°C; (e) operating temperature at 750°C; (f) operating temperature at 800°C; (g) operating temperature at 850°C. 50% CO_2, 50% N_2 feeding gas and 100% Ar sweep gas were used throughout the experiment.

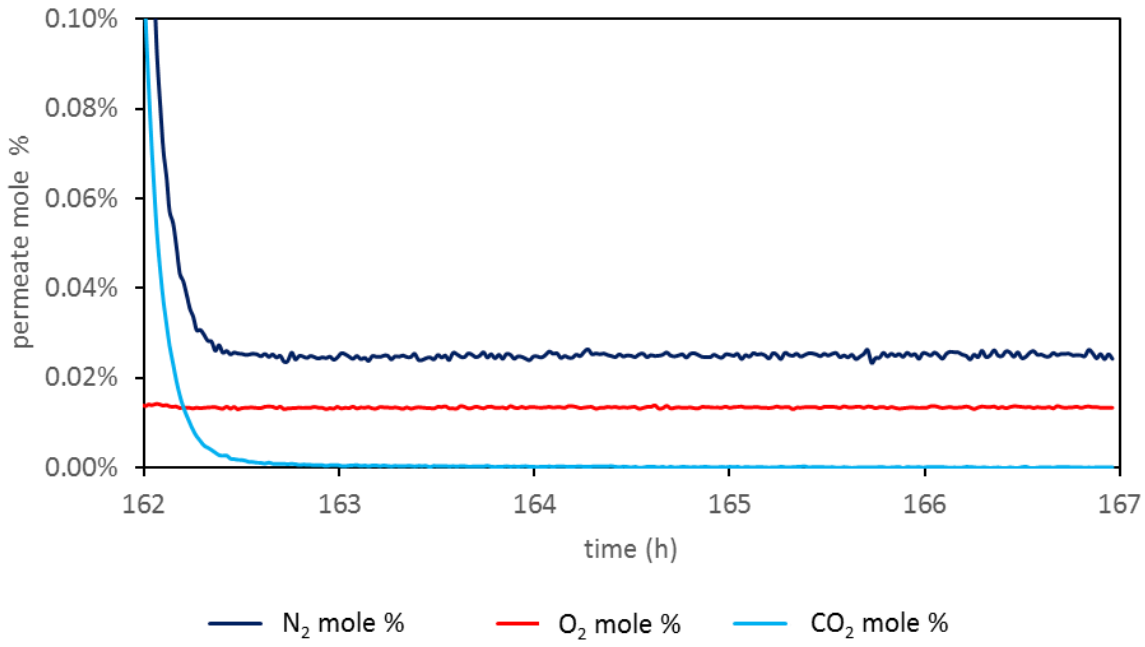

Figure 4.10: Zero gas calibration by flowing pure Argon (99.999% purity) to membrane permeate side after the downhill experiment using LSCF6428-carbonate membrane. The plot presented the information about background N_2, O_2 and CO_2 concentrations of the membrane permeate side chamber effluent into MS.

The reason behind the fluctuation and gradual stabilisation of CO_2 permeation at higher temperatures was not clear due to the complexity of molten salt chemistry and the interaction between the solid and molten phase. This observation could possibly link to the thermodynamic equilibrium of the permeate side interfacial reaction $CO_3^{2-} \leftrightarrow O^{2-} + CO_2$. The equilibrium constant for such reaction can only be related to the CO_2 partial pressure, mole fraction of oxide and carbonate in the melt by assuming the dissolution of oxide in the melt is very small. Whilst at above 800°C, there could be more oxide dissolved in the carbonate so that the molten salt was no longer an ideal dilute mixture. The equilibrium position shifts in response to the varying amount of oxide dissolution as well as the continuing CO_2 permeation. On the other hand, oxygen peaks were observed when heating up to 750°C and above. It occurred not only in this experiment but also in all repeating experiments. This could be the temperature effect to LSCF6428 nonstoichiometry as shown in Figure 2.12, in which LSCF loss lattice oxygen with rising temperature. As a result, concentration of oxygen vacancy increases and this in turn perturb the equilibrium of the interfacial reaction.

Arrhenius plot in similar style was generated for LSCF6428-carbonate membrane (Figure 4.11). The six data points for LSCF6428-carbonate membrane cannot perfectly fit into a linear line. The gradient of the overall linear fit was -9.13 with a rather large standard error of ±1.12. Based on these figures the apparent activation energy for downhill CO_2 permeation through LSCF6428-carbonate membrane was 75.9 ± 9.3 kJ/mol. There appeared to be a turning point of the gradient at above 750°C. If only the data points at 750, 800 and 850°C (the first three data from the left) were fitted, a gradient of -15.9 would be

obtained corresponding to 132.1 kJ/mol activation energy. Whilst fitting the data points solely at lower temperatures gave an activation energy of 56.4 kJ/mol. The standard errors associated with the two separate linear fits were 0.2 to 0.3 indicating better fitting into their linear regression lines.

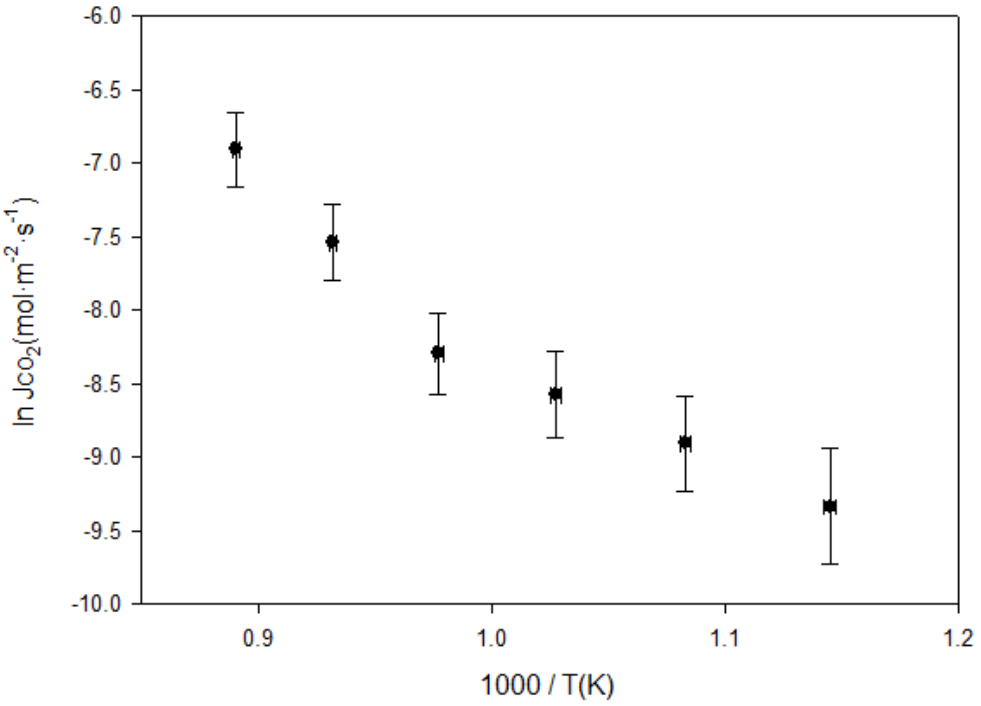

Figure 4.11: Arrhenius plot showing logarithm of CO_2 permeation flux against 1000/T for downhill CO_2 permeation experiment using LSCF6428-carbonate membrane.

In general, a change of the apparent activation energy is due to a switch of dominating CO_2 transport mechanism from one to another. In the experiments for LSCF based membranes, CO_2 permeation at lower temperature was explored. At 600-650°C, the downhill CO_2 permeation flux via electrochemical transport may be comparable with solution diffusion, since the O^{2-} conductivity in LSCF6428 is low in this temperature range. At higher temperature, the electrochemical transport became more dominating whilst solution diffusion mechanism became insignificant. The literature suggested that the activation energy for ionic conduction with LSCF6428 composition is 125.4 kJ/mol [126]. Activation energies of CO_2 molecular dissolution and diffusion in molten carbonate were on a range of 20-30 kJ/mol [127]. Based on these figures, it seemed the CO_2 permeation through this LSCF6428-carbonate membrane was still a bulk O^{2-} diffusion limiting process at high temperature. At low temperature, there was likely a combination of electrochemical transport with solution diffusion mechanism. However, complexity of the dual phase system that influences steady state CO_2 permeation was involved, such as LSCF oxygen nonstoichiometry and the shifting thermodynamic equilibrium of the interfacial reaction. These factors were not well understood but they indeed brought uncertainty in determining the apparent activation energies based on experimental data.

4.3.6. Overall discussion

Figure 4.12 summarises the downhill CO_2 permeance through alumina-carbonate, YSZ-carbonate and LSCF6428-carbonate membranes between 600 and 850°C. Several results for alumina and YSZ based membranes have been sited to fulfil broader range of operating temperature. Although the results for alumina-carbonate membrane in this work was affected by sealing issues, literature suggested CO_2 permeance and selectivity through alumina-carbonate membrane remained low without strong dependence with operating temperature. On the other hand, YSZ-carbonate and LSCF6428-carbonate membranes showed low CO_2 permeance at 600 to 650°C, but CO_2 permeance growth at above 700°C was significant, achieving CO_2/N_2 selectivity of at least 18 at 800°C in the meantime. Results for YSZ-carbonate agreed with similar membranes in the literature whilst few literatures reported downhill CO_2 permeance using the LSCF6428 composition. In addition, the membrane functionality for the dual phase membranes were validated by CO_2 downhill permeation experiments. Suitable sealant materials have been found for each type of membrane, which is beneficial for future experimental study.

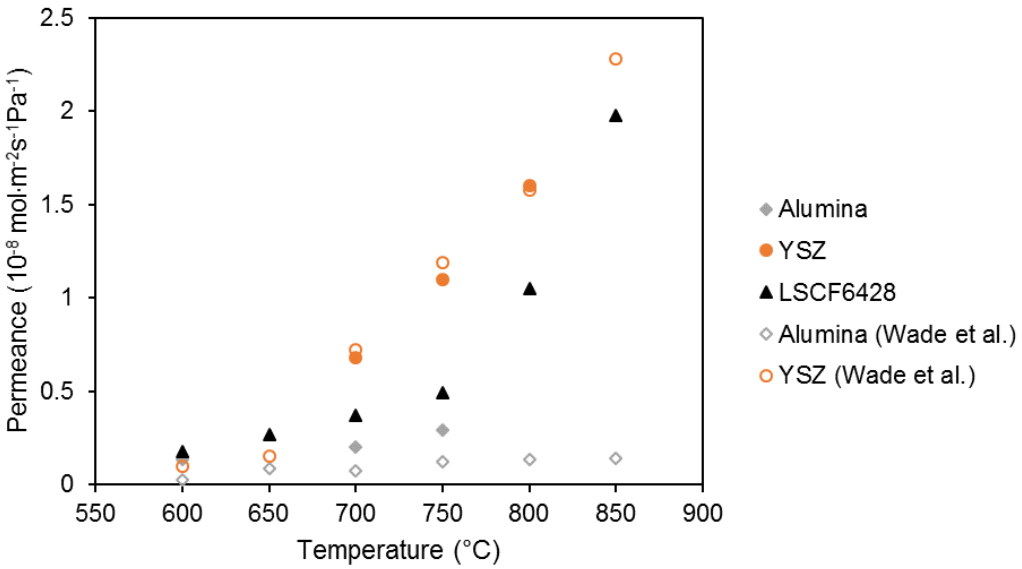

Figure 4.12: The dependence of CO_2 permeance on operating temperature for alumina-carbonate, YSZ-carbonate and LSCF6428-carbonate membranes. Data points were taken from steady state permeation at each operating temperature, focusing on an operating temperature window between 600 to 850°C. Comparisons have been made between experimental data in this research and literature by Wade et al. [53].

The comparison made in Figure 4.12 indeed suggested the ionic conductivity of membrane support can vastly promote the downhill CO_2 permeance. It was very likely the origin of such effect came from the proposed electrochemical transport mechanism. Inert alumina membranes were used as a reference material, representing the effects of non-facilitated mechanisms and direct gas-molten salt interaction. YSZ and LSCF6428 are both good oxide ion conductors especially at higher temperatures, enabling facilitated electrochemical CO_2 transport for YSZ and LSCF based dual phase membranes. The apparent activation energies for YSZ and LSCF based membranes were both close to their corresponding

activation energies of ionic conduction, which was much higher than the activation energy of CO_2 dissolution and diffusion in the melt, indicating the CO_2 permeation is a bulk O^{2-} diffusion limiting process for 1.5-2 mm thick membranes. This further supported the ionic conduction was involved in this CO_2 transport pathway.

This section has shown that ionic conductive YSZ and LSCF dual phase membranes are capable of CO_2/N_2 separation from a high CO_2 concentration gas mixture. This condition can only be satisfied by some of the pre-combustion CO_2 capture processes, since power plant and industrial flue gas have lean CO_2 content of much lower than 50%. Here, YSZ-carbonate and LSCF6428-carbonate membranes were selected for further downhill CO_2 permeation experiments that switched to a CO_2 lean feeding gas, to test whether they were potential candidates for post-combustion CO_2 capture. Alumina membranes were not further investigated due to their challenging sealing procedure and low CO_2 permeance.

4.4. Downhill CO_2-O_2 co-permeation experiments

4.4.1. Introduction and experimental procedure

This part of the study continued testing the functionality of YSZ-carbonate and LSCF6428-carbonate membranes when the feeding gas stream had low CO_2 content. In the previous section the membranes were operated under the condition with 50% CO_2 on feed side and pure Ar on permeate side. This significant chemical potential difference of CO_2 across the membrane drove the continuous and steady downhill CO_2 permeation. Nevertheless, CO_2 content is often much lower in flue gas. For example, the CO_2 concentration of the effluent gas from NGCC can be as low as 3-4% at ambient pressure. With this vastly reduced driving force, it has been a technical challenge to achieve satisfactory CO_2 permeation flux without pressurising the feed stream or vacuuming the permeate stream.

The unique feature of the flue gas is that CO_2 co-exist with O_2 rather than a reducing atmosphere as in pre-combustion. Therefore, the membranes would be exposed to not only CO_2 but also O_2 upon CO_2 capture. The existence of O_2 is important because this would trigger the proposed CO_2-O_2 co-permeation mechanism (Figure 2.6) given that the membrane solid phase material is electronic conductive. In this way, a new CO_2 transport pathway is facilitated. It is important to investigate how the existence of O_2 affects CO_2 permeation flux though the dual phase membranes.

The two candidates here were purely ionic conductive YSZ-carbonate membrane and LSCF6428-carbonate membrane with MIEC properties. Experiments were conducted by alternating between oxygen free feed stream (1% CO_2, 1% N_2 in Ar) and oxygen containing feed stream (1% CO_2, 1% N_2, 20% O_2 in Ar), such that the CO_2 permeation flux with and without O_2 on membrane feed side can be compared directly at 600 and 800°C. The 20% O_2 composition has been adopted for proving the co-permeation concept although the practical O_2 content in flue gas is lower than 10%. Disk shaped membranes have relatively low surface area and high O_2 concentration helped produce perfectly

measurable permeation flux on gas analysers. The sweep gas through the permeate side chamber was pure Ar as conventional downhill experiments. Flow diagram for these experiments were based on Figure 3.9. Instead of CO_2/N_2, two cylinders with above compositions were the feed inlet gas, with an additional four-way valve for composition alternation.

4.4.2. Results for YSZ-carbonate and LSCF6428-carbonate membranes

Experimental data of CO_2-O_2 downhill co-permeation through YSZ-carbonate membrane is present in Figure 4.13. When feeding the oxygen free stream at 600°C, CO_2 concentration on membrane permeate side was only 0.02%. N_2 and O_2 were close to their background level on mass spectrometer. Upon switching to 20% O_2 containing stream for feed side, CO_2 concentration on membrane permeate side increased slightly to 0.05%. Meanwhile, O_2 concentration also increased from 0.02% to 0.04%. Both CO_2 and O_2 concentration returned to the original level when feeding gas was switched back. At 800°C, the existence of O_2 in feeding gas still weakly promoted CO_2 permeation. However, the permeate side O_2 concentration significantly increased to 0.34%. The existence of oxygen in feeding gas more significantly enhanced CO_2 permeation flux on LSCF6428-carbonate membranes. When switching from 1% CO_2, 1% N_2 in Ar feeding gas to 1% CO_2, 1% N_2 and 20% O_2 in Ar at 600°C (Figure 4.14), permeate side CO_2 mole fraction increased from 0.01% to 0.09%. At 800°C, this increment was from 0.04% to 0.28%. The numerical results showing the effect of co-feeding O_2 for both types of membranes have been summarised in Table 4.3.

Table 4.3: The effect of co-feeding O_2 on downhill CO_2 permeation. YSZ and LSCF6428 dual phase membranes are investigated at 600 and 800°C respectively.

Membrane support	T °C	Permeate side CO_2 % Feeding 1%CO_2+1%N_2 in Ar	Permeate side CO_2 % Feeding 1%CO_2+1%N_2+20%O_2 in Ar
YSZ	600	0.02%	0.05%
YSZ	800	0.06%	0.11%
LSCF6428	600	0.01%	0.09%
LSCF6428	800	0.04%	0.28%

When O_2 was absent from the 1% CO_2 feeding gas, CO_2 permeation fluxes through both types of membranes were low regardless of operating temperature. It can be explained by the fact that the driving force dropped by almost 50 times comparing with feeding 50% CO_2. However, when 20% O_2 was present on the feed side of LSCF6428-carbonate membrane, the CO_2 flux reached 0.036 $ml \cdot min^{-1} \cdot cm^{-2}$ at 600°C and 0.11 $ml \cdot min^{-1} \cdot cm^{-2}$ at 800°C, which were comparable as feeding 50% CO_2. Technically, CO_2 permeance with O_2 co-permeation cannot be calculated using equation 4.1, since O_2 also contributed to the overall driving force (see the flux-driving force relationships in Chapter 6). For easier

comparison with normal downhill CO_2 permeation, CO_2 partial pressure difference between retentate and permeate outlet streams was assumed as the apparent driving force and the driving force from O_2 was considered as hidden. The retentate stream CO_2 concentration was measured as 0.97% at 600°C and 0.73% at 800°C during LSCF co-permeation experiments. Apparent CO_2 permeance reached 2.99 × 10^{-7} mol·m^{-2}·s^{-1}·Pa^{-1} at 600°C and 1.82 × 10^{-6} mol·m^{-2}·s^{-1}·Pa^{-1} at 800°C, which were two orders of magnitude higher than feeding 50% CO_2 at same temperatures. Therefore, co-feeding oxygen helped maintain the CO_2 permeation flux on the same level as feeding concentrated CO_2. In other word, it overcame the driving force deficiency posed by CO_2 lean feeding gas upon separation.

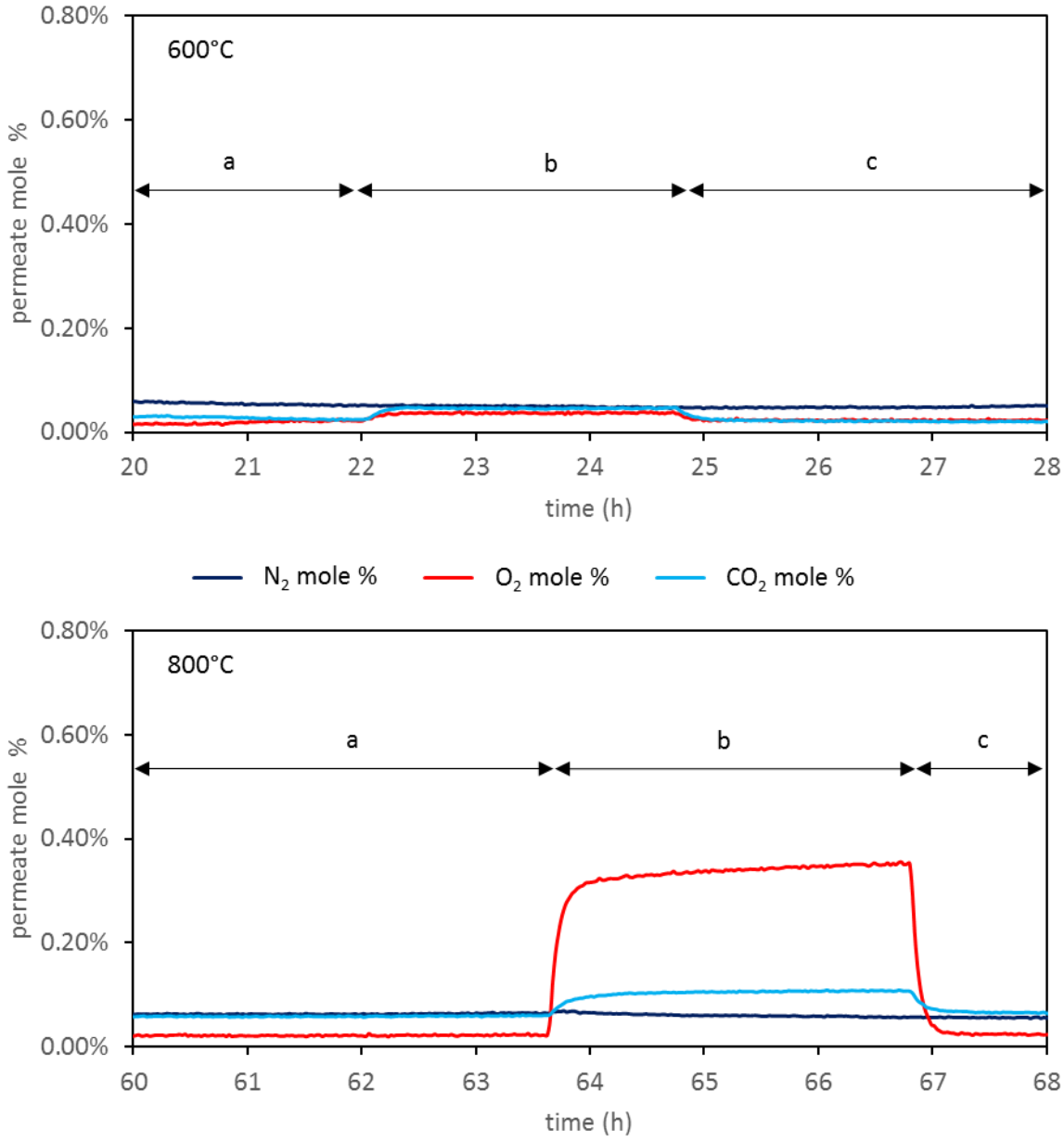

Figure 4.13: Permeate outlet gas composition during downhill CO_2-O_2 co-permeation experiment through YSZ-carbonate membrane. (a) Feeding 1% CO_2, 1% N_2 in Ar. (b) Feeding 1% CO_2, 1% N_2, 20% O_2 in Ar. (c) Switching back to 1% CO_2, 1% N_2 in Ar feeding gas. Sweep gas was pure Ar consistently.

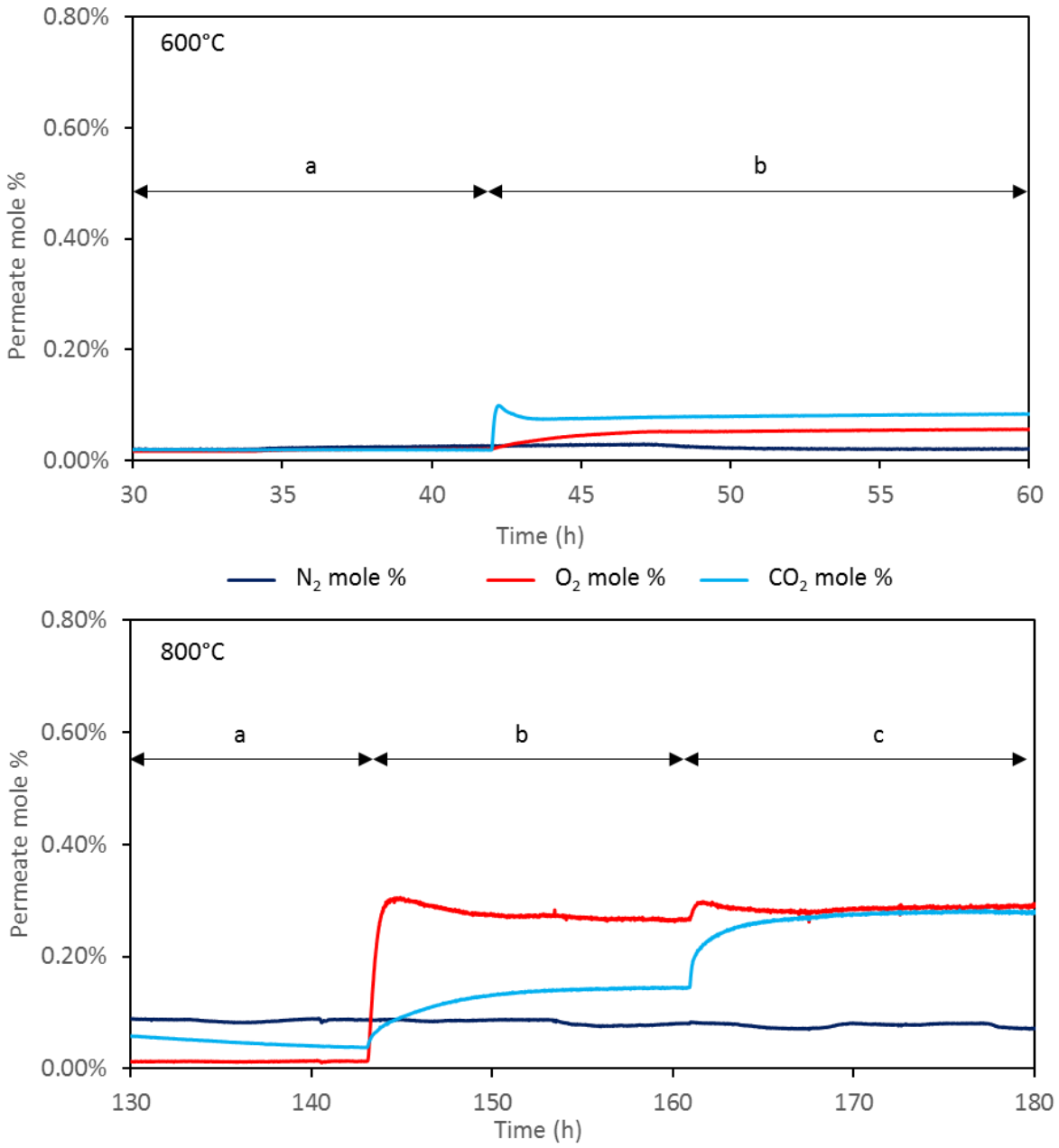

Figure 4.14: Permeate outlet gas composition during downhill CO_2-O_2 co-permeation experiment through LSCF6428-carbonate membrane. At 600°C: (a) Feeding 1% CO_2, 1% N_2 in Ar. (b) Feeding 1% CO_2, 1% N_2 and 20% O_2 in Ar. At 800°C: (a) Feeding 1% CO_2, 1% N_2 in Ar. (b) Feeding 0.5% CO_2, 0.5% N_2 and 20% O_2 in Ar. (c) Feeding 1% CO_2, 1% N_2 and 20% O_2 in Ar. Sweep gas was pure Ar consistently.

Looking at more details about CO_2 and O_2 electrochemical transport pathways through an MIEC type molten carbonate dual phase membrane, three possibilities has been proposed in the literature. Firstly, CO_2 may follow the normal O^{2-} conduction pathway by undergoing interfacial reaction (i) $CO_2 + O^{2-} \leftrightarrow CO_3^{2-}$. Secondly, the electronic conductive support allowed the co-permeation pathway by undergoing interfacial reaction (ii) $CO_2 + 1/2O_2 + 2e^- \leftrightarrow CO_3^{2-}$. Last, O_2 can transport via solid phase independently by undergoing reaction (iii) $1/2O_2 + V_{\ddot{O}} + 2e^- \leftrightarrow O_o^x$ also because of the electronic conductive support. During the co-permeation experiment at 600°C, LSCF6428 support was mainly electronic conductive

at this temperature. The co-permeation pathway could be dominating for CO_2 permeation, accompanied with independent O_2 transport through the solid phase. The CO_2 permeation via the O^{2-} conduction pathway must be insignificant (see Figure 4.15 for the comparison of conductivities). Permeate side CO_2 and O_2 mole fraction ratio of was 1.8:1, which is roughly consistent with the 2:1 stoichiometric ratio of interfacial reaction (ii). Moreover, for the co-permeation pathway the solid phase bulk diffusion was no longer the limitation. The rate limiting step changed to the carbonate ion diffusion in molten phase due to the high electronic conductivity in LSCF6428. Whilst at 800°C, the permeate side mole fraction ratio of CO_2 and O_2 dropped to 1:1. This was a clear indication that the co-permeation pathway cannot be the only transport mechanism. There may be a stronger overlapping of the three pathways at higher temperature that made the permeate side CO_2 and O_2 mole fraction ratio deviate from 2:1. It was also evident that the O_2 incorporation into the molten carbonate (reaction 2.27) very likely overlaps with the co-permeation mechanism, resulting a significant drop of the ratio to 1.1:1 [90, 91, 128].

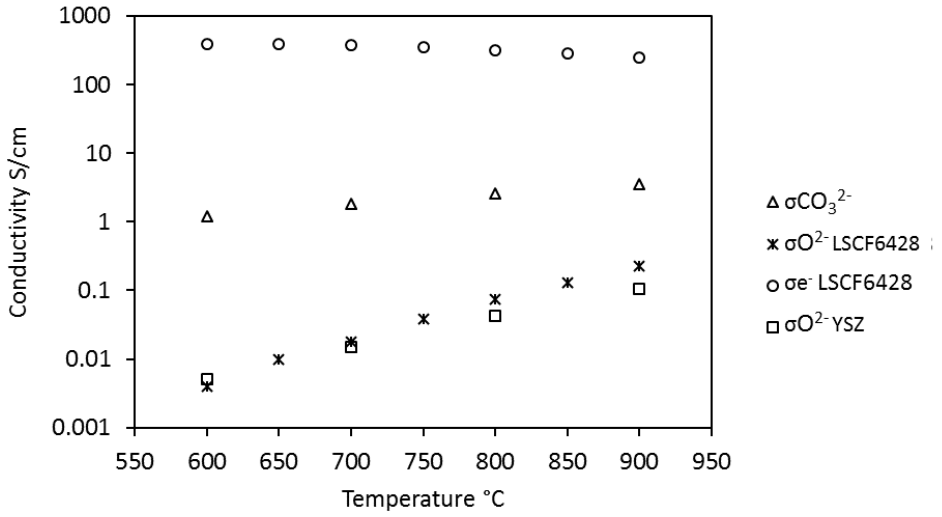

Figure 4.15: Conductivities within molten carbonate, solid YSZ and LSCF6428 against temperature. Data based on experimental measurements in the air and plotted on logarithm scale. CO_3^{2-} conductivity in the melt was generally an order of magnitude higher than solid phase O^{2-} conductivities whilst electronic conductivity in LSCF6428 was generally two orders of magnitudes higher than CO_3^{2-} conductivity [53, 126, 129].

Regarding to YSZ-carbonate membrane, O^{2-} conduction pathway was expected to be always dominating as YSZ was not considered as electronic conductive. The observation of the co-permeation experiment at 600°C in Figure 4.13 agreed with the prediction. The reason why there was a significantly larger O_2 mole fraction on membrane permeate side at 800°C was unclear. In literature, O_2 permeation flux via thick solid YSZ pellet at this temperature was a few orders of magnitude lower than that of LSCF6428 [130], indicating the independent O_2 transport via solid phase YSZ cannot be a major factor. The formation of lithium zirconate on molten salt-solid interface probably involved in the O_2 transport. Literature has proposed lithium zirconate could be used as cathode materials as lithium zirconate/Li^+ ions interaction may lead to generation of electron defects in lithium zirconate phase [131].

4.5. Summary for material selection

In this part of the research, various characterisation technologies including SEM, EDS and porosity measurements have been done. In conjunction with downhill CO_2 permeation experiments, it has been shown that the fabricated molten carbonate dual phase membranes are highly operable under 600-900°C. Membrane support material selection was based on CO_2 permeance, CO_2/N_2 selectivity as well as the affinity of membrane material with sealant material. Using inert alumina as a reference material, it has been shown that both YSZ-carbonate and LSCF6428-carbonate membranes are capable of downhill CO_2/N_2 separation under high CO_2 chemical potential difference due to the ionic conductivity of the support material. However, moving into a realistic low CO_2 chemical potential difference scenario such as flue gas CO_2 capture, only MIEC type LSCF6428-carbonate membrane sustained CO_2 permeation flux at 10^{-1} ml·min^{-1}·cm^{-2} level with the help of co-feeding 20% O_2. It is widely believed in literature that the electronic conductivity opened another electrochemical transport pathway for O_2 and CO_2 together. This allows the chemical potential gradient of O_2, which naturally presents for flue gas CO_2 capture, to be exploited.

As a summary, LSCF6428-carbonate membranes seemed to be a more flexible type of dual phase membrane. They are potentially capable of both pre-combustion CO_2 separation and post-combustion CO_2 capture from flue gas. One unique property of the LSCF based membranes are the changing oxygen nonstoichiometry against pO_2 and operating temperature. This behaviour of LSCF6428 will indeed link with their application into pre-combustion CO_2 separation where pO_2 is relatively low, and post-combustion CO_2 capture where pO_2 is relatively high. The next step of the research is therefore to focus on LSCF6428-carbonate membrane, further investigate their behaviour in reduced and oxidised atmosphere and find out how these conditions affect the CO_2 permeation flux.

5. Performance of LSCF6428 based membrane with various oxygen nonstoichiometry

5.1. Introduction

Chapter 4 has demonstrated that LSCF6428-carbonate membrane is capable of both downhill CO_2 permeation alone and downhill CO_2-O_2 co-permeation. When the driving force of CO_2 itself became much lower (i.e. 1% CO_2 feed), the co-permeation of O_2 helped the membrane maintain similar CO_2 permeation flux as feeding 50% CO_2 alone, making the apparent CO_2 permeance two orders of magnitude higher. Based on these results, LSCF6428-carbonate membrane can be promising not only in pre-combustion CO_2 separation, but also in post combustion flue gas CO_2 capture. It is essential to study the properties and performance of this membrane in depth in order to progress onto more practical applications.

Typically, pre-combustion CO_2 separation is associated with an O_2 free atmosphere and post combustion flue gas CO_2 capture is associated with much higher O_2 partial pressure. The oxygen nonstoichiometry of LSCF6428 is sensitive to a change in operating temperature as well as O_2 partial pressure. It can be an important parameter that affects the performance of LSCF6428-carbonate membranes. The dependency of LSCF6428 oxygen nonstoichiometry on temperature and O_2 partial pressure has been understood by coulometry measurements. A variation of oxygen nonstoichiometry may lead to a change of oxygen vacancy concentration within the LSCF6428 crystalline, which further affects the ionic and electronic conductivity of the LSCF6428 membrane support. However, the connection between the change of LSCF6428 oxygen nonstoichiometry and its CO_2 permeation flux remained unclear.

This chapter further investigated the change of LSCF6428 nonstoichiometry during the two targeting operation conditions: downhill CO_2/N_2 permeation (low O_2 partial pressure) as well as CO_2-O_2 co-permeation (higher O_2 partial pressure) between 600 to 850°C. In both cases, the importance of LSCF6428 nonstoichiometry on the membrane CO_2 permeation flux has been evaluated. This evaluation aimed for extracting some mechanistic insights of downhill CO_2/N_2 permeation and CO_2-O_2 co-permeation.

For downhill CO_2/N_2 permeation experiments, LSCF6428 nonstoichiometry was manually modified in a controlled atmosphere before the permeation experiment. With 50% CO_2/N_2 on feed side and pure Ar on permeate side during the experimental, the low O_2 partial pressure cannot re-equilibrate oxygen content in LSCF6428. Downhill CO_2 permeance with pre-reduced solid phase material (modified LSCF6428 oxygen content) has been experimentally determined for the first time and compared to performance of the non-reduced membrane.

For CO_2-O_2 co-permeation, LSCF6428 membrane was maintained in more oxidised state under higher oxygen partial pressure. Although there would still be a temperature effect on the oxygen nonstoichiometry of LSCF6428, the membrane cannot remain reduced with a consistent nonstoichiometry. Exploiting the O_2 chemical potential difference to enhance to overall driving force for CO_2 permeation seemed to be more attractive, which allowed uphill CO_2 permeation. Here, the study of CO_2 uphill permeation expanded from 600°C to higher temperatures. It has been focused on how LSCF6428 nonstoichiometry changes in line with the uphill operating conditions and the corresponding effect to the stability of uphill CO_2 permeation. The data would provide reference and support the validity of the flux-driving force relationship study in Chapter 6.

5.2. CO_2 downhill permeation with reduced state LSCF6428

Chapter 4.3.5 described a CO_2 downhill permeation experiment using LSCF6428-carbonate membrane without any pre-treatment. Considering the membrane support disk was sintered in the air at 1250°C followed by hot carbonate infiltration in the air at 600°C, this LSCF6428 support was expected to be in its oxidised form when the experiment started, indicating its oxygen nonstoichiometry δ was close to zero [132]. When the operating temperature was increased to 750°C and upwards (Figure 5.1), O_2 peaks above background O_2 level can be observed during heating up. The O_2 was likely from the loss of lattice oxygen in solid phase LSCF6428 rather than from the molten phase, since no O_2 release was observed during downhill CO_2 permeation experiment through alumina-carbonate membrane, which contained molten ternary carbonate of the same composition as the LSCF6428-carbonate membrane. The downhill permeating condition comprised 50% CO_2/N_2 on membrane feed side and pure Argon on permeate side. O_2 partial pressure within the reactor were expected to be on the level of 10 Pa (Figure 5.1). On this fixed pO_2, oxygen nonstoichiometry δ of LSCF6428 should rise with increasing temperature [78]. Theoretically, at the highest operating temperature (850°C) the membrane support would reach the most reduced state under this specific gas atmosphere. LSCF6428 could potentially be preserved in its reduced state due to the low pO_2 of the experimental condition. If this was the case, a pre-reduction treatment on LSCF6428 using inert gas and elevated temperature could modify its oxygen vacancy concentration and prevent the LSCF from re-oxidation while returning to lower temperature.

Therefore, it would be interesting to study the downhill CO_2 permeance through LSCF membrane in its reduced state. The LSCF6428 oxygen nonstoichiometry can be modified not only by elevating the temperature in inert gas, but also exposure under reducing atmosphere that has even lower pO_2 [78]. Here, the pre-treatment procedure was designed such that membrane disks were pre-reduced to different extent – one batch was pre-reduced under inert atmosphere whilst the other was performed under reducing atmosphere with CO, followed by hot carbonate infiltration in controlled atmosphere furnace. CO_2 downhill permeation experiment through pre-reduced LSCF6428 membranes can be carried out.

The CO_2 permeance at each temperature can be compared with the original membrane without pre-treatment. Moreover, oxygen release from the porous LSCF6428 disk during one of the pre-reductions performed under inert atmosphere was also monitored.

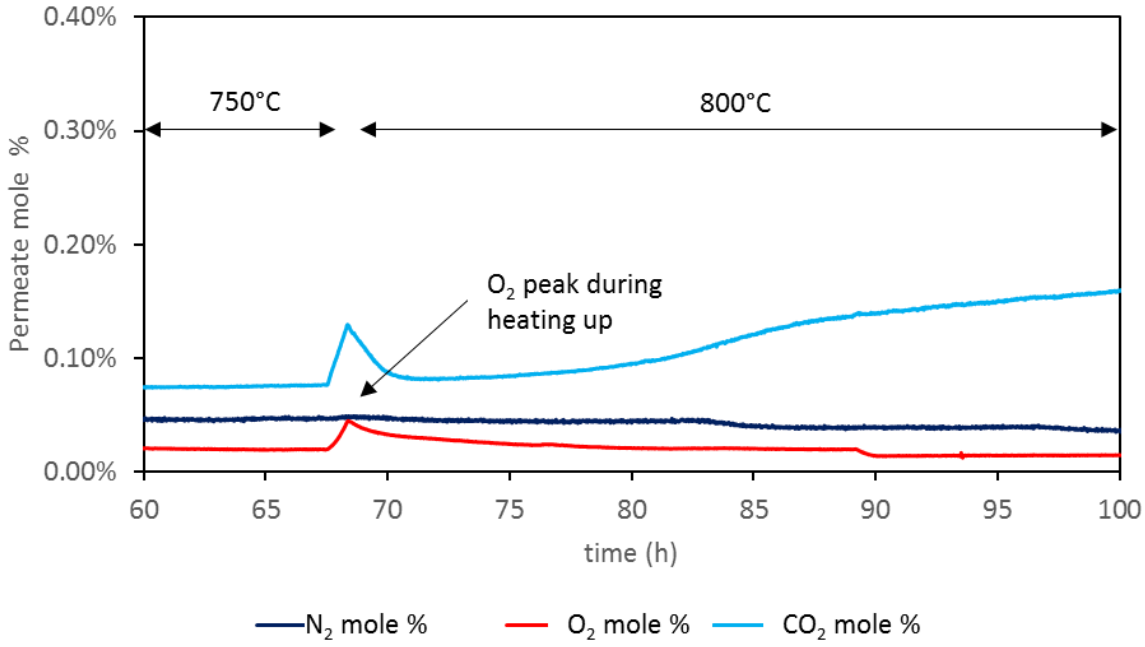

Figure 5.1: Appearance of oxygen peak while heating up from 750 to 800°C during the downhill CO_2 permeation experiment using LSCF6428-carbonate membrane, as described in Chapter 4.3.5. The gas conditions at the time was 50% CO_2 + 50% N_2 on feed side and pure Ar on permeate side.

5.2.1. Pre-reduction of LSCF6428 membrane supports

Two pellets with around 36% bulk porosity, LSCF6428_1 and LSCF6428_2 were pre-reduced in a controlled atmosphere furnace with a constant 100 ml (STP)/min flow of pure helium. This inert atmosphere was maintained throughout the pre-reduction process, and elevated temperature was adopted to increase the oxygen nonstoichiometry of the LSCF6428 pellets. The furnace temperature was increased up to 850°C at 1°C/min ramping rate, which is the highest operating temperature of the 50% CO_2 downhill experiment. After a dwelling time of 10 hours at 850°C, the furnace was cooled down to room temperature at 1°C/min. LSCF6428_1 was infiltrated under pure helium atmosphere in order to preserve the LSCF6428 nonstoichiometry. LSCF6428_2 was sent to XRD analysis.

On the other hand, another pellet LSCF6428_3 was pre-reduced in the controlled atmosphere furnace with a constant 100 ml/min flow of 2.5% CO, 2.5% CO_2 in Argon. The reduction was performed at 600°C with a dwelling time of 6 hours. At this temperature, it was a much more reducing atmosphere with a defined pO_2 of 10^{-20} Pa. The pO_2 within the system was controlled using the $CO/CO_2/O_2$ equilibrium at 600°C, the low pO_2 modified the LSCF6428 nonstoichiometry instead of elevated

temperature under inert gas. The details of the reduction for the above three pellets were summarised in Table 5.1.

Table 5.1: Pre-reduction conditions and weight changes of three porous (~36% porosity) LSCF pellets.

Pellet	Reduction time and temperature	Reduction pO_2	Weight before reduction	Weight after reduction
LSCF6428_1	850°C 10h	Undefined ~10 Pa	1.178g	1.17g
LSCF6428_2	850°C 10h	Undefined ~10 Pa	1.173g	1.167g
LSCF6428_3	600°C 6h	Defined $\sim10^{-20}$ Pa	-	Pellet fractured

Weight loss of roughly 0.008g was measured on digital balance for LSCF6428_1. This value was not considerably higher than the random error of the instrument. In order to find out the link of the weight loss with the increase of LSCF6428 oxygen nonstoichiometry, a fresh porous LSCF pellet was placed in the membrane reactor depicted in Figure 3.8 without sealing. Essentially, it became a single chamber reactor. A constant flow of 20 ml (STP)/min zero grade (99.999%) argon was continuously fed into the reactor chamber while the reactor was heated up to 600°C, dwelled for around 10 hours then heated up further to 800°C. A mass spectrometer was used to monitor the concentration of O_2 within the effluent stream out of the reactor.

Figure 5.2 shows the plot of effluent stream O_2 mole percentage against time in this pre-reduction experiment. An oxygen peak appeared when the temperature was approaching 600°C, followed by a gradual re-equilibrium as the temperature was on hold. Once the temperature started rising towards 800°C, a larger peak appeared within longer stabilisation time. As the porous LSCF6428 pellet was the only source of oxygen decomposition within the reactor chamber, this test confirmed that the LSCF6428 pellet had a more significant increase on oxygen nonstoichiometry at 800°C under inert atmosphere. The total weight loss of this pellet after the reduction was 0.0074g, equivalent to 2.31×10^{-4} mol gas phase O_2. The oxygen loss can also be estimated by integrating the peaks appeared on the plot, which gave a total 2.67×10^{-4} mol gas phase O_2 formation. This agreement also confirmed the link between the oxygen peak and the change of solid phase LSCF6428 oxygen nonstoichiometry. Nevertheless, the background pO_2 under inert atmosphere was undefined as it depended upon the gas tightness of both the reactor chamber and the inlet capillary line of the mass spectrometer. By assuming the mass spectrometer inlet line was gas tight, such that the mass spectrometer measured exactly the gas composition of the effluent stream out of the reactor chamber, the equilibrium pO_2 at 600 and 800°C were between 10 and 20 Pa.

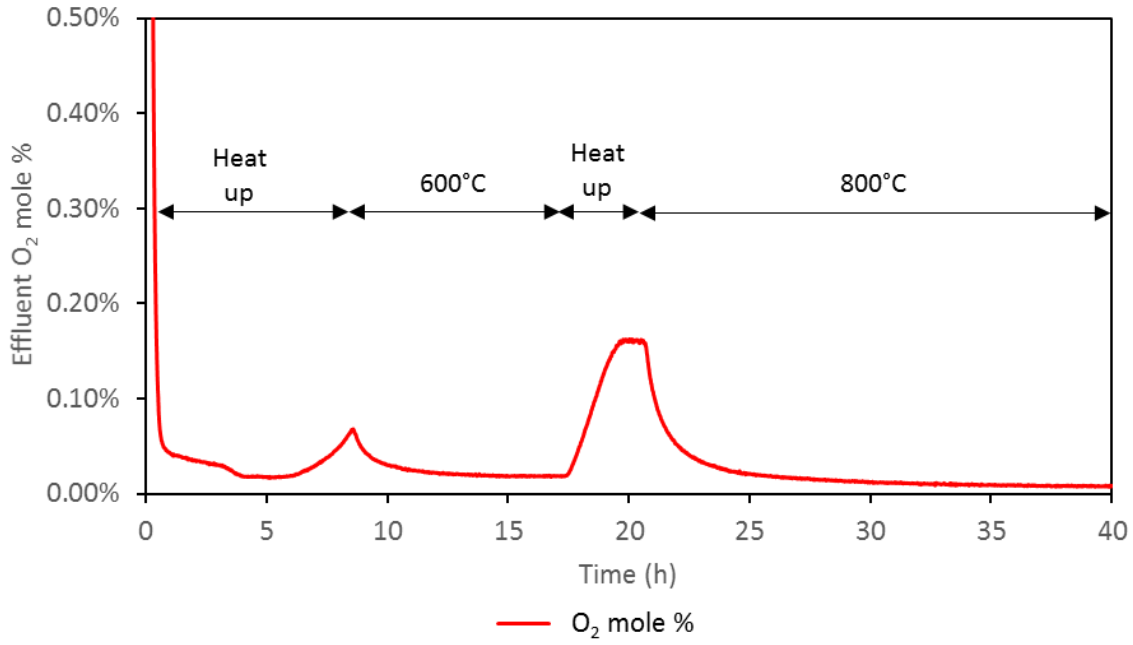

Figure 5.2: Monitoring the oxygen release during the pre-reduction of a porous LSCF6428 pellet without carbonate at 600°C and 800°C under inert atmosphere using mass spectrometer.

5.2.2. 50% CO_2 downhill permeation experiment

Once the connection between oxygen peak and the change of LSCF6428 oxygen nonstoichiometry was found, the next step forward would be looking at whether a relatively oxygen deficient LSCF6428 support exhibited different downhill CO_2 permeance comparing with the original non-reduced support. Here, the pre-reduced pellet under inert atmosphere (LSCF6428_1) was used as an example of oxygen deficient membrane. The sample reduced in 2.5% CO, 2.5% CO_2/Argon cannot be used for experiment, as it did not sustain an integrated disk shape after the exposure to the strongly reducing atmosphere. The 50% CO_2 downhill permeation experiment using LSCF6428_1 was carried out in the identical rig set-up as described in Figure 3.9. In order to start the experiment from 600°C followed by ascending operating temperature, oxygen nonstoichiometry of the pre-reduced membrane must be carefully preserved. However, a dropped oxygen background was observed when the temperature was risen to 300 or 400°C (Figure 5.3). This was possibly a sign of LSCF6428 uptaking oxygen from the background air even though background pO_2 here was similar to the pre-reduction condition (10-20 Pa). Therefore, the furnace temperature was heated up to 850°C under permeating condition, with 20 ml (STP)/min flow of 50% CO_2/N_2 on feed side and 20 ml (STP)/min flow of zero grade argon on permeate side, ensuring the support reached the desired level of oxygen deficiency again. Afterwards, the permeation experiment was carried out with descending temperature and steady state CO_2 mole fractions on membrane permeate side were measured on mass spectrometer down to 650°C with 50°C temperature intervals. There was no indication of O_2 uptake at any point of the experiment with descending temperature (Figure 5.4).

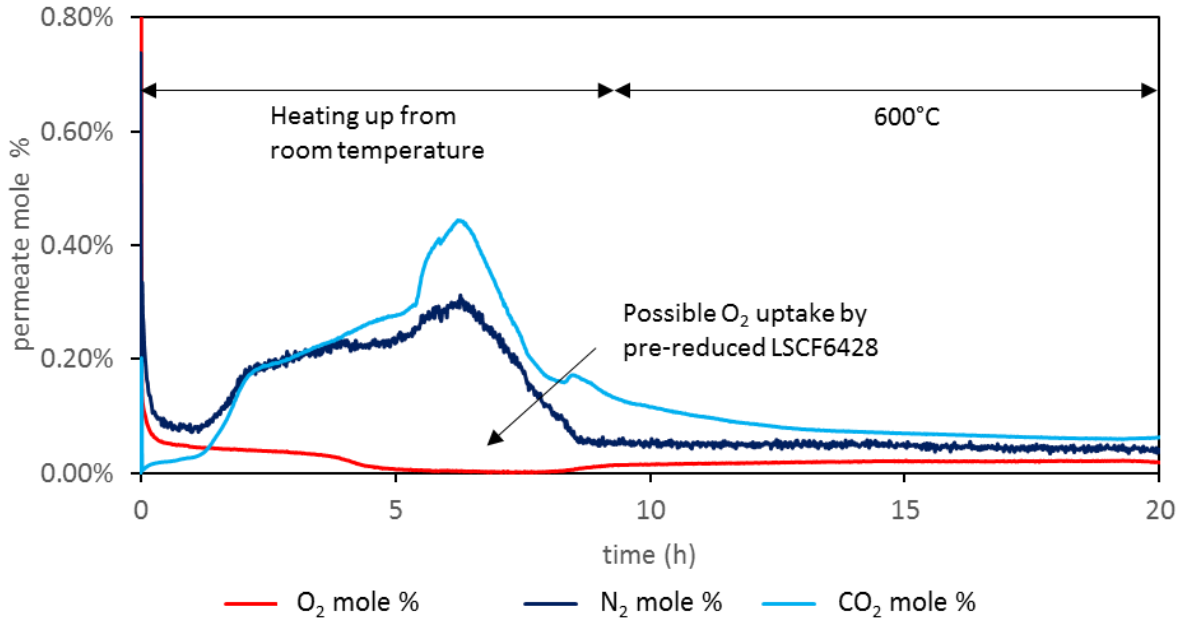

Figure 5.3: Permeate outlet gas composition for downhill CO_2 permeation experiment using LSCF6428-carbonate membrane pre-reduced under inert atmosphere. Throughout the experiment 50% CO_2/N_2 and Ar were used as feeding gas and sweep gas respectively. The figure presents the initial heating up from room temperature to 600°C, during which a dip of O_2 concentration below background level was observed.

The continuous on-line measurement of permeate side CO_2 concentration against time was shown in Figure 5.4. The membrane was initially maintained under permeating condition for more than 10 hours at 850°C. Steady state CO_2 concentration was taken for calculating the CO_2 permeance. At this highest operating temperature, the CO_2 mole fraction reached 0.39% on membrane permeate side giving a permeance 2.3×10^{-8} $mol \cdot m^{-2}s^{-1}Pa^{-1}$. Meanwhile an 80 ppm N_2 concentration was measured on mass spectrometer, consisting of background air leak as well as N_2 permeation through the membrane. Only N_2 permeance through the membrane should be accounted for CO_2/N_2 selectivity whilst it was difficult to measure the true N_2 permeance with current gas analysers. Nevertheless, it can be said the CO_2 selectivity was at least 49 since the N_2 permeation gave a permeate side N_2 concentration of no more than 80 ppm. Steady state CO_2 permeation can be observed once a new operating temperature was reached. The O_2 background during this experiment was also stabilised at 150 ppm, indicating there was negligible oxygen exchange between the background air and the LSCF6428. Hence, the LSCF6428 was indeed preserved at its reduced state. More importantly, the CO_2 permeance through the reduced state LSCF6428-carbonate membrane at lower temperature has been remarkably improved comparing with the non-reduced membrane (Figure 5.5). Although the nitrogen background increased slightly at 750°C and lower, it was unlikely to be a leak as CO_2 concentration was not affected. Therefore, it cannot invalidate the observation that the pre-reduced membrane was able to separate CO_2 with more than doubled permeance comparing with untreated membrane, particularly at lower temperatures.

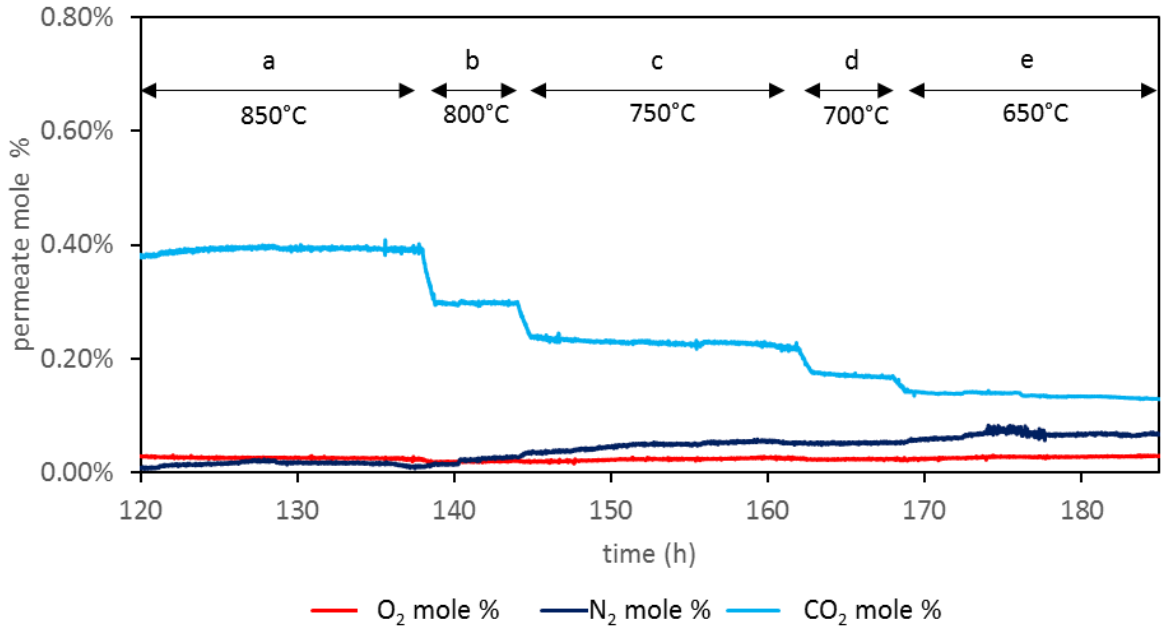

Figure 5.4: Permeate outlet gas composition for downhill CO_2 permeation experiment using LSCF6428-carbonate membrane pre-reduced under inert atmosphere. Throughout the experiment 50% CO_2/N_2 and Ar were used as feeding gas and sweep gas respectively. The figure consists of five regions: (a) CO_2 permeation starting with the highest operating temperature at 850°C; (b) CO_2 permeation at 800°C; (c) CO_2 permeation at 750°C; (d) CO_2 permeation at 700°C; (e) CO_2 permeation at 650°C.

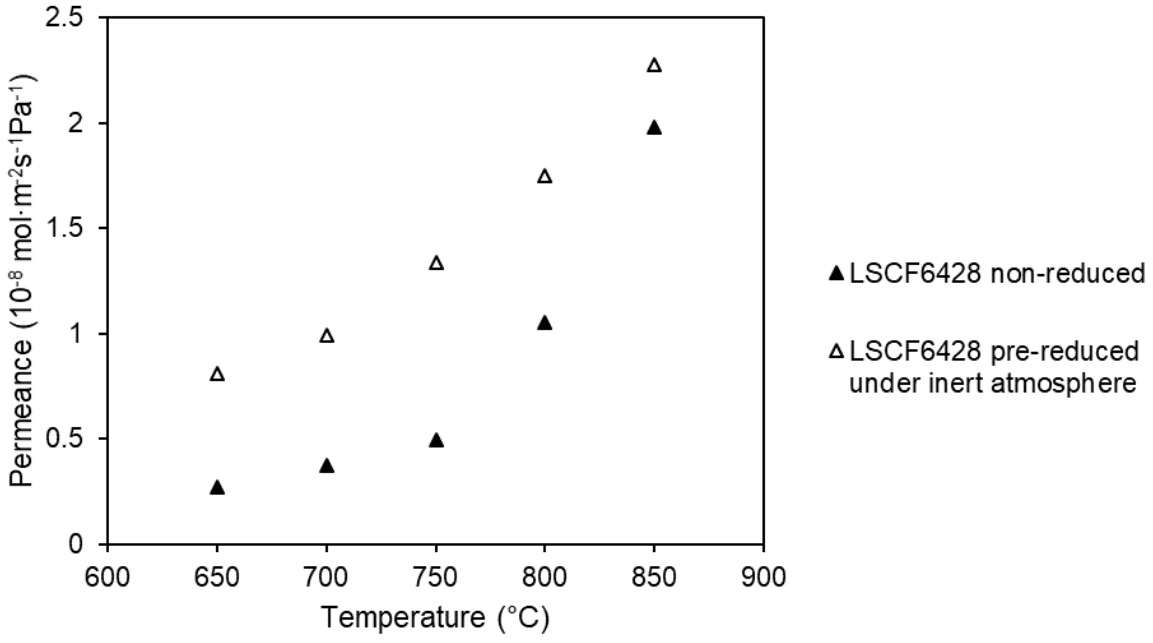

Figure 5.5: The comparison of CO_2 downhill permeance using LSCF6428-carbonate membranes in their reduced and non-reduced state. Identical permeating condition with 50%CO_2+50%N_2 on feed side and pure argon on permeate side was used. Permeance were compared over the temperature window of 650 to 850°C.

Arguably, the enhancement of CO_2 downhill permeance was attributed to the increased oxygen nonstoichiometry created by the LSCF6428 reduction. The permeance enhancement by this way was found to be reproducible. The ultimate effect of the increasing oxygen nonstoichiometry within LSCF6428 crystalline may well be an increase of its O^{2-} conductivity. It has been reported in Chapter 4.3.5 that downhill CO_2 permeation through the non-reduced LSCF6428 membrane was very likely bulk oxide ion diffusion controlled. Thus, enhancing solid phase O^{2-} conductivity would be crucial to the downhill CO_2 permeance. Arrhenius plot for the pre-reduced membrane (see Figure 5.6) was generated based on the permeation data in figure 5.5. The apparent activation energy of CO_2 permeation was 44.9 kJ/mol with a standard error of ± 2.7 kJ/mol. This was a significant deviation from 125.4 kJ/mol, which is the activation energy of oxide ion conduction (measured in the air) for LSCF6428 composition [126]. The drop on the apparent activation energy indicated the CO_2 permeation through a reduced LSCF6428-carbonate membrane may no longer limited by bulk solid phase O^{2-} diffusion. This was consistent with the assumption that the reduced LSCF6428 held higher O^{2-} conductivity. The rate-determining step was probably shifting towards a process with lower activation energy.

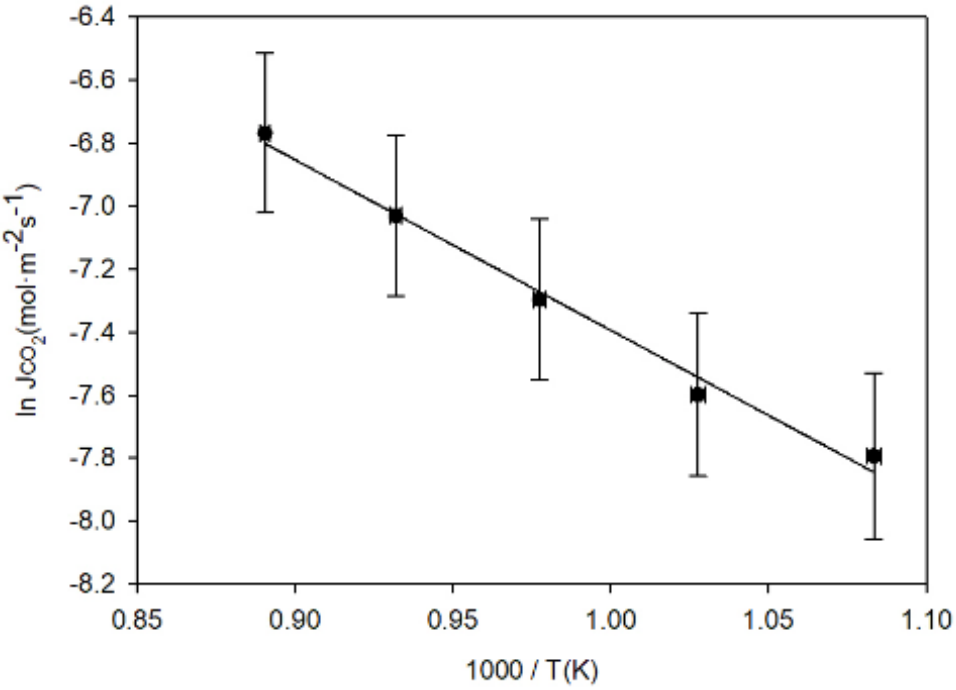

Figure 5.6: Arrhenius plot showing logarithm of CO_2 permeation flux against 1000/T for downhill CO_2 permeation through pre-reduced LSCF6428-carbonate membrane. The large error bars on vertical axis still originated from the large uncertainty of the effective permeation area.

In a way, the result of the pre-reduced LSCF6428-carbonate membrane was promising in terms of practical application in pre-combustion CO_2 separation. The operating condition of such a process is in reducing atmosphere below 550°C. Undoubtedly, enhancement of CO_2 permeation around this temperature would be desirable. Nevertheless, the mechanical strength of the membrane disk under

reducing atmosphere were crucial. It was unclear how reducing atmosphere changed the lattice structure of the LSCF6428 that gave rise to fractured disks. Moreover, extra evidence was required to explain how the change in LSCF6428 oxygen nonstoichiometry related to oxide ion conductivity. In Chapter 5.2.3, an attempt has been made to seek further explanations from the XRD analysis of the reduced LSCF6428 pellets.

5.2.3. XRD analysis of the pre-reduced LSCF6428 membrane supports

XRD analysis was chosen to determine any change within the LSCF6428 lattice upon the exposure to inert and reducing atmosphere. Two previously mentioned porous pellet of LSCF6428 in their reduced state, LSCF6428_2 and LSCF6428_3, along with a non-reduced porous LSCF6428 pellet underwent XRD analysis on their top surface. Using a Cu-Kα X-ray source, the diffracted beam intensity was collected continuously from diffraction angle (2θ) of 15° to 90°, with a step size of 0.0167°.

Firstly, the XRD pattern of the non-reduced porous LSCF6428 pellet was compared with the powder pattern of $La_{0.6}Sr_{0.4}Co_{0.2}Fe_{0.8}O_{2.99}$ (oxidised form) on Inorganic Crystal Structure Database (ICSD) (Figure 5.7). Despite the small differences in peak position at lower diffraction angle, the XRD pattern of the non-reduced LSCF6428 pellet overlapped well with the database. The peak splitting of the non-reduced sample could be due to the copper source emitting X-ray with two close wavelengths ($K\alpha_1$=0.1541 nm, $K\alpha_2$=0.1544 nm). According to the Bragg's law described in equation 3.1, the two close wavelengths from the emission source would generate peak splitting patterns.

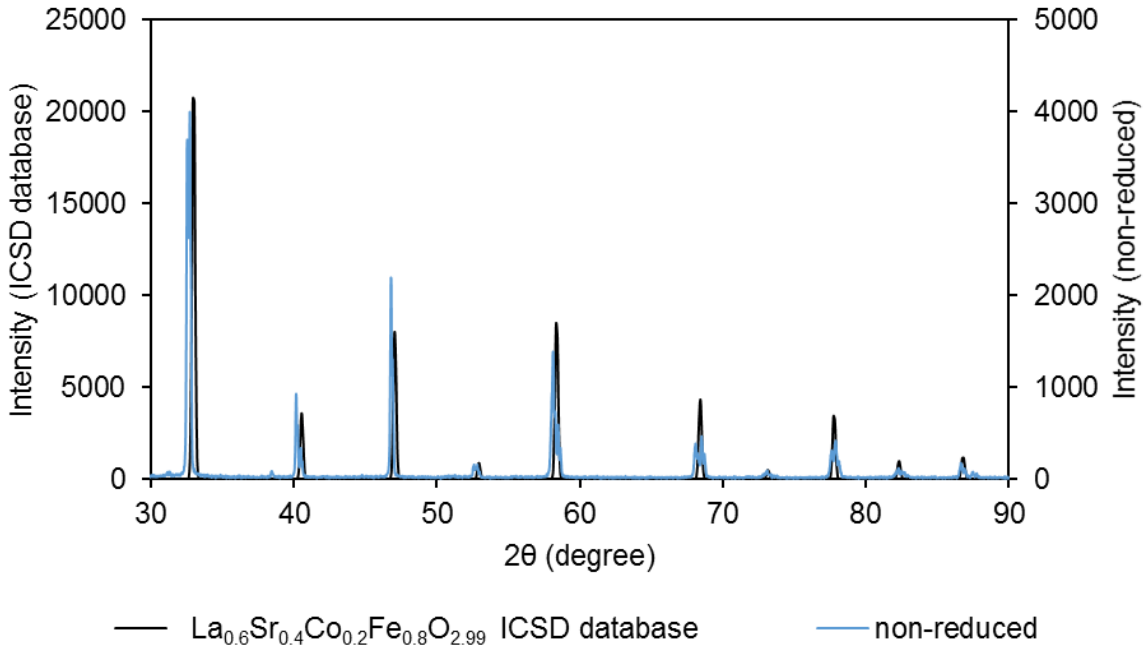

Figure 5.7: The overlapping plot for the XRD pattern of the non-reduced porous LSCF6428 pellet and the powder pattern of $La_{0.6}Sr_{0.4}Co_{0.2}Fe_{0.8}O_{2.99}$ on Inorganic Crystal Structure Database (ICSD). T. Itoh and M. Nakayama obtained the latter in-situ XRD data at 627°C under atmospheric pressure [133].

The XRD pattern of non-reduced LSCF6428 sample was compared with reduced samples under inert and CO atmosphere. Figure 5.8 revealed that more reducing sample tended to have peaks shift towards smaller diffraction angle. According to Bragg's law, smaller diffraction angle was a result of larger interplanar spacing (d) of the lattice, which further indicated lattice expansion of the crystalline phase. Other than this, no extra peak appeared, and no peak disappeared comparing with the original non-reduced LSCF6428. This was to say that the perovskite crystalline phase of the most reduced sample here would not degrade into individual metal oxide phases.

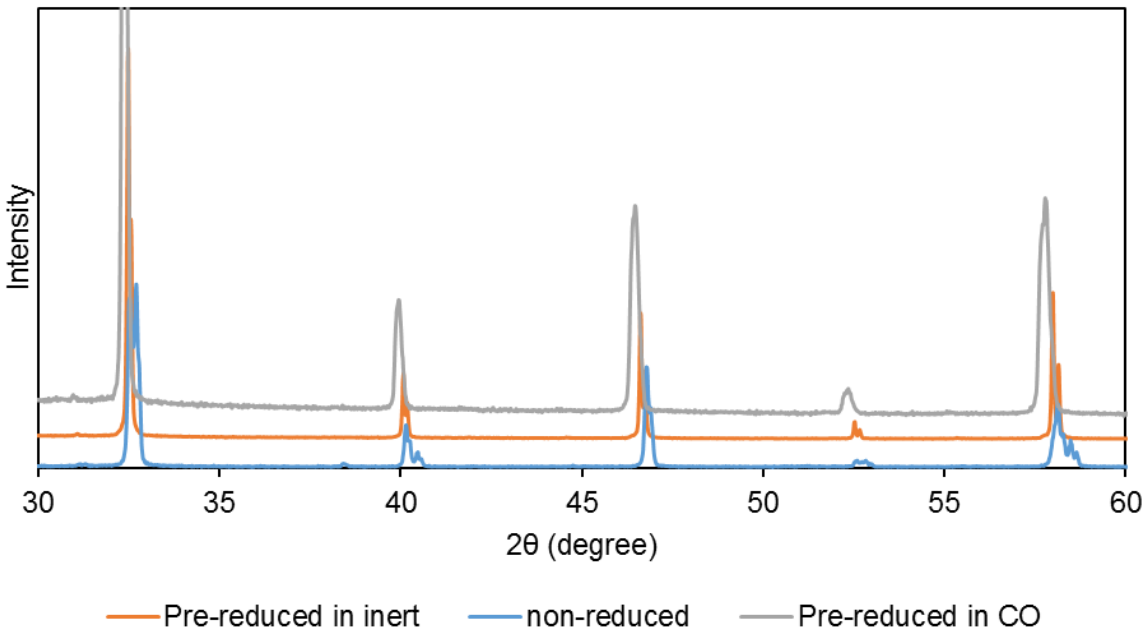

Figure 5.8: XRD patterns of the non-reduced porous LSCF6428 pellet, the porous LSCF6428 pellet reduced under inert atmosphere and porous LSCF6428 pellet reduced under 2.5% CO + 2.5% CO_2 atmosphere. Shift of peak positioning can be demonstrated on this diagram.

However, another significant feature of the XRD pattern of the most reduced sample was peak broadening. Specimen related peak broadening generally originates from two factors: the size of the crystallite and 'non-uniform' strain within the lattice. Scherrer equation correlates the mean crystallite size with peak shape and peak position of the XRD pattern (equation 5.1).

$$L_c = \frac{K_S \lambda}{\beta \cos \theta} \qquad (5.1)$$

In this equation, L_C is the mean crystallite size in Å or nm. λ is the wavelength of the X-ray in Å or nm. θ is the half of the Bragg diffraction angle 2θ. β is the difference between the observed peak full width half maxima (FWHM) in radian and the standard FWHM of the peak generated by Si (111) plane. K_S is a shape factor that has a typical value of 0.9 assuming the crystallite was spherical. Nanocrystalline materials tend to have more broadening peaks. Thus, it was possible that the crystallite size of the most

reduced sample became smaller. Besides, the peak broadening was also likely caused by lattice strain attributed to the highly reducing atmosphere the sample was exposed to. The pellet with 'non-uniform' lattice strain together with lattice expansion is prone to microcrack formation, reducing the mechanical strength of the membrane under high temperature.

It has been understood that isothermally the oxygen nonstoichiometry δ in LSCF system increases with decreasing pO_2. Figure 5.9 (a) shows the 3-δ against log pO_2 plot for LSCF6428 by J. Mizusaki et al. The oxygen partial pressure spanned from oxidising atmosphere (100% pure O_2) to mildly reducing inert atmosphere (approximately 100 ppm O_2). With the same δ values, they further studied the detailed correlation between δ and the variation of LSCF6428 crystal lattice parameters using in-situ XRD. The plot is shown on Figure 5.9 (b). Here, rhombohedral LSCF6428 lattice parameters were converted to pseudo-cubic lattice parameter a_{pc}. Isothermal lattice expansion that was purely chemical induced can be observed, and the lattice size increased linearly with increasing δ or decreasing pO_2. Higher temperature indeed has been another factor for lattice expansion. They further suggested that this chemically induced expansion was caused by reduction of B-site transition metal cations [132, 134]. Lower valence of B-site cations lead to larger cation radii when the lattice became more oxygen deficient [135].

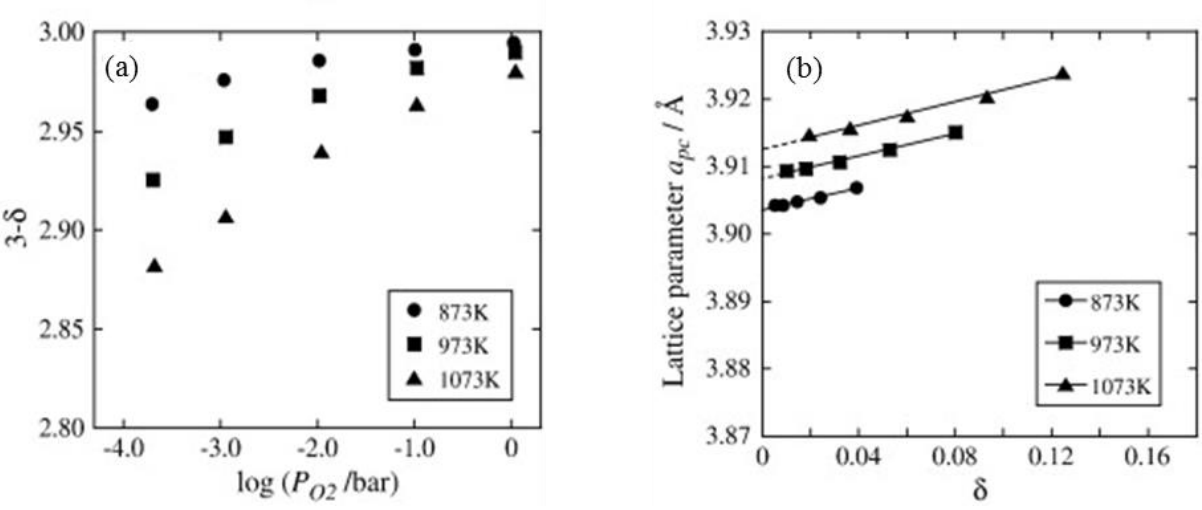

Figure 5.9: (a) Oxygen content, 3−δ, as a function of pO_2 for $La_{0.6}Sr_{0.4}Co_{0.2}Fe_{0.8}O_{3-\delta}$. (b) Pseudo-cubic lattice parameter, a_{pc}, as a function of δ, for $La_{0.6}Sr_{0.4}Co_{0.2}Fe_{0.8}O_{3-\delta}$ [132, 134]. Reproduced with permission of Elsevier.

Using the in-situ X-ray absorption spectroscopy technology, T. Itoh and M. Nakayama further recorded the drop of oxygen content and Co/Fe cations valence in LSCF6428 as a response to changing pO_2 from 10^5 to 10 Pa. Oxygen content and Co/Fe cations valence exhibited relaxation behaviour over time at both 900 and 1000K. According to the trends of the relaxation, they deduced that the oxygen ion chemical diffusion coefficient in LSCF6428 at more reduced state was higher. Furthermore, when the pO_2 changed from 10^5 to 10 Pa, the number of oxygen vacancy created per unit cell at 1000K was

roughly twice as much as 900K, whilst the lattice volume expansion from 900 to 1000K was only 0.3581 nm^3 to 0.3595 nm^3 [133], indicating an increase of oxygen vacancy concentration with increasing oxygen deficiency. Therefore, the increased CO_2 permeance of LSCF6428-carbonate membrane upon solid phase reduction can be explained as a result of higher oxide ion conductivity in bulk LSCF6428 phase.

From the operational point of view, the enhancement on oxide ion conductivity under reducing atmosphere certainly needs to compromise with the mechanical strength of the membrane. The literature has suggested that the LSCF6428 system is prone to decomposition and loss of perovskite phase when $pO_2<10^{-15}$ Pa at 600°C [132]. Hence, controlling oxygen partial pressure is important for the operability of LSCF6428-carbonate membrane applied into pre-combustion CO_2 separation.

5.3. CO_2-O_2 co-permeation with oxidised state LSCF6428

5.3.1. Brief introduction and experimental procedure

Unlike pre-combustion CO_2 separation, when LSCF6428-carbonate membrane is applied to flue gas CO_2 capture with O_2 co-permeation, the oxygen nonstoichiometry is presumed to exhibit much weaker variation with rising operating temperature due to the oxidising atmosphere. The 1% CO_2 and 20% O_2 composition has been used consistently as feeding gas for demonstrating the concept of co-permeation. The composition had a log pO_2 of roughly -0.7, giving a change of δ value of less than 0.04 from 600-800°C (see Figure 5.9a) on membrane feed side surface. Zero grade Ar cylinder has been used for sweep gas in which the O_2 content is below 10 ppm. The variation of δ value with rising operating temperature on membrane permeate side surface was unclear as O_2 permeation would affect the permeate side pO_2. In order to estimate the δ value on membrane permeate side surface, further experiment was required to determine the steady state O_2 partial pressure upon membrane permeate side between 600 to 850°C during the CO_2-O_2 co-permeation.

Nevertheless, the variation of solid phase oxygen nonstoichiometry may not influence CO_2 flux significantly in this case, since Chapter 4 ended with an argument that the CO_2 permeation flux with O_2 co-permeation was likely controlled by interfacial reaction or CO_3^{2-} ion diffusion through the melt. An Arrhenius plot of CO_2 permeation flux in presence of O_2 against operating temperature may be useful for looking closely into the mechanism of CO_2-O_2 co-permeation. This may offer an insight on how the LSCF6428 oxygen nonstoichiometry interferes the CO_2-O_2 co-permeation.

In this subchapter, downhill CO_2-O_2 co-permeation experiment through LSCF6428-carbonate membrane from 600°C to 850°C was performed with 50°C temperature increments. The ramping and cooling rates were controlled at 1°C/min as usual. LSCF6428-carbonate membrane with 42% bulk porosity and 0.256g carbonate loading (97% of theoretical maximum loading) were sealed using silver

paste. Gas cylinder with 1.04% N_2, 19.97% O_2 and 0.95% CO_2 in Ar composition (BOC, certified mixture) was used as feed inlet gas and zero grade Ar (BOC) was used as sweep gas, with flow rate of 20ml (STP)/min into both reaction chambers using similar flow system described in Chapter 3.4.2. The above compositions and flow rates were maintained throughout this experiment. Gas composition of permeate side outlet stream was analysed by mass spectrometer in series with a CO_2 IR analyser. The aim of this experiment was to perform a complementary study to Chapter 4.4 and obtain CO_2 flux over an expansive range of operating temperatures for the Arrhenius plot. On the other hand, O_2 flux over the same temperance range was also measured, which helped determine the LSCF oxygen nonstoichiometry upon membrane permeate side surface.

5.3.2. Results and discussion

The IR analyser was the primary choice for CO_2 concentration measurement in this experiment, offering improved signal resolution without drift. N_2 and O_2 compositions were analysed using on-line mass spectrometer. Looking at the broad picture, both CO_2 and O_2 permeation flux increased with ascending operating temperatures (Figure 5.10). The concentration ratio of CO_2 and O_2 on permeate side were maintained at roughly 2:1 up to 750°C, but became smaller at higher temperatures and eventually dropped to 1.2:1 at 850°C. Meanwhile, apparent CO_2 permeance of 1.27×10^{-6} $mol\cdot m^{-2}s^{-1}Pa^{-1}$ was achieved at 850°C (Figure 5.11), thanks to the large O_2 driving force that promoted CO_2 flux under such a limited driving force of CO_2 itself. Although the retentate CO_2 concentration was not analysed, it would drop to approximately 0.7% according to CO_2 mass balance on both sides of the membrane, making a narrow margin of CO_2 chemical potential difference across the membrane. The figure also showed a drop of N_2 background with ascending temperature. This was not accompanied with drop of CO_2 concentration, indicating the high N_2 concertation at 600°C was unlikely a leak. A drift of mass spectrometer signal could be a possible explanation.

High apparent CO_2 permeance was the most important feature of the downhill CO_2-O_2 co-permeation experiment. Comparing with the downhill 50% CO_2/N_2 permeation, the co-permeation obtained similar CO_2 permeation flux at relevant temperatures. At the same time, the apparent CO_2 driving force of its own was between 500 to 900 Pa (0.5% to 0.9% in terms of CO_2 mole fraction difference). The calculation of apparent CO_2 permeance in Figure 5.11 was made by considering its apparent driving force only and assuming the driving force from O_2 was hidden. In this way, apparent CO_2 permeance via co-permeation was generally two orders of magnitude higher. Precisely, for CO_2-O_2 co-permeation, the CO_2 flux cannot be simply expressed by the product of CO_2 permeance and CO_2 partial pressure difference. The driving force from O_2 must be account for, which required studying the flux-driving force models and correlations to determine the contribution of O_2 driving force. This will be shown in Chapter 6 of the thesis.

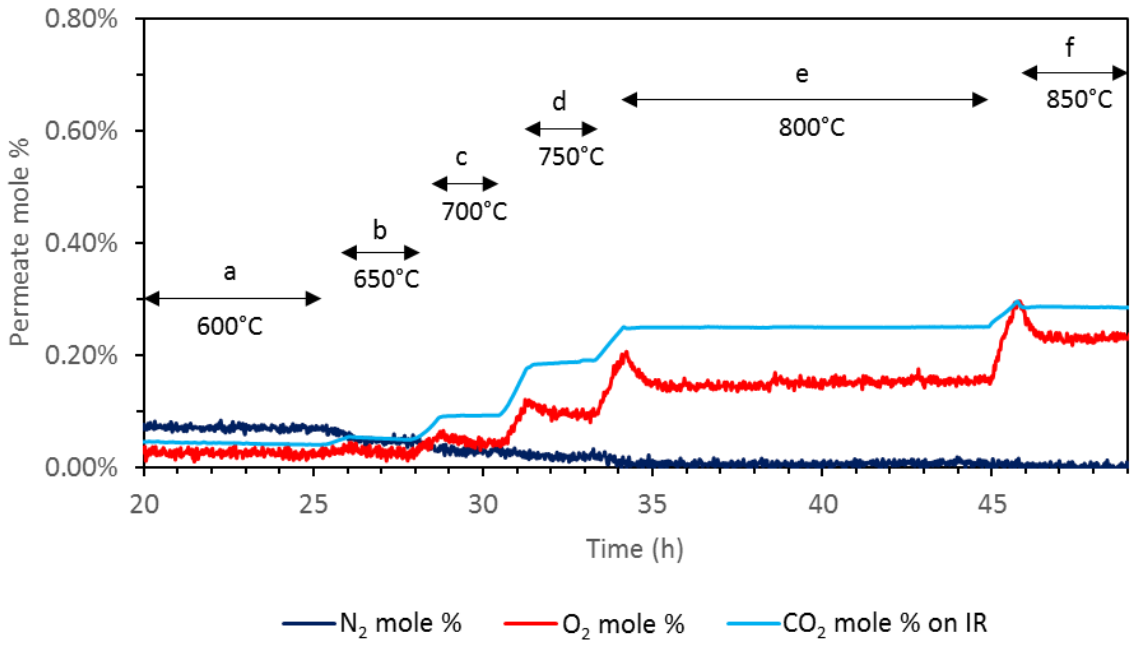

Figure 5.10: Permeate outlet gas concentrations at various operating temperatures during the downhill CO_2-O_2 co-permeation experiment. The plot consists of 6 regions: (a) operating temperature at 600°C; (b) operating temperature at 650°C; (c) operating temperature at 700°C; (d) operating temperature at 750°C; (e) operating temperature at 800°C; (f) operating temperature at 850°C.

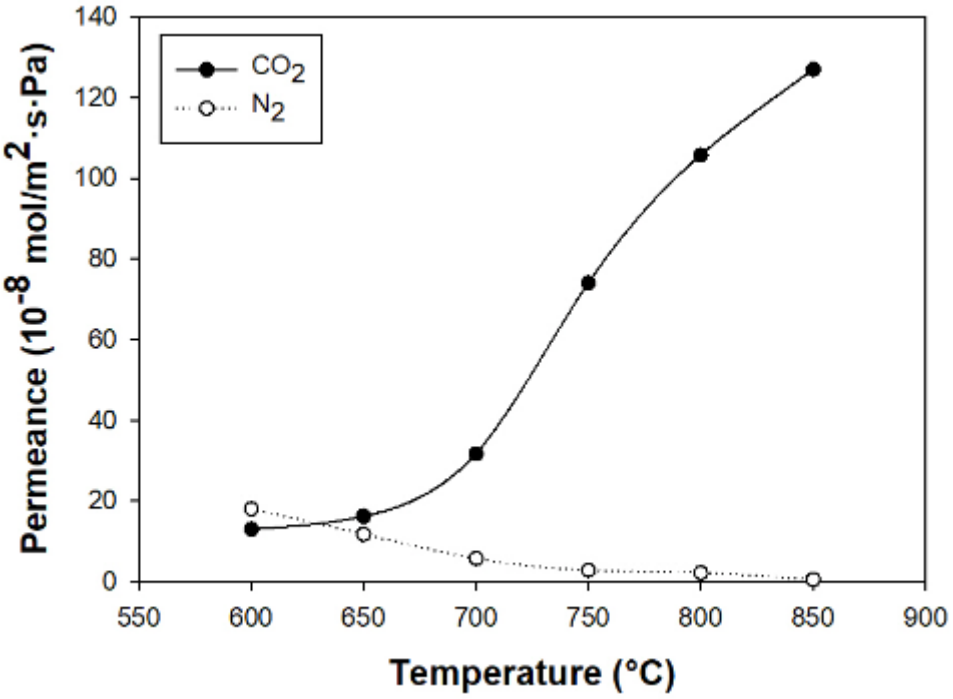

Figure 5.11: The variation of CO_2 and N_2 permeance against operating temperatures for the downhill CO_2-O_2 co-permeation experiment. N_2 permeance here comprised the N_2 background in reactor chamber and drift of mass spectrometer signal, making the CO_2/N_2 selectivity difficult to estimate.

The variation of permeation side CO_2/O_2 concentration ratio during this experiment was also noteworthy. If the proposed co-permeation mechanism were predominant, permeate side CO_2/O_2 concentration ratio would be close to 2:1. The experiment revealed that this was the case up to 750°C. Major individual permeation mechanisms, including electrochemical transport of CO_2 via the melt and O_2 transport via solid phase LSCF6428, both relied on the solid phase O^{2-} conductivity. Since O^{2-} conductivity within oxidised state LSCF6428 was relatively low between 600-750°C, individual CO_2 or O_2 flux seemed to be incomparable with their co-permeation flux. At higher temperatures, individual O_2 flux became significant due to higher O^{2-} conductivity as well as the high O_2 partial pressure difference. In contrast, individual CO_2 flux may not vastly affect the overall observed CO_2 flux, as the CO_2 concentration in feeding gas was only 1% (see Table 4.3 for 1% CO_2 downhill experiment in absence of O_2). This also explained the decreasing permeate side CO_2/O_2 ratio from 2:1 as the temperature increased. On the other hand, the O_2 incorporation mechanism [90, 91] mentioned before would still hold for this experiment. It could be more prevalent above 750°C, resulting a significantly lower CO_2/O_2 ratio.

Figure 5.11 also suggested that the CO_2 permeance did not increase exponentially with temperature. This trend was reflected as a change of the gradient at 750-800°C on the Arrhenius plot in Figure 5.12, featuring natural logarithm of CO_2 flux against 1000/T for downhill CO_2-O_2 co-permeation. In other word, as the operating temperature went higher, the temperature effect for CO_2 flux seemed to be weakening. The apparent activation energy changed from 91.8 kJ/mol at 600-700°C to 39.1 kJ/mol at 750-850°C, which was not a strong indication of a bulk oxide ion diffusion limiting process. Thus, the LSCF oxygen nonstoichiometry was unlikely posing a strong influence on the overall CO_2 flux here. However, it indeed suggested that downhill CO_2-O_2 co-permeation was not consistently rate limited by a single activated process over 600 to 850°C. This complexity cannot be analysed using the Arrhenius plot. Instead, flux-driving force models and correlations in Chapter 6 may provide further discussion from the mechanistic point of view.

Lastly, the observation of O_2 concentration on permeate outlet stream allowed estimation of the LSCF6428 oxygen nonstoichiometry upon membrane permeate side surface. In an oxygen containing system, it is still possible for LSCF6428 to become oxygen deficient (i.e. $\delta > 0$). The membrane permeate side was exposed to pO_2 of 21 to 230 Pa from 600 to 800°C. With ascending temperature, membrane support may still become locally oxygen deficient upon permeate side surface (see Table 5.2). The intensifying oxygen peaks upon rising temperatures before the stabilisation of O_2 permeation was an evidence (Figure 5.10). Although the membrane feed side was always in an oxidising atmosphere with an almost fixed pO_2 of 2×10^4 Pa, the feed side surface cannot maintain fully oxidised especially at high temperature. As a result, the solid phase LSCF6428 may exhibit non-uniform oxygen nonstoichiometry during the co-permeation experiment, assuming the diffusion of oxygen vacancy was slow. Nevertheless, the LSCF6428 phase under the presence of O_2 tended to be much more oxidised

than the inert atmosphere described earlier in Chapter 5.2. A δ value of 0.03-0.09 was unlikely posing a significant effect on an interfacial reaction or CO_3^{2-} diffusion limited CO_2-O_2 co-permeation process.

Table 5.2: Equilibrium pO_2 with membrane feed and permeate side solid phase surface at corresponding temperature. LSCF6428 oxygen nonstoichiometry δ on feed and permeate side were obtained by interpolating given temperature and pO_2 into relevant δ versus pO_2 or δ versus temperature plots in literature.

Operating Temperature	Permeate side equilibrium pO_2 (Pa)	Permeate side oxygen nonstoichiometry δ [78]	Feed side equilibrium pO_2 (Pa)	Feed side oxygen nonstoichiometry δ [132]
600°C	21	~0.02	2×10^4	~0.01
700°C	41	~0.04	2×10^4	~0.015
800°C	150	~0.07	2×10^4	~0.03
850°C	230	~0.09	2×10^4	-

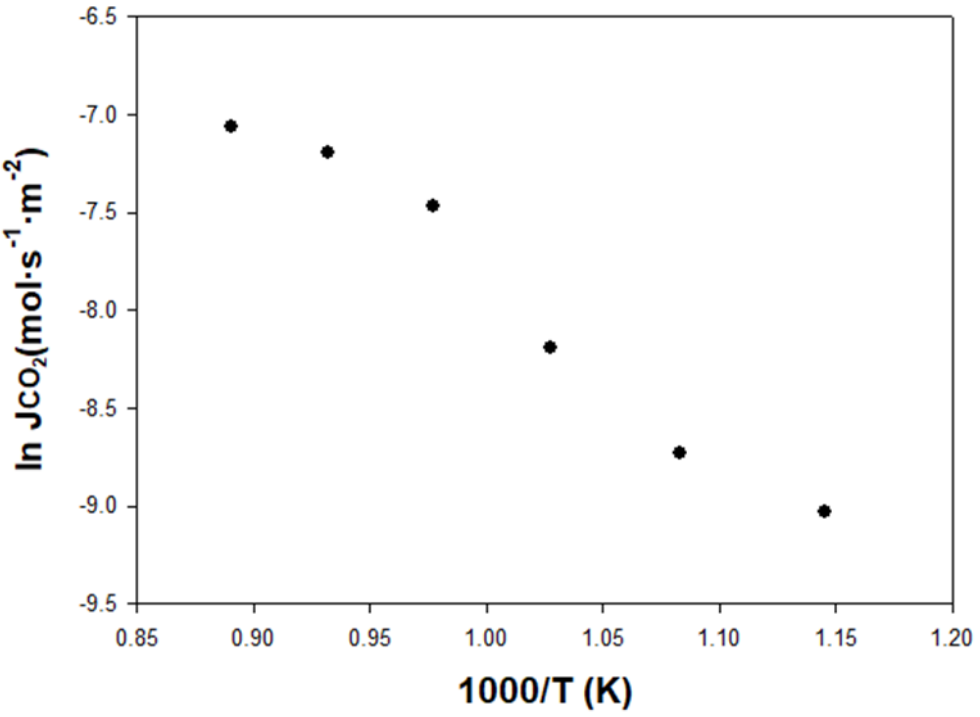

Figure 5.12: Arrhenius plot showing logarithm of CO_2 permeation flux against 1000/T for downhill CO_2-O_2 co-permeation through LSCF6428-carbonate membrane.

In short, this experiment successfully demonstrated that with the aid of O_2 co-permeation, LSCF6428-carbonate membrane was able to permeate CO_2 under low apparent CO_2 partial pressure difference of 500 to 900 Pa over the temperature range of 600 to 850°C. Comparing the effect of LSCF reduction and O_2 incorporation on the CO_2 permeance, the idea of CO_2-O_2 co-permeation vastly promoted the

apparent CO_2 permeance by almost two orders of magnitude on the same membrane design. On the other hand, improvement on bulk ionic diffusion by LSCF reduction seemed to limit the CO_2 permeance enhancement within the same order of magnitude, hence unlikely to maintain the CO_2 permeation flux under low CO_2 driving force. Having learnt that the thermodynamic driving force from the oxygen helped CO_2 molecules permeate across such a narrow margin of its own chemical potential difference (roughly 0.7% to 0.3%), it is worth exploiting this driving force further to bring CO_2 up to a more concentrated level, so that CO_2 can permeate against its own chemical potential difference. This 'uphill' operation mode could be an important step forwards to reduce the energy requirement for CO_2 capture. From Chapter 5.4, the thesis will start focusing on uphill permeation in presence of O_2 using LSCF6428-carbonate membranes.

5.4. Uphill CO_2 permeation in presence of O_2

5.4.1. Introduction and experimental set-up

Uphill CO_2 permeation specifically targets on post-combustion CO_2 capture. By using the concept of CO_2-O_2 co-permeation, CO_2 can permeate against its own chemical potential difference across the membrane. This does not violate the thermodynamic law, providing the O_2 chemical potential difference is sufficient (see equation 1.4). In practice, flue gas streams are at approximately 10^5 Pa with less than 10% CO_2 mole percentage. This driving force limitation imposed challenges on membrane based CO_2 capture system to produce downstream gas containing concentrated CO_2. Enormous energy input for compressing the feed stream or vacuuming the permeate stream is often inevitable. The importance of the uphill permeation process is that it could potentially overcome the CO_2 driving force deficiency, and partially implement the requirement of concentrating CO_2 without the energy input from gas compressor and vacuum pump.

The operating procedure of an uphill experiment is fundamentally different with a downhill experiment despite of the same membrane reactor design. In order to carry out the uphill CO_2 permeation experiment, the flow system into the high temperature membrane reactor was redesigned as shown in Figure 5.13. The experiment began with a non-permeating condition (i.e. symmetrical operation) by flowing 1.1% CO_2 in Ar into both feed (F) and permeate (P) chamber via mass flow controller 1 and 6 respectively. Once the desired operating temperature was reached, the feed side inlet gas was switched to O_2 containing stream with 0.95% CO_2, 1.04% N_2, 19.97% O_2 in Ar composition (delivered from mass flow controller 2) while keeping the gas composition of permeate chamber (i.e. permeating condition or asymmetrical operation). The gas switch between two compositions was achieved by incorporating four-way valves into the flow system. By alternating between symmetrical and asymmetrical operation, uphill permeation can be confirmed if the permeate side steady state CO_2 mole percentage under asymmetrical operation is elevated above the reference CO_2 level during non-permeating condition.

Previous 1% CO_2 and 20% O_2 composition has been consistently used for demonstrating uphill permeation in presence of O_2. This composition was easier to obtain measurable flux in order to understand the membrane performance with this specific membrane reactor design. A CO_2 IR analyser (*LI-COR LI-840A*) and a mass spectrometer (*Hiden QGA*) were used for the permeate outlet gas analysis. Meanwhile, another similar mass spectrometer (*Hiden QIC*) was used for retentate stream gas analysis. It was essential to analysis gas compositions on both sides of the membrane. Corresponding variation of retentate CO_2 concentration with permeate side based on mass balance can confirm that continuous uphill permeation is indeed occurring.

Uphill permeation using LSCF6428-carbonate membrane at 600°C have been demonstrated experimentally [28]. However, the temperature dependence of CO_2 uphill permeation was yet unknown and there was a lack of mechanistic insight. Chapter 5.4 expanded the study up to 800°C and intended to analyse the behaviour of uphill permeation from a mechanistic viewpoint. Furthermore, it was expected that LSCF6428 membrane was under the exposure of different pO_2 atmosphere due to the alternation of symmetrical (CO_2/Ar mix)/asymmetrical (CO_2/O_2/Ar mix) operation modes. Therefore, LSCF6428 nonstoichiometry could be fluctuating periodically with the operation modes. Chapter 5.4 also investigated how this fluctuation influenced the stability of uphill permeation, particularly at higher temperature (i.e. 800°C) where the LSCF6428 nonstoichiometry was more sensitive to pO_2.

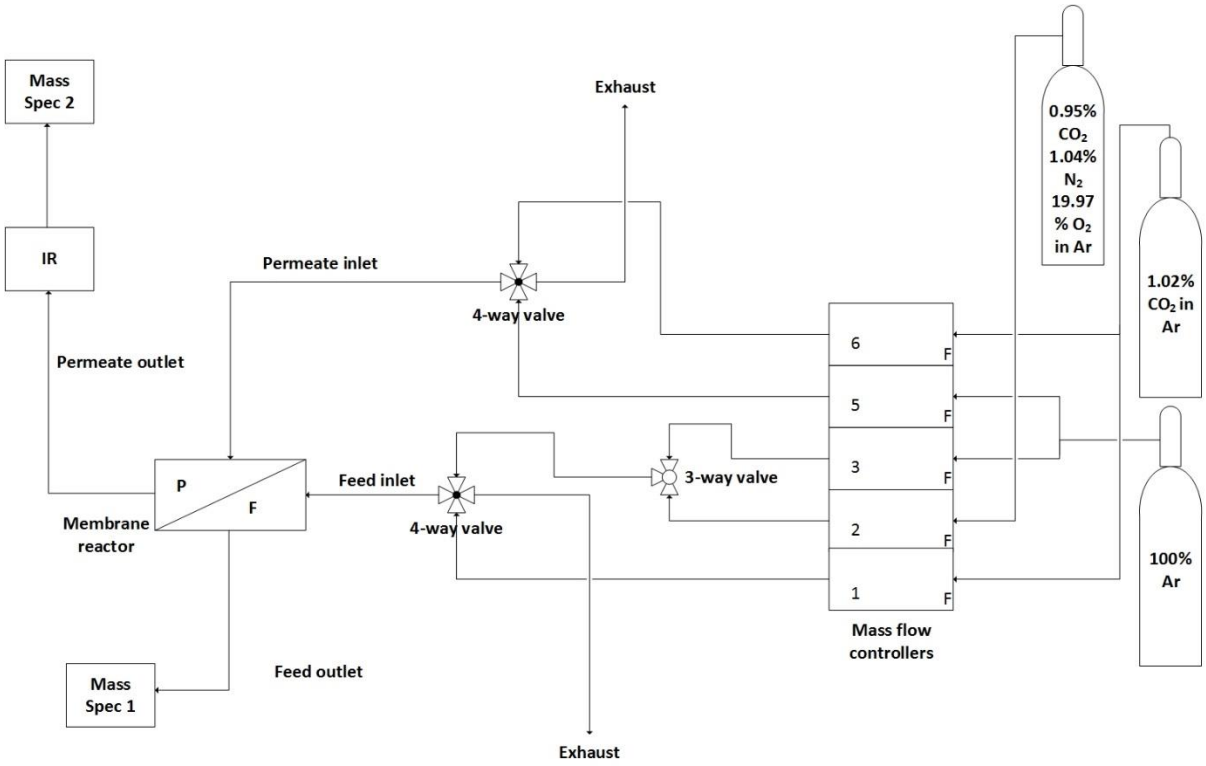

Figure 5.13: Process flow diagram redesigned for uphill CO_2 permeation experiments. Main article provided full explanation on how the flow system was utilised. A three-way valve was installed in case that the feed side reactor chamber required purging.

5.4.2. Uphill experiment at 600°C

The initial uphill CO_2 permeation experiments were performed at 600, 700 and 800°C successively, using a LSCF6428-carbonate membrane with 44% bulk porosity and 0.267g carbonate loading sealed by silver paste. The furnace was heated up to 600°C at 1°C/min under symmetrical operation (1.1% CO_2 in Ar into both reactor chambers), during which the oxygen background in the reactor was roughly 200ppm. Roughly 1.1% CO_2 was observed within both feed and permeate outlet streams under symmetrical operation at 600°C (part a of Figure 5.14), indicating a non-permeating condition. Once switching to asymmetrical operation incorporating 20% O_2 in feed inlet gas (part b of Figure 5.14), the permeate side CO_2 concentration increased from the non-permeating baseline of 1.1% and stabilised at 1.16%. Meanwhile, the retentate stream CO_2 concentration appeared to be 0.9%, which was a 0.05% drop comparing with the feed inlet CO_2 concentration of 0.95%. The second asymmetrical operation further confirmed the CO_2 mass balance and the occurrence of uphill permeation.

The uphill CO_2 permeation flux was calculated on the basis of non-permeating condition, where the baseline CO_2 mole fraction during symmetrical operation $y"_{sym}$ (0.011) was subtracted from the observed permeate side CO_2 mole fraction during uphill permeation. The calculation can be written as equation 5.2, where all the notations carry their meanings as in previous CO_2 flux calculations. A steady state uphill CO_2 flux of 1.52×10^{-4} mol·m^{-2}s^{-1} can be obtained from this uphill experiment at 600°C, which was in agreement with the result in the literature [28]. It required noting that the apparent CO_2 driving force during uphill permeation was negative. Calculating CO_2 permeance based on its apparent driving force became less meaningful here without accounting for the O_2 chemical potential difference. Detailed uphill CO_2 flux-driving force correlation incorporating the contribution from O_2 will be introduced in Chapter 6. Anyhow, CO_2 flux has been used as the primary parameter to quantify the performance of uphill permeation.

$$J_{CO_2} = \frac{F(y"_{CO_2} - y"_{sym})}{A} \qquad (5.2)$$

However, it seemed the oxygen permeation flux at 600°C in this experiment did not agree with the literature. E.Papaioannou et al. [28] reported that permeate side O_2 mole percentage stabilised at approximately 0.15% after 3 hours of asymmetrical operation. Whilst in this experiment the permeate side O_2 mole percentage under asymmetrical operation was 0.04%, merely a 0.02% increase from the background concentration. This was probably because of a different starting operation mode. E.Papaioannou et al. heated up the membrane under permeating condition (i.e. asymmetrical mode with 20% O_2 in feeding gas), followed by a brief symmetrical operation before switching back to permeating condition. In contrast, the membrane used here was kept under symmetrical mode (i.e. $pO_2 \sim 20$ Pa) for 20 hours before O_2 presented in the system. The LSCF6428 support can become oxygen deficient during this period, with nonstoichiometry δ of roughly 0.04.

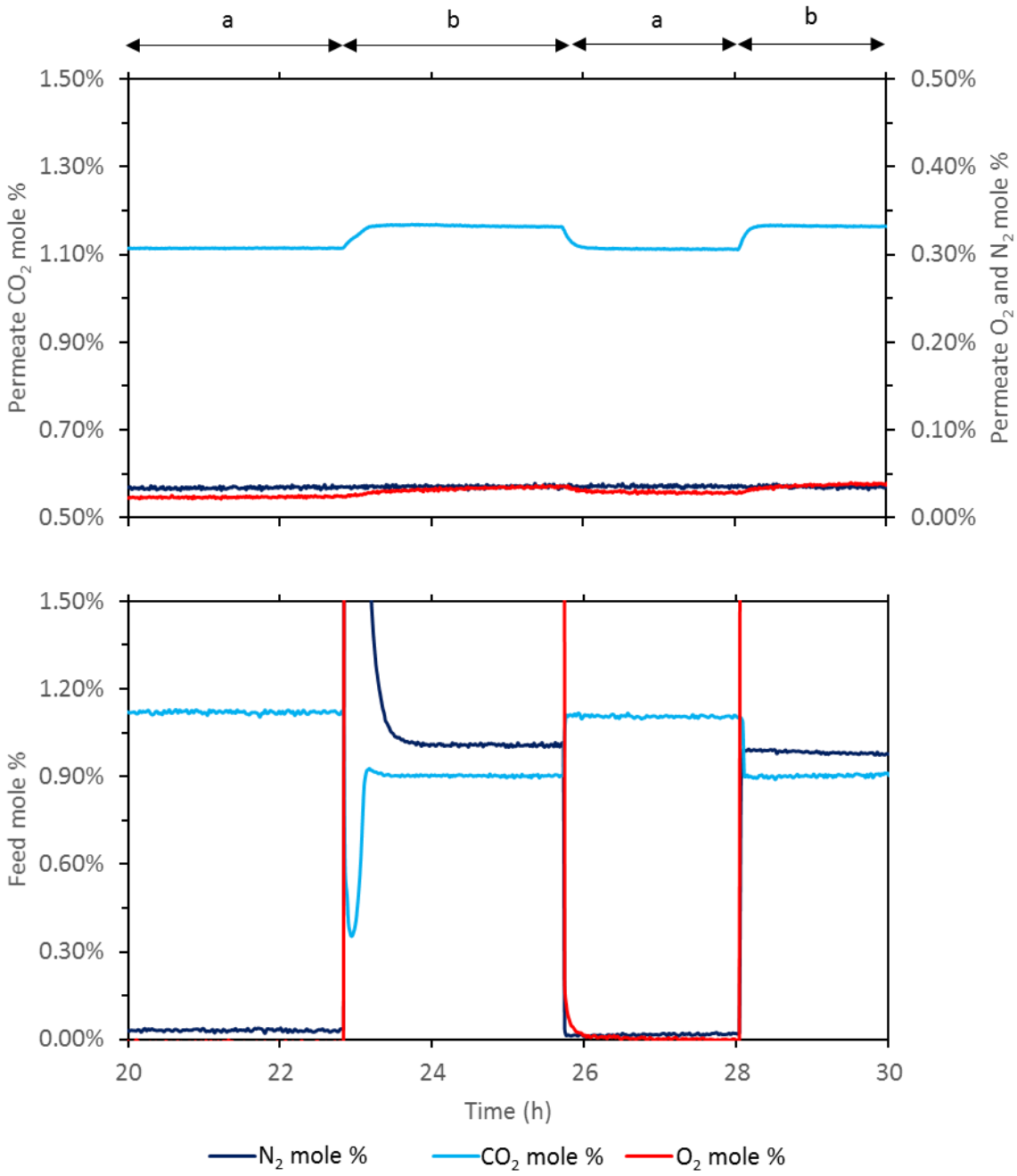

Figure 5.14: The initial uphill experiment at 600°C, alternating between (a): symmetrical operations, 1.1% CO_2 in Ar on both sides of the membrane; and (b): asymmetrical operations, 0.95% CO_2, 1.04% N_2, 19.97% O_2 in Ar on feed side and 1.1% CO_2 in Ar on permeate side. Note that the N_2 peak and CO_2 dip at the beginning of the first asymmetrical operation was likely due to air trapped within the four-way valve.

Once O_2 molecules presented on feed side, they may react and re-equilibrate with the oxygen deficient feed side LSCF6428 surface. Since the thermal effect on surface reaction kinetics of re-equilibration and oxygen mobility were both strong and they were both rather slow processes at 600°C [78, 79], the re-equilibration on permeate side surface may require O_2 supply from CO_2-O_2 co-permeation. In other words, a proportion of permeated O_2 may have been consumed for permeate side LSCF6428 re-

equilibration, leaving the O_2 mole fraction of permeate outlet stream low. This does not necessarily mean the O_2 permeation flux should be much higher through fully oxidised LSCF6428 membranes. In fact, the ratio of permeate side CO_2 and O_2 concentration increment here (~2.5:1) was closer to 2:1, which coincided with the assumption that the co-permeation mechanism dominated over individual CO_2 or O_2 transport mechanisms at 600°C.

5.4.3. Uphill experiment at 700 and 800°C

Uphill CO_2 permeation at higher temperature has never been reported in the literature. At 700°C and above, the more significant increase in LSCF6428 nonstoichiometry brings substantial changes of the membrane support properties. Firstly, a rise in oxygen vacancy concentration would enhance the O^{2-} conductivity and this in turn would promote the individual oxygen permeation flux via the solid phase. Higher O^{2-} conductivity would also enable backwards CO_2 electrochemical transport alone via the melt under uphill condition (i.e. from permeate side back to feed side), but this would be negligible due to the small driving force. On the other hand, electronic conductivity of LSCF6428 is expected to drop because of higher oxygen vacancy concentration (Figure 4.15). This is because when the temperature rises, the charge compensation of the LSCF system tends to shift from electronic to ionic compensation due to the loss of oxygen content. Each new oxygen vacancy eliminates two electron holes making the concentration of electron vacancy decrease [126]. Looking at how the combination of these factors influenced uphill CO_2 permeation at various temperatures would be beneficial for investigating uphill permeation from a mechanistic viewpoint.

The uphill CO_2 permeation experiments at 700 and 800°C were conducted using the same membrane and consistent operating procedures. The membrane was kept under asymmetrical operation when heating up to 800°C. In general, steady state uphill CO_2 flux increased with rising temperature (see Figure 5.15 and Table 5.3 for details). Gas analysis for retentate stream indicated CO_2 mass balance across the membrane during uphill permeation. The CO_2 and O_2 flux ratio at 800°C may vary on different experiments but normally smaller than 2:1. The Arrhenius plot for uphill permeation (Figure 5.16) showed an apparent activation energy of 53.7 ± 3.2 kJ/mol from 600 to 800°C. The uphill CO_2 permeation was unlikely bulk electronic diffusion limiting, since the temperature dependency of the electronic conductivity in LSCF6428 had an opposite trend to the observed CO_2 permeation flux. Interfacial reaction or CO_3^{2-} conduction through the melt was more likely the rate determining step. In fact, the thermal activation effect for the CO_3^{2-} conduction was rather weak. Janz et al. suggested the activation energy of carbonate ion conduction via molten ternary carbonate was approximately 31 kJ/mol between 670 and 1000K [84]. Based on this, the uphill permeation did not seem to be a purely CO_3^{2-} conduction limiting process. The interfacial reaction, which intrinsically had higher activation energy although remained unknown, could have been influential on the overall uphill CO_2 permeation flux at least until 800°C.

Table 5.3: Summary table of CO_2 concentrations within feed inlet, feed outlet, permeate inlet and permeate outlet streams during uphill experiments at 600-800°C.

Temperature	CO_2 concentration (mol%)			
(°C)	Feed inlet	Feed outlet (retentate)	Permeate inlet	Permeate outlet
600	0.95%	0.90%	1.11%	1.16%
700	0.95%	0.87%	1.11%	1.20%
800	0.95%	0.78%	1.11%	1.31%

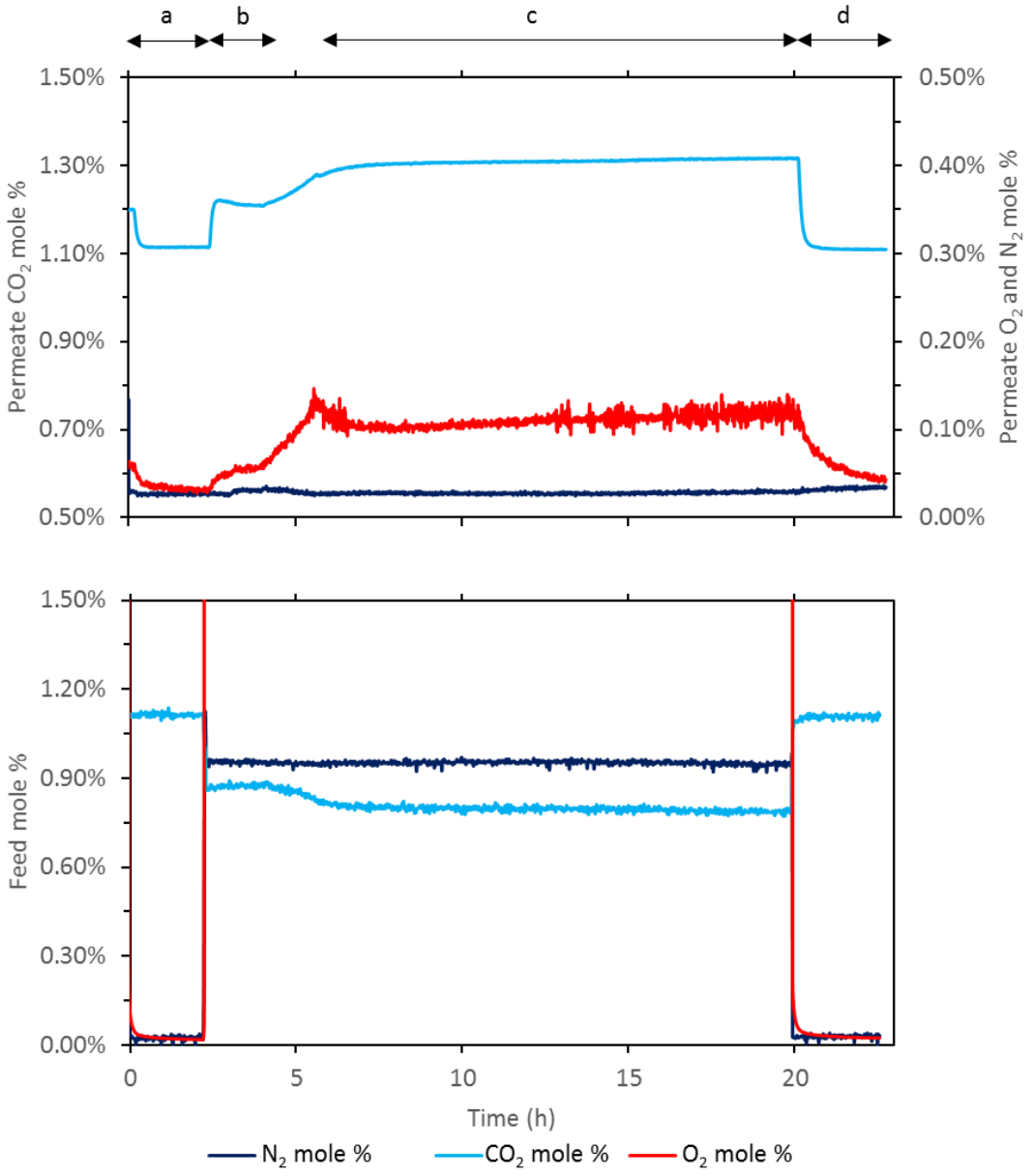

Figure 5.15: The initial uphill experiment at 700 and 800°C: (a) Symmetrical operation at 700°C; (b) Asymmetrical operation at 700°C; (c) Asymmetrical operation at 800°C; (d) Symmetrical operation at 800°C. The gas conditions of symmetrical and asymmetrical modes were the same as the experiment at 600°C.

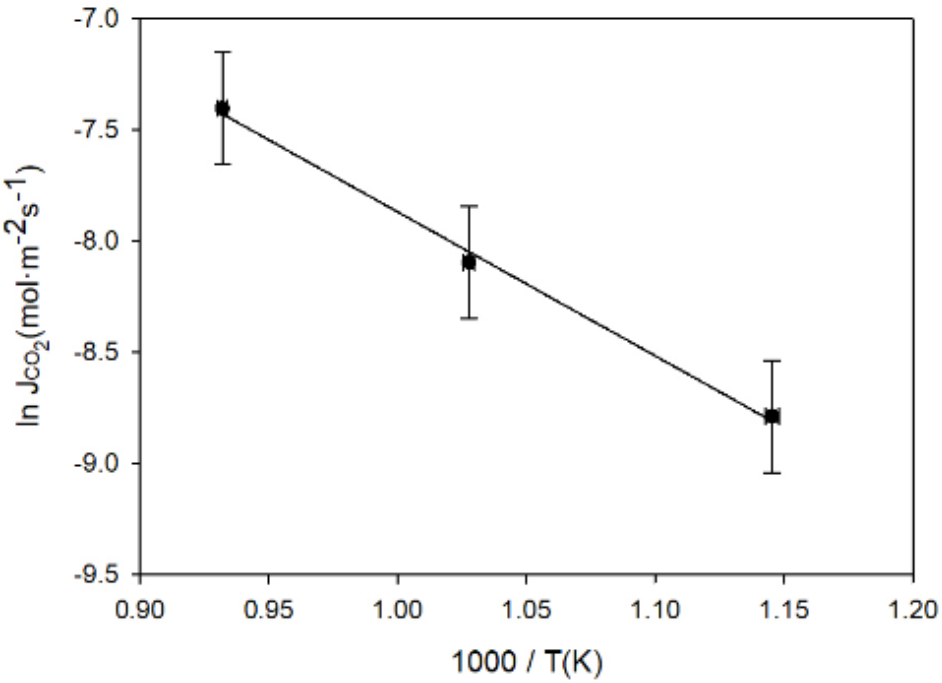

Figure 5.16: Arrhenius plot showing logarithm of uphill CO_2 permeation flux against 1000/T through LSCF6428-carbonate membrane. The operating temperatures were 600, 700 and 800°C.

Furthermore, detailed behaviour of CO_2 uphill permeation as well as O_2 permeation can be different at higher temperature, primarily due to changes in membrane properties. Sensible comparisons can be made between 600 and 800°C since the membrane properties differed significantly. The carbonate ion conductivity at 800°C would be twice as much as 600°C [53]; the oxide ion conductivity at 800°C would be 20 times higher in the LSCF6428 support [129]; the LSCF6428 oxygen nonstoichiometry at 800°C would be 0.1 to 0.15 [132] under symmetrical operation.

The initial uphill experiment at 600°C started after 20 hours exposure under symmetrical operation. Both CO_2 and O_2 permeation stabilised quickly once switching to asymmetrical operation as seen in Figure 5.14. However, this would not be the case at 800°C. For straightforward comparison, the uphill experiment at 800°C was repeated by heating up under symmetrical operation (Figure 5.17). This operation mode was maintained for roughly 15 hours at 800°C prior of switching to asymmetrical mode, where a transient CO_2 peak was observed on membrane permeate side together with a gradual increase of oxygen concentration on the same timescale. Steady state CO_2 uphill permeation and O_2 permeation were obtained after 2-3 hours. Once switching back to symmetrical operation, the O_2 concentration also declined gradually. These trends of oxygen concentration may link to O_2 uptake and release of LSCF pellet, given that at 800°C the LSCF6428 nonstoichiometry fluctuated more significantly under the two operation modes. The transient CO_2 peak corresponded to a CO_2 concertation dip on feed side (Figure 5.17 part c) whilst the reason behind it was not yet clear. However, no transient CO_2 peak was observed if heated up in oxidising atmosphere (Figure 5.15 part c). Appearance of transient CO_2 peak seemed to

be associated with how reducing the LSCF support was prior to uphill permeation. The transient low permeate side pO_2 at the beginning of the repeated uphill experiment may also temporarily enhance the driving force for uphill CO_2 permeation. Further discussion on these two possible explanations will be given on Chapter 6 and appendix III. Nevertheless, the steady state CO_2 permeation fluxes at the same temperature were always consistent regardless of operation mode the experiment started with. Although the shift of operation modes caused stronger fluctuation of LSCF oxygen nonstoichiometry at 800°C, the steady state uphill CO_2 permeation flux remained unaffected.

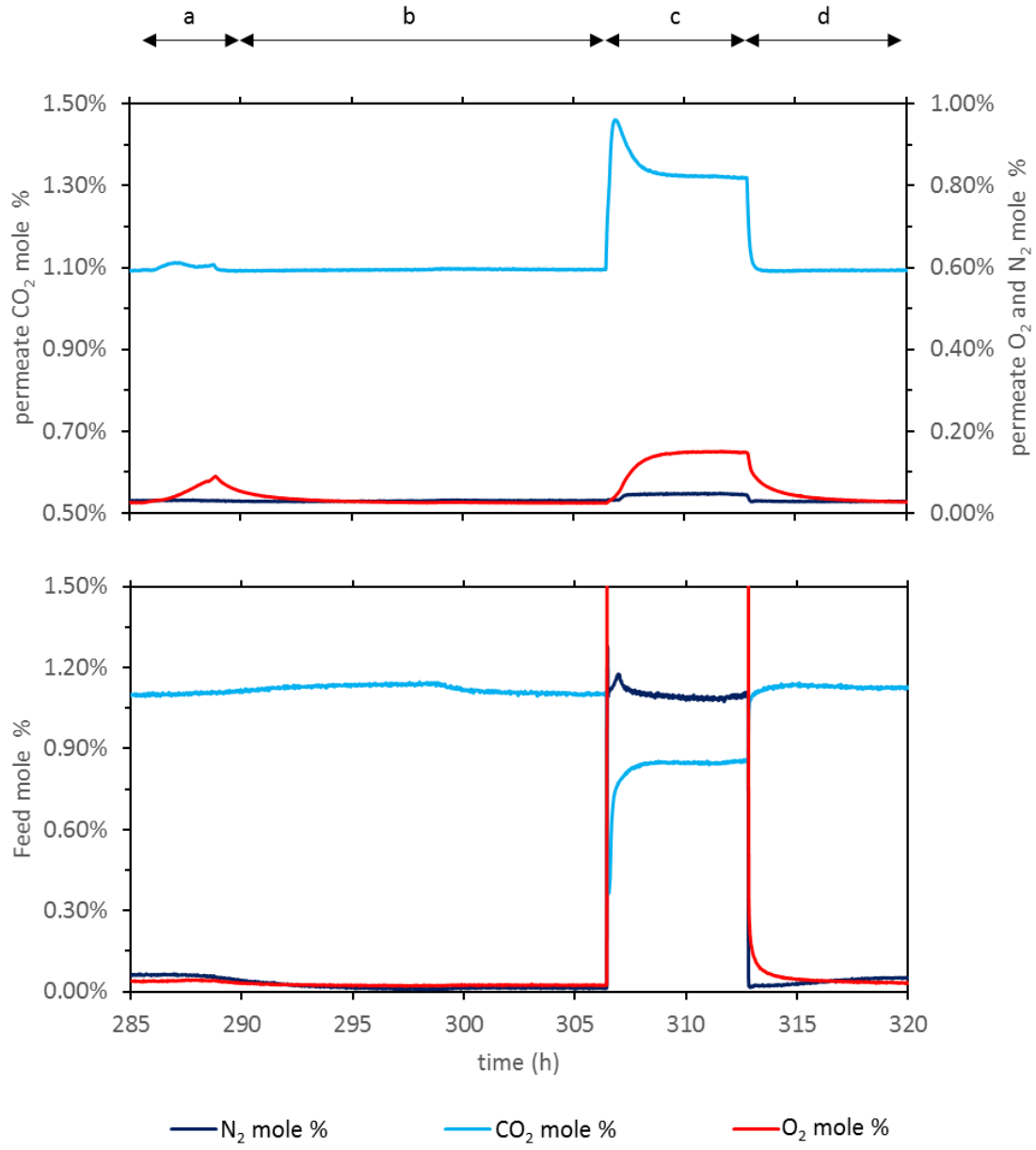

Figure 5.17: The repeated uphill experiment at 800°C heated up under symmetrical operation: (a) Symmetrical operation while heating up flowing 1.1% CO_2 in Ar on both sides of the membrane. (b) Symmetrical operation at 800°C. (c) Asymmetrical operation at 800°C flowing 1.04% CO_2, 1.05% N_2, 19.6% O_2 in Ar on feed side and 1.1% CO_2 in Ar on permeate side. (d) Switching back to symmetrical operation.

5.5. Summary

The variation of oxygen nonstoichiometry with temperature and pO_2 is a unique property of LSCF6428 membranes. This feature leads to modification of ionic and electronic conductivities within membrane solid phase, which may crucially affect the performance of CO_2 and O_2 permeation through the LSCF6428-carbonate membranes being investigated in this project. It was necessary to study the effect to the membrane performance in oxygen free atmosphere (i.e. pre-combustion CO_2 separation) and oxygen-containing atmosphere (i.e. post-combustion CO_2-O_2 co-permeation) separately. Under inert atmosphere (pO_2~10 Pa) the LSCF6428 nonstoichiometry δ can increase significantly at 850°C. This reduced state can be maintained while returning to lower temperatures (650°C-750°C) under the same pO_2. Meanwhile, downhill CO_2 permeance can be enhanced by 2-3 times higher than a non-reduced membrane between 650°C-750°C, due to higher solid phase oxygen vacancy concentration. Downhill CO_2-O_2 co-permeation and uphill permeation provided oxygen-containing atmosphere. The higher pO_2 in the reactor chambers tended to re-equilibrate with LSCF6428, leading to much lower δ values in LSCF6428 at all temperatures. Furthermore, the co-permeation mechanism did not seem to be limited by solid phase ionic/electronic conduction. Instead, the interfacial reaction and CO_3^{2-} conduction in the melt may have played important roles. Therefore, alternative approach was required to enhance the CO_2 flux based on co-permeation mechanism.

It has been found that O_2 co-permeation not only offered more effective CO_2 flux enhancement than modifying the LSCF6428 oxygen nonstoichiometry, but also allowed uphill CO_2 permeation. It has been widely discussed in the literature that the mixed electronic and ionic conducting feature of the LSCF6428 support enabled the co-permeation mechanism. Both O_2 and CO_2 involved into the interfacial reaction allowing the chemical potential gradient of O_2 to contribute to the overall driving force for the co-permeation. The CO_2 flux can be promoted by increasing the overall thermodynamic driving force. Our uphill experimental conditions certainly did not violate the thermodynamic limitation, and there seems to be rooms for further driving force enlargement by harnessing the oxygen chemical potential difference. To investigate the contribution of oxygen chemical potential difference to the overall driving force, experimental study on the flux-driving force relationships of CO_2-O_2 co-permeation would be essential, which has not been largely paid attention by existing literature. Chapter 6 of the thesis will focus on the CO_2 flux-driving force relationships experiments and proceed to further driving force enhancement by permeate side O_2 removal.

6. CO_2 flux – driving force relationships for LSCF6428-carbonate membranes

6.1. Introduction and theoretical background

6.1.1. Aims and objectives

So far, it has been experimentally demonstrated that co-feeding 20% O_2 can promote the CO_2 permeance through LSCF6428-carbonate membranes by two orders of magnitudes, and it further allowed uphill CO_2 permeation based upon 1% concentration. The concept of uphill CO_2 permeation with the aids of O_2 co-permeation is promising because it could potentially reduce the energy requirement for gas compression as in a conventional membrane based flue gas CO_2 separation process. The importance of O_2 in terms of driving force has been acknowledged by a few previous studies in dual phase membranes [28, 92, 109], whilst it is yet unclear how strongly the driving force from O_2 may affect CO_2 permeation flux. It is uncommon for researchers to explore on further enhancing CO_2 permeation flux by harnessing the driving force of O_2. Comprehensive experimental study on CO_2 flux – driving force relationships in presence of O_2 has not been established, particularly for uphill permeation.

This chapter intended to fill this gap and took a step further to investigate the CO_2 flux – driving force relationship in presence of O_2. Isothermal uphill CO_2 permeation flux at 600°C was firstly measured under a few sets of different driving forces by varying feed side CO_2 and O_2 concentrations. Comparing the experimental data with existing CO_2 permeation models can help obtain a mechanistic insight on uphill permeation. Considering the mechanism may change with different operating temperature regimes and deferent driving force regimes, isothermal uphill CO_2 flux – driving force relationships at 800°C was also obtained. The experiments were then expanded to downhill CO_2 flux under large driving forces feeding high concentration CO_2 and O_2 mix without CO_2 in sweep gas. If good continuity of CO_2 flux – driving force trends under various driving force regimes can be obtained, this trend can be used to predict the effect of enhancing thermodynamic driving force on CO_2 flux. Finally, a novel technology of driving force enchainment was employed by incorporating copper based oxygen carrier into the membrane separation system, in order to undertake permeate side O_2 removal.

6.1.2. Theoretical background and revised models

For CO_2-O_2 co-permeation through an electronic conductive or MIEC type molten carbonate dual phase membrane, a global CO_2 flux – driving force model can be derived from the first principle as shown in equation 2.39, based on the counter diffusion of the two charged species in the system: electrons back diffusion in solid phase and CO_3^{2-} ions diffusion in molten phase. This has been reviewed in Chapter 2.4.1 and both Zhang et al. [92] and Y. S. Lin et al. [48] agreed the validity of this model.

$$J_{CO_2} = J_{CO_3^{2-}} = -\frac{\sigma_c \sigma_e}{4(\sigma_c + \sigma_e)F^2}\left(\nabla \mu_{CO_2} + \frac{1}{2}\nabla \mu_{O_2}\right) \qquad (2.39)$$

$$J_{CO_2} = -\frac{\varepsilon\varphi}{\tau}\frac{RT}{4F^2\delta}\int_{p'CO_2,p'O_2}^{p''CO_2,p''O_2}\sigma_c\left(dlnp_{CO_2}+\frac{1}{2}dlnp_{O_2}\right) \qquad (6.1)$$

This model indeed holds for the LSCF6428-carbonate system being studied in this work. Moreover, the model can be further simplified into equation 6.1 given that the electronic conductivity is always two orders of magnitude higher than carbonate ion conductivity in the melt. The model consists of a microstructural term including membrane support porosity ε, tortuosity τ and carbonate volumetric fraction φ, as well as geometry term δ (membrane thickness). These parameters can be controlled by using same membrane fabrication procedure, such that the membranes fabricated in the same batch have similar geometry and microstructure. Hence, by varying CO_2 and O_2 partial pressure exposed on membrane surfaces and measuring the corresponding CO_2 flux, the experimental data can be linked to the theoretical model. However, the key question is whether the carbonate ion conductivity is a constant throughout the membrane or it is dependent on pCO_2 and pO_2.

It is necessary to analyse this problem for each individual rate-limiting scenario. Theoretically, the CO_2 transport across the membrane via the co-permeation mechanism undergoes five successive steps: (i) Mass transfer from bulk feeding gas to membrane feed side interface. (ii) Global interfacial reaction $CO_2 + 1/2O_2 + 2e^- \leftrightarrow CO_3^{2-}$ on interface I. (iii) CO_3^{2-} diffusion via the melt. (iv) Global interfacial reaction $CO_3^{2-} \leftrightarrow CO_2 + 1/2O_2 + 2e^-$ on interface II. (v) Mass transfer from membrane permeate side interface to bulk sweep gas. Although the whole process could be mass transfer limiting and the global interfacial reactions may involve rate controlling sub-steps, the carbonate ion diffusion controlling and global interfacial reaction controlling scenarios were primarily considered here for simplicity and better comparison. The scenarios were illustrated in Figure 6.1 (a-d).

Scenario (a) assumed fast CO_2 and O_2 mass transfer through the boundary layers, fast reaction at the interfaces on both sides of the membrane and slow carbonate ion diffusion via the melt. Thus, the illustration corresponds to a bulk CO_3^{2-} diffusion limiting scenario. During symmetrical operation, the carbonate ion concentration in the melt is likely to be uniform as it is in equilibrium with same pCO_2 on both sides of the membrane. Once switching to asymmetrical operation, the membrane is exposed under a certain gas phase chemical potential difference. The fast reaction on interface I rapidly generates CO_3^{2-} and the slow CO_3^{2-} diffusion causes accumulation of CO_3^{2-} concentration ($[CO_3^{2-}]'_S$) on interface I. On the other side of the membrane, rapid consumption of CO_3^{2-} makes CO_3^{2-} concentration ($[CO_3^{2-}]''_S$) on interface II drop. Hence, at steady state a chemical potential gradient of CO_3^{2-} will form within the melt, such that the CO_3^{2-} concentration is no longer uniform throughout the membrane. Based on the Nernst-Einstein equation (6.2), the CO_3^{2-} conductivity (σ_C) on feed side surface is a product of CO_3^{2-} concentration on interface I, molar charge of the ionic species (q) and the CO_3^{2-} mobility ($u_{CO_3^{2-}}$). Due to the non-uniform CO_3^{2-} concentration, corresponding CO_3^{2-} conductivity at any point within the

membrane is also a variable. Therefore, the assumption here is that the CO_3^{2-} conductivity (σ_C) in equation 6.1 cannot be assumed as a constant [92, 136].

$$\sigma_c = [CO_3^{2-}]_s q u_{CO_3^{2-}} \qquad (6.2)$$

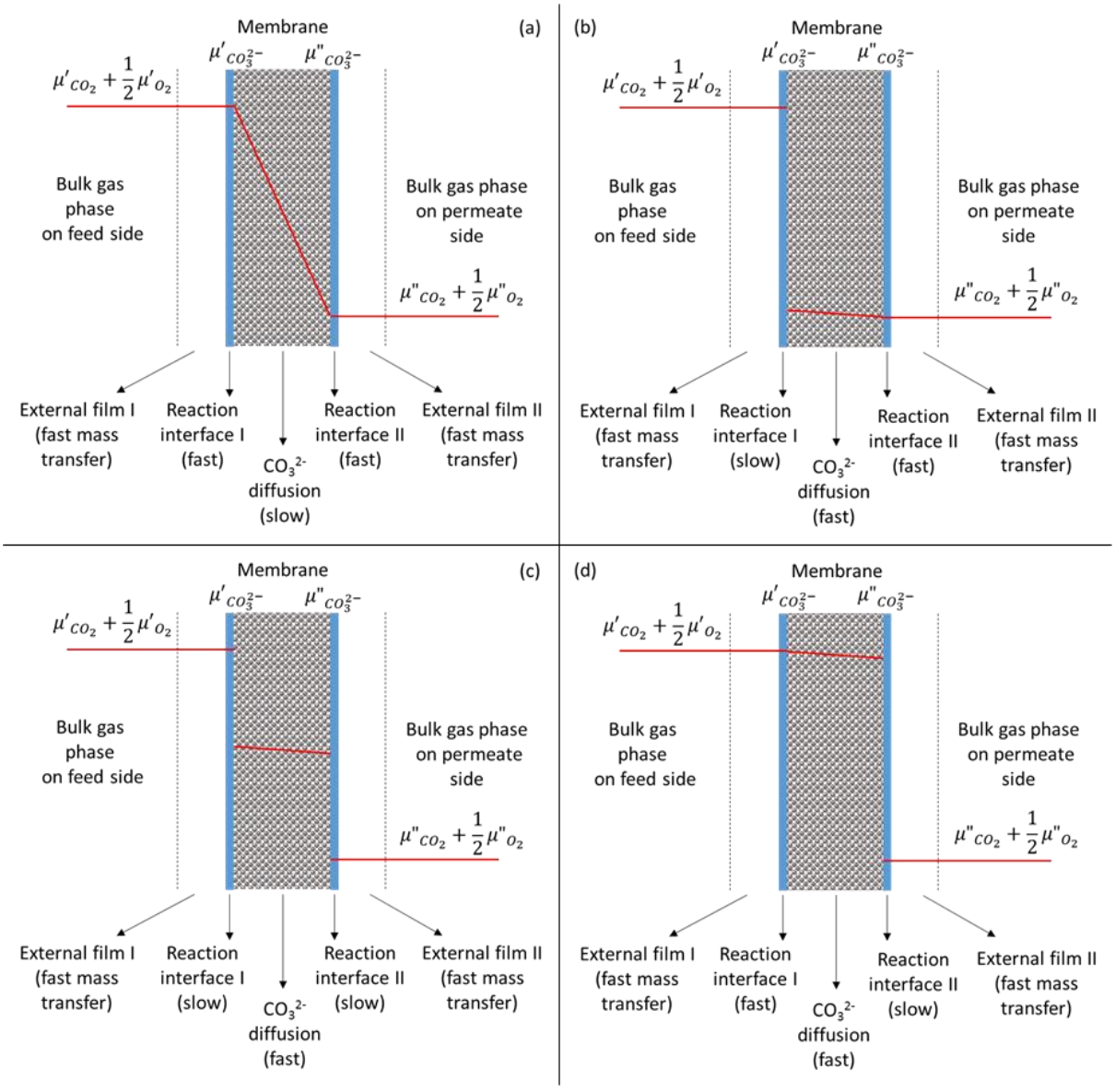

Figure 6.1: Illustration of possible rate determining steps for CO_2-O_2 co-permeation. Four scenarios are considered at this stage: (a) CO_3^{2-} diffusion limiting. (b) Feed side interfacial reaction rate limiting. (c) Permeation limited by interfacial reactions on both sides. (d) Permeate side interfacial reaction rate limiting. The levels of gas phase and molten phase chemical potentials are included for each case.

In fact, fast interfacial reactions on both sides of the membrane indicates that the reactions reach equilibrium instantaneously. Therefore, at steady state CO_2-O_2 co-permeation, the relationship between surface CO_3^{2-} concentration and feed side gas partial pressures $p'O_2$ and $p'CO_2$ can be written as:

$$[CO_3^{2-}]_s = K p'_{CO_2} p'^{1/2}_{O_2} \qquad (6.3)$$

where K is the equilibrium constant of global interfacial reaction $CO_2 + 1/2O_2 + 2e^- \leftrightarrow CO_3^{2-}$. As CO_3^{2-} concentration is a variable along the membrane, at any point the CO_3^{2-} concentration can be related to hypothetical pO_2 and pCO_2 that associated with local CO_3^{2-} chemical potential and in equilibrium with local CO_3^{2-} concentration in the melt, making the CO_3^{2-} conductivity dependant to CO_2 and O_2 partial pressures (equation 6.4). Therefore, σ_C in equation 6.1 must remain in the integral and be integrated with the partial pressure gradient. Followed by integration of equation 6.1 a linear CO_2 flux-driving force relationship is obtained (equation 6.5) instead of a logarithm correlation [92, 136].

$$\sigma_c = Kqu_{CO_3^{2-}} p_{CO_2} p_{O_2}^{1/2} \qquad (6.4)$$

$$J_{CO_2} = -\frac{\varepsilon\varphi}{\tau}\frac{RT}{4F^2\delta} Kqu_{CO_3^{2-}} \int_{p'CO_2, p'O_2}^{p"CO_2, p"O_2} p_{CO_2} p_{O_2}^{1/2} \left(dlnp_{CO_2} + \frac{1}{2} dlnp_{O_2} \right)$$

$$= -\frac{\varepsilon\varphi}{\tau}\frac{RT}{4F^2\delta} Kqu_{CO_3^{2-}} (p"_{CO_2} p"_{O_2}^{1/2} - p'_{CO_2} p'_{O_2}^{1/2}) \qquad (6.5)$$

If the CO_3^{2-} diffusion in the melt is a much faster process than interfacial reactions, the rate limiting step for CO_2 permeation shifts to interfacial reaction controlling. The rate can be controlled by reactions on both sides of the membrane, as shown in Figure 6.1 (c), as well as the reaction on either one side of the membrane shown in Figure 6.1 (b) and (d). The global reaction on permeate side interface is the reversed reaction of feed side interface. Nevertheless, due to the complexity of molten salt chemistry, the two global interfacial reactions may proceed via different routes of sub-reactions, such as peroxide ions (O_2^{2-}) or superoxide ions (O_2^-) formation, the rate of the two global reactions can be vastly different and scenarios (b) and (d) are possible. Without considering this complexity, a plain global interfacial reaction controlling CO_2 permeation is more likely scenario (c), where both sides have slow and comparable reaction rates.

Under this scenario, a switch from symmetrical to asymmetrical operation would firstly perturb the interfacial thermodynamic equilibrium on feed side. CO_3^{2-} formation would be gradual on feed side interface whilst they instantaneously diffuse across the membrane instead of accumulating on the interface. As a result, the CO_3^{2-} concentration in the melt is expected to stay nearly uniform. However, the gradual CO_3^{2-} formation leads to gradual change of CO_3^{2-} concentration in the melt over time. In response, thermodynamic equilibrium on membrane permeate side is perturbed and CO_3^{2-} consumption slowly begins. The reaction on both sides would never approach thermodynamic equilibrium. There would rather be a steady state CO_2 permeation, at which the rates of CO_3^{2-} formation and consumption are equal and CO_3^{2-} concentration in the melt stops changing.

As the gas and melt are not in equilibrium on both interfaces, a gap of gas phase and molten phase chemical potential must be present as shown in Figure 6.1 (c). The gas phase pCO_2 and pO_2 can only be related directly to reaction rate but not the carbonate concentration in the melt. Thus, we propose

that for a global interfacial reaction limiting scenario, the CO_2 permeation flux is approximately equals to the rate of interfacial reaction, with a unit of mol·m^{-2}·s^{-1}. The model for this case can be written as:

$$J_{CO_2} = r_I = k_f {p'}_{CO_2} {p'}_{O_2}^{1/2} - k_r[CO_3^{2-}] \qquad (6.6)$$

In this equation r_I represents the overall reaction rate on interface I, k_f and k_r represent the temperature dependant forward and reverse reaction rate constants respectively, [CO_3^{2-}] is the uniform carbonate concentration in the melt at any extent of the reaction. This concentration would be in equilibrium with hypothetical partial pressures $p^{eq}CO_2$ and $p^{eq}O_2$, giving a relation depicted in equation 6.7. Therefore, equation 6.6 can be rewritten as equation 6.8.

$$k_f p_{CO_2}^{eq} p_{O_2}^{eq\,1/2} = k_r[CO_3^{2-}] \qquad (6.7)$$

$$J_{CO_2} = r_I = k_f({p'}_{CO_2} {p'}_{O_2}^{1/2} - p_{CO_2}^{eq} p_{O_2}^{eq\,1/2}) \qquad (6.8)$$

Similarly, the rate of permeate side reaction r_{II} can be written as equation 6.9 as under scenario c it has been assumed the permeate side reaction is also slow. At steady state CO_2 permeation, the rate of carbonate formation and consumption would be the same ($r_I = r_{II}$), such that the CO_2 permeation flux can be expressed in terms of feed and permeate side CO_2 and O_2 partial pressures as shown in equation 6.10.

$$r_{II} = k_f(p_{CO_2}^{eq} p_{O_2}^{eq\,1/2} - {p''}_{CO_2} {p''}_{O_2}^{1/2}) \qquad (6.9)$$

$$J_{CO_2} = \frac{k_f}{2}({p'}_{CO_2} {p'}_{O_2}^{1/2} - {p''}_{CO_2} {p''}_{O_2}^{1/2}) \qquad (6.10)$$

In short, we have set up a CO_2 flux-driving force model for CO_3^{2-} diffusion limiting model based on the principle of Fickian diffusive flux, assuming the CO_3^{2-} concentration and conductivity are gaseous partial pressures dependant. On the other hand, the global interfacial reaction limiting model was set up based on the rate of reaction, assuming the CO_3^{2-} concentration and conductivity are homogeneous throughout the membrane. In both cases, the model ended up with a linear relationship between CO_2 flux and driving force that involved relevant partial pressures on both sides of the membrane. A logarithm relationship would not exist based on our assumptions. This indicated that fitting the experimental data into these models could not directly distinguish between the two different rate-limiting scenarios. Detailed data analysis may be required. Following our assumptions, when any sub-reaction of the global interfacial reaction is rate limiting, including peroxide ions (O_2^{2-}), superoxide ions (O_2^-), peroxycarbonate ions (CO_4^{2-}) and superoxycarbonate ions (CO_5^{2-}) limiting, the flux models would still be approximately equal to the corresponding reaction rates, which are proportional to the relevant reaction orders associated with pCO_2 and pO_2. Therefore, equation 2.43 and 2.44 still hold but CO_4^{2-} and CO_5^{2-} limiting cases would only correlate to oxygen partial pressure (see reaction 2.27 and 2.28).

With the revised assumptions and models, several isothermal CO_2 flux-driving force experiments were performed.

6.2. Isothermal permeation experiments with various driving forces

6.2.1. Experimental design and set-up

The simplest approach for investigating the CO_2 flux-driving force relationship is to vary the CO_2 and O_2 concentration on both sides of the membrane. However, driving force is not the only contributor of CO_2 flux. The diffusive flux model (i.e. carbonate ion diffusion limiting model) suggested that CO_2 flux may also be affected by membrane geometry, microstructure and temperature. Thus, LSCF6428 support pellets were carefully selected from the same batch of fabrication, such that they all have very similar thickness (~0.15 cm) and bulk porosity (~41%). The carbonate loading during the hot infiltration was also controlled to 0.24-0.26g. In this way, the effect from the geometrical and microstructural parameters were minimised.

The CO_2 flux-driving force experiments were only conducted isothermally considering the temperature effect on CO_2 flux. Here, the flux-driving force relationships were investigated at 600 and 800°C operating temperatures respectively. These two temperatures were chosen because it is possible that rate determining scenarios for CO_2 permeation (Figure 6.1) may change as the temperature goes significantly higher. This can be supported by the gradient change shown on the Arrhenius plots for CO_2-O_2 co-permeation through LSCF6428 membrane (see Figure 5.12 in Chapter 5.3.2). Moreover, the membrane support properties are vastly different under the two temperatures. At 600°C the LSCF6428 is almost an electronic conductor. However, at 800°C the material is much more ionic conductive but less electronic conductive. This may lead to some changes of permeation mechanisms for CO_2 and O_2.

Three sets of isothermal CO_2 flux-driving force experiments were designed to cover a broad range of driving forces. Set 1 and set 2 were designed based on uphill CO_2 permeation under relatively small driving forces. With a standard reference driving force of 1% CO_2 + 20% O_2 against 1.1% CO_2, set 1 varied the O_2 concentration of feed inlet gas from 20% down to 10%, 5%, 2% and 1% respectively whilst fixing the CO_2 concentration of feed inlet gas at 1%. On the other hand, set 2 varied the CO_2 concentration of feed inlet gas from 1% down to 0.5%, 0.4% and 0.3%, fixing the O_2 concentration at 20%. The same sweep gas composition with 1.1% CO_2 in Argon were used consistently for set 1 and set 2 experiments. CO_2 uphill permeation with lower driving forces can be explored in the meantime by approaching the thermodynamic limit at which the uphill CO_2 permeation would no longer be observable.

Uphill CO_2 permeation is a special category of CO_2-O_2 co-permeation, which the driving force regime locates towards the lower end. By replacing the 1.1% CO_2/Ar sweep gas with pure argon, it would go

into a larger driving force regime of downhill CO_2-O_2 co-permeation. If the same permeation mechanism were involved in both driving force regime, and the effects of parallel mechanisms were insignificant at larger driving forces, the CO_2 flux and driving force correlation would be consistent, leading to a connective flux-driving force plot between the two driving force regimes. It is therefore worth carrying out set 3 experiments designed with downhill CO_2-O_2 co-permeation in large driving force regime. This set of experiment varied feeding CO_2 concentration from 1% up to 25%, accompanied with variation of feeding O_2 concentration from 10% up to 20%. Pure argon was used as sweep gas in order to create large driving forces. All combinations of CO_2 and O_2 concentrations across the membrane for the three sets of flux-driving force experiments were summarised in Table 6.1.

Table 6.1: Combinations of feed and permeate inlet gas compositions for the three sets of flux-driving force experiments, covering a wide range of thermodynamic driving forces across downhill and uphill regimes.

	Feed inlet gas	**Permeate inlet (sweep) gas**
Set 1	1.04% CO_2 + 19.6% O_2	1.1% CO_2 in Ar
	1.04% CO_2 + 9.9% O_2	1.1% CO_2 in Ar
	1.05% CO_2 + 5.0% O_2	1.1% CO_2 in Ar
	1.05% CO_2 + 2.2% O_2	1.1% CO_2 in Ar
	1.05% CO_2 + 1.2% O_2	1.1% CO_2 in Ar
Set 2	1.04% CO_2 + 19.6% O_2	1.1% CO_2 in Ar
	0.52% CO_2 + 20.0% O_2	1.1% CO_2 in Ar
	0.42% CO_2 + 19.9% O_2 (800°C only)	1.1% CO_2 in Ar
	0.31% CO_2 + 19.9% O_2 (800°C only)	1.1% CO_2 in Ar
	0.21% CO_2 + 19.9% O_2 (600°C only)	1.1% CO_2 in Ar
Set 3	0.54% CO_2 + 19.8% O_2	100% Ar
	1.04% CO_2 + 19.6% O_2	100% Ar
	2.40% CO_2 + 19.1% O_2	100% Ar
	5.46% CO_2 + 17.8% O_2	100% Ar
	10.0% CO_2 + 16.0% O_2	100% Ar
	25.1% CO_2 + 10.0% O_2	100% Ar

Adjustment of gas compositions was achieved by blending two gas mixtures with certain ratios of flow rates. For instance, feed inlet gas of set 1 experiment was a blend of 1.04% CO_2, 1.05% N_2, 19.6% O_2 in argon (*BOC, Certified Mixture*) and 1.05% CO_2, 1.01% N_2 in argon (*BOC, Certified Mixture*). The total flow rate of the two streams was maintained at 20 ml/min. By changing the flow rates of the gas mixtures, the O_2 concentration can be modified whilst keeping the CO_2 concentration fixed. Similarly, set 2 experiment was a blend of 1.04% CO_2, 1.05% N_2, 19.6% O_2 in argon and 20.02% O_2 in argon

(*BOC, Certified Mixture*). Set 3 experiment was a blend of 1.04% CO_2, 1.05% N_2, 19.6% O_2 in argon and 20.02% O_2 in argon or a blend of 50.17% CO_2 in N_2 (*BOC, Certified Mixture*) and 20.02% O_2 in argon. An updated process flow diagram incorporating the gas blending is shown in Figure 6.2.

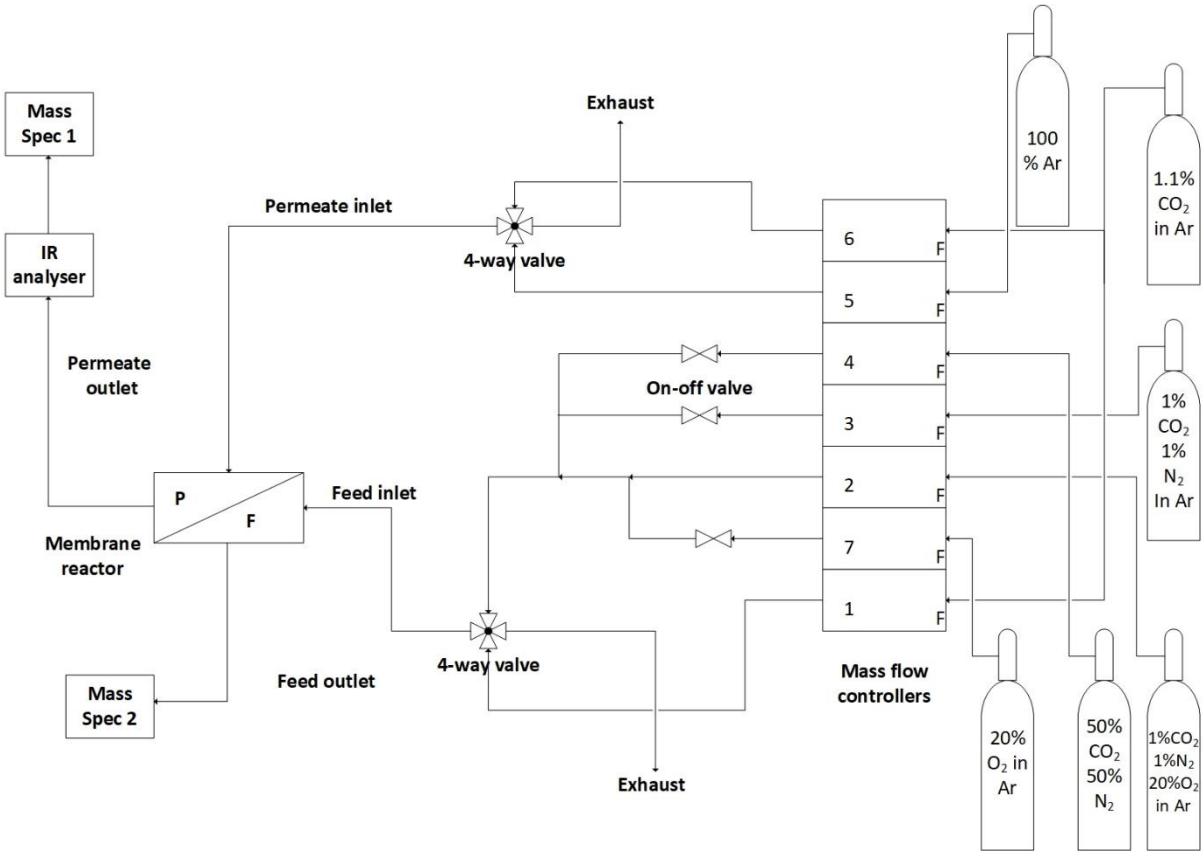

Figure 6.2: An updated process flow diagram for CO_2 flux-driving force experiments, incorporating the gas blending system located between mass flow controllers 2, 3, 4 and 7. Permeate side outlet stream were analysed on-line using CO_2 IR analyser and mass spectrometer in series; feed side outlet stream were analysed on-line using another similar mass spectrometer.

To maintain the consistency of the set 1 and set 2 experiments in line with previous uphill CO_2 permeation experiments, the LSCF6428-carbonate membranes were heated up under symmetrical operation, flowing 1.1% CO_2/Ar in both reactor chambers. Sufficiently long dwelling time (10-20 hours) was assigned to asymmetrical operation to allow the establishment of steady state CO_2 permeation. Set 3 experiments with large downhill driving forces were also began with heating up under inert atmosphere. Driving forces and permeation fluxes were quantified based on permeate outlet stream and retentate stream gas partial pressures measured by on-line gas analysers. Experimental data was fit into flux-driving force models corresponding to each rate determining scenarios. Ideally, performing all experiments using the same membrane would generate the most consistent data. Considering the duration for each set of experiment may exceed 100 hours, separate membranes from the same batch of fabrication were used for each set at each operating temperature (600 and 800°C).

6.2.2. Isothermal permeation experiments at 600°C

Figure 6.3 and 6.4 gave some examples of the reactor outlet gas analysis. It is worth pointing out that the calculation of driving forces involved gas partial pressure on feed side, p'CO_2 and p'O_2, as well as partial pressure on permeate side, p"CO_2 and p"O_2, were the outlet gas composition of the corresponding reactor chamber. It was presumed the flow patterns in both chambers were close to perfect mixing, such that the membrane was exposed to the same driving force as seen from the gas analysis for both reactor chambers. In actual practice gas flow may bypass a small proportion of permeate side chamber (see Appendix IV for residence time distribution) resulting overestimated driving forces. For uphill regime where p"O_2 was relatively small comparing with the feeding oxygen partial pressure, the feeding O_2 partial pressure can be used as an approximation. The CO_2 flux values with unit of $ml \cdot cm^{-2} \cdot min^{-1}$ were calculated according to equation 2.2 for downhill regime and equation 5.2 for uphill regime.

The measured CO_2 flux and partial pressures at 600°C were firstly fitted into the logarithm model proposed by Zhang et al. (Figure 6.5). On the horizontal axis, the driving force term with values of 0-3 were in the uphill regime, including all data points from set 1 and 2. Set 3 experiments with driving force values of 4-7 belonged to the downhill regime. The logarithmic model indicated that if the data points in this plot had a linear correlation, the CO_2-O_2 co-permeation would be a bulk CO_3^{2-} diffusion limiting process. The data points from set 1 and 2 showed linear correlations within their own set, but trends of the three sets of experiments did not seem to be connective with each other. Arguably, each individual set of experiments were performed using separate membranes, the flux and driving force measurements cannot be 100% reproducible through different membranes. Nevertheless, the set 3 experiments presented in the plot, which were performed using the same membrane, showed inconsistent trend when feeding 1% CO_2 + 20% O_2 and 0.5% CO_2 + 20% O_2. According to the model, the driving forces of these two feed compositions were similar to the 2.5% CO_2 + 19% O_2, because of smaller CO_2 and O_2 partial pressures on membrane permeate side. However, the observed fluxes were significantly lower. It could indicate that permeate side CO_2 and O_2 partial pressures could be less influential on the CO_2 flux than this model predicted.

Figure 6.6 provided another example of poorly fitted CO_2 flux-driving force correlation. When the measured CO_2 fluxes and driving forces at 600°C were fitted into equation 2.43 that described surface peroxide ions (O_2^{2-}) or superoxide ions (O_2^-) formation limiting scenarios, the data from each set of experiment neither integrated with each other, nor did the individual data set showed a good degree of linearity. Therefore, it can be concluded that the surface sub-reactions $1/2O_2 + CO_3^{2-} \leftrightarrow O_2^{2-} + CO_2$ and $3/2O_2 + CO_3^{2-} \leftrightarrow 2O_2^- + CO_2$ were unlikely the rate limiting steps for CO_2-O_2 co-permeation through LSCF6428-carbonate membranes. In addition, the other possible rate limiting sub-reactions namely peroxycarbonate ions formation ($1/2O_2 + CO_3^{2-} \leftrightarrow CO_4^{2-}$) and superoxycarbonate ions formation ($O_2 + CO_3^{2-} \leftrightarrow CO_5^{2-}$) can be directly ruled out by set 2 experiments. The flux models for these scenarios were solely pO_2 dependant. However, based on the result of set 1 and 2 experiments, the CO_2 flux not only

dropped with decreasing feed side pO_2 at constant feed side pCO_2, but also with decreasing feed side pCO_2 at constant feed side pO_2. Thus, the experimental results and the model expressions were in contradiction.

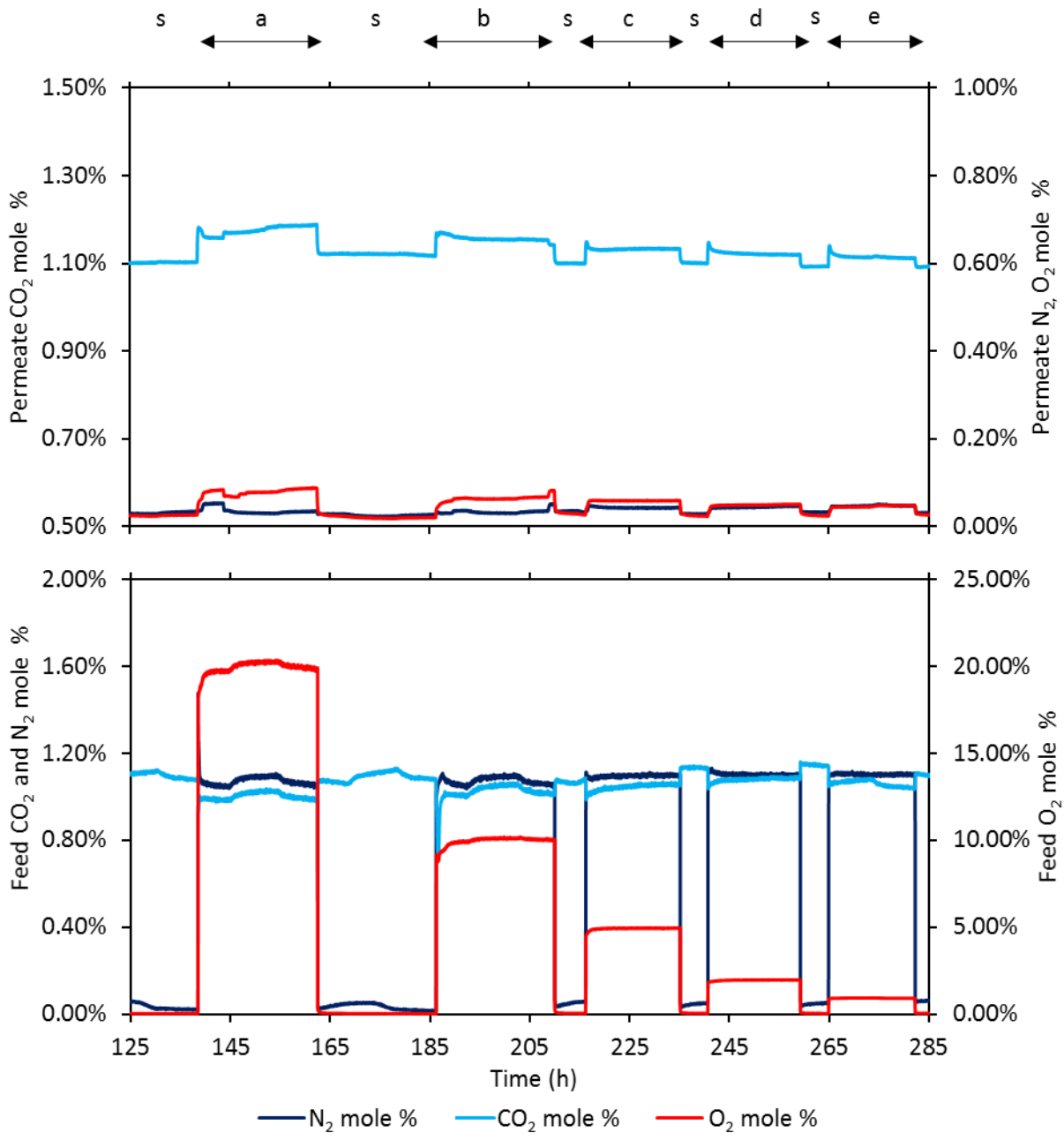

Figure 6.3: Set 1 uphill CO_2 flux-driving force experiments at 600°C consisting of four symmetrical operations (1.1% CO_2/Ar gas flow on both sides of the membrane), represented by 's'. These were alternated with five asymmetrical operations shown as region a-e: (a) feeding 1.04% CO_2 + 19.6% O_2; (b) feeding 1.04% CO_2 + 9.9% O_2; (c) feeding 1.05% CO_2 + 5.0% O_2; (d) feeding 1.05% CO_2 + 2.2% O_2; (e) feeding 1.05% CO_2 + 1.2% O_2. 1.1% CO_2/Ar composition was used as sweep gas for the entire experiment.

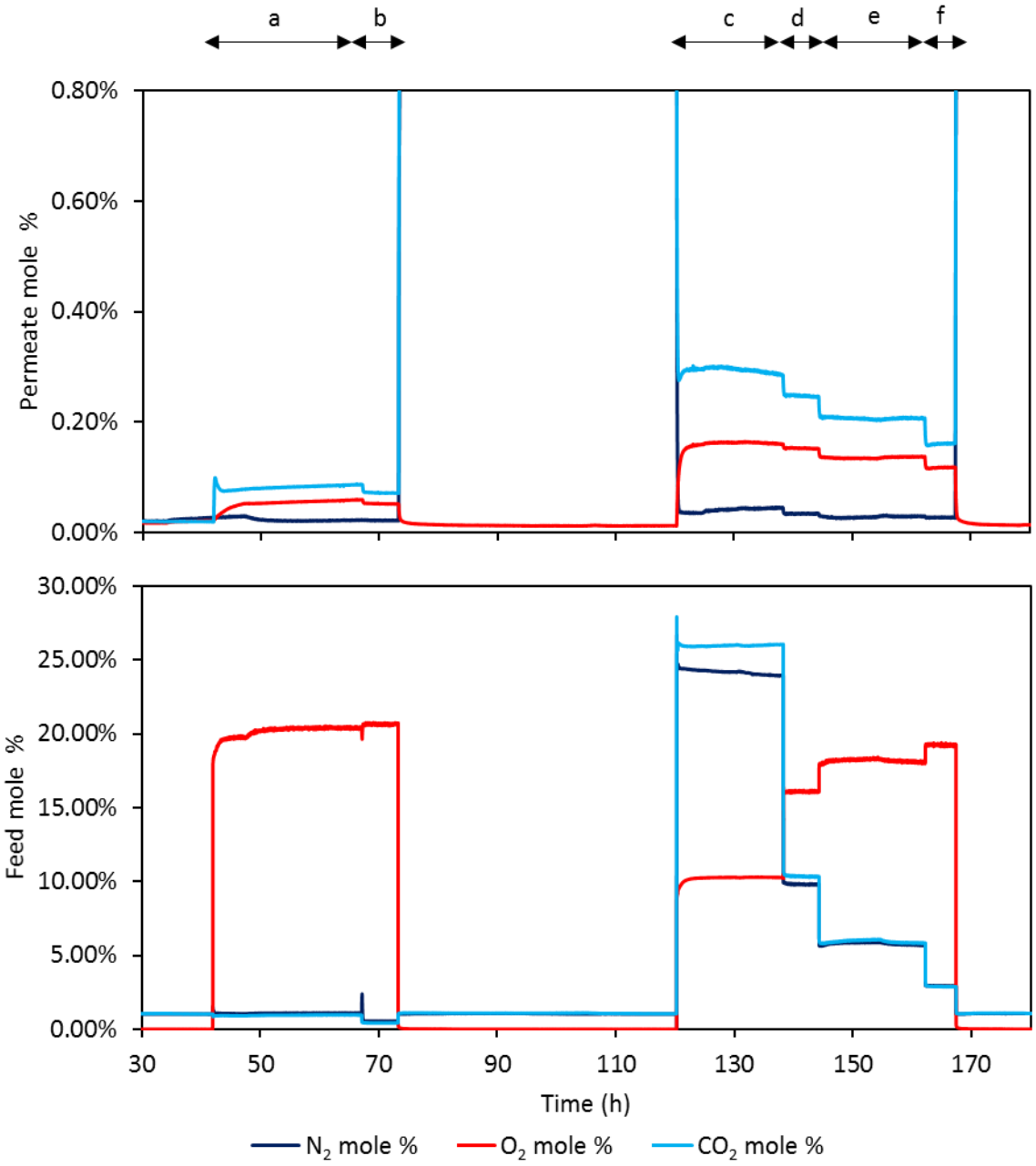

Figure 6.4: Set 3 downhill CO_2 flux-driving force experiments at 600°C consisting of six regions. (a) Feeding 1.04% CO_2 + 19.6% O_2. (b) Feeding 0.54% CO_2 + 19.8% O_2. (c) Feeding 25.1% CO_2 + 10.0% O_2. (d) Feeding 10.0% CO_2 + 16.0% O_2. (e) Feeding 5.46% CO_2 + 17.8% O_2. (f) Feeding 2.40% CO_2 + 19.1% O_2. Sweep gas was 100% Ar for region a to f. The gap between b and c represented a normal symmetrical operation keeping the membrane under 1.1% CO_2/Ar on both sides.

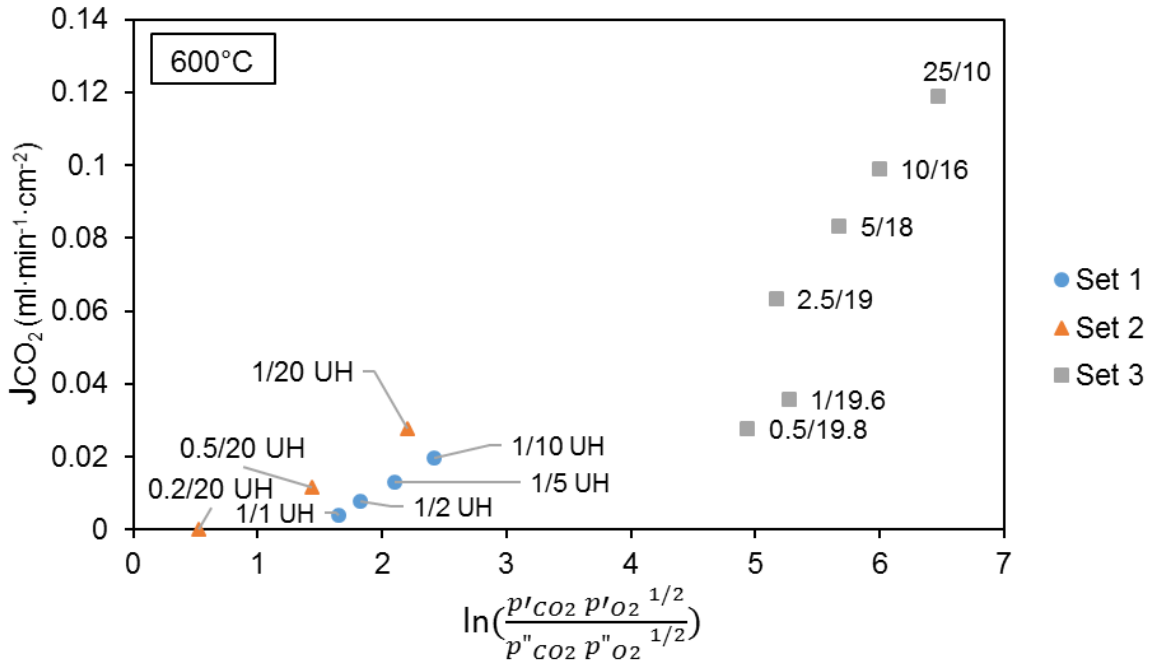

Figure 6.5: Plot of CO_2 flux against driving force using data points obtained from set 1, set 2 and set 3 experiments at 600°C, fitted into the logarithm relationship depicted in equation 2.41. Notations in a format of x/y were shown beside each point, with x representing the CO_2 mole percentages of feed inlet stream and y representing the O_2 mole percentages of feed inlet stream. UH indicates experiments in the uphill regime.

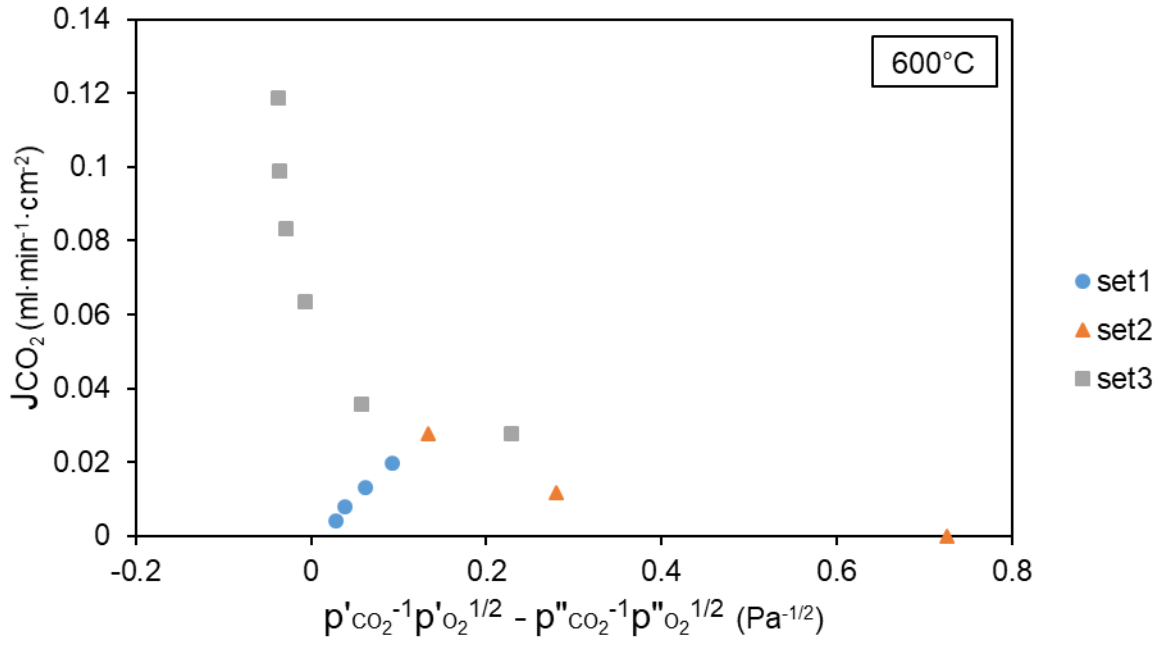

Figure 6.6: Plot of CO_2 flux against driving force using data points obtained from set 1, set 2 and set 3 experiments at 600°C, fitted into the linear relationship that described surface peroxide ions (O_2^{2-}) or superoxide ions (O_2^-) formation limiting scenarios depicted in equation 2.43 and 2.44.

In contrast, the data fit according to equation 6.5 and 6.10, which described linear CO_2 flux-driving force correlation corresponding to either bulk CO_3^{2-} diffusion limiting or global interactional reaction limiting ($CO_2 + 1/2O_2 + 2e^- \leftrightarrow CO_3^{2-}$) scenarios, showed the best integrity among all possible CO_2 flux-driving force models. Overall, the three data sets combined each other well and a coherent trend of CO_2 flux-driving force correlation can be observed (Figure 6.7).

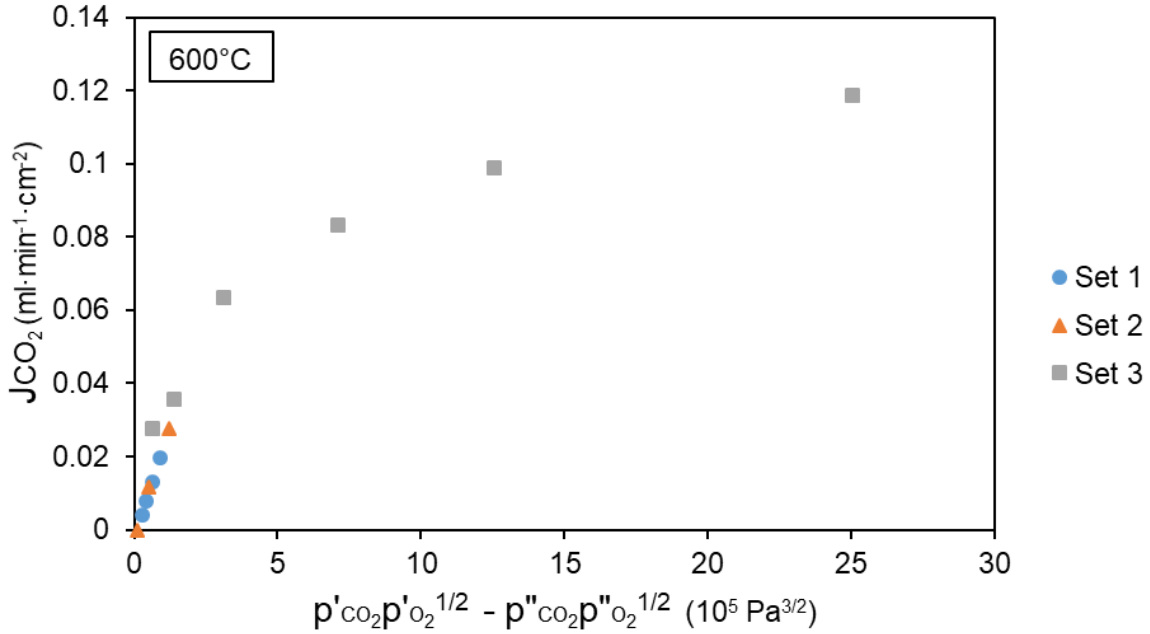

Figure 6.7: Plot of CO_2 flux against driving force using data points obtained from set 1, set 2 and set 3 experiments at 600°C, fitted into the linear relationship that described either the bulk CO_3^{2-} ion diffusion limiting scenario or the global interfacial reaction ($CO_2 + 1/2O_2 + 2e^- \leftrightarrow CO_3^{2-}$) limiting scenario depicted in equation 6.5 and 6.10 respectively.

Looking into details of the correlation in Figure 6.7, the trend remained better linearity within the uphill regime. This regime with relatively smaller driving forces were magnified in Figure 6.8, which included set 1 and set 2 data only. As the driving force expanded broader into the downhill regime, the linearity seemed to lose at above 2.5% CO_2 + 19% O_2 feeding gas composition. The CO_2 flux increased more gradually with increasing driving force and eventually turned towards an asymptote at the higher end of the driving force range. Thus, the experimental result was in favour of bulk CO_3^{2-} diffusion or global interactional reaction limiting for CO_2-O_2 co-permeation within uphill (low driving forces) regime. However, the data so far could not reveal whether the uphill regime was bulk diffusion or interfacial reaction limiting. Possible reasons for the loss of linearity in large driving force regime was unclear either. Further data analysis will be required in order to seek further explanations.

The general trend in Figure 6.7 implied that with a relatively more appropriate model, higher driving force would always lead to higher CO_2 flux. However, occasional offsets for some data points may exist. The systematic error of gas analysis and the reproducibility of the experiment could be the main reasons.

The reproducibility issue arose because it was impractical to perform all flux-driving force experiments using the same membrane, due to thermochemical degradation of the membrane and the sealant material. It has to be acknowledged that it was difficult to obtain identical O_2 flux for different membranes fabricated in the same batch. This was likely caused by minor trans-membrane leak, affecting the consistency of permeate side O_2 partial pressure. In this case, although the CO_2 flux and driving force should change correspondingly, the position of the shifted data point should still fit the appropriate model. The systematic error of gas analysis was a more significant issue, especially for uphill regime where the CO_2 flux was low. The uncertainty of mass spectrometer and CO_2 IR analyser could be up to 50-100ppm, which was high enough to deviate from main trend shown in Figure 6.7 and 6.8.

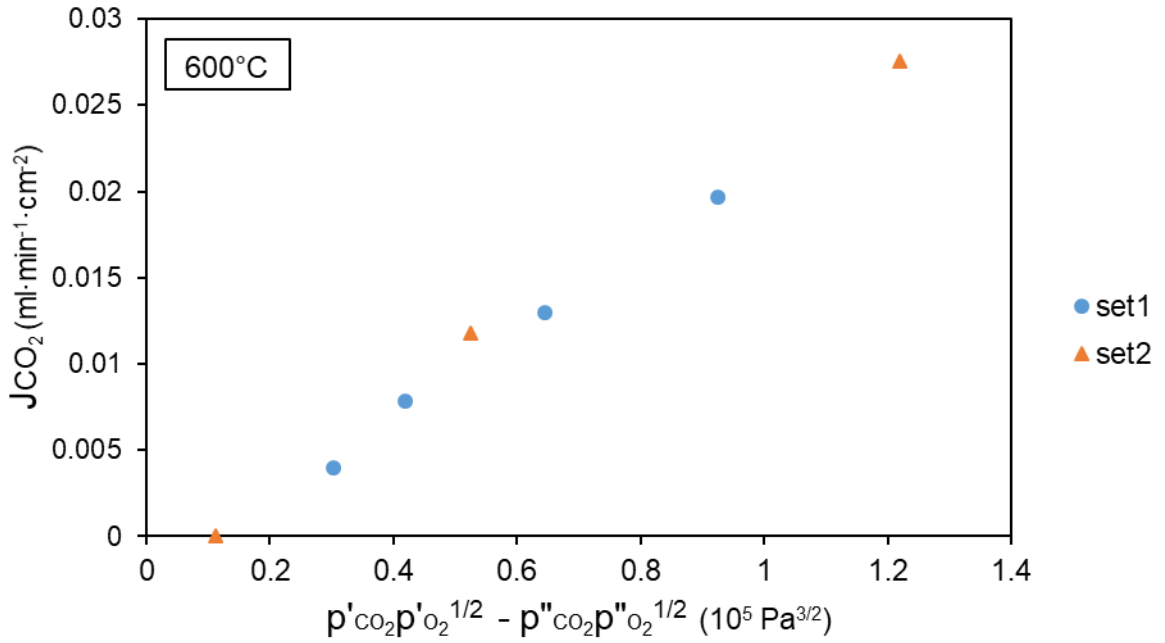

Figure 6.8: Plot of CO_2 flux against driving force using data points obtained from set 1 and set 2 only at 600°C, fitted into the linear relationship that described either the bulk CO_3^{2-} ion diffusion limiting scenario or the global interfacial reaction ($CO_2 + 1/2O_2 + 2e^- \leftrightarrow CO_3^{2-}$) limiting scenario depicted in equation 6.5 and 6.10 respectively. All data points involved in this plot located within the uphill regime.

6.2.3. Isothermal permeation experiments at 800°C

The flux-driving force experiments at 800°C followed very similar operating procedure as 600°C using the same gas analysis technologies. The original experimental data was also in a similar format as Figure 6.3 and 6.4. Here, feed and permeate side gas analysis for set 2 experiments at 800°C is shown as an example (Figure 6.9). Comparing with 600°C, the result generally exhibited two main differences at 800°C. Firstly, the CO_2 flux values were higher under the same driving force condition. Secondly, significant CO_2 transient peaks can be observed at the beginning of every asymmetrical operation, which corresponded to the more prominent LSCF6428 oxygen deficiency under symmetrical operation.

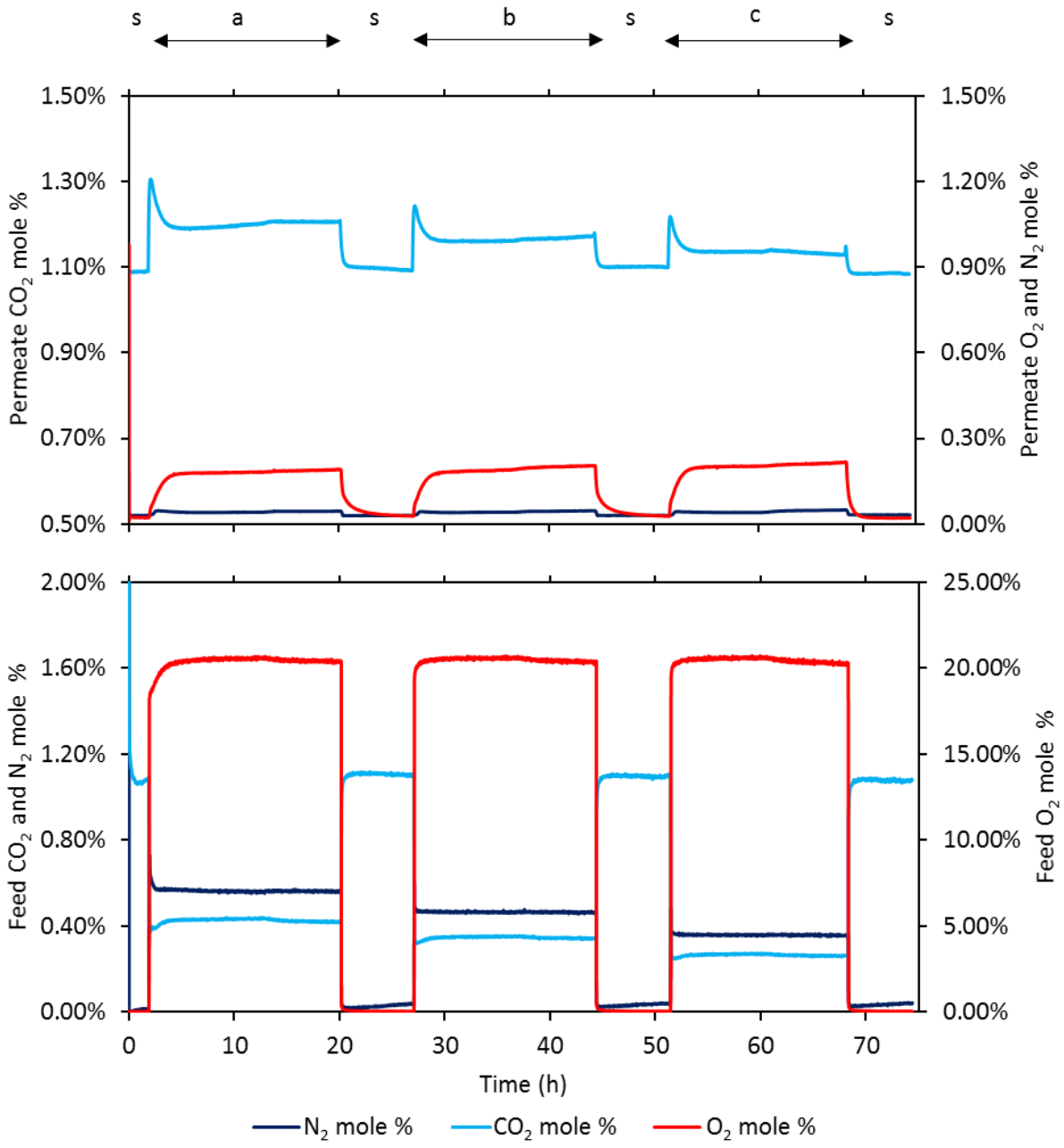

Figure 6.9: Set 2 uphill CO_2 flux-driving force experiments at 800°C consisting of four symmetrical operations represented by 's'. These were alternated with three asymmetrical operations shown as region a-c: (a) feeding 0.52% CO_2 + 20.0% O_2; (b) feeding 0.42% CO_2 + 19.9% O_2; (c) feeding 0.31% CO_2 + 19.9% O_2. The sweep gas of the experiment was a consistent 1.1% CO_2/Ar composition.

Despite the stronger variation in LSCF6428 nonstoichiometry at 800°C, the CO_2 permeation flux was able to approach steady state, the condition that satisfied the assumption made for establishing the models. The logarithm correlation fit at 800°C in Figure 6.10 failed to show a good degree of linearity. Notably, the set 1 and set 2 experiments were performed successively on the same membrane. The trend lines of the individual set clearly split. Although this was a relatively prolonged experiment, there was

no sign of deteriorating membrane sealing or trans-membrane leak based on the consistency of O_2 flux. It is more evident that at 800°C the driving force expressed in logarithm format does not represent the true driving force for CO_2-O_2 co-permeation. Plot of CO_2 flux against the driving force in the format of $p'CO_2^{-1}p'O_2^{1/2} - p''CO_2^{-1}p''O_2^{1/2}$ (Figure 6.11) showed non-linearity and discontinuity between individual sets. Therefore, surface peroxide ions (O_2^{2-}) and superoxide ions (O_2^{-}) formation limiting scenarios were also ruled out for 800°C. It can also be found that at 800 °C the CO_2 flux was dependant on both CO_2 and O_2 partial pressures, making the CO_4^{2-} and CO_5^{2-} formation mechanisms unfavourable.

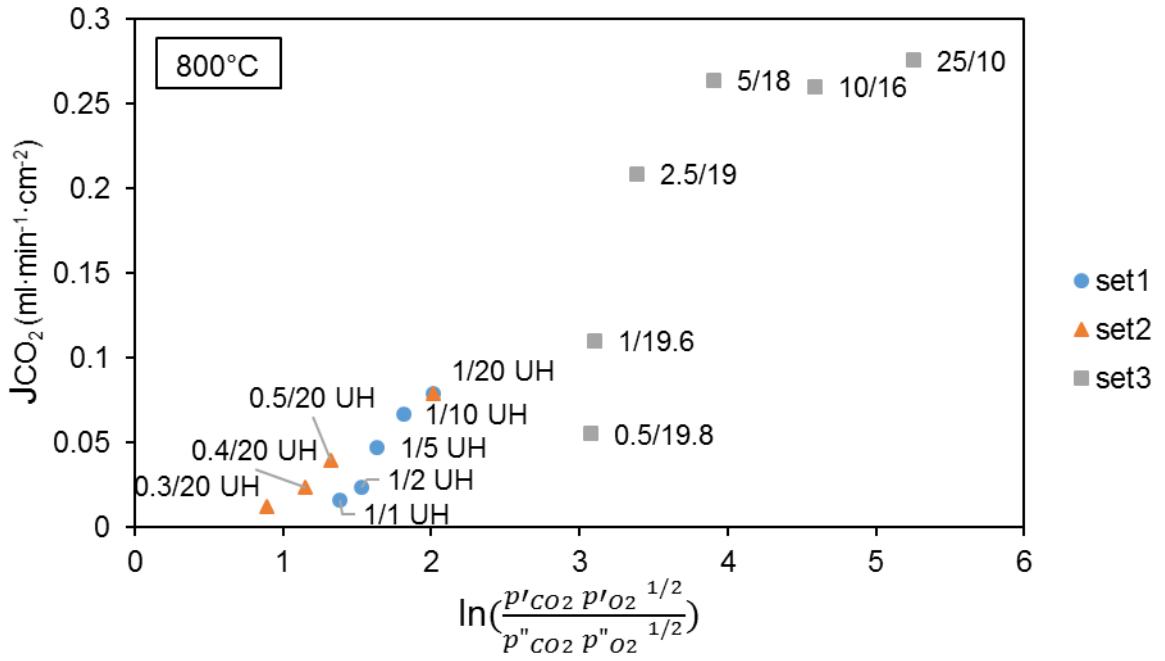

Figure 6.10: Fitting data points obtained from set 1, set 2 and set 3 experiments at 800°C into the logarithm CO_2 flux-driving force correlation. Notations in a format of x/y were shown beside each point, with x representing the CO_2 mole percentages of feed inlet stream and y representing the O_2 mole percentages of feed inlet stream. UH indicates experiments in the uphill regime.

The bulk CO_3^{2-} diffusion limiting and global interfacial reaction limiting scenarios were worth further discussions. The CO_2 flux against $p'CO_2p'O_2^{1/2} - p''CO_2p''O_2^{1/2}$ plot (Figure 6.12) still exhibit two distinct features over the two driving force regimes. The correlation showed good linearity at lower driving force (uphill regime) and tended to approach asymptote at the large end of the driving force (downhill regime). More importantly, the three data sets showed excellent continuity across the whole range of driving forces. The linear region exhibited much steeper gradient comparing with 600°C, and the region extended well beyond the uphill regime into larger driving forces, followed by a sharper approach towards the asymptote. This indicated that the data analysis could be focused on comparing the gradient of the linear regions at two operating temperatures and matching them to the proportionality parameters in equation 6.5 and 6.10. The analysis will be further discussed in Chapter 6.3 in order to obtain mechanistic insights for CO_2-O_2 co-permeation based on the experimental data.

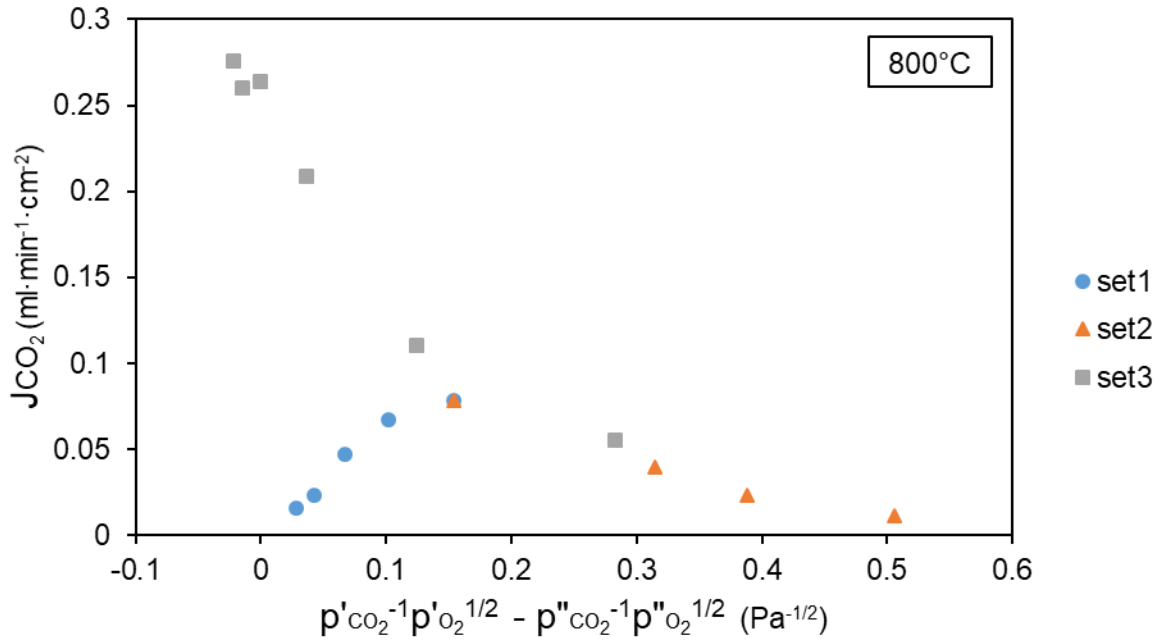

Figure 6.11: Plot of CO_2 flux against driving force ($p'CO_2^{-1}p'O_2^{1/2}$ - $p''CO_2^{-1}p''O_2^{1/2}$) at 800°C, which described surface peroxide ions (O_2^{2-}) or superoxide ions (O_2^{-}) formation limiting scenarios depicted in equation 2.43 and 2.44.

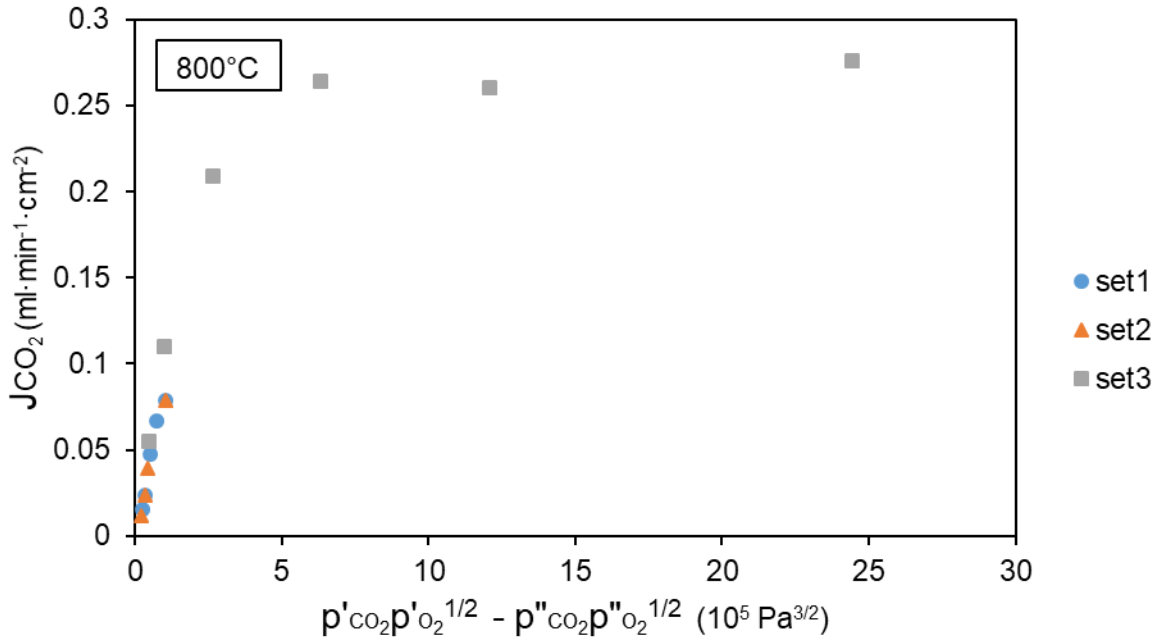

Figure 6.12: Plot of CO_2 flux against driving force ($p'CO_2p'O_2^{1/2}$ - $p''CO_2p''O_2^{1/2}$) at 800°C, which described either the bulk CO_3^{2-} ion diffusion limiting scenario or the global interfacial reaction ($CO_2 + 1/2O_2 + 2e^- \leftrightarrow CO_3^{2-}$) limiting scenario depicted in equation 6.5 and 6.10 respectively.

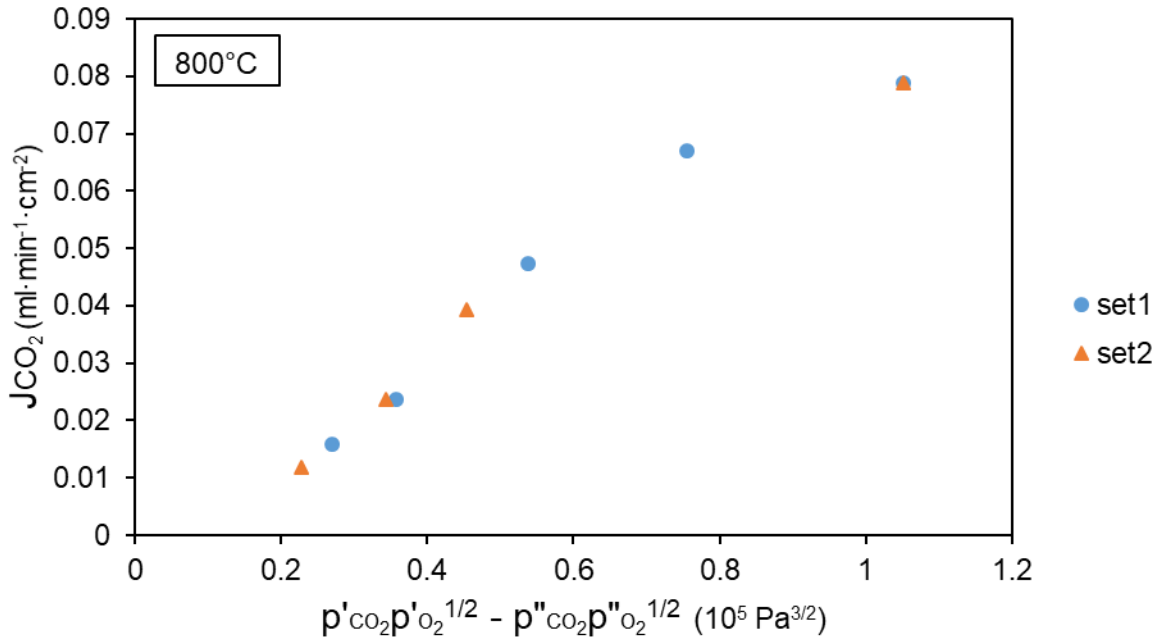

Figure 6.13: Plot of CO_2 flux against driving force ($p'CO_2p'O_2^{1/2}$ - $p''CO_2p''O_2^{1/2}$) at 800°C within the uphill regime, only using the data points obtained from set 1 and set 2 experiments.

6.3. Mechanistic insight on CO_2-O_2 co-permeation

6.3.1. Interpreting the uphill regime

Having fitted the experimental data into various models representing different rate determining scenarios, CO_2 flux against $p'CO_2p'O_2^{1/2}$ - $p''CO_2p''O_2^{1/2}$ plot was found to be the best fit. This section focuses on further discussion and interpretation based on the bulk CO_3^{2-} diffusion model and global interfacial reaction model. The data analysis started with finding out the gradients of the linear region shown in Figure 6.8 and 6.13. A linear fit line was added in Figure 6.14 for the uphill regime at 600°C. With these operating conditions, parallel mechanisms that allowed O_2 and CO_2 to transport across the membrane independently were insignificant. Thus, it is reasonable to presume that the observed uphill CO_2 permeation flux was attributed to the proposed CO_2-O_2 co-permeation mechanism. However, at 800°C much higher oxide ion conductivity in bulk LSCF6428 phase facilitated individual electrochemical transport of CO_2. The linear fitting line for 800°C in Figure 6.15 not only included the data within the uphill regime (set 1 and set 2), but also incorporated two extra data points in the downhill regime (feeding 0.5% CO_2 + 20% O_2 and 1% CO_2 + 20% O_2). For these two data points, individual CO_2 transport mechanism superimpose with the co-permeation mechanism. Flux of individual CO_2 transport was determined by the reference experiments feeding the same CO_2 concentration in absence of O_2 (Chapter 4.4) and subtracted off from the observed flux. On the other hand, the individual CO_2 transport mechanism would theoretically facilitate backwards CO_2 permeation from membrane permeate to feed

side. Due to very limited chemical potential difference of CO_2, the effect of back permeation on the observed uphill CO_2 flux was negligible.

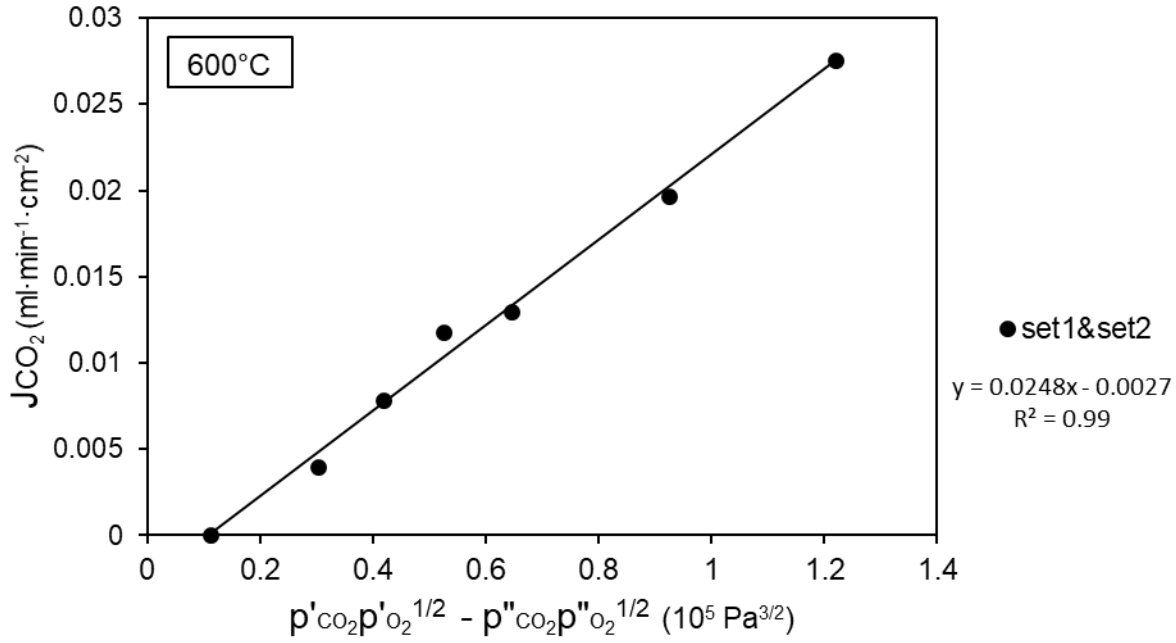

Figure 6.14: Plot of CO_2 flux against driving force ($p'CO_2p'O_2^{1/2}$ - $p''CO_2p''O_2^{1/2}$) for the linear region (uphill regime) at 600°C, incorporating the equation of the linear fit line.

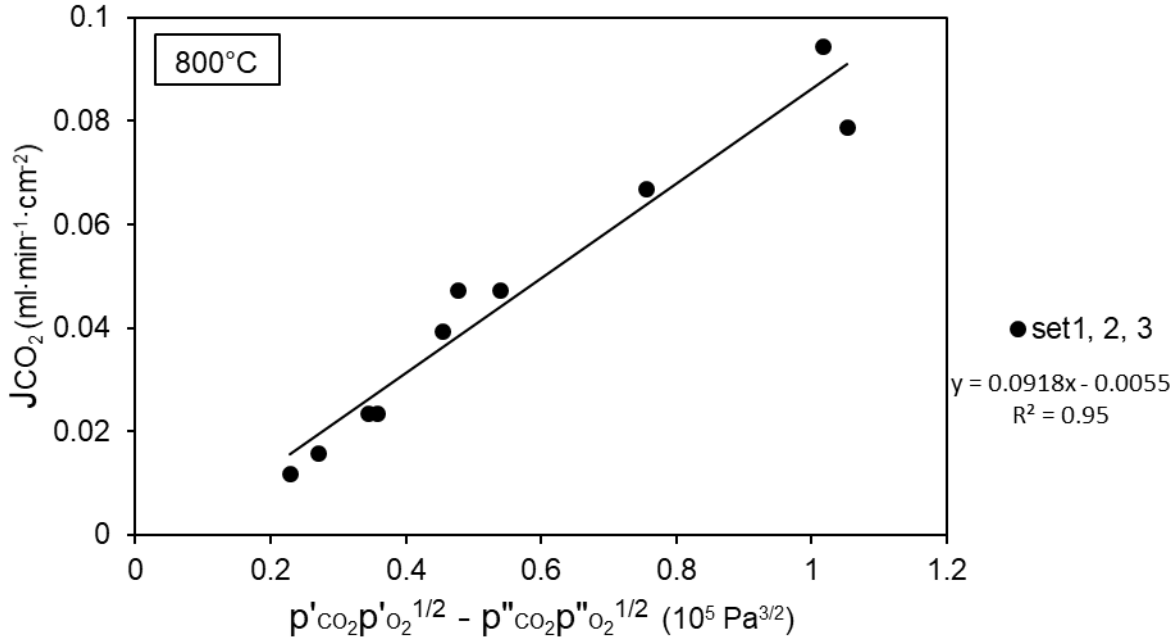

Figure 6.15: Plot of CO_2 flux against driving force ($p'CO_2p'O_2^{1/2}$ - $p''CO_2p''O_2^{1/2}$) for the linear region (uphill regime and two extra points of downhill regime) at 800°C, incorporating the equation of the linear fit line.

The gradients of the linear region at 600 and 800°C were 0.0248 and 0.0918 respectively. Linear fitting lines exhibited R^2 value of 0.99 and 0.95, indicating good degree of linearity. The gradients in standard SI unit were 1.84×10^{-9} mol·s^{-1}·m^{-2}·Pa$^{-3/2}$ for 600°C and 6.83×10^{-9} mol·s^{-1}·m^{-2}·Pa$^{-3/2}$ for 800°C, which directly linked with the proportionality factors of the model equations as shown below:

$$J_{CO_2} = \Gamma \left(p'_{CO_2} p'^{1/2}_{O_2} - p''_{CO_2} p''^{1/2}_{O_2}\right) \qquad (6.11)$$

$$\Gamma = \frac{\varepsilon\varphi}{\tau} \frac{RT}{4F^2\delta} K q u_{CO_3^{2-}} \qquad (6.12)$$

$$\Gamma = \frac{k_f}{2} \qquad (6.13)$$

Referring to equation 6.5 and 6.10, if the CO_2 permeation were bulk CO_3^{2-} diffusion limiting, the gradient Γ would be expressed as equation 6.12. If the CO_2 permeation were global interfacial reaction rate limiting, the gradient Γ would be expressed as equation 6.13. Since the global interfacial reaction rate constant k_f in unknown, it is necessary to estimate the parameters in equation 6.12 at relevant temperatures and comparing the product with the gradient of linear fit line.

Majority of the parameters in equation 6.12 are constants that independent of operating temperature. The gas constant R, Faraday constant F and membrane thickness δ have fixed values. Unitless membrane microstructural terms including porosity ε (~0.4) and turtuosity τ (~1.5) of the porous LSCF6428 network as well as carbonate volumetric fraction φ (~0.4) can be estimated based on membrane geometry and microstructural SEM analysis. The charge of a single CO_3^{2-} ion is 3.2×10^{-19}C and by multiplying this value by the Avogadro constant N_A, the molar charge of CO_3^{2-} ions q can be calculated which has a value of 1.93×10^5 C·mol^{-1} or A·s· mol^{-1}.

The equilibrium constant K of the global interfacial reaction and the CO_3^{2-} ion mobility are constants isothermally but temperature dependent. The CO_3^{2-} ion mobility can be described in terms of CO_3^{2-} self-diffusion coefficient using the Einstein relation below [86]:

$$u_{CO_3^{2-}} = \frac{zDF}{RT} \qquad (6.14)$$

Here, D is the CO_3^{2-} self-diffusion coefficient; z is the charge number of the CO_3^{2-} ion and F is the faraday constant. Spedding and Mills successfully measured the CO_3^{2-} diffusion coefficient within ternary carbonate melt using the open-ended capillary method. It turned out that the experimental diffusion coefficient values in a temperature range of 690-1130K were able to fit into an exponential diffusion equation shown as equation 6.15:

$$D = A exp\left(\frac{-E_a}{RT}\right) \qquad (6.15)$$

They obtained that the pre-exponential factor A = 1.58×10^{-7} m^2/s and the activation energy E_a = 42.2 kJ/mol [87]. Using these parameters, we can estimate that the CO_3^{2-} diffusion coefficient at 600°C is 0.47×10^{-9} m^2/s and 1.44×10^{-9} m^2/s at 800°C. According to the Einstein relation, the CO_3^{2-} ion mobility will be 1.25×10^{-8} $m^2 \cdot V^{-1} \cdot s^{-1}$ at 600°C and 3.12×10^{-8} $m^2 \cdot V^{-1} \cdot s^{-1}$ at 800°C.

The equilibrium constant K of the global interfacial reaction contributed to large uncertainty to the gradient Γ shown in equation 6.12, as the K values cannot be directly obtained from existing literatures. To take a rough estimation, it was required to split the reaction into three parts:

$$CO_2 + M_2O \leftrightarrow M_2CO_3 \qquad (6.16) \qquad K_1 = \frac{X_{M_2CO_3}}{p_{CO_2} X_{M_2O}} \qquad (6.17)$$

$$1/2O_2 + 2M^+ + 2e^- \leftrightarrow M_2O \qquad (6.18) \qquad K_2 = \frac{X_{M_2O}}{p_{O_2}^{1/2} a_{M^+}^2} \qquad (6.19)$$

$$M_2CO_3 \leftrightarrow 2M^+ + CO_3^{2-} \qquad (6.20) \qquad K_3 = \frac{a_{M^+}^2 [CO_3^{2-}]}{X_{M_2CO_3}} \qquad (6.21)$$

In reaction 6.16, 6.18 and 6.20, M represents the ternary mixture of alkali metals Li, Na and K. corresponding equilibrium constants of these equations can be written as equation 6.17, 6.19 and 6.21 where a represents activity, X represents mole fractions and $[CO_3^{2-}]$ represents carbonate concentration. The assumption here was that the molten salt and alkali metal oxides was in a form of ideal mixture. By this way, the equilibrium constants of individual parts can be calculated, if not directly available from molten salts literature. The equilibrium constant K of the global interfacial reaction would be the product of K_1, K_2 and K_3.

K_1 can be calculated from the equilibrium dissociation constant K_d, which describes the thermodynamic equilibrium of ternary carbonate with CO_2 partial pressure. This has been reviewed in Chapter 2.2.3 (see equation 2.21 to 2.23). Based on Anderson, B.K's measurement of K_d across a temperature range between 800 to 1200K using emf technique, the value of K_d was 1.81×10^{-4} Pa at 600°C and 0.140 Pa at 800°C [84]. A rearrangement of $K_1 \times K_3$ would have the following relation with K_d:

$$K_1 \times K_3 = \frac{a_{M^+}^2 [CO_3^{2-}]}{K_d \times X_{M_2CO_3}} \qquad (6.22)$$

Looking at Anderson, B.K's measurement of K_d [84] and Spedding and Mills' measurement equilibrium dissociation CO_2 pressure [87] together, it has been suggested that the mole fraction of M_2O in the melt must be in the order of 10^{-5} or smaller between 600 and 800°C to match the observed K_d and dissociation CO_2 pressure. Thus, mole fraction of M_2CO_3 in the melt was approximately 1. The activity of the M^+ ions was also assigned as unity as an approximation. The ternary carbonate mixture consisted of equal weight of Li, Na and K carbonates such that the total number of moles of carbonate ion can be obtained.

The concentration of the carbonate ions can be estimated as 2.02×10^4 mol/m^3 knowing the molten salt volume within the membrane porous network.

To estimate K_2 as shown in reaction 6.18, standard Gibbs free energies of alkali oxides formation for Li, Na and K at both 600 and 800°C are available in literature [137]. Standard Gibbs free energies of alkali ions formation can be estimated from the literature data [138], assuming the heat capacity values of the ions stay constant and their standard entropy values are small. The standard Gibbs free energy of reaction 6.18 for the ternary Li, Na and K mixture can then be averaged from the individual values according to the mole fraction ratio of 43:31:26, giving a standard Gibbs free energy of 112.6 kJ/mol at 600°C and 141.4 kJ/mol at 800°C. The equilibrium constant K_2 at 600 and 800°C can be calculated based on the same principle as equation 2.22, giving $K_2 = 1.81 \times 10^{-7}$ Pa$^{-1/2}$ and 1.29×10^{-7} Pa$^{-1/2}$ at 600 and 800°C respectively. The overall equilibrium constant K turned out to be 20.2 mol·m^{-3}·Pa$^{-3/2}$ at 600°C and 0.019 mol·m^{-3}·Pa$^{-3/2}$ at 800°C using this approach of estimation. Hence, the values of gradient Γ based on CO_3^{2-} diffusion limiting assumption were summarised in Table 6.2.

Table 6.2: Comparing the observed gradients of the linear flux-driving force correlation and the calculated theoretical gradient Γ (in equation 6.12) based on CO_3^{2-} diffusion limiting assumption.

Temperature **°C**	**Theoretical estimation** **mol·s^{-1}·m^{-2}·Pa$^{-3/2}$**	**Observed gradient** **mol·s^{-1}·m^{-2}·Pa$^{-3/2}$**
600	6.54×10^{-7}	1.84×10^{-9}
800	1.81×10^{-9}	6.83×10^{-9}

In principle, comparable theoretical and observed gradients would indicate a CO_3^{2-} diffusion limiting scenario; significantly higher theoretical gradients would indicate an interfacial reaction limiting scenario. The calculated theoretical gradient was two orders of magnitude higher than the observed value at 600°C. At higher temperature, the theoretical gradient dropped but the observed gradient increased, such that they were more comparable at 800°C. It indicated that the CO_2 permeation in the presence of O_2 were an interfacial reaction limited process at 600°C. However, the rate of CO_3^{2-} diffusion became an important factor at 800°C, although there was no direct evidence that the permeation had shifted to a purely CO_3^{2-} diffusion limiting process.

In a broader range of operating temperature, hypothetical trends of the proportionality factor Γ as a function of temperature in both reaction and diffusion rate limiting scenario were plotted in Figure 6.16. The reaction rate constant followed a trend of exponential growth with operating temperature due to a positive reaction activation energy E_{a1}. For the diffusion limiting scenario, the trend was determined by the relative temperature dependency of the CO_3^{2-} diffusion coefficient (activation energy of CO_3^{2-} diffusion E_{a2}) and the interfacial reaction equilibrium constant K (standard Gibbs free energy of the

interfacial reaction $\Delta G_r^{\ominus}$). It would be a reversed trend to the reaction limiting scenario according to previous calculation. Based on the theoretical analysis and the experimental results, it is likely that the permeation shifted from a reaction limiting to diffusion limiting process at some point above 800°C. The overall observed flux with a fixed driving force would be deviating from the exponential trend, approaching an upper limit at this point and starting to drop beyond this point. The temperature dependence of the downhill CO_2 permeance with O_2 co-permeation (Figure 5.9), which had a diving force within the linear region, was coherent with this hypothesis. Ideally, CO_2 permeance at higher temperature can be tested to provide a stronger evidence. However, with the existing set-up and sealing technology, it would be difficult to measure the CO_2 flux beyond 900°C accurately.

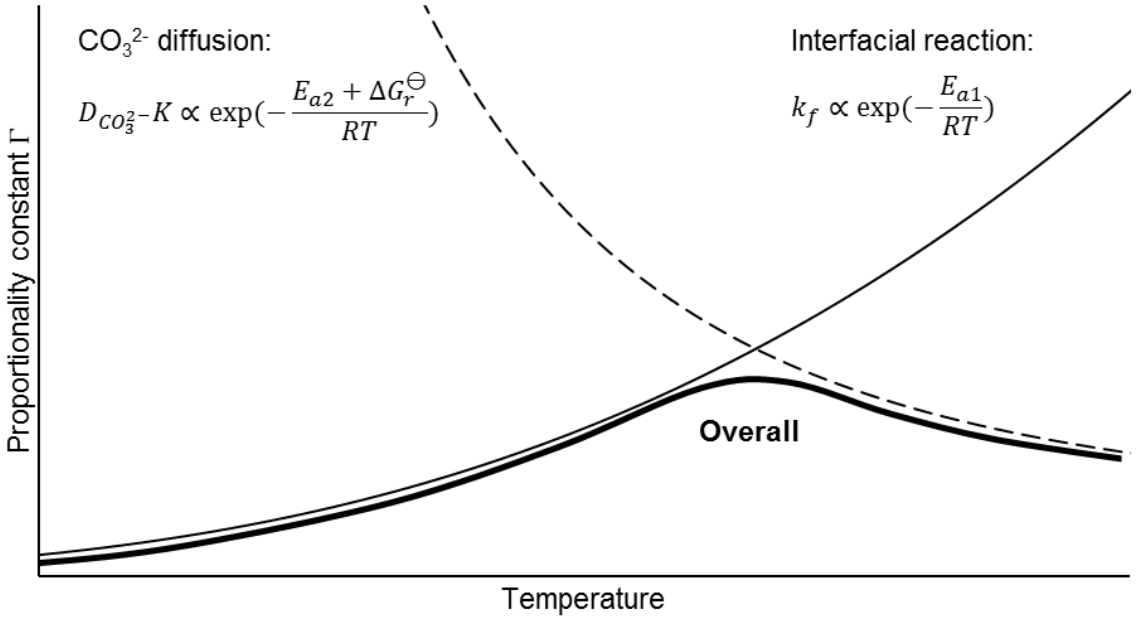

Figure 6.16: Possible trends of the proportionality constant Γ in equation 6.11 for reaction (solid line) and diffusion (dashed line) limiting scenarios with respect to operating temperature. The overall trend (thick line) represented the combinatory proportionality constant incorporating both individual trends.

It must be acknowledged that the calculated gradient was a rough estimation, especially the thermodynamic equilibrium constant of the global interfacial reaction. Nevertheless, the agreement was that the overall equilibrium constant K decreased from 600 to 800°C. Ultimately, the diffusion limiting model predicted that under the same driving force, CO_2 flux should be higher at 600°C. However, the experimental observation opposed this prediction. This means within this temperature range the global interfacial reaction cannot reach thermodynamic equilibrium instantaneously in the first place. Therefore, based on the flux-driving force correlation of the uphill regime, the permeation was unlikely to be purely bulk CO_3^{2-} diffusion limited. The global interfacial reaction cannot be assumed a faster process and may well be a determining factor for the overall CO_2 permeation flux at least below 800°C. This argument can also be supported by the apparent activation energy for uphill CO_2 permeation (53.7

kJ/mol) found in Chapter 5.4.3. With this activation energy, the ratio of CO_2 flux at 800 and 600°C under the same driving force should be 3.97 according to the Arrhenius equation, which is consistent with the gradient ratio of 3.71 found here. Whilst the activation energy of carbonate ion conduction via molten ternary carbonate (31 kJ/mol) was lower than the apparent activation energy. The possibility of the diffusion limiting scenario remained above 800°C as previously discussed.

6.3.2. Further discussion for the downhill regime

The mechanisms for uphill and downhill CO_2 permeation are fundamentally different. Purely ionic conductive ceramic-carbonate dual phase membranes exhibit little uphill CO_2 permeance in presence of O_2. A reference uphill CO_2 permeation experiment using YSZ-carbonate membrane has been carried out at both 600 and 800°C to demonstrate this (see Appendix I). Hence, in the uphill regime the CO_2 permeation relied on the electronic conductivity within the solid phase. For MIEC type solid phase material such as LSCF6428, the ionic conductivity would only promote O_2 permeation and do not form parallel transport pathways for CO_2. In the downhill regime where the CO_2 driving force of its own became significant, there can be more than one CO_2 transport pathways especially at 800°C, introducing more complexity to the CO_2 transport mechanisms. One possible explanation for the change of CO_2 flux-driving force correlation at high driving forces would be due to the fundamental change of CO_2 transport mechanisms, such that the model based on single mechanism was no longer valid.

The change of mechanisms in response to different driving force regimes and operating temperatures should not be confined to the transport steps within the membrane. Referring to the four rate limiting scenarios in Figure 6.1, only the rate determining steps associated with the membrane were considered assuming the gas phase CO_2 mass transfer was fast. Nevertheless, it is possible that the gas phase mass transfer is a slower process. For instance, if the mass transfer on the membrane permeate side film were slow (Figure 6.17), a partial pressure difference of CO_2 would build up across the boundary layer between the membrane permeate side surface and the bulk sweep gas. The diffusive flux equation governed by the gas phase mass transfer can be written as:

$$J_g = k_g\left(p^s_{CO_2} - p"_{CO_2}\right) \qquad (6.23)$$

J_g is the rate of mass transfer or the flux of gas phase molecular diffusion in $mol \cdot s^{-1} \cdot m^{-2}$; k_g is the mass transfer coefficient in gas phase in $mol \cdot s^{-1} \cdot m^{-2} \cdot Pa^{-1}$; p^sCO_2 and $p"CO_2$ are the CO_2 partial pressure on membrane permeate side surface and in bulk sweep gas respectively. Isothermally, the CO_2 permeation flux ranged over an order of magnitude across the uphill and downhill regimes. The observed permeation flux seemed to be proportional to the partial pressure with overall power of 1.5. Whilst the rate of mass transfer is linearly dependant to the partial pressure and the mass transfer coefficient stayed the same. In principle, the permeation flux could be approaching the rate of mass transfer at higher driving force of CO_2 permeation. As a result, the relative resistance by external gas phase mass transfer

may become important, which is consistent with the trend of flux-driving force correlation that turning towards an asymptote at high driving force (Figure 6.7 and 6.12).

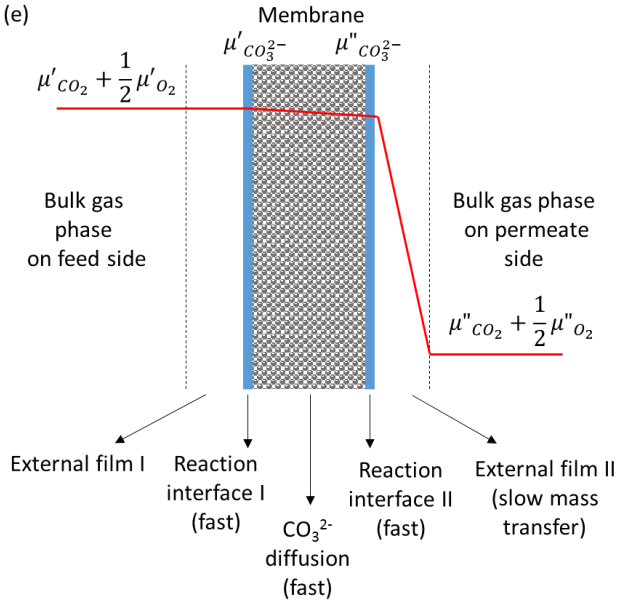

Figure 6.17: An example of another possible rate-determining scenario (e) for CO_2-O_2 co-permeation. The diagram illustrates the scenario when the CO_2 gas phase mass transfer through the external film II upon membrane permeate side surface is slower than all other steps.

It worth noting that the asymptote was particularly obvious at 800°C. The temperature dependence of the mass transfer coefficient can be further discussed. Since the diffusive mass transfer obeys Fick's Law of diffusion, the rate of mass transfer can also be written as equation 6.24. By integrating over the thickness of the external film L and the partial pressure difference, it can be shown that the mass transfer coefficient k_g is proportional to the gas phase mass diffusivity D_g and inversely proportional to temperature T and the thickness of the external film L.

$$J_g = -\frac{D_g}{RT}\frac{dp}{dL} = \frac{D_g}{RTL}(p^s_{CO_2} - p''_{CO_2}) \qquad (6.24)$$

The temperature dependency of mass diffusivity D_g can be predicted using the Stefan-Maxwell model of binary diffusion, which states $D_g \propto T^{1.5}$. Therefore, k_g is proportional to $T^{0.5}$ [139]. We have previously demonstrated exponential growth of CO_2 uphill permeation flux between 600 and 800°C, and up to 750°C for downhill permeation. If the permeation flux were more strongly temperature dependant than the rate of mass transfer, it would be possible that the mass transfer limits CO_2 transport at higher temperature. Quantitatively, literature has suggested the gas phase mass diffusivity of CO_2 molecules in the air is 1.64×10^{-5} m^2/s at 25°C and 10^5 Pa [140]. Assuming a mass transfer limiting scenario, the observed CO_2 flux at 800°C, which exceeded 2×10^{-3} $mol \cdot s^{-1} \cdot m^{-2}$ in the downhill regime with O_2 co-permeation, would be close to the rate of mass transfer. Additionally, p^SCO_2 would be close

to the feed side CO_2 partial pressure. Under such assumptions, the boundary layer thickness was roughly 20 mm. This means the rate of mass transfer cannot be assumed as a fast process if the external film is thicker than a few mm. In contrast, at 600°C, 80 mm thick boundary layer would give comparable rate of mass transfer to CO_2 flux. Hence, the resistance by the gas phase mass transfer more likely becomes important at higher operating temperature and higher CO_2 permeation flux.

6.3.3. Brief summary

Due to the complexity of the CO_2-O_2 co-permeation through LSCF6428-carbonate membranes, any single model cannot precisely predict the CO_2 transport mechanism. The transport mechanism and rate-determining step are subject to change with different operating temperatures and driving force regimes. Based on our model equations and the observed flux-driving force relationship, it can be concluded that within the uphill regime, the CO_2 flux followed a linear correlation with its driving force expressed in terms of CO_2 and O_2 partial pressures. The trend then turned towards asymptote as the driving force increased further into the downhill regime. The observed relationship matched the best with the bulk CO_3^{2-} diffusion limiting model and global interfacial reaction limiting model. However, the mechanistic insight that compared the theoretical gradient with the observed data was not directly evidential to distinguish between the two scenarios.

The study of the CO_2 flux-driving force relationship also became a useful reference for promoting CO_2 permeation flux. With the result of flux-driving force relationship in this chapter, it is feasible to further improve the uphill CO_2 permeation flux by enhancing the driving force, most practically by increasing the chemical potential difference of O_2 across the membrane. However, there seemed to be a finite limitation for the CO_2 flux thanks to the linear correlation. It would be impossible to achieve infinitely high flux at maximum driving force as the logarithm model predicted. Next, the effect of further driving force enhancement to uphill CO_2 permeation flux has been studied as an attempt to support the flux-driving force relationship found here.

6.4. CO_2-O_2 co-permeation with permeate side O_2 removal

6.4.1. Introduction and experimental design

The flux-driving force correlation experiments focused on varying the driving force by adjusting the feed side CO_2 and O_2 partial pressures. The highest O_2 partial pressure in feeding gas was 0.2 atmosphere (20% by mole). In the context of post-combustion flux gas CO_2 capture, one approach to enhance the driving force is by enriching the feed side O_2 concentration. However, to enrich the O_2 concentration further, high purity O_2 stream would be required from the air separation unit (ASU), potentially making this step much more energy intensive. Here, a novel approach that removes the membrane permeate side O_2 has been investigated to enhance the driving force for uphill CO_2 permeation.

In general, two types of methods are optional to achieve the permeate side O_2 removal: reactive removal using reducing gas or employing solid oxygen carrier material (OCM) as an 'oxygen sink'. The advantage of the reactive removal method is the reducing gas, typically H_2 or CO, can consume O_2 continuously. The product of such a reaction do not require additional downstream separation. However, it has been shown that the LSCF6428 membranes are not chemically stable under continuous exposure of reducing gas. To some extent, exposing LSCF6428 under low pO_2 risked distortion of its lattice structure and weakening its mechanical strength. More importantly, such a modification of membrane properties may intrinsically change its CO_2 permeability. Consequently, the pure effect from driving force enhancement cannot be observed.

The 'oxygen sink' method was certainly a more suitable option according to the objective of this study. Copper-based OCM was selected primarily due to its advantages in thermodynamics. O_2 removal using OCM is a cyclic process. The copper oxide must be reduced firstly to metallic copper in order to create oxygen carrier capacity. The copper then reacts with O_2 at high temperature and return to the oxide form. When CO is used as reducing gas, a full cycle of reduction and oxidation can be written as reaction 6.25 and 6.27; when H_2 is used as reducing gas, the reduction can be written as reaction 6.26 [141].

$$\mathrm{CuO\ (s) + CO\ (g) \rightarrow Cu\ (s) + CO_2\ (g)} \qquad \Delta H^0_{1073K} = -132.9\mathrm{kJ/mol} \qquad (6.25)$$

$$\mathrm{CuO\ (s) + H_2\ (g) \rightarrow Cu\ (s) + H_2O\ (g)} \qquad \Delta H^0_{1073K} = -98.9\mathrm{kJ/mol} \qquad (6.26)$$

$$\mathrm{Cu\ (s) + \frac{1}{2}O_2\ (g) \rightarrow CuO\ (s)} \qquad \Delta H^0_{1073K} = -149.4\mathrm{kJ/mol} \qquad (6.27)$$

$$\mathrm{2Cu\ (s) + \frac{1}{2}O_2\ (g) \rightarrow Cu_2O\ (s)} \qquad \Delta H^0_{1073K} = -167.3\mathrm{kJ/mol} \qquad (6.28)$$

$$\mathrm{Cu_2O\ (s) + \frac{1}{2}O_2\ (g) \rightarrow 2CuO\ (s)} \qquad \Delta H^0_{1073K} = -131.5\mathrm{kJ/mol} \qquad (6.29)$$

Since both reactions are exothermic at 800°C, a full cycle of complete reduction and oxidation can proceed using the heat of flue gas without extra energy input. The copper oxidation may occur stepwise (reaction 6.28 and 6.29) forming intermediate oxide Cu_2O [142]. Moreover, the oxidation may not complete under low O_2 partial pressure. Nevertheless, copper based OCM is beneficial in terms of energy requirements. Besides, other advantages include the relatively low cost, low toxicity and high reactivity with reducing gas [143].

Ex-situ pre-reduction of the Cu-based OCM was preferable rather than in-situ reduction, due to the same reason as the reactive O_2 removal. A reference experiment has been done to compare the uphill CO_2 permeation flux before and after 3h in-situ exposure of LSCF6428-carbonate membrane in 5% CO, 5% CO_2 mix. No OCM was incorporated into the reactor in this experiment for O_2 removal. However, transient increase of uphill CO_2 flux was observed after the CO exposure. Over the next 2-3 hours,

uphill CO_2 flux gradually stabilised towards steady state as before the CO exposure (see Appendix III). This result demonstrated how the in-situ reduction of OCM affected the stability of uphill CO_2 permeation, which could interfere with the effect from OCM originally interested.

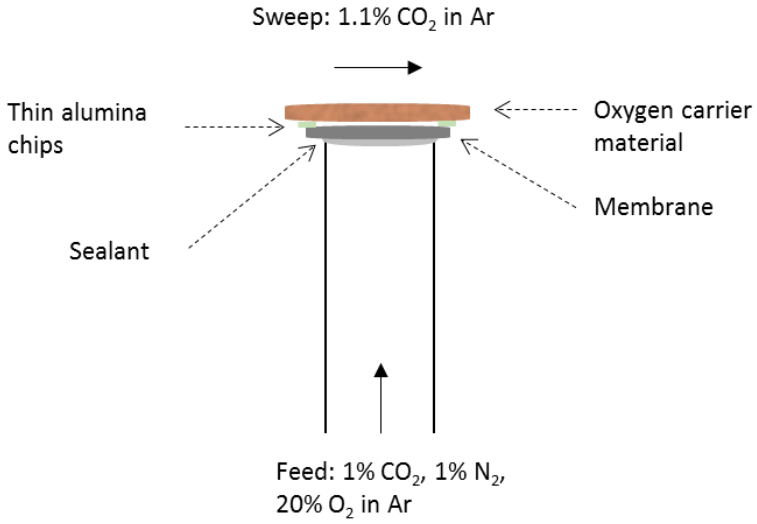

Figure 6.18: Illustrating the reactor design of the LSCF6428-carbonate membrane combined oxygen carrier material for permeate side O_2 removal. Pre-reduced copper based OCM pellet was employed in this study. OCM and the membrane were physically separated using thin alumina chips.

The main experimental design was to incorporate pre-reduced Cu-based OCM on top of the membrane permeate side surface. Thin alumina chips with thickness of approximately 0.6 mm was pasted between the membrane and OCM to avoid any physical contact (Figure 6.18), which could lead to cross-contamination and deactivate both membrane and OCM. Experiments were conducted following the same operating procedure as a normal uphill experiment, heating up under symmetrical operation to preserve the reduced Cu. The initial asymmetrical operation was maintained to the point that the Cu was fully oxidised, followed by switching back to symmetrical operation. Following repeat asymmetrical operations were therefore run without active Cu. The effect of the OCM can be found by comparing the uphill CO_2 flux with and without active Cu.

6.4.2. Oxygen carrier synthesis

In this work, we aimed to synthesis OCM with CuO particles supported on porous refractory materials such as alumina. Various methods have been attempted including co-precipitation, wet impregnation and wet mixing. Co-precipitation of copper nitrate and aluminium nitrate precursors with addition of sodium carbonate solution was able to produce samples with CuO loading up to 80 wt%. However, CuO particles was supported on copper aluminate ($CuAl_2O_4$), which formed via the CuO and Al_2O_3 interaction during high temperature calcination of the precipitate [141]. The suitability of copper aluminate as support material was unknown as it was not chemically stable especially in reducing gas. On the other hand, vacuum wet impregnation of porous α-alumina disk in copper nitrate solution

avoided the copper aluminate formation, but the solubility of copper nitrate limited the CuO loading below 10 wt%. Wet mixing method was employed in this project since it compromised the copper aluminate formation and CuO loading issues [144].

Wet mixed Cu-based oxygen carrier was prepared by mixing 8.8 g $Al(OH)_3$ (Sigma–Aldrich, reagent grade) and 5.62 g $Ca(OH)_2$ (Fisher Scientific, > 98%) powders in 400 ml de-ionised water on a 50°C hot plate for 2 h. Next, 15 g CuO powder (Fisher Scientific, Reagent ACS, ≥ 99%) was added to the suspension and the mixture was stirred for a further 24 hours. The well-mixed suspension was dried in the oven at 80°C for 48 hours, followed by crushing in a mechanical mortar and pestle miller. The grinded powder was palletised into disk shape with weight of approximately 1g each, before high temperature calcination at 1000°C for 3 hours. During the heating up, the hydroxides decomposed into oxides. The presence of calcium oxide allowed the formation of calcium aluminate phase and prohibited copper aluminate formation. The product pellets were expected to be 60 wt% CuO supported on calcium aluminate, which is a suitable support material for copper based OCM.

The calcined pellets were characterised using SEM and XRD techniques. Cross-sectional SEM image (Figure 6.19) revealed the surface morphology of the CuO particles incorporated into the support. Majority of the particles exhibited 1-10 μm diameters, although some submicron particles may also present. The EDS analysis using back scattered electrons confirmed the Cu and Al elements. Detailed phase and compositional analysis were carried out using XRD. Three phases were detected according to the XRD pattern fit of a wet mixed pellet (Figure 6.20). They were tenorite (CuO phase with monoclinic structure), mayenite ($Ca_{12}Al_{14}O_{33}$ phase with cubic structure) and krotite ($CaAl_2O_4$ phase with monoclinic structure). Phase quantification was performed using Rietveld refinement. The result showed that the composition of the wet mixed pellet was mainly CuO and $Ca_{12}Al_{14}O_{33}$. CuO loading of this CuO-$Ca_{12}Al_{14}O_{33}$ sample appeared to be 64.7 wt%, close to the expected loading of 60 wt%.

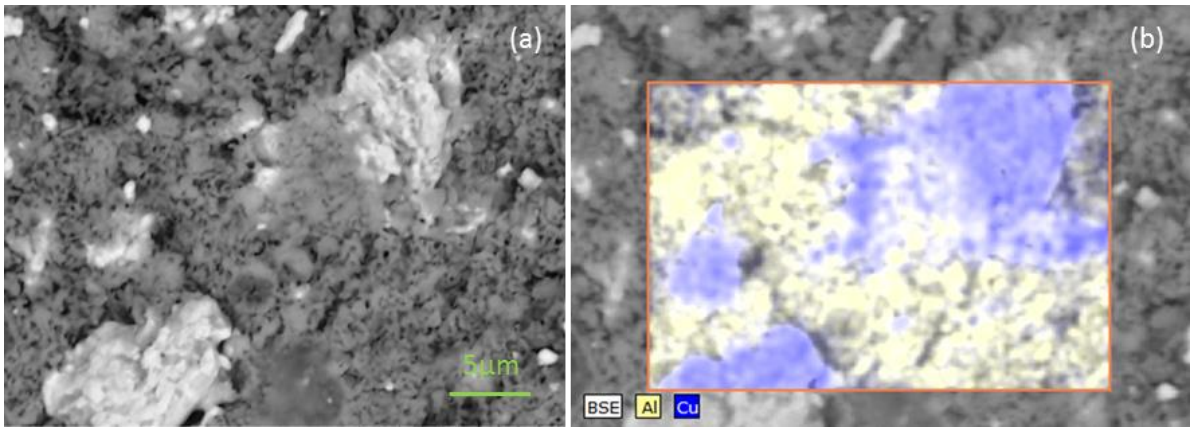

Figure 6.19: (a) Cross-sectional SEM image of a wet mixed CuO-$Ca_{12}Al_{14}O_{33}$ pellet. Image has 6.0k magnification on 5μm scale. (b) EDS mapping of the same image showing the distribution of CuO particles.

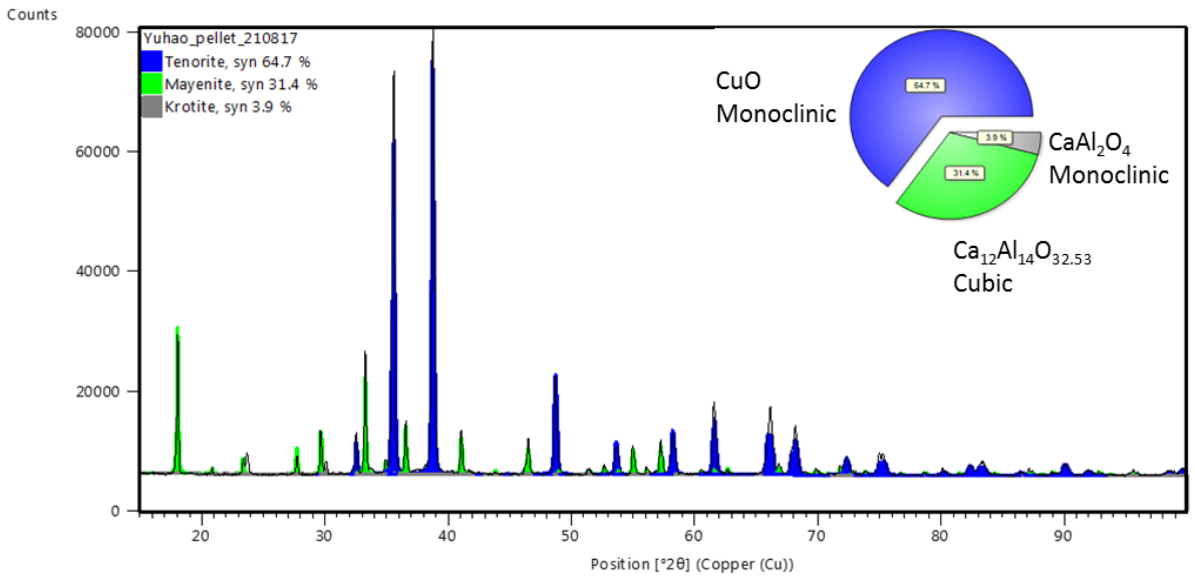

Figure 6.20: XRD pattern fit and phase quantification of a wet mixed CuO-$Ca_{12}Al_{14}O_{33}$ pellet.

6.4.3. Pre-reduction of oxygen carrier material

The reduction of a CuO-$Ca_{12}Al_{14}O_{33}$ pellet was monitored using a mass spectrometer in order to understand the duration of the reduction process. This reduction experiment was carried out isothermally at 800°C in the membrane reactor. Unlike a membrane permeation experiment, the CuO-$Ca_{12}Al_{14}O_{33}$ pellet was placed on top of the alumina supporting tube without sealing. A Swagelok plug blocked the feed side outlet. The reactor was essentially a single chamber reactor with a feed inlet stream and an effluent stream that directed to gas analysis.

The pellet was heated up at 1°C/min in 100% Ar atmosphere, followed by switching to 5% CO in Ar at 800°C with 40 ml/min flow rate. Figure 6.21 shows the variation of O_2, CO and CO_2 within the effluent stream. Before introducing CO, the O_2 background was between 650 to 700 ppm, indicating the CuO probably started to undergo oxygen uncoupling at 800°C due to the inert atmosphere [144]. The full reduction was completed after 3 hours of CO flow when CO_2 concentration approached 0% and CO concentration stabilised at 5%. The weight of the pellet dropped from 0.812g to 0.698g after reduction. The 0.114g weight loss corresponded to 7.12 mmol loss of oxygen atoms from the pellet. Thus, the original pellet contained 0.57g CuO and the reduced pellet contained 0.456g Cu, giving 65 wt% Cu loading. Alternatively, the area under the CO_2 production curved can be integrated out to estimate the total CO_2 release. This value turned out to be 6.81 mmol, corresponding to 0.109g weight loss because of CuO reduction. The agreement confirmed that the desirable CuO and Cu loading were achieved.

With this experiment as a reference, more CuO-$Ca_{12}Al_{14}O_{33}$ pellets can be reduced batch-wise inside controlled atmosphere furnace. The reducing gas can be either 5% CO in Ar or 5% H_2 in Ar. Both exhibited similar duration of reduction and resulted similar weight loss. The procedure was as follows: heating up to 800°C at 1°C/min in 100% Ar; switch to reducing gas of 30-40 ml/min for 5 hours; switch

back to 100% Ar and cool down to room temperature at 2°C/min. The carrying capacity of the Cu-$Ca_{12}Al_{14}O_{33}$ pellets, defined by moles of Cu (calculated from CO_2 production) per unit weight of reduced OCM, was around 9.75×10^{-3} mol/g. Assuming a steady O_2 flux of 0.04 ml·min^{-1}·cm^{-2} through the membrane at 800°C, full oxidation of such OCM pellet would take roughly 60 hours.

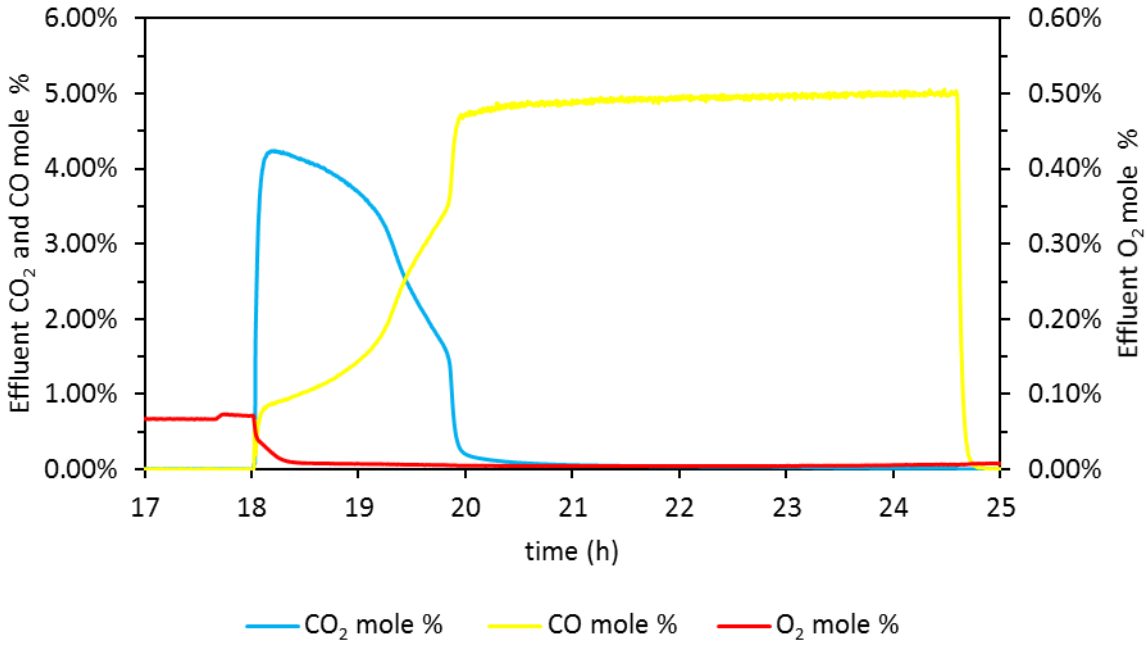

Figure 6.21: Effluent CO_2, O_2 and CO mole percentage analysed by mass spectrometer during the reduction of a CuO-$Ca_{12}Al_{14}O_{33}$ pellet using 5% CO.

6.4.4. Uphill experiment with permeate side O_2 removal

At 600°C, 1% CO_2 in Ar was used for symmetrical operation. At the beginning of the first asymmetrical operation ('a' in Figure 6.22), uphill CO_2 permeation can be observed whilst there was no significant change in permeate side O_2 concentration. This was due to the Cu successfully removed O_2 on membrane permeate side and controlled the bulk gas phase O_2 concentration down to 30 ppm. At the same time, temporary uphill CO_2 flux of 2.77×10^{-4} mol·m^{-2}·s^{-1} was measured (Figure 6.23). However, this permeation flux did not stabilise for more than 1 h, followed by a gradual decrease of the permeate CO_2 mole fraction, accompanied by gradual increase of O_2 concentration. The second asymmetrical operation ('b' in Figure 6.22) showed a more stable uphill permeation whilst the Cu was further oxidised. At the end of the second asymmetrical operation, O_2 concentration grew to 300 ppm. Meanwhile uphill CO_2 flux stabilised at 1.84×10^{-4} mol·m^{-2}·s^{-1} throughout the second asymmetrical operation, which is similar to previous uphill CO_2 permeation experiments as well as in the literature [28]. It has been understood that at 600°C the symmetrical operation would not significantly modify the LSCF6428 oxygen nonstoichiometry, and transient CO_2 peak was not commonly observed at the start of asymmetrical operation. It seemed when the Cu actively removed O_2 down to 30 ppm, the uphill CO_2

flux was indeed temporarily elevated by around 50%. It can also be supported by the dip in CO_2 concentration within the retentate stream on the same time scale. Towards the end of the experiment, permeate side O_2 concentration continued increasing gradually. The OCM pellet did not reach its full oxygen carrier capacity (see Figure 6.24) due to the relatively low O_2 permeation flux at 600°C. Nevertheless, further variation of permeate side O_2 concentration during the second asymmetrical operation brought little change on the uphill CO_2 permeation flux.

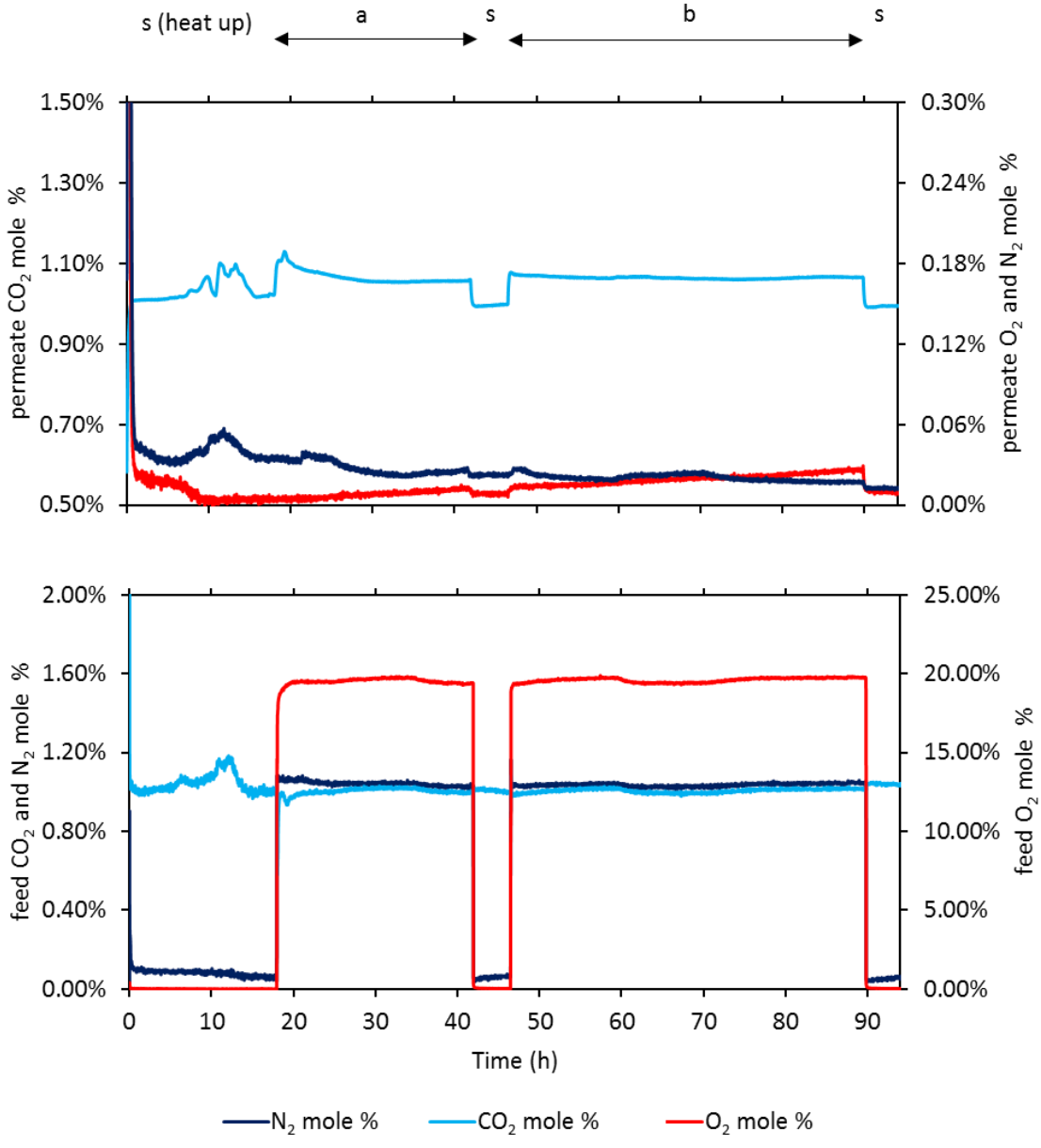

Figure 6.22: Uphill CO_2 permeation experiment at 600°C with pre-reduced Cu-$Ca_{12}Al_{14}O_{33}$ pellet on membrane permeate side for O_2 removal. Experiment started with heating up under symmetrical operation, flowing 1% CO_2 in Ar into both reactor chambers. Two asymmetrical operations (denoted by 'a' and 'b') were conducted using 1.04% CO_2, 1.05% N_2, 19.6% O_2 in Ar as feeding gas and 1% CO_2/Ar as sweep gas. These were alternated with symmetrical operations (denoted by 's').

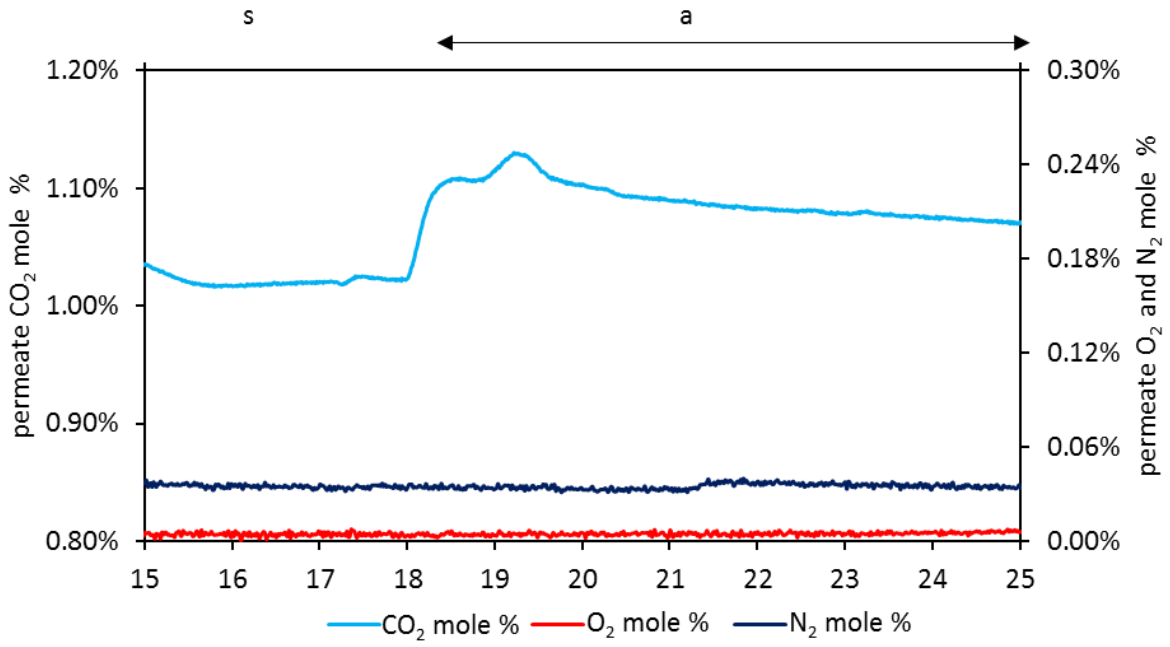

Figure 6.23: Uphill CO_2 permeation experiment at 600°C, highlighting the temporarily higher uphill permeation when Cu is actively removing O_2 on membrane permeate side.

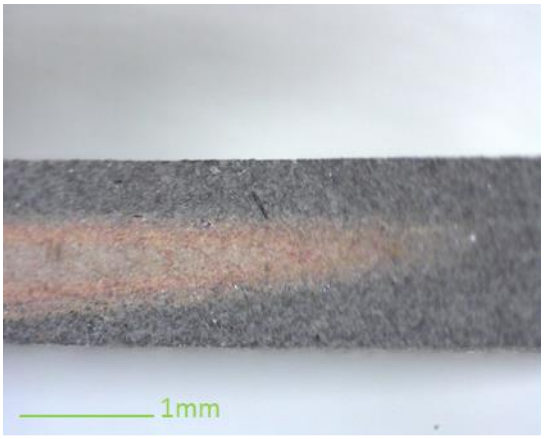

Figure 6.24: Cross-sectional image of the Cu-based OCM pellet under digital microscope after uphill CO_2 permeation experiment at 600°C. The black edges and red core indicated that the pellet was not fully oxidised.

Identical operating procedure was exploited for the experiment at 800°C (Figure 6.25), using fresh membrane and pre-reduced Cu-$Ca_{12}Al_{14}O_{33}$ pellet. 1.1% CO_2 in Ar was used for symmetrical operation. Initially, Cu actively controlled the permeate side O_2 concentration down to the level of 200 ppm during the first asymmetrical operation ('a' in Figure 6.25). At this point, steady state uphill CO_2 flux of 7.62 × 10^{-4} mol·m^{-2}·s^{-1} was observed after a transient CO_2 peak. Since the membrane intrinsically exhibited higher O_2 permeation flux at 800°C, the growth of permeate side O_2 concentration was faster than that of 600°C. O_2 concentration approached a temporary steady state following a rapid increase to around 1000 ppm. During the second asymmetrical operation ('b' in Figure 6.25), O_2 concentration departed from the steady state and rapidly increased to around 3400 ppm. Thanks to the more significant variation

of permeate side O_2 concentration, it can be identified that the uphill CO_2 flux dropped in response to each rapid growth of O_2 concentration. The steady state O_2 concentration also allowed CO_2 flux to stabilise, thus a CO_2 flux can be quantified at each stage of Cu oxidation. At the end of the second asymmetrical operation, steady state uphill CO_2 flux of 5.86×10^{-4} mol·m^{-2}·s^{-1} was observed, which was comparable to previous uphill experiment at 800°C without incorporating OCM. Therefore, removing permeate side O_2 concentration to 200 ppm at 800°C enhanced the uphill CO_2 flux by 30%.

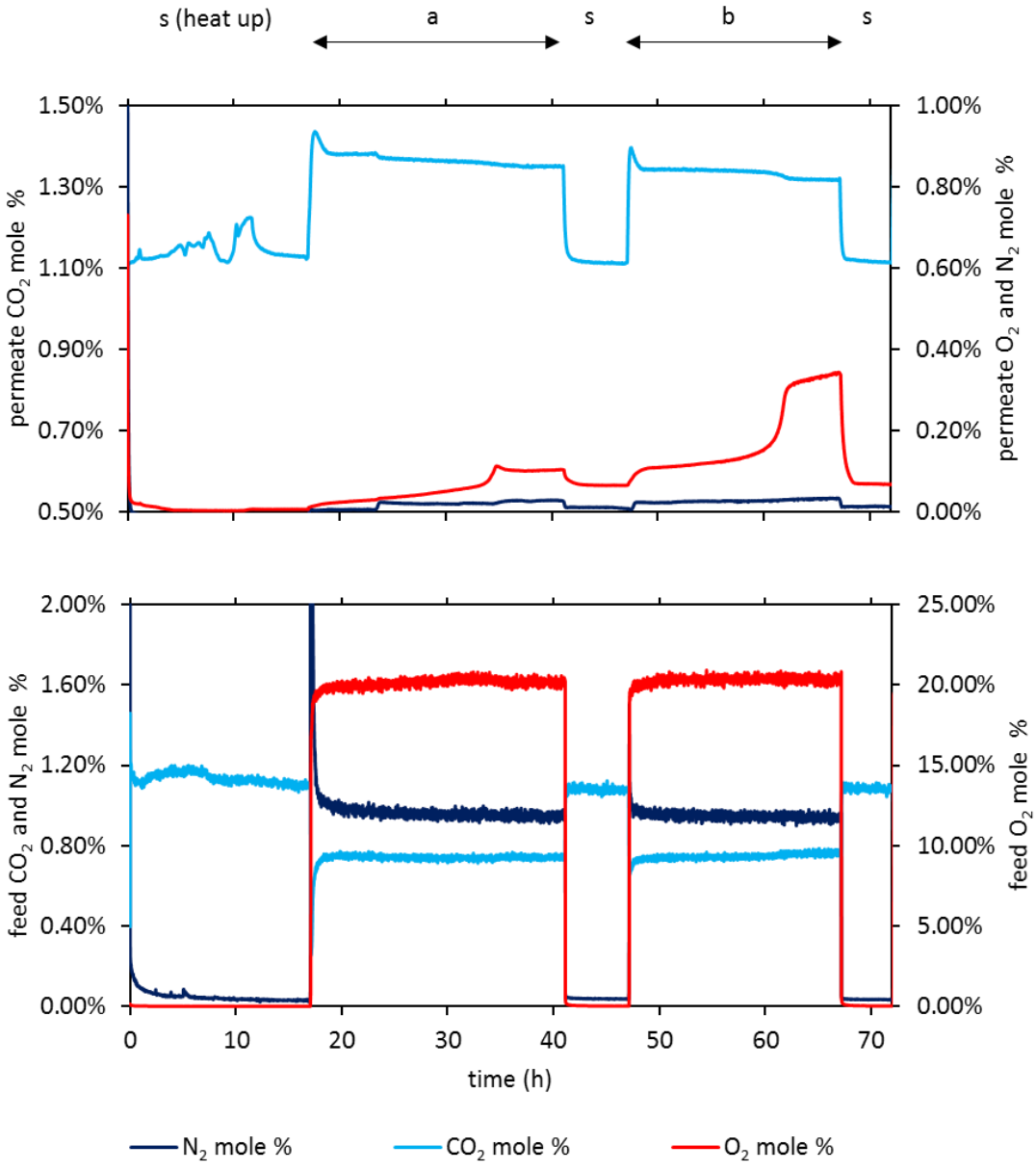

Figure 6.25: Uphill CO_2 permeation experiment at 800°C with pre-reduced Cu-$Ca_{12}Al_{14}O_{33}$ pellet on membrane permeate side for O_2 removal. Experiment started with heating up under symmetrical operation, flowing 1.1% CO_2 in Ar into both reactor chambers. Two asymmetrical operations (denoted by 'a' and 'b') were conducted using 0.98% CO_2, 1.03% N_2, 20.12% O_2 in Ar as feeding gas and 1.1% CO_2/Ar as sweep gas. These were alternated with symmetrical operations (denoted by 's').

Table 6.3: The change of uphill CO_2 flux in response to permeate side O_2 removal. Data based upon the experiments described in Figure 6.22 and 6.25.

Temperature (°C)	Permeate side O_2 concentration (ppm)	Uphill CO_2 permeation flux ($mol \cdot m^{-2} \cdot s^{-1}$)
600	30	2.77×10^{-4}
600	300	1.84×10^{-4}
800	200	7.62×10^{-4}
800	3400	5.86×10^{-4}

6.4.5. Thermodynamics and kinetics discussion

It is necessary to perform thermodynamic and kinetic analysis on the copper oxidation reaction in order to seek further interpretation on the experimental results. Thermodynamically, the permeate side O_2 partial pressure observed in the experiments would always allow Cu oxidation to proceed. Although the O_2 concentration was as low as 30 ppm at 600°C, 10^{-3} Pa O_2 partial pressure would be sufficient to oxidise metallic copper below 900°C (see Figure 6.26 a), and 3.04 Pa would allow the oxidation to proceed further to CuO (see Figure 6.26 b). Therefore, at 600°C there was always a thermodynamic driving force for complete Cu oxidation despite of the low O_2 permeation flux. At 800°C, the O_2 concentration was initially rising from 200 to 1000 ppm. At this point O_2 concentration stabilised and it was exactly the equilibrium position between O_2 and Cu_2O at 800°C (see Figure 6.26 b). Since permeate side O_2 concentration should have been higher than 1000 ppm without the presence of OCM, the Cu_2O/CuO equilibrium was overcome later allowing further oxidation to CuO. Either way, the thermodynamic analysis showed that the oxygen capacity of the OCM could be utilised to its maximum.

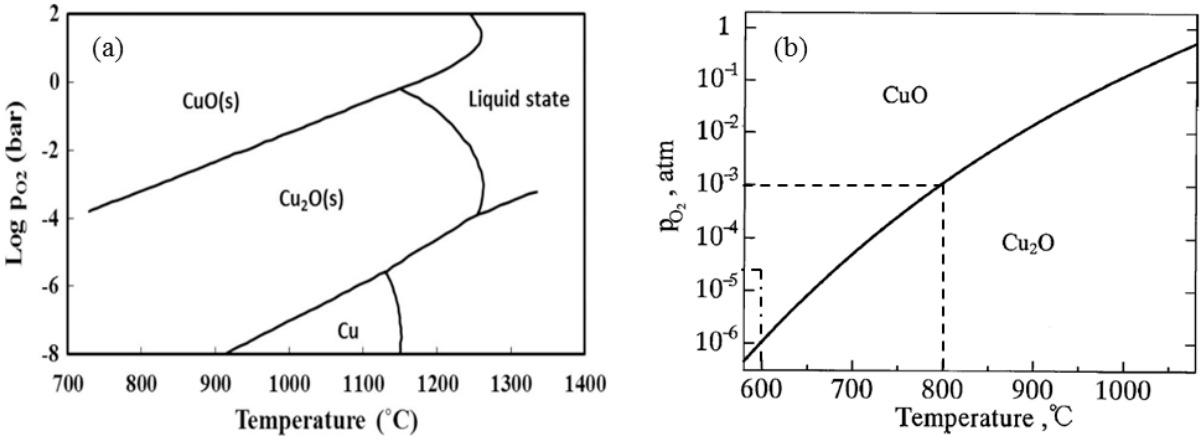

Figure 6.26: (a) Phase diagram for Cu oxidation to Cu_2O and CuO between 700 to 1400°C [145]. (b) Phase diagram for Cu_2O oxidation to CuO between 600 to 1000°C [146]. The solid lines represent the equilibrium pO_2 as a function of temperature; the dashed and dashed/dot lines mark for the experimental conditions appeared in this work. Reproduced with permission of Elsevier and Springer Nature.

On the kinetics aspect of the copper oxidation, various literatures have suggested that the reaction was controlled to a considerable extent by external mass transfer at above 600°C [142, 144]. Furthermore, solid phase diffusion of the gas molecules through pores of the OCM was slow with respect to the intrinsic chemical reaction rate [142]. In the context of the experimental design in this work (Figure 6.18), two mass transfer resistances for O_2 existed, including external gas phase diffusion from membrane permeate side surface to the OCM pellet surface, and internal solid phase pore diffusion of O_2 into the OCM pellet. Since there was no bulk gas flow through the volume between the membrane and OCM pellet, the mass transfer of O_2 within the entire volume was essentially gas phase diffusion. The experimental set-up in this work minimised the membrane-OCM spacing down to 0.6-1 mm. However, this distance may not be sufficiently small to make the mass transfer resistance negligible. In this case, a gas phase mass transfer would control the rate of O_2 removal, resulting a local O_2 concentration build-up upon membrane permeate side surface. Ultimately, the observed driving force for uphill CO_2 permeation may overestimate the true driving force exerted across the membrane surfaces. Meanwhile, the resistance of solid phase pore diffusion became important once the Cu particles residing on the surface of OCM pellet were consumed (see Figure 6.24), which could be another rate-determining step for O_2 removal.

Referring to Figure 6.22 and 6.25, the effect of the permeate side O_2 removal on promoting uphill CO_2 flux using copper based OCM seemed to be limited. There are two possible interpretations for the experimental results: the intrinsic linear flux-driving force relationship of CO_2-O_2 co-permeation does not offer sufficient room for flux improvement, or the external and internal mass transfer resistances for O_2 removal suppressed the driving force enhancement across the membrane. The two possibilities are further analysed individually.

Taking the uphill CO_2 permeation experiment with permeate side O_2 removal at 800°C (Figure 6.25) as an example, the linear CO_2 flux-driving force relationship (Figure 6.15) can be used to predict the corresponding CO_2 flux when permeate side O_2 was removed to 200 ppm. With steady state retentate CO_2 and O_2 partial pressure of 740 and 2.03×10^4 Pa, as well as permeate side CO_2 and O_2 partial pressure of 1.40×10^3 and 20.3 Pa, the driving force with O_2 removal would be 9.91×10^4 $Pa^{3/2}$ on the horizontal axis. Substituting into the linear fit equation, the predicted CO_2 flux would be 6.42×10^{-4} $mol \cdot m^{-2} \cdot s^{-1}$, which is comparable to the observed flux. Since the enhanced driving force with O_2 removal was not beyond the upper range of the linear fit plot in Figure 6.15, the linear flux-driving force model essentially predicted that removing permeate side O_2 down to 200 ppm would not significantly promote the uphill permeation flux.

On the other hand, the estimated gas phase O_2 mass transfer flux through the membrane-OCM spacing can be compared with the O_2 permeation flux across the membrane. The O_2 flux without active Cu at the end of section 'b' in Figure 6.25 was approximately 9.9×10^{-4} $mol \cdot m^{-2} \cdot s^{-1}$. Assuming the O_2

transport was limited by the gas phase mass transfer, O_2 mass diffusivity was 1.4×10^{-4} m^2/s at 800°C [139] and membrane-OCM spacing was 1 mm, the estimated O_2 mass transfer flux through the membrane-OCM spacing was 0.31 $mol \cdot s^{-1} \cdot m^{-2}$ according to equation 6.23 and 6.24. This value was more than two orders of magnitudes higher than the observed O_2 flux without active copper, indicating the gas phase mass transfer resistance through the 1 mm thick spacing cannot be significant. Altogether, the restraint for the promotion of uphill CO_2 flux may well come from the intrinsic linear flux-driving force relationship of CO_2-O_2 co-permeation, rather than the mass transfer resistances for O_2 removal.

6.5. Summary

In this chapter, theoretical models for CO_2-O_2 co-permeation through LSCF6428-carbonate membranes have been established. Isothermal flux-driving force correlation have been studied experimentally over a wide range of driving forces and experimental results were fitted into each individual model. The experimental data best matched with the linear flux-driving force models, which narrowed down the rate-determining step for CO_2-O_2 co-permeation to either bulk CO_3^{2-} diffusion or global interfacial reaction. The observed flux-driving force correlation appeared linear within the uphill driving force regime but tended to approach asymptote at large downhill diving forces. The experimental data was further compared with theoretical calculation. Operating temperature seemed to play an important role for both uphill and downhill regime. For the linear uphill regime, it was likely that the permeation was global interfacial reaction limited below 800°C whilst the effect of bulk CO_3^{2-} diffusion kicked in from 800°C. For the downhill regime, the much larger CO_2 flux made the gas phase CO_2 mass transfer on membrane permeate side significant, particularly at higher operating temperature.

Although the experimental data did not provide firm evidences about the mechanism of the CO_2-O_2 co-permeation, the logarithm flux-driving relationship has been ruled out and the CO_2 flux appeared to be proportional to $p'CO_2 p'O_2^{1/2} - p''CO_2 p''O_2^{1/2}$ in the uphill regime. The aim of the flux-driving force study was to predict how strongly the flux would respond to an enhanced driving force. For instance, the idea of O_2 removal on membrane permeate side would vastly promote CO_2 flux for a logarithm flux-driving force correlation. However, the linear correlation in this work showed that there would be limited promotion of CO_2 flux by removing O_2 from membrane permeate side. This has been experimentally verified later by incorporating copper based OCM on membrane permeate side. The observed CO_2 flux with permeate side O_2 removal coincided with the prediction of the linear flux-driving force model.

7. Conclusions and future work

7.1. Conclusions of the project

This project has been primarily focused on exploiting the idea of O_2 co-permeation on CO_2 permeable ceramic-carbonate dual phase membranes, such that the CO_2 permeation flux can be promoted by enhancing the overall thermodynamic driving force. It has been shown that by co-feeding 10^3 Pa CO_2 and 2×10^4 Pa O_2, CO_2 permeation flux reached 0.036 and 0.11 $ml \cdot min^{-1} \cdot cm^{-2}$ at 600°C and 800°C respectively, using mixed ionic and electronic conductive LSCF6428-carbonate membranes. The fluxes were 7-9 times higher than feeding 10^3 Pa CO_2 in absence of O_2 and comparable to the CO_2 flux when feeding 5×10^4 Pa CO_2 alone. This effect did not appear on purely ionic conductive YSZ-carbonate membranes. Mechanistically, the electronic conductivity of LSCF6428 based membranes played a key role on facilitating CO_2-O_2 co-permeation.

The project also explored the properties of solid phase LSCF6428 as a membrane support material. The LSCF6428-carbonate membranes were selected for further investigation because of their flexibility. The applications of such a membrane are not limited by the presence of O_2. A low O_2 partial pressure atmosphere can increase the oxygen nonstoichiometry within the LSCF6428 support and create higher oxygen vacancy concentration. It has been demonstrated that a pre-reduced LSCF6428-carbonate membrane under inert atmosphere (pO_2~10Pa) enhanced downhill CO_2 permeance by 2-3 times comparing with non-reduced membrane, especially at lower operating temperature around 650°C.

Although this was a promising result in the context of pre-combustion CO_2 capture, the idea that utilised the thermodynamic driving force from O_2 to boost CO_2 permeation flux seemed to be more meaningful in the context of post-combustion CO_2 capture where CO_2 partial pressure is relatively low. This driving force can be utilised to a further extent so that uphill CO_2 has been enabled through LSCF6428 based membranes. Practically, it provides a potential way to separate CO_2 without compression and with certain degree of CO_2 purification in the meantime. This can possibly make the CO_2 capture process more cost effective and less energy intensive, given that the uphill CO_2 permeate flux can be further improved.

Enhancing the overall thermodynamic driving force for CO_2-O_2 co-permeation was the novel approach to promoting CO_2 permeation flux proposed in this project. Permeate side O_2 removal was thought to be a promising option to achieve the driving force enhancement with minimum energy requirement. In order to predict how significantly the O_2 removal can enhance the CO_2 flux, models for CO_2 flux-driving force relationship has been established for several rate-determining scenarios, followed by performing flux-driving force experiments to validate the models. Experimental data at 600 and 800°C both fitted better to a linear flux-driving force relationship rather than logarithm relationship in uphill driving force regime, corresponding to either bulk CO_3^{2-} diffusion limiting or global interfacial reaction limiting

scenario. By comparing the gradient of the linear fit lines with the theoretical gradient associated with the bulk CO_3^{2-} diffusion limiting scenario, it was likely that the uphill CO_2 permeation with O_2 co-permeation were limited by global interfacial reaction at 600°C, whilst the rate determining step may gradually shift to bulk CO_3^{2-} diffusion at 800°C and above. This result indicated that there would be limited effect to CO_2 flux even though the permeate side O_2 partial pressure was infinitesimal.

Further on, the project explored uphill CO_2 permeation experiments with permeate side O_2 removal using copper-based oxygen carrier. The oxygen carrier successfully removed permeate side O_2 concentration down to 30 ppm at 600°C and 200ppm at 800°C. However, no steady state CO_2 permeation has been observed at 600°C due to gradual increase of permeate side O_2 concentration. On the other hand, the increase of permeate side O_2 concentration at 800°C exhibited a 'stepwise' behaviour. Steady state uphill CO_2 permeation flux was 7.62×10^{-4} $mol \cdot m^{-2} \cdot s^{-1}$ at 200 ppm permeate side O_2 concentration. Comparing with 5.86×10^{-4} $mol \cdot m^{-2} \cdot s^{-1}$ without active O_2 removal, it achieved a flux enhancement of 30%. Having analysed that the intrinsic kinetics of copper oxidation and gas phase mass transfer were unlikely limiting the rate of O_2 uptake, this result was certainly coherent with the prediction of the linear flux-driving force correlation, which indicated a finite limitation of the flux promotion via permeate side O_2 removal, as opposed to infinite flux promotion for the logarithm model.

To summarise the project, co-feeding O_2 through LSCF6428-carbonate dual phase membranes indeed promoted CO_2 permeation flux via enhancing the overall driving force. For downhill CO_2 permeation with 1% CO_2 and 20% O_2, CO_2 permeation flux of 7.5×10^{-4} $mol \cdot m^{-2} \cdot s^{-1}$ has been obtained at 800°C. The equivalent CO_2 permeance was 1.06×10^{-6} $mol \cdot m^{-2} s^{-1} Pa^{-1}$ if only the partial pressure difference of CO_2 was considered as the apparent driving force. This value is comparable to the minimum membrane permeance threshold proposed by Merkel et al. (1.34×10^{-6} $mol \cdot m^{-2} s^{-1} Pa^{-1}$) [93] that any feed stream compression possibly becomes unnecessary (see Chapter 2.4.2). The uphill CO_2 flux co-feeding 20% O_2 also approached similar flux at 800°C, regardless of the permeate side O_2 removal. Here, the role of O_2 co-permeation is essentially a replacement of driving force from mechanical compression to the overall internal chemical potential difference. Although the permeate side O_2 removal exhibited limited uphill CO_2 flux enhancement, the copper based oxygen carrier is capable of removing O_2 to below 200 ppm on membrane permeate side. Therefore, the practical benefit of a membrane reactor integrated with oxygen carrier is downstream O_2 separation and utilisation.

7.2. Future work

Apart from driving force enhancement for promoting uphill CO_2 permeation flux, permeate side O_2 removal has another potential application, which is CO_2 enrichment. Depending on the model shown in equation 6.5 and 6.10, if permeate side O_2 partial pressure $p''^{1/2}_{O_2}$ were decreased to 10 times lower, theoretically the CO_2 partial pressure p''_{CO_2} would be allowed to go $\sqrt{10}$ times higher while keeping the driving force the same. With the current membrane reactor system without permeate side O_2 removal, CO_2 can permeate from 0.3% against 1.13% at 800℃ to the extreme extent (see Figure 6.9). The permeate stream CO_2 concentration could be enriched beyond 1.13% at the same flux with O_2 removal. For industrial CO_2 capture or separation processes using the concept of uphill CO_2 permeation, downstream CO_2 enrichment mainly has two options: enriching CO_2 stepwise using cascade uphill membrane reactors with sweep gas, or vacuuming permeate side stream without sweep gas. Both induce extra energy input and capital cost. The incorporation of permeate side O_2 removal can potentially mitigate the energy requirement and capital cost for downstream CO_2 enrichment. However, when permeate side CO_2 concentration becomes higher, uphill CO_2 permeation flux can be affected by many factors, including backwards CO_2 permeation and thermodynamic limitation of permeate side interfacial reaction. Additionally, it can be challenging to obtain measurable flux on gas analyser on a high CO_2 concentration baseline. Anyhow, future experiments may focus on a potential application of direct CO_2 capture from the air (400-500 ppm) followed by enrichment. Membrane can also be upgraded to hollow fibre geometry that has substantially higher surface area, incorporating oxygen carrier in powder form on either shell or tube side of the reactor.

On the uphill CO_2 flux aspect, it will be interesting to study the effect of O_2 removal without any mass transfer resistance. From a practical consideration, reactive O_2 removal using continuous flow of sweep gas containing a H_2/H_2O mix can be attempted. The water vapour can be easily separated out of CO_2 in the downstream. However, silver or stainless steel membrane supports are more preferable than LSCF6428. The H_2O-molten salt interaction may also affect CO_2 flux, bringing complexity on the permeation mechanisms. Double-layer disk of membrane combined with oxygen carrier, which consists of an oxygen carrier layer adhered on top of an electronic conductive dual phase membrane layer, has been another proposal to eliminate the gas phase mass transfer. Successful experiments will contribute to better understanding on the CO_2-O_2 flux-driving force relationship studied in this project.

Reference

1. *Global Energy & CO_2 Status Report - 2017.* OECD/IEA, Paris. **IEA (International Energy Agency) (2018)**.
2. *CO_2 EMISSIONS FROM FUEL COMBUSTION Highlights (2017 edition).* OECD/IEA, Paris. **IEA (International Energy Agency) (2017)**.
3. *Global climate in context as the world approaches 1˚C above pre-industrial for the first time.* 9th November 2015, Met Office.
4. Masson-Delmotte, V., et al., *IPCC, 2018: Global Warming of 1.5°C. An IPCC Special Report on the impacts of global warming of 1.5°C above pre-industrial levels and related global greenhouse gas emission pathways, in the context of strengthening the global response to the threat of climate change, sustainable development, and efforts to eradicate poverty.* 2018.
5. Pachauri, R.K. and A. Reisinger, *IPCC, 2007: Climate Change 2007: Synthesis Report. Contribution of Working Groups I, II and III to the Fourth Assessment Report of the Intergovernmental Panel on Climate Change* IPCC, Geneva, Switzerland: p. 104.
6. *Outlook for Natural Gas, Excerpt from World Energy Outlook 2017.* OECD/IEA, Paris. **IEA (International Energy Agency) (2018)**.
7. Pires, J.C.M., et al., *Recent developments on carbon capture and storage: An overview.* Chemical Engineering Research and Design, 2011. **89**(9): p. 1446-1460.
8. Boot-Handford, M.E., et al., *Carbon capture and storage update.* Energy & Environmental Science, 2014. **7**(1): p. 130-189.
9. Figueroa, J.D., et al., *Advances in CO_2 capture technology—The U.S. Department of Energy's Carbon Sequestration Program.* International Journal of Greenhouse Gas Control, 2008. **2**(1): p. 9-20.
10. Bhown, A.S. and B.C. Freeman, *Analysis and Status of Post-Combustion Carbon Dioxide Capture Technologies.* Environmental Science & Technology, 2011. **45**(20): p. 8624-8632.
11. Holloway., S. and W.J. Rowley., *Environmental Sustainability of Electricity Generation Systems with Carbon Dioxide Capture and Storage - Working Paper.* 2008. **UK ENERGY RESEARCH CENTRE**.
12. Leung, D.Y.C., G. Caramanna, and M.M. Maroto-Valer, *An overview of current status of carbon dioxide capture and storage technologies.* Renewable and Sustainable Energy Reviews, 2014. **39**: p. 426-443.
13. Vaccarelli, M., R. Carapellucci, and L. Giordano, *Energy and Economic Analysis of the CO_2 Capture from Flue Gas of Combined Cycle Power Plants.* Energy Procedia, 2014. **45**: p. 1165-1174.
14. Anantharaman, R., et al., *Dual phase high-temperature membranes for CO_2 separation - performance assessment in post- and pre-combustion processes.* Faraday Discussions, 2016. **192**(0): p. 251-269.
15. Scholes, C.A., et al., *CO_2 capture from pre-combustion processes—Strategies for membrane gas separation.* International Journal of Greenhouse Gas Control, 2010. **4**(5): p. 739-755.
16. Bui, M., et al., *Carbon capture and storage (CCS): the way forward.* Energy & Environmental Science, 2018. **11**(5): p. 1062-1176.
17. MacDowell, N., et al., *An overview of CO_2 capture technologies.* Energy & Environmental Science, 2010. **3**(11): p. 1645-1669.
18. Wang, Y., et al., *A Review of Post-combustion CO_2 Capture Technologies from Coal-fired Power Plants.* Energy Procedia, 2017. **114**: p. 650-665.
19. Krishnamurthy, S., et al., *CO_2 capture from dry flue gas by vacuum swing adsorption: A pilot plant study.* AIChE Journal, 2014. **60**(5): p. 1830-1842.
20. Lockwood, T., *A Compararitive Review of Next-generation Carbon Capture Technologies for Coal-fired Power Plant.* Energy Procedia, 2017. **114**: p. 2658-2670.
21. Ramasubramanian, K. and W.S.W. Ho, *Recent developments on membranes for post-combustion carbon capture.* Current Opinion in Chemical Engineering, 2011. **1**(1): p. 47-54.
22. Merkel, T.C., M. Zhou, and R.W. Baker, *Carbon dioxide capture with membranes at an IGCC power plant.* Journal of Membrane Science, 2012. **389**: p. 441-450.

23. Xue, E., M. O'Keeffe, and J.R.H. Ross, *Water-gas shift conversion using a feed with a low steam to carbon monoxide ratio and containing sulphur.* Catalysis Today, 1996. **30**(1): p. 107-118.
24. Subramanian, A.S.R., et al., *A Comparison of Post-combustion Capture Technologies for the NGCC.* Energy Procedia, 2017. **114**: p. 2631-2641.
25. Bounaceur, R., et al., *Membrane processes for post-combustion carbon dioxide capture: A parametric study.* Energy, 2006. **31**(14): p. 2556-2570.
26. Favre, E., *Carbon dioxide recovery from post-combustion processes: Can gas permeation membranes compete with absorption?* Journal of Membrane Science, 2007. **294**(1): p. 50-59.
27. Favre, E., *Membrane processes and postcombustion carbon dioxide capture: Challenges and prospects.* Chemical Engineering Journal, 2011. **171**(3): p. 782-793.
28. Papaioannou, E.I., H. Qi, and I.S. Metcalfe, *'Uphill' permeation of carbon dioxide across a composite molten salt-ceramic membrane.* Journal of Membrane Science, 2015. **485**: p. 87-93.
29. Favre, E., R. Bounaceur, and D. Roizard, *A hybrid process combining oxygen enriched air combustion and membrane separation for post-combustion carbon dioxide capture.* Separation and Purification Technology, 2009. **68**(1): p. 30-36.
30. Sreedhar, I., et al., *Process and engineering trends in membrane based carbon capture.* Renewable and Sustainable Energy Reviews, 2017. **68**: p. 659-684.
31. Li, K., *Ceramic Membranes and Membrane Processes*, in *Ceramic Membranes for Separation and Reaction*. 2007, John Wiley & Sons, Ltd.
32. Kong, J. and K. Li, *An improved gas permeation method for characterising and predicting the performance of microporous asymmetric hollow fibre membranes used in gas absorption.* Journal of Membrane Science, 2001. **182**(1): p. 271-281.
33. W. Liepmann , H., *Gas kinetics and gas dynamics of orifice flow*. Vol. 10. 1961. 65-79.
34. Sotirchos, S.V. and V.N. Burganos, *Transport of Gases in Porous Membranes.* MRS Bulletin, 1999. **24**(3): p. 41-45.
35. Rackley, S.A., *Carbon Capture and Storage*. 2010, Elsevier.
36. Knudsen, M., *Die Gesetze der Molekularströmung und der inneren Reibungsströmung der Gase durch Röhren.* Annalen der Physik, 1909. **333**(1): p. 75-130.
37. Khalilpour, R., et al., *Membrane-based carbon capture from flue gas: a review.* Journal of Cleaner Production, 2015. **103**: p. 286-300.
38. Koros, W.J. and G.K. Fleming, *Membrane-based gas separation.* Journal of Membrane Science, 1993. **83**(1): p. 1-80.
39. Ismail, A.F., et al., *Transport Mechanism of Carbon Membranes*, in *Carbon-based Membranes for Separation Processes*. 2011, Springer New York: New York, NY. p. 5-16.
40. Yeo, Z.Y., et al., *Conventional processes and membrane technology for carbon dioxide removal from natural gas: A review.* Journal of Natural Gas Chemistry, 2012. **21**(3): p. 282-298.
41. Brunetti, A., et al., *Membrane technologies for CO_2 separation.* Journal of Membrane Science, 2010. **359**(1): p. 115-125.
42. Zaman, M. and J.H. Lee, *Carbon capture from stationary power generation sources: A review of the current status of the technologies.* Korean Journal of Chemical Engineering, 2013. **30**(8): p. 1497-1526.
43. Dushyant, S., R.L. David, and W.P. Henry, *A Review of Carbon Dioxide Selective Membranes: A Topical Report*. 2003, ; National Energy Technology Lab., Pittsburgh, PA (US); National Energy Technology Lab., Morgantown, WV (US). p. Medium: ED; Size: 1,040 pages.
44. Bredesen, R., K. Jordal, and O. Bolland, *High-temperature membranes in power generation with CO_2 capture.* Chemical Engineering and Processing: Process Intensification, 2004. **43**(9): p. 1129-1158.
45. Tong, Z. and W.S.W. Ho, *Facilitated transport membranes for CO_2 separation and capture.* Separation Science and Technology, 2017. **52**(2): p. 156-167.

46. Kasahara, S., et al., *Effect of water in ionic liquids on CO_2 permeability in amino acid ionic liquid-based facilitated transport membranes.* Journal of Membrane Science, 2012. **415-416**: p. 168-175.
47. Myers, C., et al., *High temperature separation of carbon dioxide/hydrogen mixtures using facilitated supported ionic liquid membranes.* Journal of Membrane Science, 2008. **322**(1): p. 28-31.
48. Chung, S.J., et al., *Dual-Phase Metal−Carbonate Membrane for High-Temperature Carbon Dioxide Separation.* Industrial & Engineering Chemistry Research, 2005. **44**(21): p. 7999-8006.
49. Anderson, M. and Y.S. Lin, *Carbonate–ceramic dual-phase membrane for carbon dioxide separation.* Journal of Membrane Science, 2010. **357**(1–2): p. 122-129.
50. Antolini, E., *The stability of molten carbonate fuel cell electrodes: A review of recent improvements.* Applied Energy, 2011. **88**(12): p. 4274-4293.
51. Turco, M., *Treatment of Biogas for Feeding High Temperature Fuel Cells.* Springer International Publishing, 2016.
52. Ghezel-Ayagh, H., et al., *Electrochemical Membrane Technology for Carbon Dioxide Capture from Flue Gas.* Energy Procedia, 2017. **108**: p. 2-9.
53. Wade, J.L., et al., *Composite electrolyte membranes for high temperature CO_2 separation.* Journal of Membrane Science, 2011. **369**(1–2): p. 20-29.
54. Nie, L., et al., *Effects of pore formers on microstructure and performance of cathode membranes for solid oxide fuel cells.* Journal of Power Sources, 2011. **196**(23): p. 9975-9979.
55. Zhang, G., E.I. Papaioannou, and I.S. Metcalfe, *Selective, high-temperature permeation of nitrogen oxides using a supported molten salt membrane.* Energy & Environmental Science, 2015. **8**(4): p. 1220-1223.
56. Tomkins., R.P.T. and N.P. Bansal., *Gases in Molten Salts.* Pergamon: Amsterdam, 1991: p. 95-275.
57. Di Felice, L., et al., *New high temperature sealing technique and permeability data for hollow fiber BSCF perovskite membranes.* Chemical Engineering and Processing: Process Intensification, 2016. **107**: p. 206-219.
58. Lin.Y.S. and S.J. Chung, *Dual Phase Membrane for High temperature CO_2 Separation.* Technical Progress Report. (Annual), 2002. **09/01/02. 08/30/03.**
59. Bhatia, S., C.Y. Thien, and A.R. Mohamed, *Oxidative coupling of methane (OCM) in a catalytic membrane reactor and comparison of its performance with other catalytic reactors.* Chemical Engineering Journal, 2009. **148**(2): p. 525-532.
60. Hatcher, J., et al., *Development and testing of an intermediate temperature glass sealant for use in mixed ionic and electronic conducting membrane reactors.* Solid State Ionics, 2010. **181**(15): p. 767-774.
61. Zhu, X., et al., *Operation of perovskite membrane under vacuum and elevated pressures for high-purity oxygen production.* Journal of Membrane Science, 2009. **345**(1): p. 47-52.
62. Wade, J.L., K.S. Lackner, and A.C. West, *Transport model for a high temperature, mixed conducting CO_2 separation membrane.* Solid State Ionics, 2007. **178**(27–28): p. 1530-1540.
63. Rui, Z., et al., *Modeling and analysis of carbon dioxide permeation through ceramic-carbonate dual-phase membranes.* Journal of Membrane Science, 2009. **345**(1): p. 110-118.
64. Li, Y., et al., *Performance of ionic-conducting ceramic/carbonate composite material as solid oxide fuel cell electrolyte and CO_2 permeation membrane.* Catalysis Today, 2009. **148**(3): p. 303-309.
65. Shackelford., J.F. and W. Alexander., *CRC materials science and engineering handbook 3rd ed* CRC press, 2001.
66. Lin, F.J.T., L.C. Jonghe, and M.N. Rahaman, *Microstructure Refinement of Sintered Alumina by a Two-Step Sintering Technique.* Journal of the American Ceramic Society, 1997. **80**(9): p. 2269-2277.
67. Kaur, G., *SOFC Technology: Its Working and Components*, in *Solid Oxide Fuel Cell Components: Interfacial Compatibility of SOFC Glass Seals*. 2016, Springer International Publishing: Cham. p. 79-122.

68. Thursfield, A. and I.S. Metcalfe, *High temperature gas separation through dual ion-conducting membranes.* Current Opinion in Chemical Engineering, 2013. **2**(2): p. 217-222.
69. Weppner, W., *Electronic transport properties and electrically induced p-n junction in ZrO2 + 10 m/o Y2O3.* Journal of Solid State Chemistry, 1977. **20**(3): p. 305-314.
70. Kharton, V.V., F.M.B. Marques, and A. Atkinson, *Transport properties of solid oxide electrolyte ceramics: a brief review.* Solid State Ionics, 2004. **174**(1): p. 135-149.
71. Ida, J.-i. and Y.S. Lin, *Mechanism of High-Temperature CO_2 Sorption on Lithium Zirconate.* Environmental Science & Technology, 2003. **37**(9): p. 1999-2004.
72. Tai, L.W., et al., *Structure and electrical properties of $La_{1-x}Sr_xCo_{1-y}Fe_yO_3$. Part 2. The system $La_{1-x}Sr_xCo_{0.2}Fe_{0.8}O_3$.* Solid State Ionics, 1995. **76**(3): p. 273-283.
73. Tai, L.W., et al., *Structure and electrical properties of $La_{1-x}Sr_xCo_{1-y}Fe_yO_3$. Part 1. The system $La_{0.8}Sr_{0.2}Co_{1-y}Fe_yO_3$.* Solid State Ionics, 1995. **76**(3): p. 259-271.
74. Anderson., H.U., et al., *Review of the Structural and Electrical Properties of the (La,Sr)(Co,Fe)O_3 System.* The Electrochem. Soc. , 1994. **Proc. of the 4th Intl. Symp. on Solid Oxide Fuel Cells**: p. 375-384.
75. Benson, S.J., R.J. Chater, and J.A. Kilner, *Oxygen diffusion and surface exchange in the mixed conducting perovskite $La_{0.6}Sr_{0.4}Fe_{0.8}Co_{0.2}O_{3-d}$.* 1997, The Electrochemical Society 1998. p. 596-609.
76. Larramendi, I.R.d., et al., *Perovskite Materials - Synthesis, Characterisation, Properties, and Applications, Chapter 20: Designing Perovskite Oxides for Solid Oxide Fuel Cells* 2016.
77. Scott, S.P., et al., *Reactivity of LSCF perovskites.* Solid State Ionics, 2002. **152-153**: p. 777-781.
78. Sahibzada, M., et al., *Solid Electrolyte Coulometric Studies of Oxide State and Kinetics.* Chemical Engineering Research and Design, 2000. **78**(7): p. 965-970.
79. Xu, S.J. and W.J. Thomson, *Stability of $La_{0.6}Sr_{0.4}Co_{0.2}Fe_{0.8}O_{3-\delta}$ Perovskite Membranes in Reducing and Nonreducing Environments.* Industrial & Engineering Chemistry Research, 1998. **37**(4): p. 1290-1299.
80. Teraoka, Y., et al., *OXYGEN PERMEATION THROUGH PEROVSKITE-TYPE OXIDES.* Chemistry Letters, 1985. **14**(11): p. 1743-1746.
81. Kojima, T., et al., *Density, Surface Tension, and Electrical Conductivity of Ternary Molten Carbonate System $Li_2CO_3 – Na_2CO_3 – K_2CO_3$ and Methods for Their Estimation.* Journal of The Electrochemical Society, 2008. **155**(7): p. F150-F156.
82. Näfe, H., *Conductivity of Alkali Carbonates, Carbonate-Based Composite Electrolytes and IT-SOFC.* ECS Journal of Solid State Science and Technology, 2014. **3**(2): p. N7-N14.
83. Ward, A.T. and G.J. Janz, *Molten carbonate electrolytes: Electrical conductance, density and surface tension of binary and ternary mixtures.* Electrochimica Acta, 1965. **10**(8): p. 849-857.
84. Janz., G.J., et al., *Physical Properties Data Compilations Relevant to Energy Storage. II. Molten Salts: Data on Single and Multi-Component Salt Systems.* U.S. DEPARTMENT OF COMMERCE, NATIONAL BUREAU OF STANDARDS, 1979.
85. White, S.H. and U.M. Twardoch, *The solubility and electrochemistry of alkali metal oxides in the molten eutectic mixture of lithium carbonate-sodium carbonate-potassium carbonate.* Journal of Applied Electrochemistry, 1989. **19**(6): p. 901-910.
86. Atkins, P.W., *Atkins' physical chemistry*. 11th edition.. ed. Physical chemistry, ed. J. De Paula and J. Keeler. 2017: Oxford : Oxford University Press.
87. Spedding, P.L. and R. Mills, *Trace-Ion Diffusion in Molten Alkali Carbonates.* Journal of The Electrochemical Society, 1965. **112**(6): p. 594-599.
88. Lorenz, P.K. and G.J. Janz, *Determination of the CO_2 dissociation pressures of molten carbonates by an EMF technique.* Electrochimica Acta, 1970. **15**(12): p. 2001-2005.
89. Mutch, G.A., et al., *Supported molten-salt membranes for carbon dioxide permeation.* Journal of Materials Chemistry A, 2019. **7**(21): p. 12951-12973.
90. Tong, J., et al., *Remarkable O_2 permeation through a mixed conducting carbon capture membrane functionalized by atomic layer deposition.* Journal of Materials Chemistry A, 2016. **4**(5): p. 1828-1837.

91. Fang, J., et al., *CO_2 capture performance of silver-carbonate membrane with electrochemically dealloyed porous silver matrix.* Journal of Membrane Science, 2017. **523**: p. 439-445.
92. Zhang, L., et al., *Fast electrochemical CO_2 transport through a dense metal-carbonate membrane: A new mechanistic insight.* Journal of Membrane Science, 2014. **468**: p. 373-379.
93. Merkel, T.C., et al., *Power plant post-combustion carbon dioxide capture: An opportunity for membranes.* Journal of Membrane Science, 2010. **359**(1): p. 126-139.
94. Ortiz-Landeros, J., T. Norton, and Y.S. Lin, *Effects of support pore structure on carbon dioxide permeation of ceramic-carbonate dual-phase membranes.* Chemical Engineering Science, 2013. **104**: p. 891-898.
95. Zhang, L., et al., *High CO_2 permeation flux enabled by highly interconnected three-dimensional ionic channels in selective CO_2 separation membranes.* Energy & Environmental Science, 2012. **5**(8): p. 8310-8317.
96. Lu, B. and Y.S. Lin, *Synthesis and characterization of thin ceramic-carbonate dual-phase membranes for carbon dioxide separation.* Journal of Membrane Science, 2013. **444**: p. 402-411.
97. Zuo, M., et al., *Ionic conducting ceramic–carbonate dual phase hollow fibre membranes for high temperature carbon dioxide separation.* Journal of Membrane Science, 2014. **458**: p. 58-65.
98. Ahn, H., et al., *YSZ-carbonate dual-phase membranes for high temperature carbon dioxide separation.* Journal of Industrial and Engineering Chemistry, 2014. **20**(5): p. 3703-3708.
99. Chen, T., et al., *High CO_2 permeability of ceramic-carbonate dual-phase hollow fiber membrane at medium-high temperature.* Journal of Membrane Science, 2020. **597**: p. 117770.
100. Patrício, S.G., et al., *High performance composite CO_2 separation membranes.* Journal of Membrane Science, 2014. **471**(0): p. 211-218.
101. Xu, N., et al., *Silver-molten carbonate composite as a new high-flux membrane for electrochemical separation of CO_2 from flue gas.* Journal of Membrane Science, 2012. **401-402**: p. 190-194.
102. Ishihara, T., N.M. Sammes, and O. Yamamoto, *Chapter 4 - Electrolytes*, in *High Temperature and Solid Oxide Fuel Cells*, S.C. Singhal and K. Kendall, Editors. 2003, Elsevier Science: Amsterdam. p. 83-117.
103. Zheng, Y., et al., *Synthesis and characterization of $Ce_{0.8}Sm_{0.2}O_{1.9}$ nanopowders using an acrylamide polymerization process.* Journal of Rare Earths, 2010. **28**(1): p. 92-95.
104. Dong, X., H.-C. Wu, and Y.S. Lin, *CO_2 permeation through asymmetric thin tubular ceramic-carbonate dual-phase membranes.* Journal of Membrane Science, 2018. **564**: p. 73-81.
105. Norton, T.T., J. Ortiz-Landeros, and Y.S. Lin, *Stability of La–Sr–Co–Fe Oxide–Carbonate Dual-Phase Membranes for Carbon Dioxide Separation at High Temperatures.* Industrial & Engineering Chemistry Research, 2014. **53**(6): p. 2432-2440.
106. Zhuang, S., et al., *Perovskite oxide and carbonate composite membrane for carbon dioxide transport.* Materials Letters, 2019. **236**: p. 329-333.
107. Tong, J., et al., *Electrochemical separation of CO_2 from a simulated flue gas with high-temperature ceramic–carbonate membrane: New observations.* Journal of Membrane Science, 2015. **477**: p. 1-6.
108. Zhang, L., *Dual-Phase Mixed Ion and Electron Conducting CO_2-Selective Permeation Membranes.* 2013. **Doctoral dissertation**.
109. Fang, J., J. Tong, and K. Huang, *A superior mixed electron and carbonate-ion conducting metal-carbonate composite membrane for advanced flue-gas carbon capture.* Journal of Membrane Science, 2016. **505**: p. 225-230.
110. Qi, H., *Porous $La_xSr_{(1-x)}Co_yFe_{(1-y)}O_{(3-d)}$ - molten alkali metal carbonate membranes for CO_2 permeation.* Newcastle University, 2016. **PhD Thesis**.
111. Goldstein, J.I., et al., *Electron Beam—Specimen Interactions: Interaction Volume*, in *Scanning Electron Microscopy and X-Ray Microanalysis*. 2018, Springer New York: New York, NY. p. 1-14.

112. *Introduction to SEM.* Hitachi official website, (https://www.hitachi-hightech.com/global/tm/what/intro/).
113. Dinnebier, R.E. and S.J.L. Billinge, *Chapter 1 Principles of Powder Diffraction*, in *Powder Diffraction: Theory and Practice*. 2008, The Royal Society of Chemistry. p. 1-19.
114. Waseda, Y., E. Matsubara, and K. Shinoda, *Diffraction from Polycrystalline Samples and Determination of Crystal Structure*, in *X-Ray Diffraction Crystallography: Introduction, Examples and Solved Problems*, Y. Waseda, E. Matsubara, and K. Shinoda, Editors. 2011, Springer Berlin Heidelberg: Berlin, Heidelberg. p. 107-167.
115. Abell, A.B., K.L. Willis, and D.A. Lange, *Mercury Intrusion Porosimetry and Image Analysis of Cement-Based Materials.* Journal of Colloid and Interface Science, 1999. **211**(1): p. 39-44.
116. Tyrer-Tomkinson, I., *MASsoft Professional Version 7 Training Manual*. **Hiden Analytical**.
117. Coplen Tyler, B., et al., *Isotope-abundance variations of selected elements (IUPAC Technical Report)*, in *Pure and Applied Chemistry*. 2002. p. 1987.
118. Fraga, S.C., et al., *A novel time lag method for the analysis of mixed gas diffusion in polymeric membranes by on-line mass spectrometry: Method development and validation.* Journal of Membrane Science, 2018. **561**: p. 39-58.
119. D'Autry, W., et al., *Characterization and Improvement of Signal Drift Associated with Electron Ionization Quadrupole Mass Spectrometry.* Analytical Chemistry, 2010. **82**(15): p. 6480-6486.
120. *LI-840A CO_2/H_2O Analyzer Instruction Manual.* 2016. **LI-COR**.
121. Lamouri, S., et al., *Control of the γ-alumina to α-alumina phase transformation for an optimized alumina densification.* Boletín de la Sociedad Española de Cerámica y Vidrio, 2017. **56**(2): p. 47-54.
122. T. B. Polla, P., et al., *Evaluation of electrical conductivity and density of 8 mol% yttria-stabilized zirconia produced by Spark Plasma Sintering*. 2016. 123-135.
123. Chen, Z., *Mechanical Properties of $La_{0.6}Sr_{0.4}Co_{0.2}Fe_{0.8}O_3$ Fuel Cell Electrodes.* URI: http://hdl.handle.net/10044/1/24705, 2014.
124. Claes, P., B. Thirion, and J. Glibert, *Solubility of CO_2 in the molten Na_2CO_3—K_2CO_3 (42 mol %) eutectic mixture at 800 °C.* Electrochimica Acta, 1996. **41**(1): p. 141-146.
125. Prins-Jansen, J.A., et al., *A Three-Phase Homogeneous Model for Porous Electrodes in Molten-Carbonate Fuel Cells.* Journal of The Electrochemical Society, 1996. **143**(5): p. 1617-1628.
126. Stevenson, J.W., et al., *Electrochemical Properties of Mixed Conducting Perovskites $La_{1-x}M_xCo_{1-y}Fe_yO_{3-\delta}$ (M = Sr, Ba, Ca).* Journal of The Electrochemical Society, 1996. **143**(9): p. 2722-2729.
127. Nguyen, H.V.P., et al., *A New Cathode for Reduced-Temperature Molten Carbonate Fuel Cells.* Journal of The Electrochemical Society, 2014. **161**(14): p. F1458-F1467.
128. Xing, W., et al., *Improved CO_2 flux by dissolution of oxide ions into the molten carbonate phase of dual-phase CO_2 separation membranes.* Separation and Purification Technology, 2019. **212**: p. 723-727.
129. Zink, P.A., et al., *Analysis of the Electronic and Ionic Conductivity of Calcium-Doped Lanthanum Ferrite.* Electrochemical and Solid-State Letters, 2009. **12**(10): p. B141-B143.
130. Bouwmeester, H.J.M. and A.J. Burggraaf, *Chapter 10 Dense ceramic membranes for oxygen separation*, in *Membrane Science and Technology*, A.J. Burggraaf and L. Cot, Editors. 1996, Elsevier. p. 435-528.
131. Yuhua, D., *Electronic structural and electrochemical properties of lithium zirconates and their capabilities of CO_2 capture: A first-principles density-functional theory and phonon dynamics approach.* Journal of Renewable and Sustainable Energy, 2011. **3**(1): p. 013102.
132. Hashimoto, S.-i., et al., *Oxygen nonstoichiometry and thermo-chemical stability of $La_{0.6}Sr_{0.4}Co_{1-y}Fe_yO_{3-\delta}$ (y=0.2, 0.4, 0.6, 0.8).* Solid State Ionics, 2010. **181**(37): p. 1713-1719.
133. Itoh, T. and M. Nakayama, *Using in situ X-ray absorption spectroscopy to study the local structure and oxygen ion conduction mechanism in $(La_{0.6}Sr_{0.4})(Co_{0.2}Fe_{0.8})O_{3-\delta}$.* Journal of Solid State Chemistry, 2012. **192**: p. 38-46.

134. Hashimoto, S.-i., et al., *Thermal and chemical lattice expansibility of $La_{0.6}Sr_{0.4}Co_{1-y}Fe_yO_{3-\delta}$ (y=0.2, 0.4, 0.6 and 0.8).* Solid State Ionics, 2011. **186**(1): p. 37-43.
135. Zuev, A., L. Singheiser, and K. Hilpert, *Defect structure and isothermal expansion of A-site and B-site substituted lanthanum chromites.* Solid State Ionics, 2002. **147**(1): p. 1-11.
136. Zhang, L., et al., *Flux of silver-carbonate membranes for post-combustion CO_2 capture: The effects of membrane thickness, gas concentration and time.* Journal of Membrane Science, 2014. **455**: p. 162-167.
137. Robie, R.A. and B.S. Hemingway, *Thermodynamic properties of minerals and related substances at 298.15 K and 1 bar (10^5 pascals) pressure and at higher temperatures*, in *Bulletin*. 1995.
138. Shock, E.L. and H.C. Helgeson, *Calculation of the thermodynamic and transport properties of aqueous species at high pressures and temperatures: Correlation algorithms for ionic species and equation of state predictions to 5 kb and 1000°C.* Geochimica et Cosmochimica Acta, 1988. **52**(8): p. 2009-2036.
139. Chhabra, R. and V. Shankar, *Coulson and Richardson's Chemical Engineering, Volume 1B - Heat and Mass Transfer - Fundamentals and Applications (7th Edition)*. 2018, Elsevier.
140. Dr. Don, W.G. and Z.S. Dr. Marylee, *TRANSPORT PROPERTIES*, in *Perry's Chemical Engineers' Handbook, 9th Edition*. 2019, McGraw Hill Professional, Access Engineering.
141. Chuang, S.Y., et al., *Development and performance of Cu-based oxygen carriers for chemical-looping combustion.* Combustion and Flame, 2008. **154**(1): p. 109-121.
142. Chuang, S.Y., et al., *Kinetics of the Oxidation of a Co-precipitated Mixture of Cu and Al_2O_3 by O_2 for Chemical-Looping Combustion.* Energy & Fuels, 2010. **24**(7): p. 3917-3927.
143. Fan, L.-S. and F. Li, *Chemical Looping Technology and Its Fossil Energy Conversion Applications.* Industrial & Engineering Chemistry Research, 2010. **49**(21): p. 10200-10211.
144. Hu, W., et al., *Kinetics of oxygen uncoupling of a copper based oxygen carrier.* Applied Energy, 2016. **161**: p. 92-100.
145. Silakhori, M., et al., *Comparing the thermodynamic potential of alternative liquid metal oxides for the storage of solar thermal energy*. Vol. 157. 2017. 251-258.
146. Zhu, Y., K. Mimura, and M. Isshiki, *Oxidation Mechanism of Cu_2O to CuO at 600–1050°C.* Oxidation of Metals, 2004. **62**(3): p. 207-222.

Appendix I: Uphill CO_2 permeation experiment using YSZ-carbonate membrane

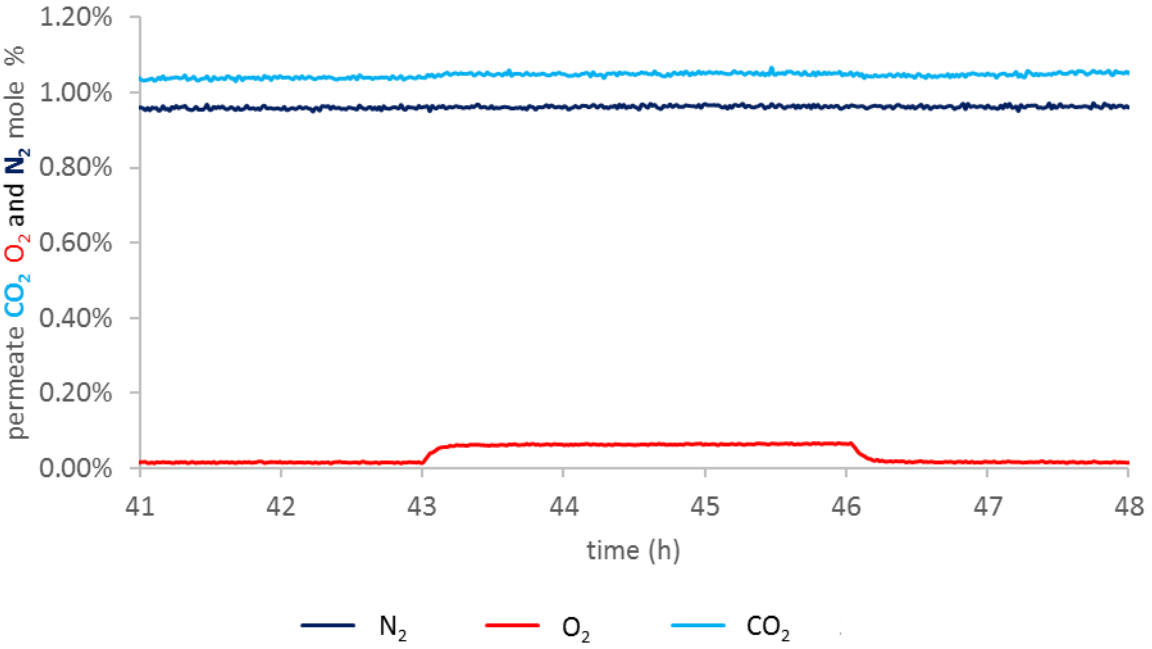

Figure A. 1: Permeate outlet gas composition during uphill CO_2 permeation experiment using YSZ-carbonate membrane at 600°C. 41-43th/46-48th hour: symmetrical operation flowing 1% CO_2, 1% N_2 in Ar into both reactor chambers; 43-46th hour: asymmetrical operation switching feed inlet gas to 1% CO_2, 1% N_2, 20% O_2 in Ar and maintaining same permeate inlet gas.

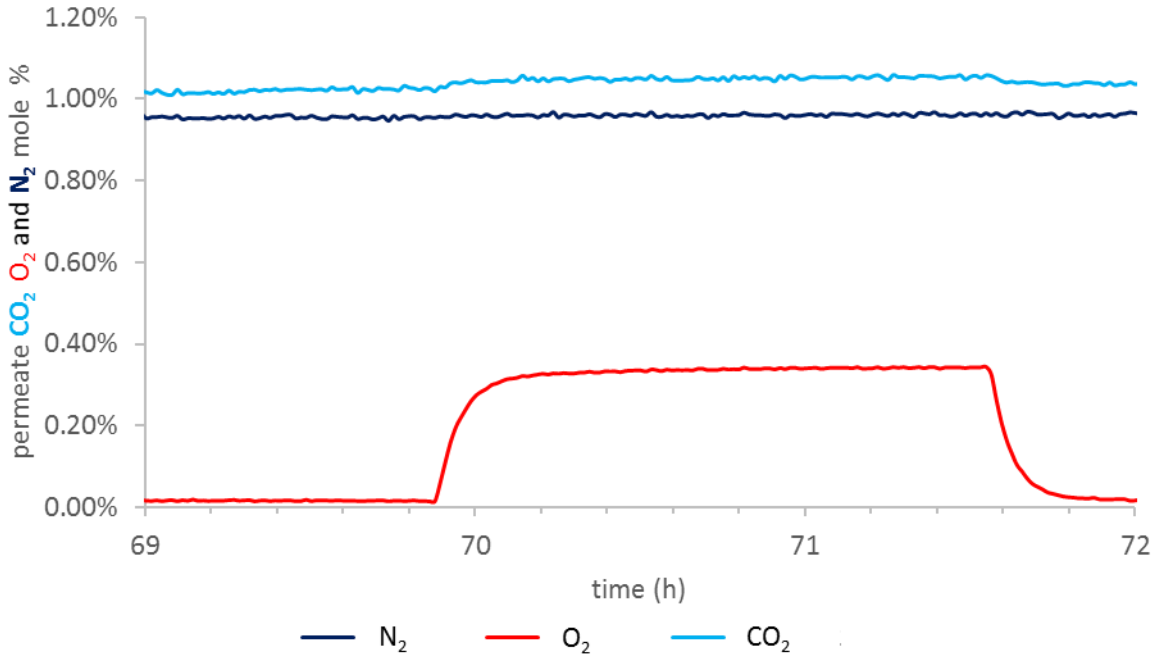

Figure A. 2: Permeate outlet gas composition during uphill CO_2 permeation experiment using YSZ-carbonate membrane at 800°C. 69-70th/71.5-72th hour: symmetrical operation; 70-71.5th hour: asymmetrical operation.

Appendix II: 'Zero flux' condition for CO_2 flux-driving force experiments

The following plots show the complementary results for the set 2 uphill CO_2 flux-driving force experiments that varying feed side CO_2 concentration and co-feeding 20% O_2. At 600°C, zero uphill CO_2 flux was observed when feeding 0.2% CO_2 and 20% O_2 (Figure A.3). Interestingly, the driving force with this condition was slightly above zero according to the linear flux-driving force model (see equation 6.5 and 6.10). The observation did not agree with the models, which predicted 'zero flux' should be observed at zero driving force.

When the same driving force condition was applied at 800°C, a backwards CO_2 permeation from permeate side to feed side was observed at steady state, following a transient CO_2 peak on permeate side (Figure A.4). This can be explained by the increase of solid phase O^{2-} conductivity allowing measurable backwards CO_2 permeation flux along the direction of CO_2 driving force itself. The results also indicated that with a CO_2 partial pressure difference of 0.9%, the backwards CO_2 permeation was only negligible at 600°C but not 800°C. In fact, the observed uphill CO_2 flux was a superimposed flux along forwards and backwards directions. The models, however, ignored the contribution of backwards permeation. This assumption became invalid under such a driving force condition at 800°C. At 600°C, the disagreement between the observed and the theoretical 'zero flux' condition could be that the flux was unmeasurable by the gas analyser when the driving force was decreased to a certain extent.

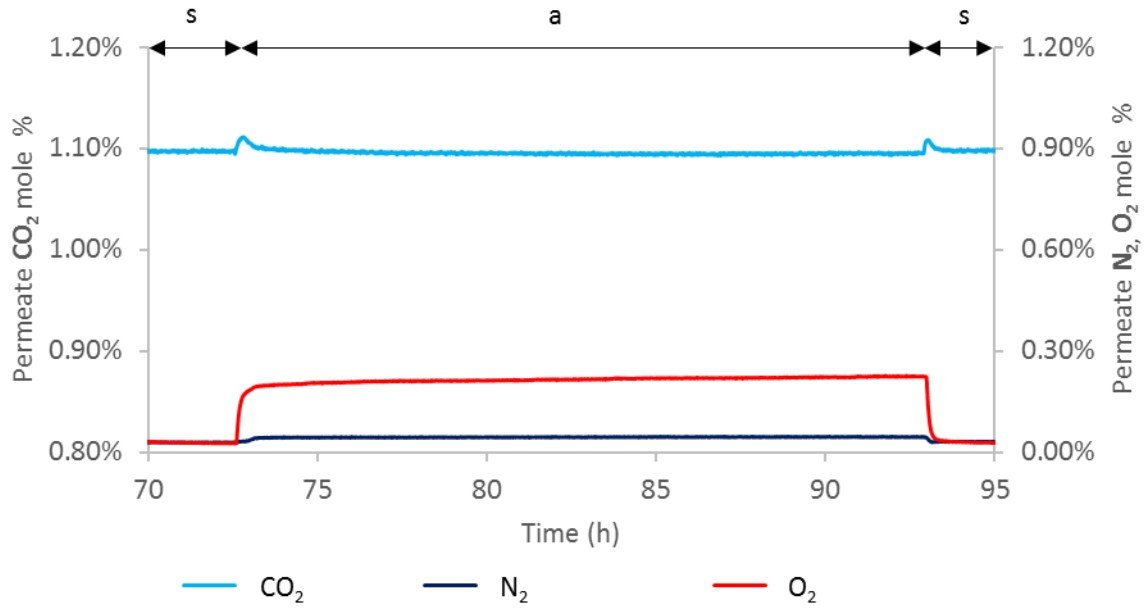

Figure A. 3: Permeate outlet gas composition during uphill CO_2 permeation experiment using LSCF6428-carbonate membrane at 600°C. s: symmetrical operation flowing 1.1% CO_2 in Ar into both reactor chambers; a: asymmetrical operation switching feed inlet gas to 0.2% CO_2, 0.2% N_2, 20% O_2 in Ar and maintaining same permeate inlet gas.

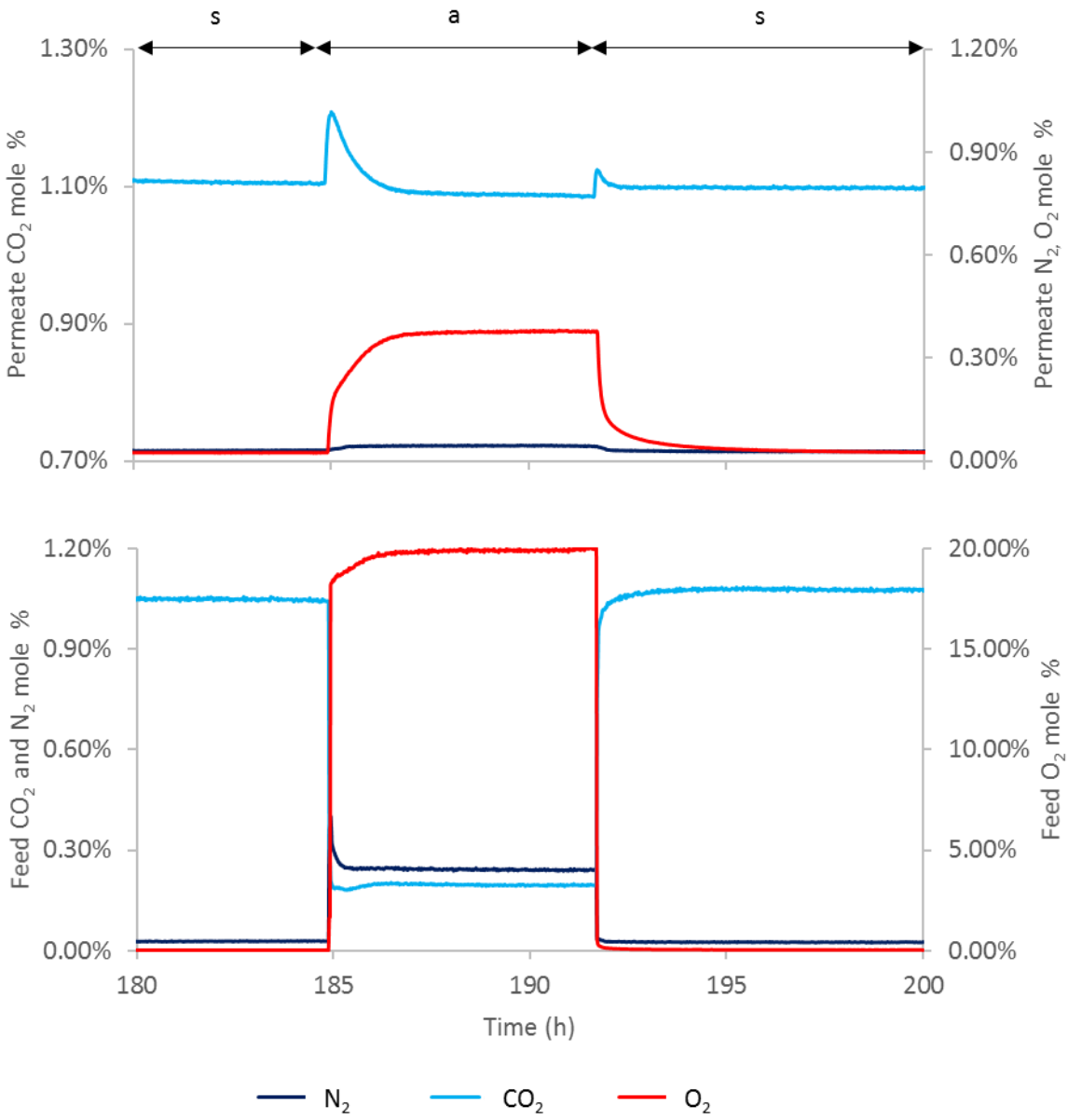

Figure A. 4: Permeate (top) and feed (bottom) outlet gas composition during uphill CO_2 permeation experiment using LSCF6428-carbonate membrane at 800°C. s: symmetrical operation flowing 1.1% CO_2 in Ar into both reactor chambers; a: asymmetrical operation switching feed inlet gas to 0.2% CO_2, 0.2% N_2, 20% O_2 in Ar and maintaining same permeate inlet gas.

Appendix III: Reference uphill experiment before/after CO exposure

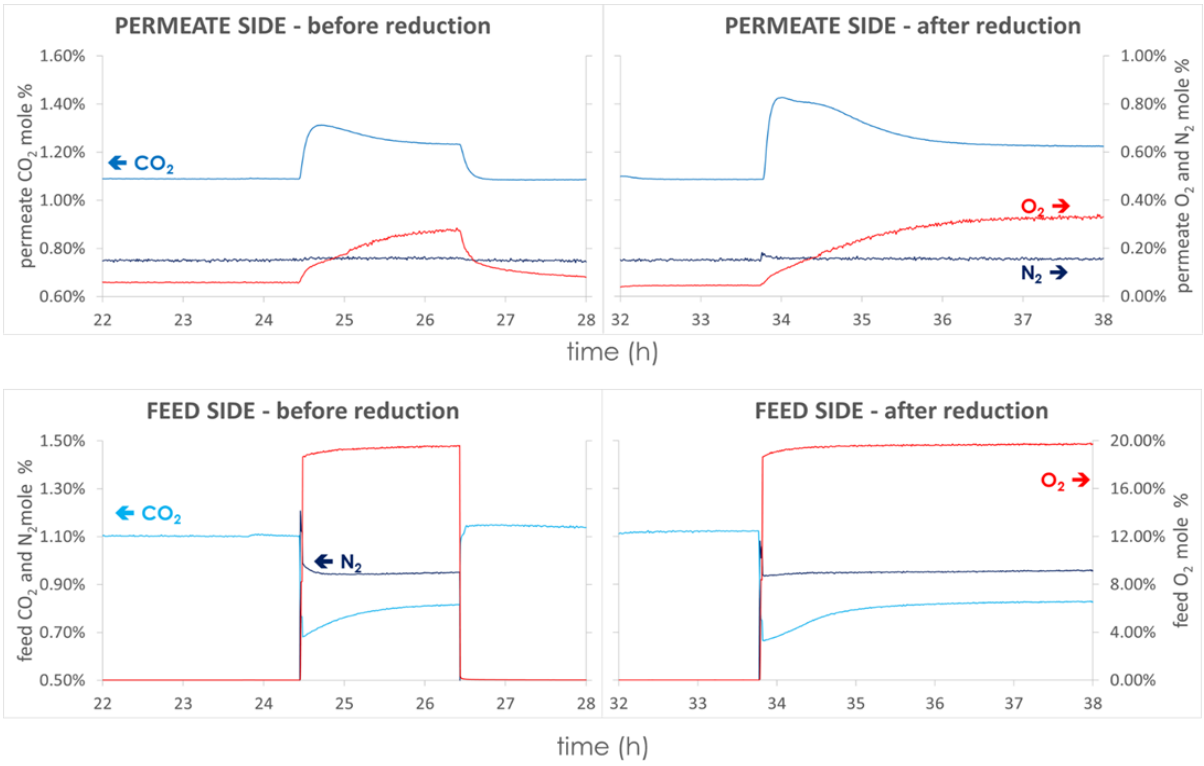

Figure A. 5: Reference uphill CO_2 permeation experiment at 800°C with the following operating procedures: 22nd-24.5th, 26.5-28th and 32nd-34th hour - symmetrical operation flowing 1.1% CO_2/Ar into both reactor chambers. 24.5-26.5th hour – asymmetrical operation switching feed inlet gas to 1% CO_2, 1% N_2, 20% O_2 in Ar and maintaining the same permeate inlet gas. 28th-32nd hour: 4 hours continuous exposure of 5% CO, 5% CO_2/Ar on membrane permeate side. 34-38th hour – asymmetrical operation after the CO exposure.

For the uphill CO_2 permeation experiment with permeate side O_2 removal, in-situ CuO reduction would also reduce the LSCF membrane support. Any change of CO_2 permeation flux after in-situ reduction can arise from the modification of membrane oxygen nonstoichiometry. This reference uphill CO_2 permeation experiment was designed to test the effect of CO exposure to CO_2 permeation flux, without OCM for permeate side O_2 removal. The CO exposure simulated the in-situ reduction process. The uphill CO_2 flux before and after the CO exposure were compared. During the second asymmetrical operation after the CO exposure, a higher transient CO_2 peak can be observed on permeate side. Corresponding transient CO_2 dip on feed side was also lower than before CO exposure. It worth noting that at the peak values of the transient CO_2 concentration, the permeate side oxygen concentrations were similar before and after CO exposure. Therefore, the peak was not due to driving force enhancement. It was more likely caused by the modification of the membrane support material by reducing gas. Continuous feeding of O_2 allowed the support nonstoichiometry to recover, giving same steady state uphill CO_2 flux regardless of the CO exposure. Overall, the reference experiment revealed that in-situ reduction of OCM would affect transient uphill CO_2 permeation flux and interrupt with any true effect due to driving force enhancement.

Appendix IV: Residence time distribution of the membrane reactor

Residence time distribution (RTD) for the dual chamber membrane reactor was measured using the principle of tracer experiments. The inlet gas flow into the two chambers was initially 1.05% CO_2/Ar. Once steady state concentration was observed, inlet gas flow for both chambers were switched to pure Ar. The declining curve of CO_2 concentration C(t) for each chamber was monitored using gas analysers. Furthermore, normalised residence time distribution function over time E(t) was calculated using the flowing equation:

$$E(t) = \frac{C(t)}{\int_0^\infty C(t)dt} \qquad (A.1)$$

The mean residence time $\bar{t}$ for each reactor chamber can be calculated as:

$$\bar{t} = \int_0^\infty t\, E(t)\, dt = \frac{\int_0^\infty t\, C(t)\, dt}{\int_0^\infty C(t)dt} \qquad (A.2)$$

This can be compared with the space time τ of the reactor chambers, defined as the volume of the reactor chamber V_R divided by the volumetric flow rate of the inlet gas F:

$$\tau = \frac{V_R}{F} \qquad (A.3)$$

The measured mean residence time $\bar{t}$ based on the residence time distribution were 3.5 minutes for feed side chamber and 5.4 minutes for permeate side chamber. The feed and permeate chamber volumes were roughly 12cm^3 and 175cm^3 respectively. A 4m PFA tubing with 1/8-inch inner diameter was used to connect between the feed side chamber outlet and mass spectrometer, creating extra 28cm^3 volume. The space time τ for feed and permeate chamber were 2 minutes and 8.75 minutes respectively.

For the feed chamber, the mean residence time $\bar{t}$ was larger than the space time τ, indicating that flow recirculation may exist from the feed chamber the mass spectrometer. However, the space time may have been underestimated since the volume of the capillary inlet of mass spectrometer was not accounted. IR gas analyser was used for the permeate chamber without introducing extra volume. The mean residence time $\bar{t}$ of the permeate chamber was smaller than space time τ, indicating some volume of the permeate chamber was bypassed. Considering the geometry of the permeate chamber (see Figure 3.8), a small proportion sweep gas flow may not pass the membrane permeate side surface before reaching the chamber outlet. Precisely, the observed gas concentration would be an underestimation of gas concentration upon membrane permeate side surface. Given that the mean residence time $\bar{t}$ was not vastly different from the space time τ for both chambers, it was reasonable to assume the detected gas concentrations on gas analysers were approximately equal to the bulk gas phase concentration upon membrane surfaces.

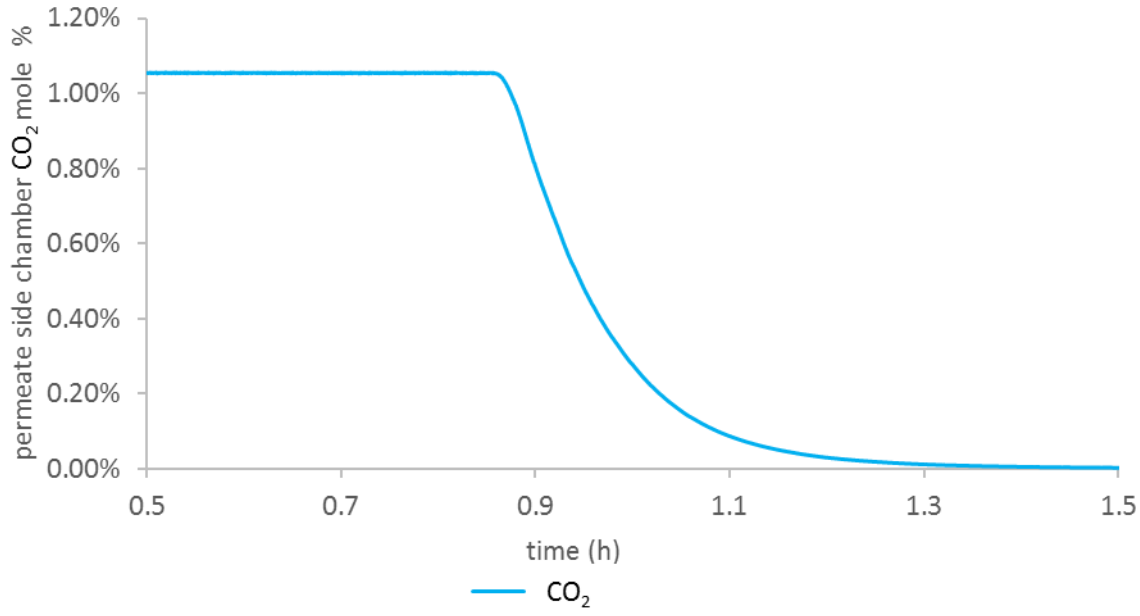

Figure A. 6: The variation of CO_2 concentration over time C(t) during the tracer experiment for permeate side reactor chamber. Chamber inlet gas was initially 1.05% CO_2, followed by a switch to pure Ar.

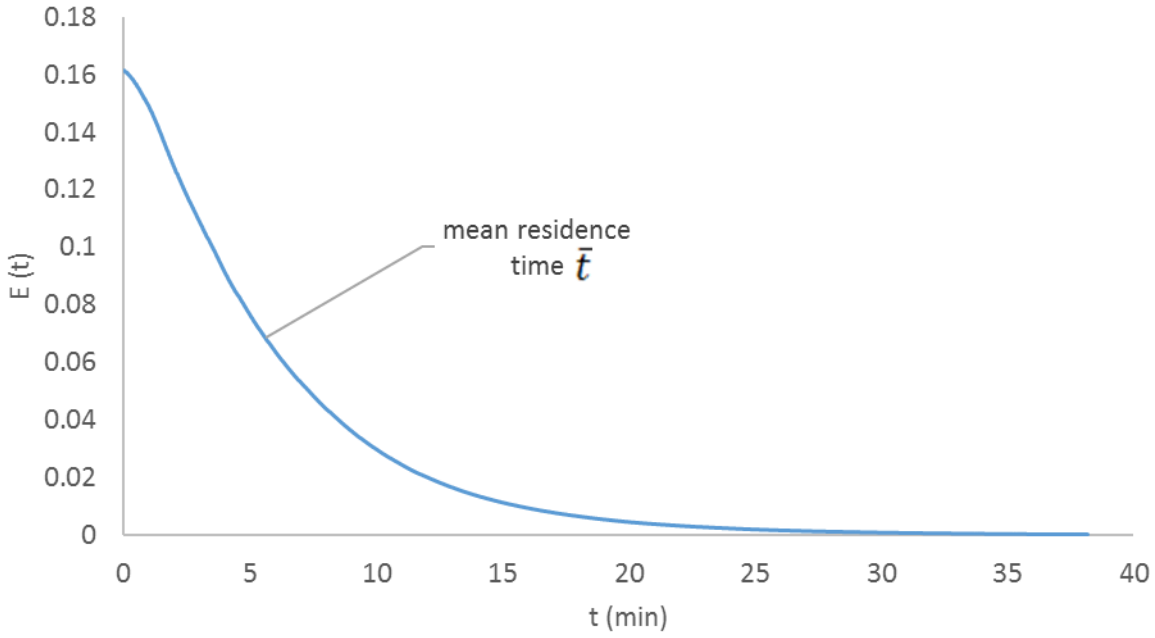

Figure A. 7: The residence time distribution function over time E(t) during the tracer experiment for permeate side reactor chamber. Chamber inlet gas was initially 1.05% CO_2, followed by a switch to pure Ar.

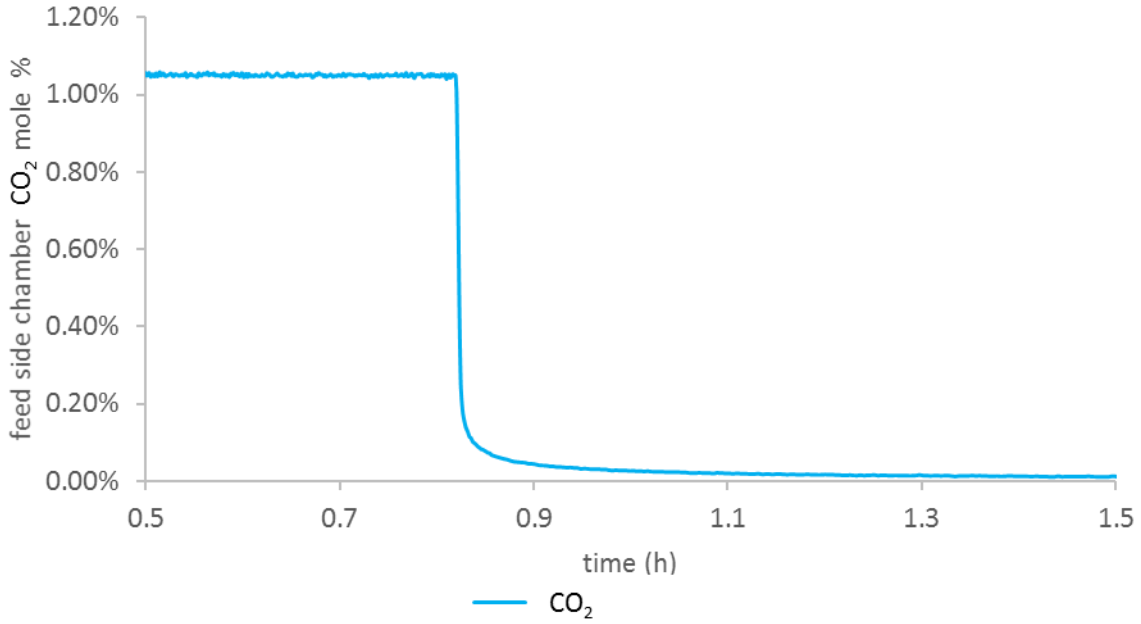

Figure A. 8: The variation of CO_2 concentration over time C(t) during the tracer experiment for feed side reactor chamber. Chamber inlet gas was initially 1.05% CO_2, followed by a switch to pure Ar.

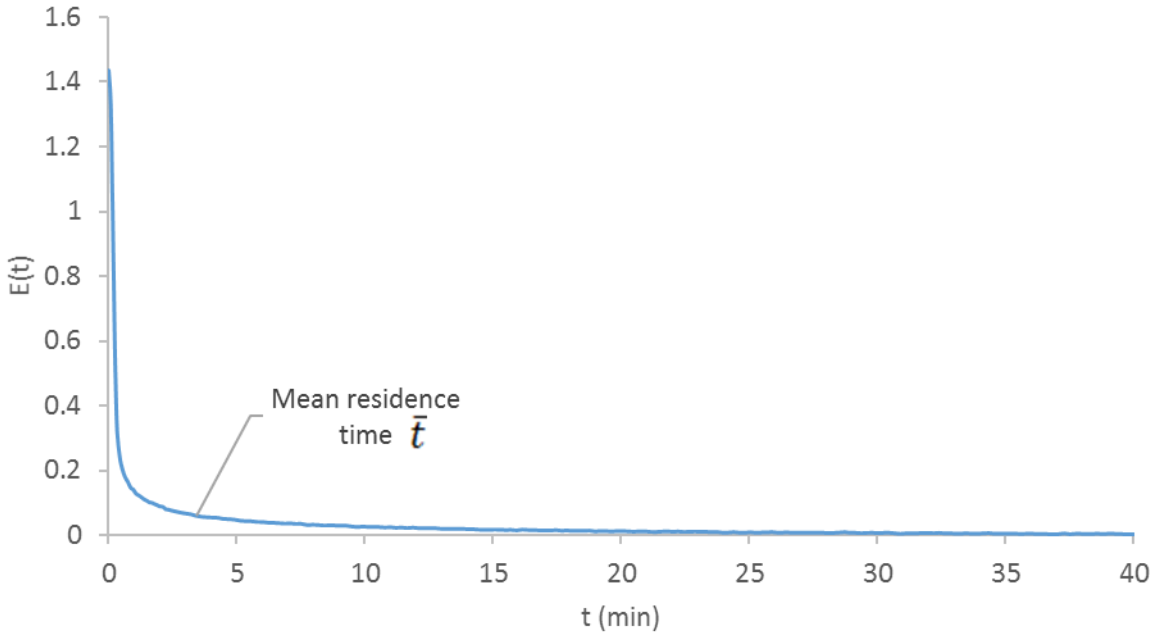

Figure A. 9: The residence time distribution function over time E(t) during the tracer experiment for feed side reactor chamber. Chamber inlet gas was initially 1.05% CO_2, followed by a switch to pure Ar.